SLAC-R-674
UC-414

A Precise Measurement of the Spin Structure Functions G**P(2) G**D(2) from SLAC Experiment E155X*

Dustin Edward McNulty

Stanford Linear Accelerator Center
Stanford University
Stanford, CA 94309

SLAC-Report-674
August 2002

Prepared for the Department of Energy
under contract number DE-AC03-76SF00515

Printed in the United States of America. Available from the National Technical Information Service, U.S. Department of Commerce, 5285 Port Royal Road, Springfield, VA 22161.

* Ph.D. thesis, University of Virginia, Charlottesville, VA 22901.

A PRECISE MEASUREMENT OF THE SPIN STRUCTURE FUNCTIONS g_2^p AND g_2^d FROM SLAC EXPERIMENT E155X

Dustin Edward McNulty
Fairfax, Virginia

B.S., James Madison University, 1994
M.A., University of Virginia, 2001

A Dissertation Presented to the Graduate
Faculty of the University of Virginia
in Candidacy for the Degree of Doctor of Philosophy

Department of Physics

University of Virginia
August, 2002

_____

_____

_____

_____

_____

Abstract

A precision measurement of the deep inelastic polarized structure functions $g_2^p(x,Q^2)$ and $g_2^d(x,Q^2)$ and the virtual photon asymmetries $A_2^p(x,Q^2)$ and $A_2^d(x,Q^2)$ has been made by the E155x collaboration in the ranges $0.02 < x < 0.8$ and 0.7 (GeV/c)^2 $< Q^2 < 20$ (GeV/c)^2. The transverse asymmetry ($A_\perp$) was measured at SLAC using 29.1 and 32.3 GeV longitudinally polarized electrons incident on transversely polarized target protons and deuterons; the scattered electrons were detected by three fixed angle spectrometers at 2.75°, 5.5°, and 10.5° from the beam line. g_2 was extracted using the measured $A_\perp$, an E155 phenomenological fit to g_1/F_1, and the SLAC fit to $R(x,Q^2)$; the function F_1 was obtained from the most recent NMC fit to $F_2(x,Q^2)$. The errors on g_2 for both proton and deuteron are more than three times smaller than those of the previously existing world data set, thus enabling the data to resolve clearly between g_2^{ww} and zero as well as make distinctions between various models. In addition, the Burkhardt-Cottingham and Efremov-Leader-Teryaev sum rules were evaluated over the measured kinematic region, as well as the d_2 twist-3 matrix element for the proton and neutron.

Acknowledgements

The success of E155x is attributed to the 82 members of its collaboration and the first-rate staff and facilities at SLAC. I feel privileged to have worked with such an outstanding group of physicists and I would like to thank them all. I would especially like to thank Donald Crabb, Donal Day, Oscar Rondon, Stephen Bültmann, Ray Arnold, Peter Bosted, Steve Rock, and Lee Sorrell for their tremendous contributions and for their commitment to the students. I would also like to extend my deepest gratitude to my fellow thesis students: Nawal Benmouna and Paul Depietro.

Special thanks to my advisor, Dr. Donald Crabb, for providing me the opportunity to participate in this experiment and guiding me through the completion of my dissertation.

Thanks to the past and present students of the UVA polarized target group for several years of support and companionship.

As I reflect upon everything that has made this work possible, I realize that I owe much of my success and accomplishments in life to my parents, Craig and Donna McNulty, and my brother Chris. Your unending love and support have guided me through life and allowed me to achieve my goals. I am eternally grateful for the confidence, wisdom, and strength you have instilled in me. Not many souls are as fortunate as I.

Finally, I dedicate this work to the love of my life, my wife Kerrie Bauer. I could not have completed this project without the continuous love and encouragement you gave me. Along our journey together, we have discovered the true meanings of sacrifice and perseverance while simultaneously experiencing the true joys in life–our children.

Contents

List of Figures

List of Tables

Chapter 1

Introduction

The seeds of nuclear physics took root nearly a century ago with the discovery of the nuclear atom model by Rutherford in 1910. His discovery was born out of clever insight and data analysis from some of the first particle scattering experiments ever conducted. Around 1920, Rutherford coined the term 'proton' to refer to the positively charged nucleon, and predicted the existence of a neutral nucleon–he referred to as the 'neutron'. The discovery of the neutron by Chadwick in 1932 firmly established the prevailing nuclear model in which protons and neutrons were viewed as the basic nuclear constituents of all elements.

In 1935, Yukawa proposed that the 'strong' short-range nuclear force, responsible for binding nucleons within a nucleus, was created by the exchange of 'π-mesons' between the nucleons. His theory predicted the mass of the π-meson, or pion, and in 1947 it was discovered using cosmic ray studies. Many predicted, and new, particles were being discovered in this era at an astonishing rate: Antiparticles, neutrinos, muons, pions, kaons, and other exotic particles. The growing data base of new particles combined with studies of particle decays and resonances gave rise to distinctions between different classes of particles based on the types of interactions

in which they participated. Leptons (electrons, muons, neutrinos, etc.) are particles which do not experience the strong-nuclear force; hadrons (protons, neutrons, pions, etc.) are particles that do experience the strong-nuclear force. Furthermore, leptons are considered as structureless point-like fundamental particles, whereas hadrons are composite. In 1964, Gell-Mann and Zweig proposed that 'quark' particles were the fundamental building blocks of hadrons: A three quark composite particle is called a baryon (proton, neutron, Lambda, etc.) and a quark-antiquark particle is called a meson (pion, kaon, eta, etc.). In that same year, the concept of the 'gluon' as the exchange particle mediating the strong-nuclear force between quarks was introduced along with the concept of color-charged quarks and gluons. Soon thereafter, work began on the gluon theory of quark interactions governed by the quantum dynamics of color-charges; this theory is known as quantum chromodynamics (QCD).

The first confirmation of the existence of quarks and gluons came in the late 1960s and early 1970s, respectively. During this time, the final formulations of QCD theory and the development of the 'Standard Model' took place. The Standard Model is the theory of fundamental particles and how they interact; it describes how the four known fundamental forces in the universe (electromagnetic, weak and strong-nuclear, and gravity) are created by the exchange of 'bosons' (zero or integer-spin particles) between the fundamental half-integer spin particles known as 'fermions' (leptons and quarks). The exchange boson associated with the familiar electromagnetic interaction described by quantum electrodynamics (QED) is the photon. The intermediate vector bosons ($W^{\pm}$ and Z^0) of the weak-nuclear force were discovered in the early 1980s. During the last three decades, the Standard model (for all forces but gravity) has proven to be a remarkably successful theory whose predictions are routinely tested by experiment.

The theoretical progress discussed above was paralleled by advances in the ex-

perimental techniques needed to test the theories. For example, advances in particle accelerator and detector technologies produced enterprising particle scattering experiments, with ever increasing measurement precision, which tested and expanded the realms of theoretical knowledge. In the 1950s, Hofstadter and others pioneered the use of electron scattering to probe the 'structure' of the nucleon. In this work, the deviations of the measured cross sections from those expected from elastic scattering off point-like target nucleons were associated with electromagnetic 'form' factors. From the measurement of these form factors, information regarding the size and shape of electric and magnetic field distributions in the nucleon could be extracted. At higher incident electron energies and greater momentum transfer between the electrons and target nucleons, inelastic scattering form factors (or structure functions) provided details of the momentum distributions of the nucleon's constituents. In fact, elastic and inelastic electron-proton scattering experiments conducted at the Stanford Linear Accelerator Center (SLAC) in the late 1960s led to the eventual confirmation of quarks. From these experiments, it was found that the inelastic cross sections exhibited 'scaling' behavior when plotted using a variable introduced by Bjorken. The observation of Bjorken scaling implied that the cross sections were largely independent of the momentum transfer (Q^2) of the interaction. This phenomenon initiated, and was soon explained by, the introduction of the quark parton model (QPM) by Feynman.

With further theoretical and technological advances in the facilities available to particle scattering experiments, the ability to probe the 'spin' structure of nucleons became possible. Experiments conducted with spin-polarized leptons scattered from spin-polarized nucleons allow a determination of the spin structure functions analogous to the unpolarized structure functions or form factors discussed above. Measurements of these functions, which vary with the energy and momentum of the

exchange boson, provide information and insight regarding the spin distributions of the nucleon's constituents. These measurements also provide tests of the QPM and certain aspects of QCD. In particular, spin structure function measurements allow for a test of the fundamental Bjorken sum rule–which relates the difference in the first moments of g_1 for the proton and neutron to the axial/axial-vector coupling constant ratio, g_A/g_V, obtained from measurements of neutron β-decay. It is commonly understood that the viability of QCD as the theory of strong interactions rests on the verification of Bjorken's sum rule.

The first deep inelastic scattering experiments with polarized leptons and polarized nucleons were performed at SLAC in the mid 1970s and early 1980s [1–3]. In these early experiments, large asymmetries were observed in the cross sections for different helicity configurations as predicted by the QPM, and the first measurement of the g_1 spin structure function of the proton was produced. The improved statistical precision in the g_1^p measurement performed by the European Muon Collaboration (EMC) at CERN in the mid 1980s [4] revealed an unexpected low contribution of the quarks' spin to the overall proton spin. They found this contribution to be only ~ 10 % instead of the QPM expectation of ~ 60 %. This result initiated the so-called 'spin-crisis'–which stirred much activity on both experimental and theoretical fronts with the purpose of verifying and reconciling the discrepancy. As a consequence, several polarized lepton-nucleon deep inelastic scattering experiments were performed during the past decade.

The g_1 structure function of the neutron was first measured at SLAC during experiment E142 [5, 6]. Both g_1 and g_2 spin structure functions of the proton and deuteron were measured at CERN by the spin muon collaboration (SMC) [7–9]. Upgrades to the experimental facilities at SLAC produced a new generation of precision spin structure function measurements: E143 [10–15], E154 [16–18], E155 [19–22], and

E155x. The HERMES spin physics experiments at DESY started in 1995 and are planned to continue until 2006; they have thus far reported results for $g_1^{p,n}$ [23, 24]. A chronology of these experiments listed with the structure functions they measured is given in Table 1.1.

The unexpected low value of the quarks' spin contribution to the overall proton spin found by EMC has since been confirmed by several different collaborations. Although the current value of this contribution (~ 30 %) is still significantly below the naive QPM expectation, there is no longer a 'crisis' in terms of understanding the composition of the nucleon's spin; this is due to advancements in theoretical knowledge which are discussed further in the next chapter. Also, the Bjorken sum rule has not been found to be violated by any experiments performed to date.

During the first half of the past decade, most experimental and theoretical activity was centered around g_1 measurements with little interest in g_2; g_2 was simply viewed

Exp. Facility/ Collab. Name	Year	Target Material(s)		Structure Fnct(s) Meas					
		proton	deut or neut	g_1^p	g_2^p	g_1^d	g_2^d	g_1^n	g_2^n
SLAC/E80	1976	$C_4H_9(OH)$	– –	√					
SLAC/E130	1983	$C_4H_9(OH)$	– –	√					
CERN/EMC	1988	$^{14}NH_3$	– –	√					
SLAC/E142	1993	– –	^{3}He gas					√	
CERN/SMC	1994	$C_4H_9(OH)$	$C_4D_9(OD)$	√	√	√	√		
SLAC/E143	1995	$^{15}NH_3$	$^{15}ND_3$	√	√	√	√		
SLAC/E154	1997	– –	^{3}He gas					√	√
DESY/HERMES	1997	H gas	^{3}He gas	√				√	
SLAC/E155	1998	$^{15}NH_3$	^{6}LiD	√	√	√	√		
SLAC/E155x	2002	$^{15}NH_3$	^{6}LiD		√		√		

Table 1.1: Twenty-five year history of experiments measuring the spin-polarized structure functions g_1 and g_2 of the proton, deuteron, and neutron. The date listed gives the year of the collaboration's first publication. The experiments at CERN scattered polarized muons (μ^+) with energies between 100 and 200 GeV, those at SLAC used polarized electrons between 5 and 50 GeV, and DESY used 28 GeV polarized positrons.

as a small correction to g_1. When it became apparent that g_1 was on its way to being well understood, attention shifted to g_2 measurements and interpretations. Since g_2 contains contributions from both twist-2 and twist-3 operators in the leading order $1/Q^2$ expansion, (whereas g_1 and the unpolarized structure functions contain only twist-2 contributions), a precision g_2 measurement would allow, for the first time, tests of lattice QCD and operator product expansion (OPE) predictions for the d_2 twist-3 matrix element. Furthermore, the precision g_2 data from E155x will also provide the first meaningful tests of the Burkhardt-Cottingham (BC) and Efremov-Leader-Teryaev (ELT) sum rules.

The subject of this dissertation is the experiment E155x, which was conducted at SLAC between February 26 and May 5, 1999. The experiment measured the cross section asymmetries, $A_\perp^{p,d}$, using longitudinally polarized electrons scattered from transversely polarized fixed proton and deuteron targets. The structure functions, $g_2^{p,d}$, and the virtual photon asymmetries, $A_2^{p,d}$, were extracted from the measured asymmetries. The following paragraph will highlight the topics discussed in the remaining chapters of this dissertation.

The general formalism for deep inelastic scattering is presented in Chapter 2. This chapter develops the experimental asymmetries and relates them to the structure functions and virtual photon asymmetries. The interpretation of the structure functions within the QPM are presented and the d_2 twist-3 matrix element from the OPE and the BC and ELT sum rules are defined. Chapter 3 details the experimental setup including the SLAC electron beam components, polarized solid proton and deuteron targets, and the three fixed angle spectrometers. Chapter 4 covers the data reduction and data analysis. The results of the experiment are given in Chapter 5, and a summary of the experiment with concluding remarks and future prospects is given in Chapter 6. Data tables of the experimental asymmetry, the g_2 spin structure

function, and the A_2 virtual photon asymmetry for the proton and deuteron are given in Appendix A and B, respectively.

Chapter 2

Theory

2.1 Lepton-Nucleon Deep Inelastic Scattering

The process of scattering a high energy lepton from a target nucleon with a momentum transfer, Q^2, greater than the target mass equivalent ($1\ (\mathrm{GeV/c^2})^2$) and an invariant mass beyond the nuclear resonances ($W^2 > 4\ (\mathrm{GeV/c^2})^2$) classifies the scattering as deeply inelastic. It is understood that at these energies, the virtual photon exchanged between the scattered lepton and target nucleon probes electromagnetic forces at very small distance scales deep within the nucleon. And at such high momentum transfer, the target nucleon will typically break apart and result in a jet of hadrons in the forward direction.

At the kinematics of E155x and most other DIS experiments of this kind, the invoked neutral current scattering events are dominated by the single photon exchange mechanism shown in Figure 2.1*. For this diagram, the scattered lepton is detected at an angle θ after exchanging a virtual photon of four-momentum q^μ with a nucleon.

*There is also a small probability of scattering via Z° boson exchange (the neutral weak force mediator). This possibility requires attention and will be discussed in Section 4.4.5.

All relevant variables for Figure 2.1 are listed and defined in Table 2.1.

For the process of Figure 2.1, the differential cross section for detecting the scattered lepton within the solid angle $d\Omega$ and with energy between E' and $E' + dE'$ can be expressed as

$$\frac{d^2\sigma}{d\Omega\, dE'} = \frac{\alpha^2}{Q^4}\frac{E'}{E} L_{\mu\nu} W^{\mu\nu}. \tag{2.1}$$

Here, α is the fine structure constant and $L_{\mu\nu}$ and $W_{\mu\nu}$ are the leptonic and hadronic tensors respectively. These tensors completely describe the state (momentum and spin) of their respective particles before and after their photon vertices. The leptonic current tensor is fundamental and can be expressed exactly in terms of known quantities using the Feynman rules. Summing over final lepton helicity states, and separating the tensor into symmetric (S) and antisymmetric (A) components with respect to μ, ν interchange, the purely electromagnetic lepton current is described by

$$L_{\mu\nu} = 2L^{(S)}_{\mu\nu} + 2iL^{(A)}_{\mu\nu}, \tag{2.2}$$

with

$$L^{(S)}_{\mu\nu} = k_\mu k'_\nu + k'_\mu k_\nu - g_{\mu\nu}(k \cdot k' - m^2) \tag{2.3}$$

$$L^{(A)}_{\mu\nu} = m\epsilon_{\mu\nu\alpha\beta} s^\alpha q^\beta, \tag{2.4}$$

where $g_{\mu\nu}$ is the space-time metric and $\epsilon_{\mu\nu\alpha\beta}$ is the totally antisymmetric tensor.

The expression describing the hadronic vertex, however, is inexact and requires the use of four independent, incalculable DIS form factors that account for the composite electromagnetic nature of the nucleon. Taking into consideration the requirements of parity conservation, charge conjugation invariance, covariance, and electromagnetic charge conservation, the purely electromagnetic hadronic tensor is constrained to the

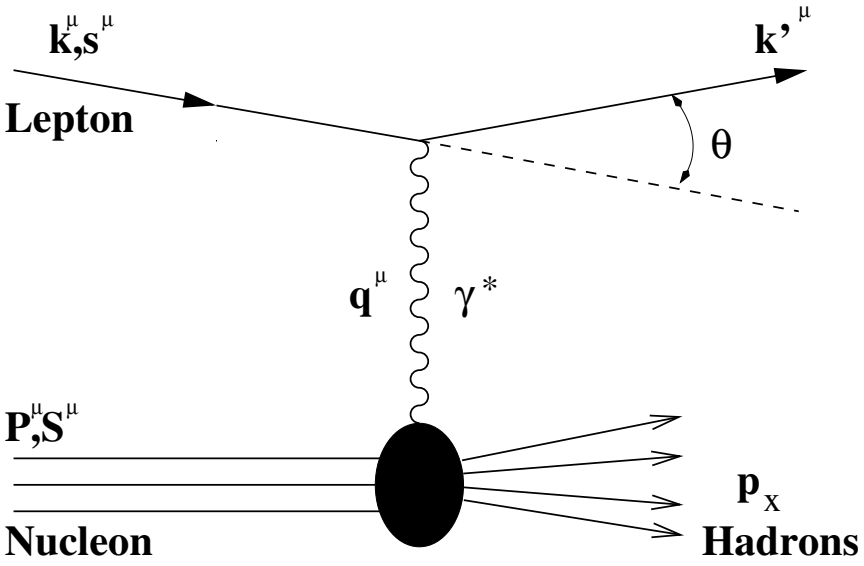

Figure 2.1: Single photon exchange Feynman diagram for the inclusive deep inelastic scattering of a lepton from a nucleon. The diagram depicts the lepton-photon vertex as well known and point-like, whereas the nucleon-photon vertex is represented as complicated and relatively unknown.

Variable	Value/Expression	Meaning
m		Rest mass of incident lepton
M		Rest mass of target nucleon
E		Lab frame initial lepton energy
k^μ	$(E, 0, 0, \lvert\vec{k}\rvert)$	Initial 4-momentum of lepton
s^μ	$\frac{1}{m}(\lvert\vec{k}\rvert, 0, 0, E)$	Initial spin vector of lepton (longitudinal)
P^μ	$(M, 0, 0, 0)$	Initial 4-momentum of target nucleon (at rest)
S^μ	$(0, \vec{S})$	Initial Spin vector of nucleon
E'		Lab frame final lepton energy
k'^μ	$(E', \vec{k'})$	Final 4-momentum of lepton
θ		Lab frame lepton scattering angle
q^μ	$k - k'$	4-momentum of the virtual photon
ν	$E - E'$ or $(P \cdot q)/2M$	Lab frame energy of virtual photon
Q^2	$-q^2$ or $4EE'\sin^2(\theta/2)$	Virtual photon 4-momentum squared
x	$Q^2/2M\nu$	Fraction of nucleon momentum carried by the struck quark
y	ν/E	Fraction of energy lost by lepton
W^2	p_x^2 or $M^2 + 2M\nu - Q^2$	Invariant mass squared of hadronic final state

Table 2.1: Kinematic quantities relevant for lab frame calculations of deep inelastic scattering from stationary targets.

form

$$W_{\mu\nu} = W_{\mu\nu}^{(S)} + iW_{\mu\nu}^{(A)}, \tag{2.5}$$

with

$$\begin{aligned} W_{\mu\nu}^{(S)} &= \frac{1}{M}\left(-g_{\mu\nu} + \frac{q_\mu q_\nu}{Q^2}\right)F_1(\nu, Q^2) \\ &\quad + \frac{1}{M^2\nu}\left(P_\mu - \frac{P\cdot q}{Q^2}q_\mu\right)\left(P_\nu - \frac{P\cdot q}{Q^2}q_\nu\right)F_2(\nu, Q^2) \qquad (2.6) \\ W_{\mu\nu}^{(A)} &= \frac{\epsilon_{\mu\nu\alpha\beta}}{M\nu}q^\alpha S^\beta g_1(\nu, Q^2) \\ &\quad + \frac{\epsilon_{\mu\nu\alpha\beta}q^\alpha}{M^2\nu^2}\Big[(P\cdot q)S^\beta - (S\cdot q)P^\beta\Big]g_2(\nu, Q^2), \qquad (2.7) \end{aligned}$$

where the $F_1(\nu, Q^2)$ and $F_2(\nu, Q^2)$ form factors are known as the spin-averaged structure functions, while $g_1(\nu, Q^2)$ and $g_2(\nu, Q^2)$ are the spin dependent structure functions.

2.1.1 Unpolarized DIS

Upon examination of the above equations, it can be seen that for unpolarized lepton-nucleon scattering, the cross section depends on only the symmetric components of the current tensors and is written as

$$\sigma^{unp} = \frac{d^2\sigma^{unp}}{d\Omega\, dE'} = \frac{\alpha^2}{Q^4}\frac{E'}{E}2L_{\mu\nu}^{(S)}W^{\mu\nu(S)}. \tag{2.8}$$

In the laboratory frame, Equation 2.8 can be written, using Equations 2.3 and 2.6 and neglecting the lepton mass, as

$$\sigma^{unp} = \frac{4\alpha^2 E'^2\cos^2\left(\frac{\theta}{2}\right)}{Q^4 M}\left[2F_1\sin^2\left(\frac{\theta}{2}\right) + \frac{M}{\nu}F_2\cos^2\left(\frac{\theta}{2}\right)\right]. \tag{2.9}$$

Thus spin-averaged DIS experiments provide a way of probing the F_1 and F_2 structure functions.

The extraction of these structure functions from the first measurements of σ^{unp} in the late 1960's provided some of the first direct experimental evidence of nucleon substructure. This subject will be further discussed in Section 2.3; it is however pertinent to mention the 'scaling' hypothesis here, which was advanced by J.D. Bjorken in 1969 [25]. This theory states that in the deep inelastic (or scaling) limit, when $Q^2, \nu \longrightarrow \infty$ but the ratio $\frac{Q^2}{\nu}$ remains finite, the structure functions become void of any separate Q^2 or ν dependence and are instead only dependent on x (defined as $\frac{Q^2}{2M\nu}$). In other words, the structure functions in this limit, are said to scale with x (interpreted here as the fraction of total nucleon momentum carried by the struck quark) and be completely independent of the energy scale of the interaction up to logarithms of Q^2 generated by radiative corrections. That is:

$$F_1(\nu, Q^2) \equiv F_1(x, Q^2) \xrightarrow[Q^2, \nu \to \infty]{lim} F_1(x), \tag{2.10}$$

$$F_2(\nu, Q^2) \equiv F_2(x, Q^2) \xrightarrow[Q^2, \nu \to \infty]{lim} F_2(x). \tag{2.11}$$

2.1.2 Polarized DIS

For the case of polarized scattering (both lepton and nucleon spin-polarized), the cross section becomes dependent on $L_{\mu\nu}^{(A)} W^{\mu\nu(A)}$ as well. By studying the difference between cross sections of opposite target polarization, the symmetric tensor contributions of Equation 2.8 cancel, and only the polarized structure function dependence remains. Although g_1 and g_2 cannot be independently measured, their individual contributions to the cross section difference can be separately enhanced, depending on certain target spin configurations, thereby allowing one to be kinematically favored over the other.

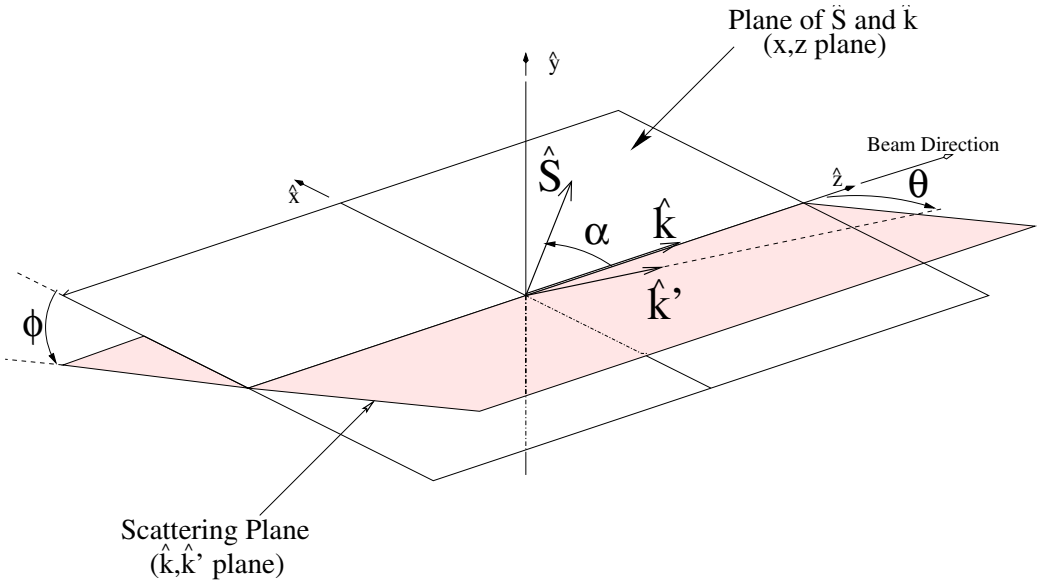

Figure 2.2: Laboratory frame coordinate system defining the general angular kinematics of polarized scattering.

Figure 2.2 illustrates the kinematic angles involved in the scattering; ϕ is the tilt of the scattering plane, θ is the angle between $\hat{k}$ and $\hat{k}'$, and α (the angle between $\hat{k}$ and $\hat{S}$) defines the target spin orientation which is experimentally constrained to lie in the horizontal (x, z) plane. For this situation, the generalized expression for the difference between cross sections with opposite target polarization is

$$\begin{aligned}\sigma^{\uparrow,-\hat{S}} - \sigma^{\uparrow,\hat{S}} &= \frac{d^2\sigma^{\uparrow,-\hat{S}}}{d\Omega\, dE'} - \frac{d^2\sigma^{\uparrow,\hat{S}}}{d\Omega\, dE'} \\ &= \frac{4\alpha^2}{Q^2 M\nu^2}\frac{E'}{E}\Big[(E\cos\alpha + E'\cos\Theta)\nu g_1 + 2EE'(\cos\Theta - \cos\alpha)g_2\Big], \quad (2.12)\end{aligned}$$

where $\uparrow$ and $\pm\hat{S}$ represent lepton[†] and nucleon spin respectively, and Θ is the angle between $\hat{k}'$ and $\hat{S}$.

For the purpose of measuring the spin structure functions, there are two favor-

[†]Polarized lepton scattering experiments always use longitudinally polarized leptons because any other orientation suppresses the cross sections.

able target spin configurations: longitudinal and transverse. The longitudinal mode scatters polarized leptons from target nucleons with spin aligned or anti-aligned with the beam direction ($\alpha = 0$ or π). This corresponds to $\Theta \longrightarrow \theta$, and the cross section difference of Equation 2.12 to leading order in $\frac{m}{E}$ becomes

$$\sigma^{\uparrow\Downarrow} - \sigma^{\uparrow\Uparrow} = \frac{4\alpha^2}{Q^2 M\nu^2}\frac{E'}{E}\left[(E + E'\cos\theta)\nu g_1 - Q^2 g_2\right]. \tag{2.13}$$

Here, it is apparent that for small scattering angles θ, g_1 is much more accessible than g_2 for longitudinal target spins.

The transverse spin configuration, however, favors the measurement of g_2. In this mode, which was utilized solely during E155x , longitudinal leptons are scattered from nucleons polarized transverse to the beam direction ($\alpha = \frac{\pi}{2}$ or $\frac{3\pi}{2}$). For these spin orientations, $\cos\Theta \longrightarrow \pm\sin\theta\cos\phi$ and to leading order in $\frac{m}{E}$, Equation 2.12 becomes

$$\sigma^{\uparrow\Leftarrow} - \sigma^{\uparrow\Rightarrow} = \frac{4\alpha^2}{Q^2 M\nu}\frac{E'^2}{E}\sin\theta\cos\phi(g_1 + \frac{2E}{\nu}g_2). \tag{2.14}$$

Here, the difference exhibits a strong dependence on the tilt of the scattering plane ϕ, and the contribution of g_2 is amplified by a factor $\frac{2E}{\nu}$ (which ranges between ~ 3 and ~ 10 for E155x) with respect to g_1's contribution.

As was the case for the unpolarized structure functions, the spin structure functions are also known to approximately scale with x. The scaled versions of g_1 and g_2 are:

$$g_1(\nu, Q^2) \equiv g_1(x, Q^2)\xrightarrow[Q^2,\,\nu\to\infty]{lim} g_1(x), \tag{2.15}$$

$$g_2(\nu, Q^2) \equiv g_2(x, Q^2)\xrightarrow[Q^2,\,\nu\to\infty]{lim} g_2(x). \tag{2.16}$$

Due to the difficulty in precisely measuring the absolute cross sections of Equation 2.12, the preferred method of acquiring the spin structure functions is to extract them from asymmetry measurements. There are two asymmetries that can be formed from polarized lepton-nucleon differential cross sections, and these correspond directly to the two target spin configurations discussed above. The parallel asymmetry $A_{\parallel}$ and the perpendicular asymmetry $A_{\perp}$ are defined as:

$$A_{\parallel} = \frac{\sigma^{\uparrow\Downarrow} - \sigma^{\uparrow\Uparrow}}{\sigma^{\uparrow\Downarrow} + \sigma^{\uparrow\Uparrow}}, \qquad A_{\perp} = \frac{\sigma^{\uparrow\Leftarrow} - \sigma^{\uparrow\Rightarrow}}{\sigma^{\uparrow\Leftarrow} + \sigma^{\uparrow\Rightarrow}}. \tag{2.17}$$

Frequently reversing the target and/or beam polarization, while performing these types of measurements, enables the slow-varying common factors of the numerator and denominator, such as detection efficiency and spectrometer acceptance, to cancel and thus reduce experimental uncertainties as well as systematic errors. Moreover, since the cross sections are proportional to the event rates–defined as the number of scattered leptons detected per number of incident leptons–the asymmetry measurements are largely reduced to an exercise in counting.

For E155x, the asymmetries are expressed in terms of experimentally measured or calculated quantities as

$$A_{\perp(\parallel)} = \frac{1}{f P_b P_t C_1}\left(A_{raw}^{\uparrow,\Leftrightarrow(\Updownarrow)} - P_b A_{EW}^{\uparrow,\Leftrightarrow(\Updownarrow)}\right) + C_2 A_{\perp(\parallel)}^{other}, \tag{2.18}$$

with

$$A_{raw}^{\uparrow,\Leftrightarrow(\Updownarrow)} = \left[\frac{\left(\frac{N}{Q_b}\right)^{\uparrow,\Leftarrow(\Downarrow)} - \left(\frac{N}{Q_b}\right)^{\uparrow,\Rightarrow(\Uparrow)}}{\left(\frac{N}{Q_b}\right)^{\uparrow,\Leftarrow(\Downarrow)} + \left(\frac{N}{Q_b}\right)^{\uparrow,\Rightarrow(\Uparrow)}}\right]. \tag{2.19}$$

N and Q_b are, respectively, the corrected[‡] number of events and beam charge ac-

[‡]The collected E155x events were corrected for non-DIS electron contamination as well as pions misidentified as electrons.

cumulated for the specific spin configuration; P_b and P_t are the beam and target polarizations; f is the dilution factor (defined as the ratio of polarizable nucleons to total nucleons seen by the beam); $P_b A_{EW}$ is a very small correction accounting for the contamination of electroweak scattering events to A_{raw}; C_1 and C_2 are target nuclear correction factors, and A^{other} is the asymmetry of the other target species (i.e., for measuring $A_\perp^{deuteron}$, $A_\perp^{other} = A_\perp^{proton}$). All of the above inefficiency and correction factors, as well as the application of radiative corrections to Equation 2.18, are detailed in Sections 4.4 and 4.5.

Using Equations 2.13 and 2.14 and noting that the denominators of Equation 2.17 are just twice the unpolarized cross section (σ^{unp}), the 'counts' asymmetries can be written in terms of the structure functions as:

$$A_\parallel(x,Q^2) = f_K \left[(E + E'\cos\theta) g_1(x,Q^2) - \frac{Q^2}{\nu} g_2(x,Q^2) \right], \tag{2.20}$$

$$A_\perp(x,Q^2) = f_K E' \sin\theta \cos\phi \left[g_1(x,Q^2) + \frac{2E}{\nu} g_2(x,Q^2) \right], \tag{2.21}$$

with the factor

$$f_K = \frac{tan^2(\frac{\theta}{2})}{\nu F_1(x,Q^2)\sin^2(\frac{\theta}{2}) + \frac{M}{2} F_2(x,Q^2)\cos^2(\frac{\theta}{2})}. \tag{2.22}$$

Likewise, the structure functions can be written in terms of the asymmetries as:

$$g_1(x,Q^2) = \frac{1}{f_K(E+E')} \left[A_\parallel + \frac{tan(\frac{\theta}{2})}{\cos\phi} A_\perp \right], \tag{2.23}$$

$$g_2(x,Q^2) = \frac{y}{2 f_K (E+E')} \left[\frac{E + E'\cos\theta}{E'\sin\theta\cos\phi} A_\perp - A_\parallel \right]. \tag{2.24}$$

Here, the kinematic coefficients of $A_\perp$ suppress its contribution to $g_1(x,Q^2)$, while

they enhance it for $g_2(x, Q^2)$.

2.2 Virtual Photon Asymmetries

Much insight into the nature and interpretation of the structure functions can be achieved by analyzing the process of Figure 2.1 in terms of the virtual photon. Using the Optical theorem, the absorption of the virtual photon by the nucleon ($\gamma^* N \longrightarrow X$) can be related to the imaginary part of the forward virtual photon-nucleon Compton scattering amplitudes. These imaginary amplitudes are defined as

$$\mathrm{Im}(\mathcal{M}_{a,b;c,d}) = \epsilon^{\mu}_{\lambda_a} \epsilon^{\nu *}_{\lambda_c} \left(W^{(S)}_{\mu\nu} + i W^{(A)}_{\mu\nu} \right), \tag{2.25}$$

where the four amplitude subscripts refer to the helicities of the photon and nucleon initial (a, b) and final (c, d) states, respectively, the ϵ_λ terms are the virtual photon polarization four vectors (two transverse ($s_{\gamma^*} = \pm 1$) and one scalar or longitudinal ($s_{\gamma^*} = 0$)), and the hadronic tensor terms have been previously defined in Equations 2.6 and 2.7.

For a spin-$\frac{1}{2}$ target, there are four independent virtual Compton scattering helicity amplitudes under the constraints of parity and time reversal invariance, and these can be written in terms of the structure functions as

$$\frac{4\pi^2\alpha}{K}\mathrm{Im}(\mathcal{M}_{1,-\frac{1}{2};1,-\frac{1}{2}}) \equiv \sigma^T_{1/2} = \frac{4\pi^2\alpha}{K}\frac{1}{M}\left(F_1 + g_1 - \gamma^2 g_2\right), \tag{2.26}$$

$$\frac{4\pi^2\alpha}{K}\mathrm{Im}(\mathcal{M}_{1,\frac{1}{2};1,\frac{1}{2}}) \equiv \sigma^T_{3/2} = \frac{4\pi^2\alpha}{K}\frac{1}{M}\left(F_1 - g_1 + \gamma^2 g_2\right), \tag{2.27}$$

$$\frac{4\pi^2\alpha}{K}\mathrm{Im}(\mathcal{M}_{1,-\frac{1}{2};0,\frac{1}{2}}) \equiv \sigma^{TL}_{1/2} = \frac{4\pi^2\alpha}{K}\frac{\sqrt{\gamma^2}}{M}\left(g_1 + g_2\right), \tag{2.28}$$

$$\frac{4\pi^2\alpha}{K}\mathrm{Im}(\mathcal{M}_{0,\frac{1}{2};0,\frac{1}{2}}) \equiv \sigma^L_{1/2} = \frac{4\pi^2\alpha}{K}\frac{1}{M\nu}\left(M(1+\frac{1}{\gamma^2})F_2 - \nu F_1\right), \tag{2.29}$$

where the virtual photon flux factor $K = \nu - \frac{Q^2}{2Mx}$ is conventionally defined as the energy required for a real photon to create the state X, and γ^2 is defined as $\frac{Q^2}{\nu^2}$. The virtual photo-absorption cross sections defined in the above equations have subscripts referring to the total spin of the photon-nucleon system projected along the incident lepton direction, and superscripts referring to the initial and final photon polarization: T for transverse, L for longitudinal, and TL represents the situation in which the photon polarization orientation changes during the interaction. The total longitudinal and transverse photo-absorption cross sections are defined as:

$$\sigma^L \equiv \sigma^L_{1/2}, \tag{2.30}$$

$$\sigma^T \equiv \frac{1}{2}\left(\sigma^T_{1/2} + \sigma^T_{3/2}\right) = \frac{4\pi^2\alpha}{K}\frac{F_1}{M}. \tag{2.31}$$

Two independent 'physics' asymmetries, A_1 and A_2, for virtual photo-absorption cross sections can now be formed. These asymmetries represent the underlying physical interactions that give rise to the measured 'count' asymmetries ($A_{\|}$ and $A_{\perp}$). A_1 and A_2 are defined as:

$$A_1 = \frac{\left(\sigma^T_{1/2} - \sigma^T_{3/2}\right)}{\left(\sigma^T_{1/2} + \sigma^T_{3/2}\right)}, \qquad A_2 = \frac{\sigma^{TL}_{1/2}}{\sigma^T}. \tag{2.32}$$

Here, an obvious relationship between A_1 and $A_{\|}$ is evident in that $\sigma^T_{1/2}$ is comparable to $\sigma^{\uparrow\Downarrow}$, and $\sigma^T_{3/2}$ is comparable to $\sigma^{\uparrow\Uparrow}$. A similar comparison between A_2 and $A_{\perp}$ is made less obvious by the lack of an opposite scalar photon polarization. Instead, A_2 is defined as the interference between transverse and longitudinal amplitudes (σ^{TL}) relative to the total transverse amplitude (σ^T).

Substituting Equations 2.26 - 2.28 into the above equations, the photo-absorption

asymmetries can be expressed in terms of the structure functions as:

$$A_1(x,Q^2) = \frac{1}{F_1(x,Q^2)}\left(g_1(x,Q^2) - \gamma^2 g_2(x,Q^2)\right), \tag{2.33}$$

$$A_2(x,Q^2) = \frac{1}{F_1(x,Q^2)}\sqrt{\gamma^2}\left(g_1(x,Q^2) + g_2(x,Q^2)\right). \tag{2.34}$$

Likewise, the structure functions can be written in terms of the absorption asymmetries as:

$$g_1(x,Q^2) = \frac{F_1(x,Q^2)}{1+\gamma^2}\left(A_1(x,Q^2) + \sqrt{\gamma^2}A_2(x,Q^2)\right), \tag{2.35}$$

$$g_2(x,Q^2) = \frac{F_1(x,Q^2)}{1+\gamma^2}\left(\frac{A_2(x,Q^2)}{\sqrt{\gamma^2}} - A_1(x,Q^2)\right). \tag{2.36}$$

A_1 and A_2 can be written in terms of the lepton-scattering asymmetries as:

$$A_1(x,Q^2) = \frac{1}{1+\eta\zeta}\left(\frac{A_{\parallel}(x,Q^2)}{D(x,Q^2)} - \frac{\eta A_{\perp}(x,Q^2)}{d(x,Q^2)}\right), \tag{2.37}$$

$$A_2(x,Q^2) = \frac{1}{1+\eta\zeta}\left(\frac{\zeta A_{\parallel}(x,Q^2)}{D(x,Q^2)} + \frac{A_{\perp}(x,Q^2)}{d(x,Q^2)}\right), \tag{2.38}$$

with the inverse relations given by:

$$A_{\parallel}(x,Q^2) = D(x,Q^2)\left(A_1(x,Q^2) + \eta A_2(x,Q^2)\right), \tag{2.39}$$

$$A_{\perp}(x,Q^2) = d(x,Q^2)\left(A_2(x,Q^2) - \zeta A_1(x,Q^2)\right), \tag{2.40}$$

where the depolarization factors D and d, and the additional kinematic parameters η and ζ are defined in Table 2.2. Also shown (but not defined) in this table is the function $R(x,Q^2)$, which is defined as the ratio of total longitudinal to transverse photo-absorption cross sections. Using Equations 2.29 and 2.31, $R(x,Q^2)$ is written

as

$$R(x,Q^2) \equiv \frac{\sigma^L}{\sigma^T} = \frac{F_2(x,Q^2)}{F_1(x,Q^2)}\frac{(1+\gamma^2)}{2x} - 1. \tag{2.41}$$

This expression can be rearranged to provide a relationship between F_1 and F_2, namely

$$F_1(x,Q^2) = F_2(x,Q^2)\frac{1+\gamma^2}{2x\left[1+R(x,Q^2)\right]}. \tag{2.42}$$

Setting R equal to zero in Equation 2.41, as would be the case for scattering from point-like spin-$\frac{1}{2}$ particles (since they can only absorb transverse photons and not longitudinal ones), and evaluating the expression in the deep inelastic limit ($\gamma^2 \to 0$)

Quantity	Expression
$D(x,Q^2)$	$\frac{\frac{1}{E}\left(E-\epsilon E'\right)}{1+\epsilon R(x,Q^2)}$
$d(x,Q^2)$	$D(x,Q^2)\sqrt{\frac{2\epsilon}{1+\epsilon}}$
η	$\frac{\epsilon\sqrt{Q^2}}{E-\epsilon E'}$
ζ	$\eta\frac{1+\epsilon}{2\epsilon}$
ϵ	$\frac{1}{1+2\left(1+\frac{1}{\gamma^2}\right)tan^2\left(\frac{\theta}{2}\right)}$
γ^2	$\frac{Q^2}{\nu^2}$

Table 2.2: Additional factors and kinematic variables. The factors D and d account for the ability of the virtual photon to possess both longitudinal and transverse polarization components. The so-called virtual photon polarization parameter, $\epsilon \in [0,1]$, gives an indication of the longitudinal polarization contribution to the cross section ($\epsilon = 1$ for the greatest, and $\epsilon = 0$ (real photons) for no contribution).

yields the well-known Callan-Gross relation [26]

$$F_2(x,Q^2) = 2xF_1(x,Q^2). \tag{2.43}$$

2.2.1 A_2 positivity limit

E155x performed a measurement of $A_\perp$, and thus a measurement of A_2. Before this, little experimental data had been accumulated for A_2[13, 17, 19], and hence it was not well understood. However, it is expected that in DIS energy regimes, A_2 is very small. This is readily seen from Equation 2.34, where A_2 is proportional to the product of two quantities that are typically much less than 1, namely $\sqrt{\gamma^2}$ (for DIS kinematics), and the sum of $g_1(x,Q^2)$ and $g_2(x,Q^2)$. Furthermore, a positive upper-bound can be formulated for A_2 [27] by evaluating the absorption cross sections that comprise it in terms of the virtual photon's helicity state transition probability amplitudes A_T and A_L. In terms of these amplitudes, the magnitude of A_2 can be written as

$$|A_2| = \frac{|\langle A_L|A_T\rangle|^2}{|\langle A_T|A_T\rangle|^2}. \tag{2.44}$$

Using the Schwartz inequality, the magnitude can be rewritten as

$$|A_2| \leq \frac{|\langle A_L|A_L\rangle| \cdot |\langle A_T|A_T\rangle|}{|\langle A_T|A_T\rangle|^2} = \frac{|\langle A_L|A_L\rangle|}{|\langle A_T|A_T\rangle|}, \tag{2.45}$$

which implies the positivity limit for A_2:

$$|A_2(x,Q^2)| \leq \sqrt{R(x,Q^2)}. \tag{2.46}$$

In a recent paper [28], a stronger, more accurate, bound on the A_2 asymmetry has

been rediscovered from past literature. This improvement on the positivity condition has only recently become useful due to higher precision transverse target nucleon experiments and increasing amounts of A_1 data. The new positivity constraint is

$$|A_2(x,Q^2)| \leq \sqrt{\frac{1}{2}\left[1+A_1(x,Q^2)\right]R(x,Q^2)}, \tag{2.47}$$

which takes into consideration the fact that the $\sigma^T_{3/2}$ amplitude does not contribute to the interference term ($\sigma^{TL}_{1/2}$).

2.3 Quark Parton Model

The intrinsic value of structure function measurements resides in their influence on the advancement of our understanding of matter. The scaling behavior exhibited by early measurements of the unpolarized structure functions provided clear evidence of nucleon substructure. The interpretation of this and other early DIS results by R. P. Feynman [29] prompted him to put forth the notion that the nucleon was composed of dynamic point-like scattering centers, called partons.

The quark parton model (QPM) provided the first theoretical framework facilitating an interpretation of the DIS structure functions. The simplest QPM approximates the nucleon, in the infinite momentum frame (the scaling limit), as a collection of co-linear, non-interacting partons each carrying a fraction x of the total nucleon momentum. This approximation implies that the DIS cross section be the sum of incoherent elastic scattering cross sections of the individual partons. This, in turn, leads to the association of the structure functions with parton distribution functions, $p_i^{\uparrow}(x,Q^2)$ and $p_i^{\downarrow}(x,Q^2)$, which can be viewed as the likelihood of finding within a nucleon partons of flavor i, spin aligned $\uparrow$ or anti-aligned $\downarrow$ with the nucleon spin,

and momentum fraction between x and $x + dx$. It is important to point out that, in this model, any parton momentum transverse to the nucleon momentum is negligibly small, and thus quantities that probe the transverse distributions, such as σ^L, and consequently σ^{TL}, R, A_2, and g_2, are zero and have no simple QPM interpretation. Nevertheless, it is beneficial to examine the role of the other structure functions within this framework.

2.3.1 F_1 and F_2 Interpretation

By identifying Feynman's partons with the previously postulated nucleon constituents [30, 31] called quarks (q) and antiquarks ($\bar{q}$), the unpolarized structure functions can be expressed in terms of the quark distribution functions,

$$q_i(x) = q_i^{\uparrow}(x) + q_i^{\downarrow}(x), \qquad \bar{q}_i(x) = \bar{q}_i^{\uparrow}(x) + \bar{q}_i^{\downarrow}(x), \tag{2.48}$$

as:

$$F_1(x) = \frac{1}{2} \sum_i e_i^2 \left[q_i(x) + \bar{q}_i(x) \right], \tag{2.49}$$

$$F_2(x) = x \sum_i e_i^2 \left[q_i(x) + \bar{q}_i(x) \right], \tag{2.50}$$

where e_i is the electromagnetic charge of the quarks having flavor i. The sum over the value of $F_2(x)$, or likewise x times the sum of all quark and antiquark flavor distributions, for all x, was historically expected to be unity. However, it is experimentally observed to be $\sim \frac{1}{2}$, implying that the charged constituents of the nucleon account for only $\sim 50\%$ of its total momentum. This observation suggested that neutral partons

(gluons[§]) must also participate in the scattering and carry a significant portion of the nucleon momentum.

The participation of the gluon in the DIS reaction can be observed experimentally as the Q^2 dependence of the structure functions at a given x. For example, Figure 2.3 displays F_2^d as a function of Q^2. Here, the trend at higher constant x, for F_2 to decrease as Q^2 increases, indicates the increasing probability that the exchanged virtual photon probes a quark that has radiated a gluon. The opposite trend at lower x (for F_2 to increase as Q^2 increases) indicates that larger distributions of low x quarks and antiquarks are found at higher probing energies. These low x distributions are interpreted as the quark-antiquark 'sea' content of the nucleon and are thought to originate from the very gluons that were radiated at high x.

2.3.2 g_1 and g_2 Interpretation

The polarized structure function $g_1(x, Q^2)$ is proportional to the difference in the parton distributions with opposite helicity $(p_i^{\uparrow}(x, Q^2) - p_i^{\downarrow}(x, Q^2))$. In terms of the nucleon's charged constituents, g_1 is expressed as

$$g_1(x) = \frac{1}{2} \sum_i e_i^2 \left[\Delta q_i(x) + \Delta \bar{q}_i(x)\right], \tag{2.51}$$

with

$$\Delta q_i(x) = q_i^{\uparrow}(x) - q_i^{\downarrow}(x), \qquad \Delta \bar{q}_i(x) = \bar{q}_i^{\uparrow}(x) - \bar{q}_i^{\downarrow}(x). \tag{2.52}$$

The above equations indicate that g_1 provides a measure of the quark and antiquark helicity content of the nucleon. Performing the sum in Equation 2.51 over light quark

[§]The gluon is the electromagnetically neutral and massless vector boson mediating the strong-nuclear force responsible for binding quarks. The strong color charge, which both quarks and gluons possess, dictates the strength of the interaction which has inner workings and degrees of freedom governed by the theory of quantum chromodynamics (QCD).

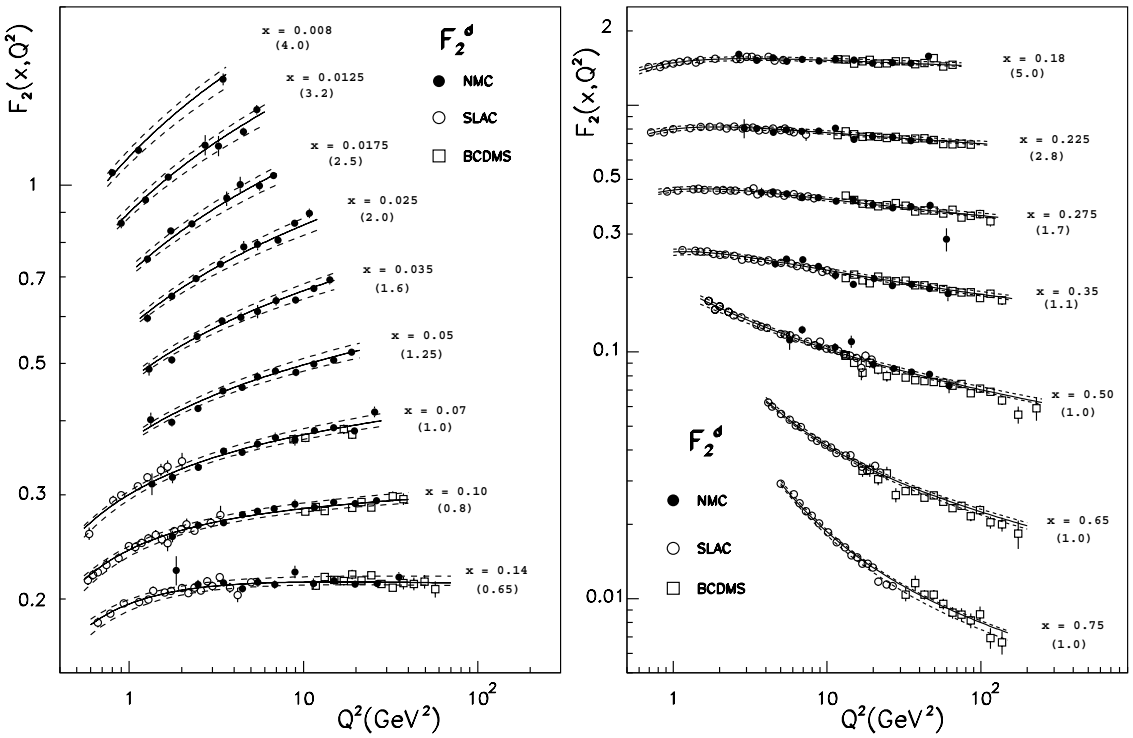

Figure 2.3: Deuteron $F_2(Q^2)$ [32], at various values of x, multiplied by the quantities in parentheses to spread them vertically for ease of viewing.

flavors[¶] $i = u, d, s$ (corresponding to up, down, and strange quarks respectively), and noting that the quark flavor charges are $e_u = +\frac{2}{3}$, $e_d = -\frac{1}{3}$, and $e_s = -\frac{1}{3}$, yields the following relation

$$g_1(x) = \frac{1}{2}\left(\frac{4}{9}\left[\Delta q_u(x) + \Delta\bar{q}_u(x)\right] + \frac{1}{9}\left[\Delta q_d(x) + \Delta\bar{q}_d(x)\right] + \frac{1}{9}\left[\Delta q_s(x) + \Delta\bar{q}_s(x)\right]\right), \tag{2.53}$$

with the net quark helicity contribution to the overall nucleon spin defined as

$$\Delta\Sigma(x) = \left[\Delta q_u(x) + \Delta\bar{q}_u(x) + \Delta q_d(x) + \Delta\bar{q}_d(x) + \Delta q_s(x) + \Delta\bar{q}_s(x)\right]. \tag{2.54}$$

[¶] The contribution from heavy quark flavors $i = c, b, t$ (corresponding to charm, bottom, and top quarks respectively) is negligible.

The initial (naive) assumption that the quarks carried all of the nucleon spin, implying that

$$S_{nucleon} \equiv \frac{1}{2} = \frac{1}{2}\int_0^1 \Delta\Sigma(x)dx, \tag{2.55}$$

was found to be drastically violated by the EMC experiment [4] which produced the first non-statistics dominated measurement of $g_1^p(x)$. Here, a value for $\Delta\Sigma$ was extracted[‖] from calculations of the first moment of g_1^p, defined as

$$\Gamma^1_{g_1^p} = \int_0^1 g_1^p(x)dx, \tag{2.56}$$

and found to be more consistent with 0 than 1. Since the verification and refinement of this result by the experiments that followed, it became increasingly apparent that the simple QPM prediction and/or interpretation of the g_1 structure function was in jeopardy and that a theoretical re-evaluation was needed to resolve the issue. The non-intuitive low value of $\Delta\Sigma$ found by EMC is now believed to have resulted from the anomalous gluon contribution to the flavor singlet axial current matrix element a_0 [33]. This implies that Equation 2.51 should be modified to include the difference in helicity distributions of polarized gluons in the nucleon.

It should be noted that an additional possible source for the unexpected low value of Γ_1^p (and thus $\Delta\Sigma$) could stem from the not well-known $q\bar{q}$-sea contribution to the net spin, or more explicitly, the small x ($x \longrightarrow 0$) behavior of $g_1(x)$. Figure 2.4 displays the current state of the world database on precision measurements of $g_1(x, 5\ \mathrm{GeV}^2)$ with special emphasis on the E155 data.

There is no analogous QPM interpretation for g_2; it is predicted to be zero. However, from past experiments [13, 16, 21] and predictions based on models [34–37], g_2

[‖]Using measurements of the hyperon β-decay F and D constants. For a discussion of this technique, refer to [38].

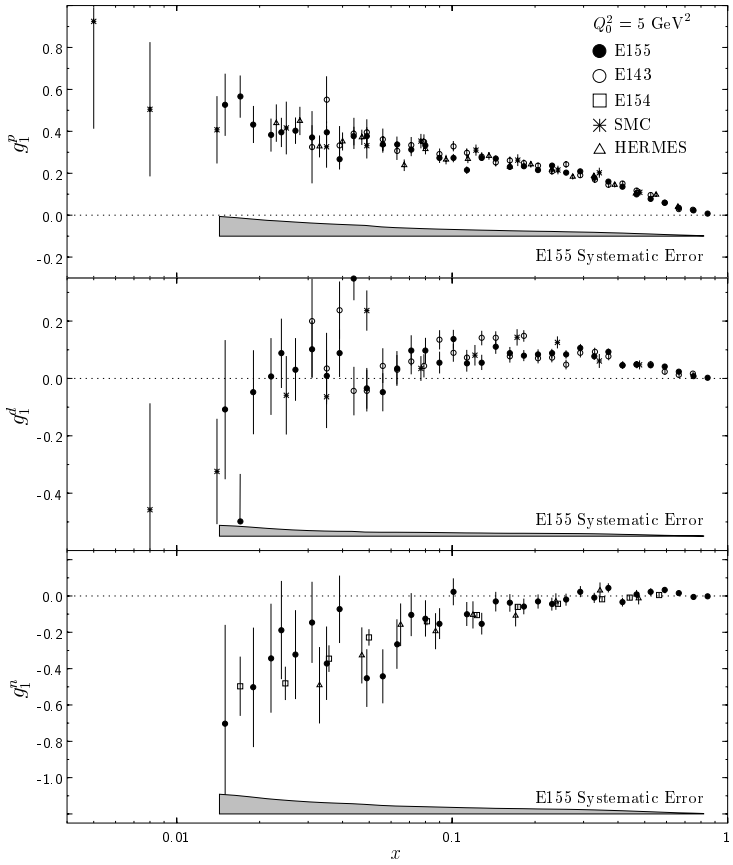

Figure 2.4: E155 $g_1(x)$ results for proton, deuteron, and neutron shown with world data at an average value of $Q^2 = 5$ GeV^2.

is known to be small but non-zero. This can be reconciled in the QPM by realizing that Q^2 and ν are large but finite under experimental conditions. Hence, small values of A_2 and g_2 are expected to result from transverse momentum distributions arising from intrinsic Fermi motion and/or QCD effects. The effect of these quark momentum distributions, within the framework of this model, is to bring the quark masses slightly off shell ($m_q \neq xM$); g_2 can then be interpreted in this context as the amount of g_1 in the momentum degrees of freedom transverse to the total nucleon momentum. That is

$$g_2(x) = \frac{1}{2}\sum_i e_i^2 \left(\frac{m_q}{xM} - 1\right)\left[\left(q_i^{\uparrow}(x) - q_i^{\downarrow}(x)\right) + \left(\bar{q}_i^{\uparrow}(x) - \bar{q}_i^{\downarrow}(x)\right)\right]. \qquad (2.57)$$

However, due to the sensitivity of this calculation to the unknown effective quark mass, m_q, the above interpretation is not expected to yield a reliable prediction of g_2. Instead, a different approach is needed for understanding g_2.

2.4 Operator Product Expansion

The limited ability (or inability) of the QPM to incorporate transverse parton momentum and helicity distribution effects (e.g. quark interactions, gluon emission, etc.) within its framework leads to a non-intuitive interpretation of g_1 and a null result for g_2. To help remedy these shortcomings as well as provide a different viewpoint into the meaning of the spin structure functions, especially g_2, the operator product expansion (OPE) analysis can be applied to DIS. First developed by K. G. Wilson in the early 1960's, the OPE provides a method for approximating g_2 by evaluating the product of singular operators contained in the forward matrix element for the virtual Compton scattering process. The following discussion, which closely follows the treatment of Kodaira *et. al.* [39], briefly describes this technique.

The hadronic tensor developed at the beginning of this chapter can be described as the Fourier transform of the commutator of currents sandwiched between polarized nucleon states with four-momentum P and covariant spin S:

$$W_{\mu\nu}(\nu, Q^2) = \frac{1}{2\pi} \int d^4z e^{iq\cdot z} \langle P, S | \left[J_\mu(z), J_\nu(0) \right] | P, S \rangle , \tag{2.58}$$

$$\equiv W^{(S)}_{\mu\nu} + i W^{(A)}_{\mu\nu}, \tag{2.59}$$

where q is the 4-momentum transfer ($Q^2 = -q^2$), J_μ and J_ν are electromagnetic currents evaluated at their respective space-time coordinates, and once again the tensor can be split into symmetric and antisymmetric components under $\mu \leftrightarrow \nu$.

The amplitude $T_{\mu\nu}$, which is closely related to the forward matrix element for virtual photon-nucleon Compton scattering, can be written in terms of the time-ordered product of the currents as [33]

$$T_{\mu\nu}(\nu, Q^2) = i \int d^4z e^{iq\cdot z} \langle P,S| T(J_\mu(z)J_\nu(0)) |P,S\rangle , \tag{2.60}$$

$$\equiv T^{(S)}_{\mu\nu} + iT^{(A)}_{\mu\nu}, \tag{2.61}$$

where

$$W^{(S,A)}_{\mu\nu} = \frac{1}{\pi}\mathrm{Im}T^{(S,A)}_{\mu\nu}. \tag{2.62}$$

In the deep inelastic limit, the singular behavior of $J(z)J(0)$ for z near the light cone (i.e. for $z^2 \approx 0$) dominates the behavior of $W_{\mu\nu}$. The result of Wilson's OPE is that this singular behavior of the current operators can be isolated in non-operator functions multiplied by non-singular operators. The general OPE result relevant for the case of unpolarized scattering can be written as

$$J_\mu(z)J_\nu(0) \propto \sum_{j,n} \tilde{C}^n_j(z^2) z_{\mu_1}...z_{\mu_n} \hat{O}^{j\mu_1\cdots\mu_n}(0) \tag{2.63}$$

$$+ [\text{terms antisymmetric under } \mu \leftrightarrow \nu]. \tag{2.64}$$

The non-singular operators $\hat{O}^{j\mu_1\cdots\mu_n}(0)$ are referred to as 'spin-n' operators and are evaluated at $z = 0$. The coefficient functions $\tilde{C}^n_j(z^2)$ are singular as $z^2 \longrightarrow 0$. If the mass dimension of the current J is defined as d_J and that of $\hat{O}^j$ is defined as $\hat{d}_j$, then on naive dimensional grounds, the behavior of the singular coefficients is expected to be [40]

$$\tilde{C}^n_j(z^2) \stackrel{z^2\to 0}{\longrightarrow} \left(\frac{1}{z^2}\right)^{\frac{1}{2}(2d_J - \tau_j)}, \tag{2.65}$$

where $\tau_j = \hat{d}_j - n$ is called the 'twist' of the operator $\hat{O}_j$. From the sign of the twist

exponent in Equation 2.65, the smaller τ_j is, the more singular $\tilde{C}_j^n$ will be. Thus, the lowest twist operators will dominate the behavior of the hadronic tensor. In analyzing a product of currents, the properties of the OPE operators are such that the lowest twist occurring will always be $\tau = 2$.

The above simplified example of the OPE results for the spin-averaged case were given as a means of introducing the concept of twist as well as some of the general properties of the expansion coefficients and operators. The remainder of this section will discuss the OPE results relevant for the case of polarized scattering. The goal of this discussion is to develop a set of sum rules for certain moments of the spin structure functions and relate them to unknown matrix elements.

For spin-dependent DIS using a massless quark model, Wilson's OPE can be written completely as

$$\begin{aligned} J_\mu(z)J_\nu(0) \;\simeq\; & [\text{terms symmetric under } \mu \leftrightarrow \nu] \\ & - i\sum_n \frac{[1-(-1)^n]}{2} z_{\mu_1}\ldots z_{\mu_{n-2}} \sum_i \Bigg\{ \epsilon_{\mu\nu\lambda\sigma}\delta^\lambda z_{\mu_{n-1}} \frac{1}{z^2} \\ & \times E_{1,i}^n(z^2) R_{1,i}^{\sigma\mu_1\ldots\mu_{n-1}} \\ & + (\epsilon_{\mu\rho\lambda\sigma}\delta_\nu\delta^\rho - \epsilon_{\nu\rho\lambda\sigma}\delta_\mu\delta^\rho - \epsilon_{\mu\nu\lambda\sigma}\Box) \\ & \times E_{2,i}^n(z^2) R_{2,i}^{\lambda\sigma\mu_1\ldots\mu_{n-2}} \Bigg\}. \end{aligned} \tag{2.66}$$

The operators R_1 with coefficients E_1 are of twist-2 and the operators R_2 with coefficients E_2 are of twist-3. The index i labels various operators of equal twist which may appear in the expansion. The operator $R_{1,i}^{\sigma\mu_1\ldots\mu_{n-1}}$ is totally symmetric in its Lorentz indices while $R_{2,i}^{\lambda\sigma\mu_1\ldots\mu_{n-2}}$ is symmetric in $\sigma\mu_1\ldots\mu_{n-2}$ and antisymmetric in $\lambda\sigma$. It should be noted that the coefficient functions $E(z^2)$ are also functions of the renormalized QCD coupling constant, g.

The Fourier transform of the time-ordered product of currents corresponding to Equation 2.66 is

$$
\begin{aligned}
i\int d^4z e^{iq\cdot z}T(J_\mu(z)J_\nu(0)) \;\simeq\; & [\text{terms symmetric under } \mu\leftrightarrow\nu] \\
& - i\sum_{n=1}\frac{[1-(-1)^n]}{2}\left(\frac{2}{Q^2}\right)^n q_{\mu_1}\cdots q_{\mu_{n-2}}\sum_i\Big\{\epsilon_{\mu\nu\lambda\sigma}q^\lambda q_{\mu_{n-1}} \\
& \times E^n_{1,i}(Q^2)R^{\sigma\mu_1\cdots\mu_{n-1}}_{1,i} \\
& + (\epsilon_{\mu\rho\lambda\sigma}q_\nu q^\rho - \epsilon_{\nu\rho\lambda\sigma}q_\mu q^\rho - q^2\epsilon_{\mu\nu\lambda\sigma})\frac{n-1}{n} \\
& \times E^n_{2,i}(Q^2)R^{\lambda\sigma\mu_1\cdots\mu_{n-2}}_{2,i}\Big\}. \qquad (2.67)
\end{aligned}
$$

The matrix elements of the operators are defined as

$$\langle P,S|\, R^{\sigma\mu_1\cdots\mu_{n-1}}_{1,i}\,|P,S\rangle = \frac{-2a^i_n}{n}\{S^\sigma P^{\mu_1}...P^{\mu_{n-1}}\}_{\hat{s}}, \qquad (2.68)$$

$$\langle P,S|\, R^{\lambda\sigma\mu_1\cdots\mu_{n-2}}_{2,i}\,|P,S\rangle = d^i_n(S^\sigma P^\lambda - S^\lambda P^\sigma)P^{\mu_1}...P^{\mu_{n-2}}, \qquad (2.69)$$

where $\{\ \}_{\hat{s}}$ implies symmetrization of indices. The factors a^i_n and d^i_n reflect the unknown, non-perturbative aspect of the interaction dynamics [33] and can only be determined from experiment.

The moment sum rules for g_1 and g_2 can now be formulated by substituting the light-cone expansion of Equation 2.66 into Equation 2.60 and using Equations 2.67, 2.68, and 2.69. The result is

$$\int_0^1 dx\ x^n g_1(x,Q^2) = \frac{1}{2}\sum_i a^i_n E^n_{1,i}(Q^2,g) \qquad n=0,2...,(2.70)$$

$$\int_0^1 dx\ x^n g_2(x,Q^2) = \frac{n}{2n+2}\sum_i\left[a^i_n E^n_{1,i}(Q^2,g) - d^i_n E^n_{2,i}(Q^2,g)\right]\ n=2,4....(2.71)$$

It is important to note here that the OPE only gives information about the odd

moments of $g_{1,2}(x,Q^2)$. Furthermore, the above sum rule for g_2 does not necessarily hold for its first moment as indicated by the lack of an $n=0$ term (the first moment of g_2 is addressed in Section 2.6). The above coefficient functions are calculated using perturbative QCD as a power series expansion in the coupling g [33]. These coefficients are arranged in Equation 2.67 such that for free fields (i.e. $g=0$), their values are:

$$E^n_{1,i}(Q^2, g=0) = 1, \qquad E^n_{2,i}(Q^2, g=0) = 1. \tag{2.72}$$

Thus, in the free field approximation, the above sum rules reduce to

$$\Gamma^{(n+1)}_{g_1} = \int_0^1 dx\ x^n g_1(x,Q^2) = \frac{1}{2}\sum_i a^i_n \qquad n=0,2,4..., \tag{2.73}$$

$$\Gamma^{(n+1)}_{g_2} = \int_0^1 dx\ x^n g_2(x,Q^2) = \frac{n}{2n+2}\sum_i \left[a^i_n - d^i_n\right] \quad n=2,4,6... \ . \tag{2.74}$$

The a^i_n and d^i_n are the reduced matrix elements of the twist-2 and twist-3 operators, respectively, and as was mentioned above, they can only be determined from experiment. A calculation of d^i_2 for the proton and neutron has been determined from the E155x experiment in the measured x range for an average Q^2 of 5 (GeV/c)^2. The method of the calculation and its interpretation are given in the next section; its results are presented in Section 5.5.

2.5 Wandzura-Wilczek g_2 Model

Before describing the method used to calculate the d_2 twist-3 matrix element, it is instructive to introduce the Wandzura-Wilczek model for g_2 (referred to as g_2^{ww}). Assuming that the twist-3 terms in Equation 2.74 are zero and that the sum rules

derived in the previous section are valid for all integer n, Equations 2.73 and 2.74 can be solved to yield an expression for a twist-2 only approximation of g_2. This calculation was first performed by Wandzura and Wilczek [41], and the result was the following prediction for g_2:

$$g_2^{ww}(x,Q^2) = -g_1(x,Q^2) + \int_x^1 \frac{g_1(x',Q^2)}{x'}dx'. \tag{2.75}$$

As will be shown in Chapter 5, this prediction turns out to follow closely the E155x g_2 results. However, the additional twist-3 contribution to g_2 should not be neglected at finite Q^2. A complete description for g_2 (up to twist-3) can be written as

$$g_2(x,Q^2) = g_2^{ww}(x,Q^2) - \int_x^1 \frac{\partial}{\partial y}\left(\frac{m}{M}h_T(x',Q^2) + \xi(x',Q^2)\right)\frac{dx'}{x'}, \tag{2.76}$$

where m is the effective quark mass, M is the nucleon mass, h_T is an additional twist-2 term describing the fraction of transverse polarization of the nucleon carried by its quarks (referred to as the 'quark transversity'), and the twist-3 term, ξ, is related to quark-gluon correlations in the nucleon. To represent the deviation of g_2 from g_2^{ww}, the structure function is commonly written as

$$g_2(x,Q^2) = g_2^{ww}(x,Q^2) + \overline{g_2}(x,Q^2). \tag{2.77}$$

Due to the suppression of the quark transversity by the quark to nucleon mass ratio, $\frac{m}{M}$, any deviation of g_2 from g_2^{ww} will be primarily from the twist-3 quark gluon term. The E155x data is precise enough that statistically significant differences between g_2 and g_2^{ww} can be used to estimate the size of the twist-3 contribution.

From the OPE sum rules of Equations 2.73 and 2.74, evaluated for $n = 2$, d_2 for

the proton and neutron can be written as

$$d_2^{p,n} = 2\int_0^1 dx\ x^2 \left[g_1^{p,n}(x,Q^2) + \frac{3}{2} g_2^{p,n}(x,Q^2) \right], \tag{2.78}$$

and in terms of $\overline{g_2}$, this equation becomes

$$d_2^{p,n} = 3\int_0^1 dx\ x^2 \overline{g_2}^{p,n}(x,Q^2). \tag{2.79}$$

This is the expression used to extract d_2 from the E155x g_2 data.

2.6 Sum Rules

Two specific sum rules are evaluated using the E155x data: The Burkhardt-Cottingham sum rule for the first moment of g_2, and the Efremov-Leader-Teryaev sum rule which involves the valence quark contributions to the second moment of $(g_1 + 2g_2)$. This section briefly describes these two sum rules.

2.6.1 Burkhardt-Cottingham

The Burkhardt-Cottingham (BC) sum rule states that the first moment of $g_2(x)$ vanishes [42]:

$$\Gamma_{g_2}^1 = \int_0^1 dx\ g_2(x) = 0. \tag{2.80}$$

As shown in Section 2.4, this result does not follow strictly from the OPE sum rules since $n = 0$ is not included in Equation 2.71. It was derived from virtual Compton scattering dispersion relations, and its validity relies on the lack of singularities in g_2 as $x \longrightarrow 0$. It is worthwhile to note that the first moment of g_2^{ww} is identically zero by definition, however, once again, the expression for g_2^{ww} also does not strictly

follow from the OPE and furthermore it assumes a zero twist-3 contribution. Thus, any significant deviations of g_2 from g_2^{ww} may invalidate this sum rule.

2.6.2 Efremov-Leader-Teryaev

The Efremov-Leader-Teryaev (ELT) sum rule, derived from a general field-theoretic approach [43], produces a set of sum rules for the even moments of the structure functions (in contrast to the OPE's odd moment sum rules of Section 2.4). Moreover, these even sum rules involve only the valence contributions to the structure functions. In the particular case of the second moment sum rules, it has been proved rigorously [43] that the hadronic matrix element vanishes. This produces an exact sum rule that does not rely on neglecting twist-3 contributions and it is expressed as

$$\int_0^1 dx\ x\left[g_1^V(x) + 2g_2^V(x)\right] = 0, \tag{2.81}$$

where V denotes the valence parts of the structure functions. Assuming that the sea quark distributions in protons and neutrons are the same, this sum rule takes the form

$$\int_0^1 dx\ x\left[g_1^p(x) + 2g_2^p(x) - g_1^n(x) - 2g_2^n(x)\right] = 0, \tag{2.82}$$

which can be calculated from measurements of the proton and neutron spin structure functions.

The results of the BC and ELT sum rule calculations in the E155x measured x range at an average Q^2 of 5 $(\mathrm{GeV/c})^2$ are presented in Section 5.4.

Chapter 3

Experimental Apparatus

SLAC experiment E155x was dedicated to measuring the transverse asymmetry ($A_\perp$) for protons and deuterons in the kinematic range $0.02 < x < 0.8$ and 0.7 (GeV/c)^2 $< Q^2 < 20$ (GeV/c)^2 using a longitudinally polarized 29.1 and 32.3 GeV electron beam and transversely dynamically polarized solid $^{15}NH_3$ and ^{6}LiD targets. The average beam polarization was 83 % , and the average target polarizations were 70 % and 22 % for $^{15}NH_3$ and ^{6}LiD respectively. Scattered electrons were detected simultaneously in three fixed-angle large-acceptance magnetic spectrometers at 2.75°, 5.5°, and 10.5° with respect to the beamline.

3.1 SLAC Beam Components

3.1.1 Polarized Source

The source for SLAC's polarized electron beam is shown in Figure 3.1. It consists of a strained-lattice Gallium Arsenide (GaAs) photocathode excited with circularly polarized photons generated by a pulsed Ti:sapphire laser system [44]. The circularly polarized photons incident on the photocathode excite the valence electrons into the

conduction band where they are extracted at high voltage and transported into the accelerator. The polarization of the conduction band electrons is dependent on the helicity of the photon polarization which is pseudo-randomly switched between Left and Right-handedness on a pulse to pulse basis to reduce systematic errors.

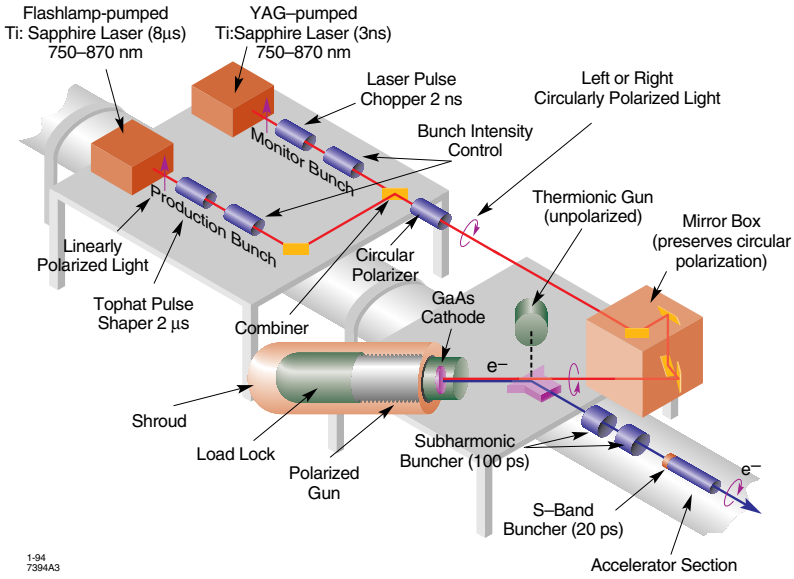

Figure 3.1: Schematic layout of the Polarized Source at SLAC.

The use of a GaAs photocathode polarized source has been in development at SLAC since the mid 1970's; further developments in the 80's and early 90's, at SLAC and elsewhere, led to the discovery that mechanically strained GaAs was capable of much higher polarizations (approaching 100% as compared to 50% for unstrained). Figure 3.2 shows the energy level diagrams for both unstrained and strained GaAs. In the unstrained case, there is a degeneracy in the z-component of angular momentum ($m_j = \pm \frac{1}{2}, \pm \frac{3}{2}$) for the J = $\frac{3}{2}$ valence band. Furthermore, the transition from the $m_j = \pm \frac{3}{2}$ states to the conduction band are three times more probable than those from the $m_j = \pm \frac{1}{2}$ states (which flip helicity during transition); thus the maximum polarization achievable with an unstrained GaAs source is 50 %.

If a thin (~ 0.1 μm) layer of GaAs is grown on a Gallium Arsenide Phosphorus (GaAsP) substrate, a compressive strain is induced in the thin GaAs layer due to the slight 1% lattice mismatch[45]. This strain splits the degeneracy in the J = $\frac{3}{2}$ states by $\sim$ 50 meV, thus allowing a finely tuned laser to select only the transitions from the $m_j = \pm \frac{3}{2}$ states to the conduction band. In theory this technique is capable of producing 100% polarizations, in practice $\sim$ 85% polarizations are achieved.

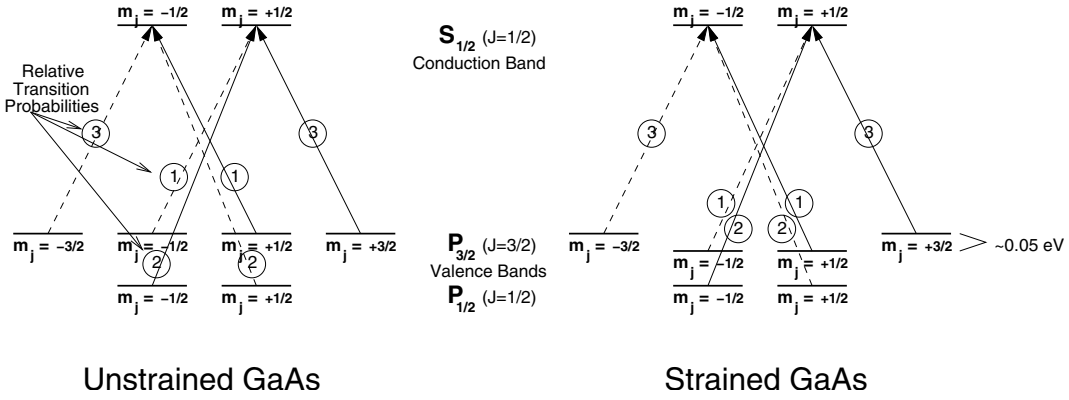

Figure 3.2: Energy levels of unstrained and strained GaAs. Dotted and solid transition lines are induced by right and left-handed absorbed photons respectively.

3.1.2 Beam Acceleration and Transport

The beamline components used in fixed-target experiments at SLAC are illustrated in Figure 3.3. The SLAC linac was constructed between 1962 and 1966. It is 2 miles long and utilizes the common 'disk-loaded' accelerator concept to propel the beam through evacuated Copper cavities located 25 feet below ground. To fuel the acceleration, powerful (67 MW peak output power) klystrons pump microwaves at 2856 MHz into the beamline using waveguides as depicted in Figure 3.4. The total accelerator structure uses 240 klystrons divided among 30 sectors and has a maximum achievable beam energy of $\sim$ 52 GeV. Each sector also contains magnets for steering and

shaping the beam pulses as well as additional components for monitoring the beam position and current.

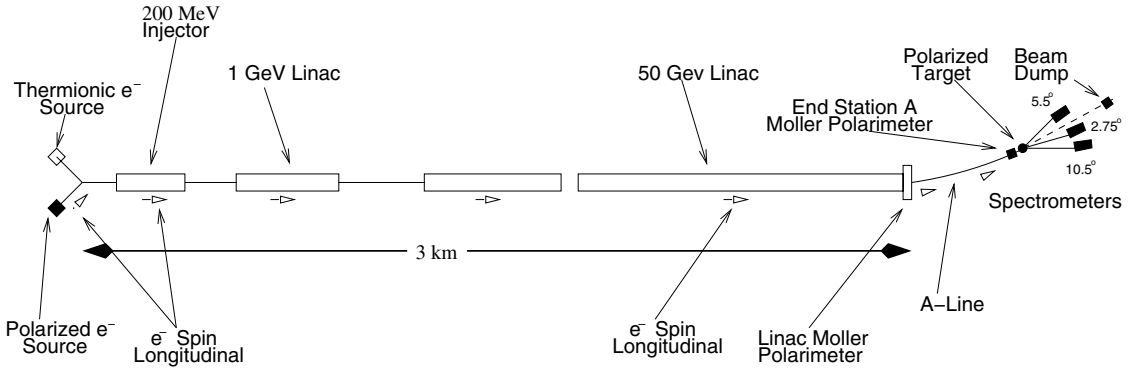

Figure 3.3: Schematic overview (not to scale) of the SLAC beamline. Also shown are the A-line transport and end station A target and spectrometers.

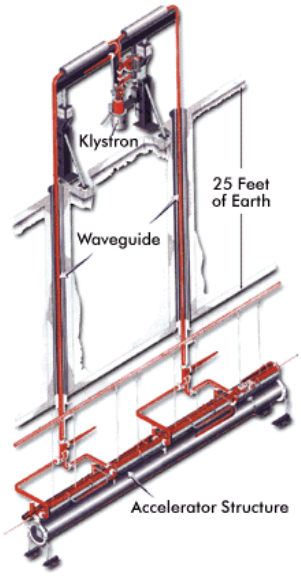

Figure 3.4: Illustration of klystron waveguides

The electron bunches created at the source are injected into the 3.2 km linac and accelerated eastward to the desired energy. At the end of the linac, the beam is deflected 0.5° northward into the A-line by two magnets in the beam switch-yard.

The A-line consists of a 24° bend designed to deliver the beam to end station A (ESA). Figure 3.5 is a schematic of the A-line bend which is accomplished by 12 large dipole magnets operated in series as well as several small corrector magnets (for fine tuning) and quadrupoles[46]; also shown is the momentum defining collimator SL-10 which was set to keep the beam's energy spread below 0.8% FWHM. Due to the electron's successive emission of synchrotron radiation at each large bend, trimcoils were added to consecutive dipole pairs such that slightly less current was given to the magnets further downstream. (Note that synchrotron radiation losses were not very significant for E155x as they amounted to less than 0.5% energy loss.) A 13^{th} reference dipole identical and connected in series to the other 12 dipoles (but located external from the beamline in an above ground control building) housed a flipcoil which provided machine control center (MCC) a measurement of the beam energy at the target. An independent (perhaps more accurate) measurement of the beam energy at the target was provided by the ESA Møller polarimeter (see Section 3.1.3 for a discussion of the Møller polarimeter).

The Møller cross-check of the flipcoil energy measurement utilized the electron's spin precession during the A-line bend. The amount of precession $\Delta\phi$, which is caused by the anomalous magnetic moment of the electron, is given by

$$\Delta\phi = \frac{E}{m_e}\frac{(g_e - 2)}{2}\theta_b, \tag{3.1}$$

where g_e is the g-factor of the electron and θ_b is 24.5°. To retain the maximum longitudinal electron polarization after the bend, the amount of precession must equal $n\pi$ radians where n is an integer. This requirement fixes the allowable accelerator energies to specific values; the two energies used for E155x , corresponding to n values of 9 and 10, were 29.16 and 32.41 GeV respectively. By varying the amount of A-line

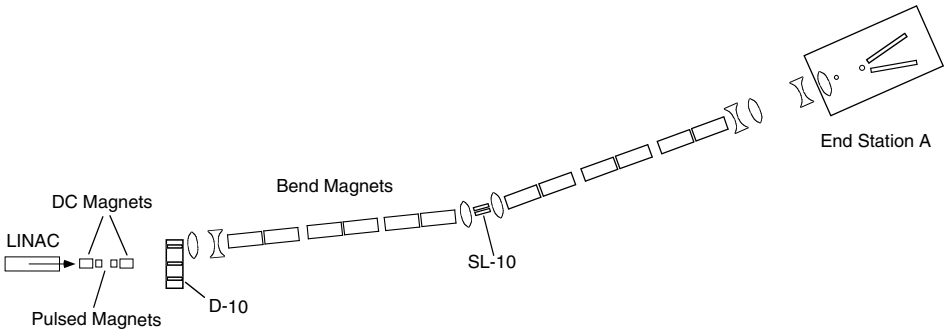

Figure 3.5: Schematic of the A-line bend.

bending, and measuring the subsequent variation in beam precession using the Møller, a precise determination of the beam energy can be made. The Møller beam energy scan performed during E155x indicated that the flipcoil measurement was 40 MeV too high [47] implying that the two measurements were in agreement at the 99.9 % level.

After completing the 24.5° bend, the beam was longitudinally polarized either opposite or the same as before the bend depending on whether there were an odd or even number of half-processions. At this point, the beam is in line to collide with the ESA target located approximately 60 meters downstream. The following section attempts to describe the remaining beamline (or beam-related) components that were vital to the success of the experiment.

3.1.3 End Station A Beamline Components

The experimental hall, ESA, contained the final components necessary for MCC operators to deliver quality, low-emittance rastered beam pulses (or spills) to the target. ESA also housed the components necessary for counting house A (CHA) operators to monitor the beam characteristics (spot size, position, current, and polarization). Two pairs of Helmholtz coils located at the entrance to the ESA alcove were responsible for

rastering the beam pulses over a circular area of the target. This provided uniform coverage over the target material and reduced the adverse effects of beam heating and radiation damage to the material (these effects are discussed in Section 3.2.4). The ESA single arm Møller polarimeter was used to measure the beam polarization at various intervals throughout the experiment. A pair of toroids measured the beam charge which determined the current, and the foil-array and roller screens indicated the beam spill's position and size characteristics. There was also, in addition to the standard straight-through beamline, a chicane system of magnets necessary for the perpendicular target magnet configuration. After the beam passed through the target, the non-interacting electrons proceeded through the last chicane magnet which directed them straight to beam dump east (BDE) via a large shielded beam-pipe, while the interacting electrons with the proper kinematics were transported into one of three momentum analyzing spectrometers. BDE is a water-cooled device, capable of absorbing high amounts of power, located in a tunnel in the side of a hill behind ESA. Figure 3.6 displays the location of various ESA beamline components.

Beam Monitors

Many devices were used by MCC and CHA operators to monitor the beam spill characteristics. Two fluorescent roller screens made of mylar coated with zinc sulfide, located in the ESA alcove (not shown in Figure 3.6), were used during beam tuning to observe the beam spot size and steering in ESA. The screens fluoresced when struck by the beam, showing its position and shape. The beam could be steered to center it on cross-hairs which were projected on the screens. Cameras transmitted pictures of the roller screens to video monitors in MCC and CHA. When the beam tuning was complete, the screens were rolled out of the path of the beam. Another device which provided beam position information was the traveling wave beam posi-

tion monitor (TWBPM) located just upstream of the target. The TWBPM utilized radio-frequency cavities to produce signals proportional to the horizontal and vertical displacement of the beam from the center of the beamline. These signals were incorporated into MCC's beam position feedback system.

The primary device used to determine the position and size of the beam at the target was the foil array. Located approximately 11 meters downstream of the target, the foil array consisted of two arrays of 48 foil pairs; one array oriented horizontally, and the other vertically. The foils were made of 25 μm thick aluminum placed at 1 mm intervals. Each foil pair consisted of an emitter and collector foil with a high

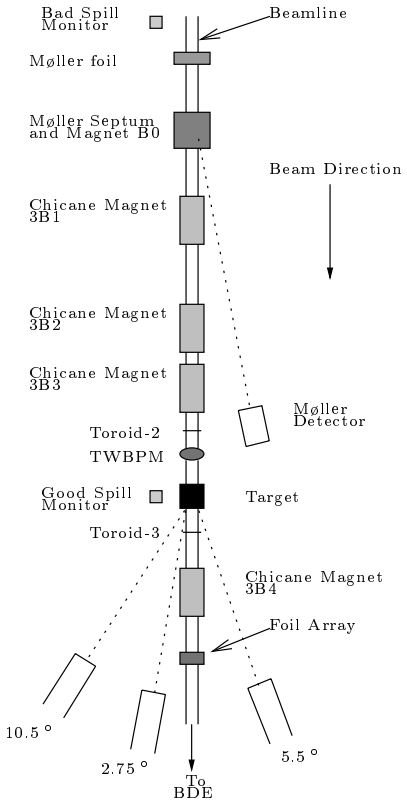

Figure 3.6: Schematic top view of ESA beamline components (not to scale). The Møller foil was placed in the beamline only when beam polarization measurements were performed.

voltage potential between them. When the beam passed through a foil, it produced secondary electrons which were accumulated at the collector foil; this generated a signal which was read out by an amplitude-to-digital converter (ADC). The typical beam spot size was ~ 1 mm in the horizontal direction and slightly less in the vertical direction.

The number of electrons contained in each beam spill was measured by two toroidal current monitors. Toroid-2 was located approximately 9 meters upstream and toroid-3 approximately 5.5 meters downstream of the target. Each current monitor consisted of an iron ring, encircling the beam line, with a wire coiled around it. When the beam passed through the ring, it induced a current in the wire which was amplified and measured by an ADC. The signal from the toroids was proportional to the number of electrons in the spill. The toroids were calibrated several times a day (refer to Section 4.1.1). Typically, there were approximately 2 to 3×10^9 electrons contained in each spill depending on which target and beam energy was used.

The final beam monitoring components to be mentioned here are the 'good' and 'bad' spill monitors. These devices consisted of a plastic scintillating paddle read out by a photomultiplier tube (PMT). The output from the PMT was passed to an ADC and an oscilloscope. Cameras transmitted the oscilloscope trace to video monitors in MCC and CHA. The bad spill monitor was located about a meter off the beamline near the entrance to ESA. It was responsible for detecting particles resulting from the beam scraping upstream beamline components due to poor steering or low beam quality. Little or no signal from the bad spill monitor indicated a stable beam which cleanly passed through the beamline. The good spill monitor was positioned a meter off the beamline at the target location. A large uniform signal from this monitor indicated that the beam was on target. Spikes or erratic characteristics in this monitor's trace could indicate that the beam was near the target cell edge and/or

slightly mis-steered as it entered ESA. If the good spill monitor became too erratic or non-uniform across the time-width of the spill ($\sim$ 450 ns), MCC operators would perform small adjustments of the pulse shape and steering.

Møller Polarimetry

The beam polarization for E155x was determined from polarized Møller scattering. Møller scattering is defined as elastic electron-electron scattering. If both the beam and (fixed) Møller target are spin-polarized, the cross section at a given scattering angle and beam energy is dependent on the magnitude and relative orientation of the reaction participant's polarization. In other words, a Møller asymmetry exists between the cross sections resulting from electrons with parallel spins and those resulting from electrons with antiparallel spins. By measuring this asymmetry with knowledge of the beam energy, scattering angle, and Møller target polarization, the beam polarization can be accurately determined.

The cross section for polarized Møller scattering is given by

$$\frac{d\sigma}{d\Omega} = \frac{d\sigma_0}{d\Omega}\left(1 + \sum_{i,j=x,y,z} P_b^i A_{ij}(\theta_{cm}) P_T^j\right), \tag{3.2}$$

where $\frac{d\sigma_0}{d\Omega}$ is the unpolarized Møller cross section, P_b^i and P_T^j are the beam and Møller target polarization, and $A_{ij}(\theta_{cm})$ is the asymmetry at the center-of-mass scattering angle (θ_{cm}) resulting from the i,j beam and target polarization configuration. The z axis is defined along the beam direction, and the y axis is normal to the scattering

plane [48]. The various asymmetry components are given by

$$A_{xy} = A_{yx} = A_{yz} = A_{zy} = 0, \tag{3.3}$$

$$-A_{xx} = A_{yy} = \frac{\sin^4\theta_{cm}}{(3+\cos^2\theta_{cm})^2}, \tag{3.4}$$

$$A_{xz} = A_{zx} = -\frac{2\sin^3\theta_{cm}\cos\theta_{cm}}{\gamma(4-\sin^2\theta_{cm})}, \tag{3.5}$$

$$A_{zz} = -\frac{(7+\cos^2\theta_{cm})\sin^2\theta_{cm}}{(3+\cos^2\theta_{cm})^2}. \tag{3.6}$$

The asymmetry A_{zz} is the theoretical longitudinal Møller asymmetry whose measurement allows for a determination of the longitudinal beam polarization. The measured Møller asymmetry can be expressed as

$$A^{M\o ller}_{measured} = \frac{\sigma^{\uparrow\uparrow} - \sigma^{\uparrow\downarrow}}{\sigma^{\uparrow\uparrow} + \sigma^{\uparrow\downarrow}} = P_b^z P_T^z A_{zz}. \tag{3.7}$$

Thus the beam polarization is given by

$$P_b \equiv P_b^z = \frac{A^{M\o ller}_{measured}}{P_T^z A_{zz}}. \tag{3.8}$$

E155x utilized the ESA single-arm Møller polarimeter to measure the Møller asymmetry by detecting only one of the scattered electrons. Figure 3.7 displays the setup and detectors for this polarimeter. In past SLAC ESA experiments, a double-arm Møller polarimeter was also used; this detector (which uses the same target, bending magnet (B0), and collimators as the single-arm) determines the Møller asymmetry by detecting both scattered electrons in coincidence. The remainder of this section will be limited to a discussion of the single-arm polarimeter only.

The ESA Møller polarimeter uses a thin ferromagnetic foil as its polarized target. During past experiments, several different target foils with thicknesses varying be-

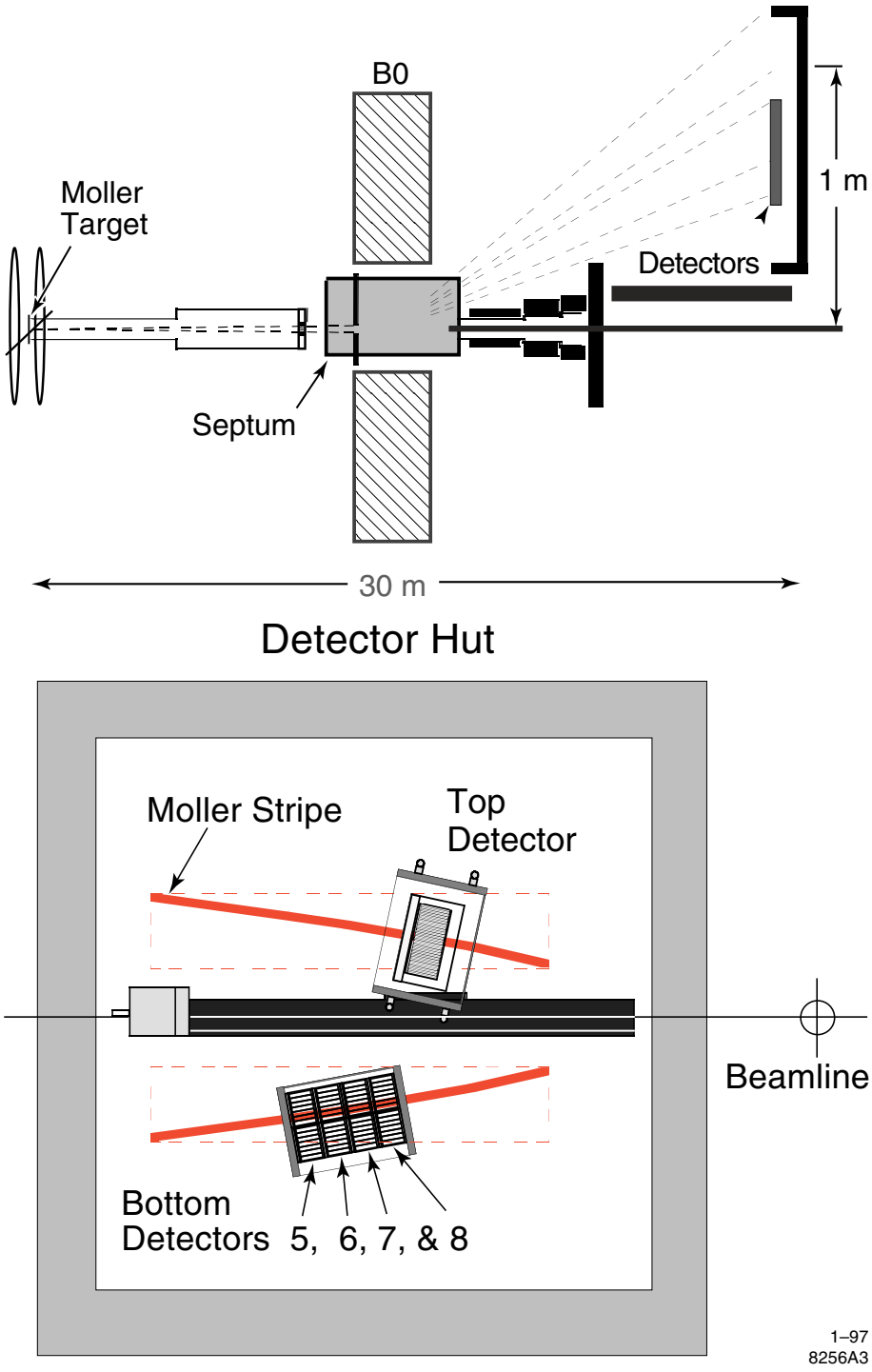

Figure 3.7: Top view of the Møller polarimeter design (upper figure) and downstream view of the Møller detector components (lower figure) as they were configured for E154 [48]. Note that for E155 and E155x, the top and bottom detectors occupied the bottom and top locations respectively.

tween 20 μm to 154 μm were used. Each target was made from a foil of Permendur* and was approximately 3 cm wide by 35 cm long, and each could be individually moved in and out of the beamline remotely. For E155x, all of the Møller data was taken with the 154 μm foil. The atomic electrons in the foil were polarized (along the plane of the foil) by a 100 Gauss magnetic field produced from Helmholtz coils centered around the beamline at the target's location. The foil was positioned at an angle of 20.7° with respect to the beamline (see Figure 3.7) to produce a longitudinal component to the target electron's polarization. The overall electron polarization in the foil, measured just prior to E155x, was approximately 8.3 %–which agreed with the post E155 measurement to better than 0.1 % [47].

A collimating tungsten mask, located approximately 10 m downstream of the target foil, with a wedge-shaped opening above and below the hole for the beam, was used to define the acceptance of the Møller detectors. The mask provided a θ acceptance of 3.59 mrad to 8.96 mrad, and ϕ (azimuthal) acceptances of 0.20 rad for the upper aperture and 0.22 rad for the lower aperture [48]. A momentum analyzing dipole magnet (B0) with a central field of $\sim$ 1 T was used to bend the scattered electron trajectories horizontally toward the Møller detectors. The unscattered beam, which passed straight through the central hole in the mask, traveled through an iron septum that shielded it from B0's field.

The scattered electrons deflected by the B0 magnet formed a stripe at the Møller detectors (as shown in Figure 3.7) which were located approximately 29 m downstream from the target foil. These detectors consisted of five silicon strip detectors, each consisting of two 4 cm $\times$ 6 cm $\times$ 300 μm silicon pad devices. The lower detector (shown as the top detector in Figure 3.7) consisted of one finely segmented silicon detector, and the upper detector (shown as the bottom detector in Figure 3.7) consisted

*A polarizable metal consisting of 49 % Fe, 49 % Co, and 2 % V.

of four coarsely segmented silicon detectors. The fine detector had 48 instrumented channels, each 2.18 mm tall, spanning the 12 cm height of the detector. The four coarse detectors each had 12 instrumented channels, each 8.69 mm tall, along their 12 cm height [48]. Both detectors were angled such that the Møller stripe was aligned parallel with the width of the channels. The fine detector was mounted on an actuating x-y stage that could be controlled remotely to position the detector anywhere within the acceptance.

The total charge deposited in each channel per beam spill was integrated by charge sensitive preamplifiers and then read out by an ADC. These values were then written to tape along with the relevant beam information (charge and helicity) which together was used to form the Møller asymmetry. The results of the beam polarization measurements are given in Section 4.4.1.

Chicane Magnets

A chicane system of four dipole magnets was used to steer the beam properly to and from the transversely polarized (nuclear) target. This system consisted of three magnets before the target magnet and one after the target magnet. The configuration of the dipoles showing a schematic of the beam trajectory through the chicane magnets and target magnet is shown in Figure 3.8. The first chicane deflected the beam in the same direction as the target magnet, while the remaining three deflected it in the opposite direction. Each chicane magnet was energized such that it possessed half the bending power of the target magnet. The responsibility of the upstream chicane magnets was to position the beam so that its momentum and spin vectors at the center of the target were parallel with the momentum and spin vectors of the beam before it entered the first chicane. The responsibility of the downstream chicane magnet was to ensure that the (unscattered) beam coming from the target made it

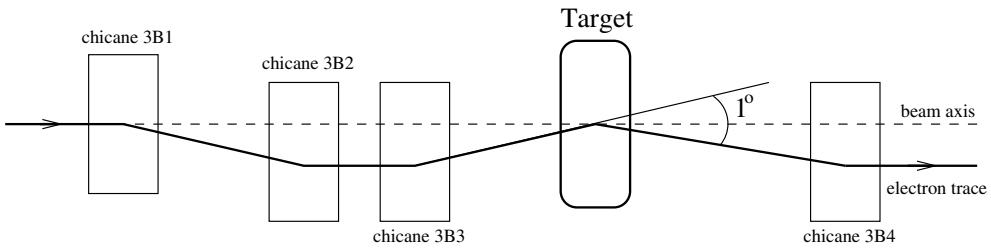

Figure 3.8: Diagram of the Chicane magnet system used for the perpendicular target mode.

into the beam pipe directing it to BDE.

After running at the beam energy proposed for E155x (29 GeV) for nearly two weeks, it was concluded that, at that beam energy, the chicane system did not have enough bending power to steer the beam cleanly into the beam pipe downstream of chicane-3B4. This was evidenced by the large background rates seen by the detectors due to the beam scraping the inside of the pipe. Attempts to alleviate the extremely high rates seen in the 2.75° and 5.5° spectrometers were only accomplished by lowering the beam current below 1×10^9 e^-/spill. At this current, the statistical precision of the experiment's measurement would not be reached in the given timeframe. Thus, it was decided to run the experiment at the next highest allowable beam energy (32 GeV). This allowed the chicane magnets to do their job properly, and the background rates in the detectors were reduced to acceptable levels at the proposed current of $\sim 2 \times 10^9$ e^-/spill. Three weeks later, during a short planned maintenance period (in which the target was changed from proton to deuteron), a small 30 Amp/1.5 kGauss dipole magnet (referred to as the 'kicker') was installed between the target and 3B4. The kicker magnet had the same polarity as 3B4 and provided the extra bending power needed to pass the beam cleanly through the downstream beam pipe. This reduced the background rates to normal levels and enabled the experiment to operate at the optimal beam energy and current.

3.2 Polarized Target

The targets utilized for E155x were solid dynamically polarized nucleon targets of $^{15}NH_3$ for protons or ^{6}LiD for deuterons. The free nucleons in the target material were polarized via dynamic nuclear polarization (DNP) at a temperature of 1 K in a 5 T magnetic field using 140 GHz microwaves. A ^{4}He evaporation refrigerator with over a Watt of cooling power at 1 K cooled the target. A superconducting split-Helmholtz coil magnet generated a homogeneous (1 in 10^4) 5 T field at the target cell. The microwaves driving the DNP process were generated by an extended interaction oscillator (EIO) tube and delivered to the target cell through a system of waveguides. The polarization of the target material was determined by nuclear magnetic resonance (NMR) measurements using a tuned series RCL circuit.

3.2.1 Theoretical Overview

Solid polarized fixed target systems have been in development for nearly half a century and have been in use at particle accelerator laboratories since the 1960's. Today, they are widely used in particle and nuclear physics research programs around the world and have proven to be an invaluable tool in the investigation of nucleon spin-structure. The crucial features of a solid polarized target are three-fold: The percent polarization attainable, the material's concentration of polarizable nucleons, and its resistance to radiation damage. Historically, the best polarized targets were typically made of chemically doped frozen alcohols. These targets were capable of high polarizations but suffered from poor resistance to radiation damage. In 1979, high proton polarizations were discovered in irradiation doped, frozen $^{14}NH_3$, and subsequent studies revealed that it also possessed extremely good polarization resistance to radiation damage [49]. Since then, ammonia and other inorganic crystalline solids (e.g. lithium hydrides)

have often been the material of choice for fixed polarized target experiments using high intensity particle beams. The remainder of this section will outline the fundamental theory describing the polarization of a system of nuclei, how this polarization is enhanced, and finally how the polarization is measured.

All nuclei with a net spin (or unpaired nucleon spin) possess a magnetic moment $\vec{\mu}$ that, when placed in an external magnetic field $\vec{B}$, tends to align itself with the direction of the field. This is simply a consequence of the particle seeking the lowest possible energy state associated with the $\vec{\mu} \cdot \vec{B}$ interaction. Depending on the strength of the magnetic field and the spin temperature of the system, this alignment produces a natural net polarization of the material. For example, the deuteron's natural polarization at 1 K in a 5 T field is ~ 0.1 %.

The most common measure of this polarization is known as 'vector' polarization, P, and is defined as simply the population (N) difference between spin aligned and anti-aligned (with the $\vec{B}$ field) divided by the total population. For the case of spin-$\frac{1}{2}$ protons, this is

$$P_{spin\frac{1}{2}} = \frac{N_{+\frac{1}{2}} - N_{-\frac{1}{2}}}{N_{+\frac{1}{2}} + N_{-\frac{1}{2}}}, \tag{3.9}$$

while for spin-1 deuterons, it is

$$P_{spin1} = \frac{N_{+1} - N_{-1}}{N_{+1} + N_0 + N_{-1}}. \tag{3.10}$$

As can be seen from Equation 3.10, the deuteron possesses $(2J + 1) = 3$ possible orientations of the spin along the axis of the magnetic field (where J is the spin of the nuclei). This gives rise to the N_0 term and thus a quantity known as the 'tensor'

polarization, A, which can be written as

$$A = \frac{N_{+1} + N_{-1} - 2N_0}{N_{+1} + N_0 + N_{-1}}. \tag{3.11}$$

The above quantity A, which can range between -2 and $+1$, is shown just for completeness and is not relevant for this experiment. For the remainder of this paper, the use of the term polarization will refer to the common 'vector' polarization which simply ranges between -1 and $+1$.

A more precise definition for the polarization of a system of nuclei is acquired through the use of statistical analysis. When a group of spins is placed in a magnetic field, each spin aligns in one of the $(2J + 1)$ possible orientations. Given that each spin state (or orientation) has equal probability, and that there are no restrictions on the number of nuclei that can occupy a given state, then the arrangement of spins for the system will follow the Maxwell-Boltzmann distribution. Furthermore, at thermal equilibrium, the distribution of nuclei among the available energy (spin) states will take the most probable distribution consistent with the total available energy and number of particles.

For spin-$\frac{1}{2}$ protons, this leads to the relative populations

$$\frac{N_{-\frac{1}{2}}}{N_{+\frac{1}{2}}} = e^{-\Delta E/kT} = e^{-2\mu_p B/kT}, \tag{3.12}$$

where k is the Boltzmann constant and T is the spin temperature. Substituting Equation 3.12 into Equation 3.9 then leads to

$$P_{spin\frac{1}{2}} = \tanh(\frac{\mu_p B}{kT}). \tag{3.13}$$

For spin-1 deuterons, Boltzmann statistics leads to the relative populations

$$\frac{N_{-1}}{N_0} = \frac{N_0}{N_{+1}} = e^{-\Delta E/kT} = e^{-\mu_d B/kT}. \tag{3.14}$$

Substituting Equation 3.14 into Equation 3.10 yields

$$P_{spin1} = \frac{4\tanh(\frac{\mu_d B}{2kT})}{3 + \tanh^2(\frac{\mu_d B}{2kT})}. \tag{3.15}$$

From Equation 3.13, the thermal equilibrium (TE) polarization for protons at 5 T and 1 K is ~ 0.5 %. But for electrons, which couple much more strongly to the external field, their TE polarization (under the same conditions) is nearly 100 %. This natural polarization of the electrons, given proper preparation of the target material, can be used to manipulate the nuclear spin-state populations through the hyperfine interaction. This can lead to an enhanced nuclear polarization compared to its TE value and is the subject of the next subsection.

DNP Enhancement

Dynamic nuclear polarization has long been used as a technique to enhance the nuclear polarization of materials and has broad-based applications in many fields of study. The concept underlying DNP enhancement is to provide a mechanism by which the natural polarization of a material's unpaired electron spins can be transferred to its unpaired nucleon spins. To supply the unpaired electrons that facilitate this process, it is required that the material be doped with paramagnetic centers (e.g. free radicals). These are essentially free electron spins which, through their creation of a localized effective magnetic field, couple to neighboring nuclei spins. This coupling, often referred to as the hyperfine interaction (HFI), is the key ingredient required to

orientate dynamically the target nucleons by means of spin transitions that would otherwise be forbidden.

To illustrate the mechanics of the DNP process, it is instructive to examine the Hamiltonian for a single electron and nucleon in an external magnetic field. This Hamiltonian consists of two Zeeman terms and a third term arising from the HFI and is written as

$$H = \vec{\boldsymbol{\mu}}_{\boldsymbol{e}} \cdot \vec{\boldsymbol{B}} + \vec{\boldsymbol{\mu}}_{\boldsymbol{n}} \cdot \vec{\boldsymbol{B}} + H_{int}. \tag{3.16}$$

Figure 3.9 displays the split energy levels implied by the above Hamiltonian. Without the interaction term, H_{int}, only the electron paramagnetic resonant (EPR) transitions and NMR transitions are permitted due to dipole selection rules. With the addition of the HFI, mixing occurs between the two allowed transitions resulting in the possibility for the forbidden transition. The method of DNP employed by the target system, commonly referred to as the 'solid-effect', induces the forbidden transitions by driving them with electromagnetic radiation [50].

By irradiating the material with photons of frequency $f_{\rm DNP} = \frac{1}{2\pi}(\omega_e \pm \omega_n)$, where ω_e and ω_n are the electron and nucleon resonant Larmor angular frequencies, the desired transition in which the electron and nucleon spin are simultaneously flipped results. For a 5 T field, $\frac{1}{2\pi}\omega_e$ is approximately 140.126 GHz. For protons, $\frac{1}{2\pi}\omega_n = 2\mu_p B/h \approx 213$ MHz. This implies that microwaves of frequency $f_{\rm DNP} = 139.9$ GHz can be used to align nucleon spins with the $\vec{B}$ field (positive polarizations), whereas $f_{\rm DNP} = 140.3$ GHz anti-aligns the nucleon spins–creating negative polarizations. For deuterons, $\frac{1}{2\pi}\omega_n = \mu_d B/h \approx 32.7$ MHz; implying that frequencies of 140.09 GHz and 140.16 GHz produce positive and negative polarizations respectively.

Thus far, it has been shown how the polarization of unpaired electrons can be transferred to their neighboring nucleons. However, this process only occurs in very

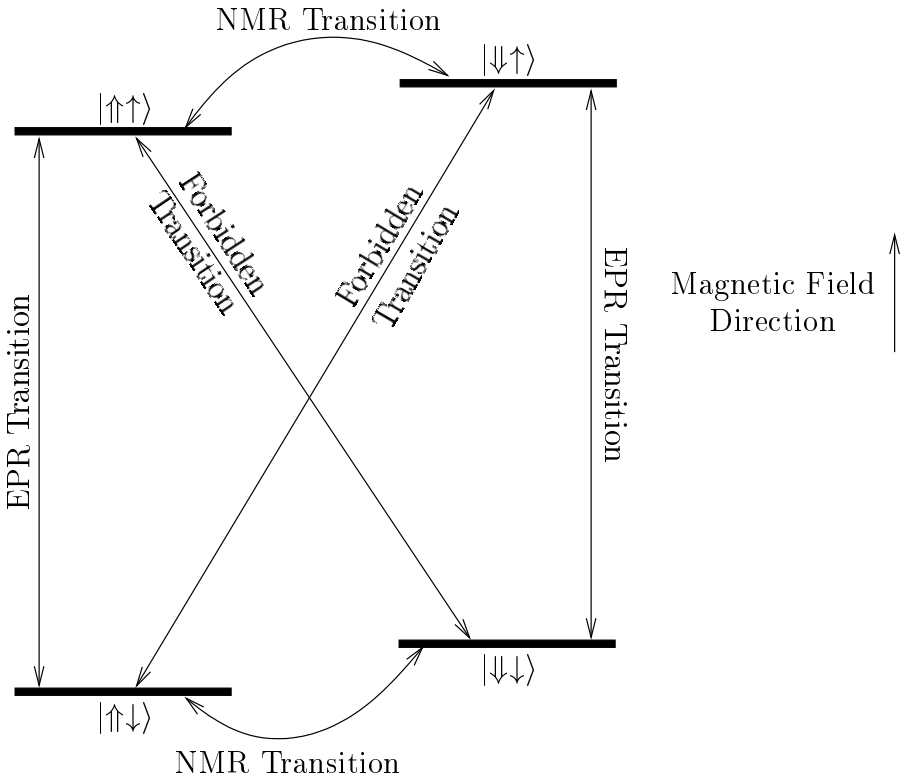

Figure 3.9: Level diagram for a nucleon-electron system in a magnetic field [51]. The energy of the states increases from top to bottom. EPR transitions induce an electron spin flip only whereas NMR transitions induce the nucleon spin flip only.

localized regions around the paramagnetic centers which are separated by vast seas of nuclei that do not experience these transitions. Thus, additional mechanisms are required to produce a material-wide nuclear polarization enhancement. By the process of 'spin-diffusion', the dynamically polarized nucleons transfer their polarization to other nearby nucleons via the nucleon-nucleon spin-spin interaction. This disperses the polarization enhancement outward from the paramagnetic centers and over time eventually increases the nuclear spin ordering in the material. However, since spin-diffusion is a relatively short distance phenomenon, DNP enhancement relies heavily on the process of 'thermal mixing'. This is the process by which induced electron spin transitions are propagated throughout the material via electron spin 'flip-flop'

interactions in an attempt to maintain (or reestablish) thermal equilibrium. And each time an electron spin is flipped, there is a probability that it will take a nearby nucleon with it.

The final essential feature contributing to the success of DNP enhancement is that the relaxation of the electron and nucleon spin take place primarily through thermal coupling with the lattice. Since the probability of these transitions is more than five orders of magnitude greater for electrons than nucleons [52], the nuclear polarization is allowed to build up while the rapidly relaxing electron spins are reused for further DNP.

NMR Measurement

The absolute nuclear polarization of the target was determined by continuous-wave NMR. In this technique, the material is exposed to a continuous radio-frequency (RF) signal with a time-varying magnetic field transverse to the static external field. The perturbing RF field is swept through a small range of frequencies (ν) centered about the Larmor frequency ($\frac{1}{2\pi}\omega_n$) of the nuclear spin species. At each frequency, the response of the material is dictated by its net nuclear magnetization or more explicitly by its magnetic susceptibility

$$\chi(\nu) = \chi'(\nu) + i\chi''(\nu), \tag{3.17}$$

where χ' is the dispersive and χ'' the absorptive component. The sum of the absorptive component over all frequencies (or equivalently, the smaller range stated above) has been shown to be directly proportional to the net polarization of the material [53].

An indirect measurement of χ is made possible by measuring the inductance of a simple coil embedded inside the target cavity and surrounded by target material. For

completely unpolarized material, the inductance is just a constant L_0; the presence of nuclear magnetization modifies the inductance to the form

$$L(\nu) = L_0[1 + 4\pi\eta\chi(\nu)], \tag{3.18}$$

where η is the coil filling factor or more explicitly a measure of the material's coupling to the coil RF. By incorporating the inductor's impedance into a resonant RCL circuit and tuning its capacitive parameters, the reactive part of the impedance (containing the dispersive susceptibility component χ') cancels leaving only the resistive part which contains χ''. The voltage output from such a tuned circuit at resonance can then be used to determine the target polarization. The design and operation of this circuit are detailed in Section 3.2.5.

3.2.2 Target Setup

The setup for the E155x polarized target was the same as that for E143 and E155. It consisted of a vacuum insulated, liquid nitrogen (LN_2) shielded, liquid helium (LHe) cryostat with an Oxford Instruments 5.1 Tesla superconducting magnet and ^{4}He evaporation refrigerator. This arrangement is shown in Figure 3.10. The target material was contained in cylindrical cavities attached to an 'insert' (see Section 3.2.3 for details) which was installed through the refrigerator from the top of the cryostat.

The cryostat's internal vacuum was maintained at $\sim 10^{-7}$ torr to provide a high degree of insulation between the cryogen reservoirs and from the outside world. A 57 liter LN_2 reservoir shielded the 85 liter LHe reservoir and inner-cryostat components from the room temperature (300 K) thermal radiation from the cryostat's outer walls. The liquid levels were automatically maintained by individual 2000 l dewars which were manually refilled about every two weeks. For added convenience and

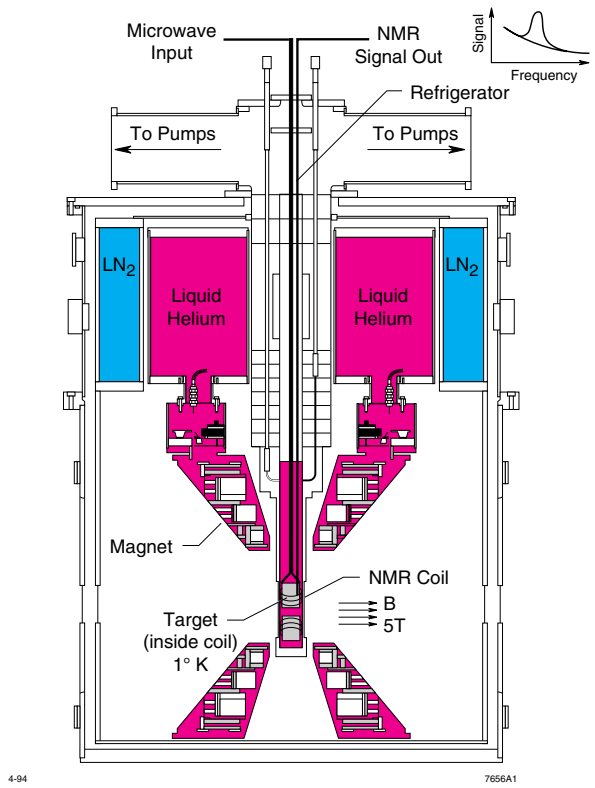

Figure 3.10: The E155x polarized target cryostat, refrigerator, and magnet assembly. For the transverse target configuration of E155x, the electron beam (not shown) comes out of the page at the center of the magnet geometry.

efficiency, the magnet reservoir was filled from an intermediary 500 l buffer dewar.

Magnet

The large, highly uniform magnetic field requirements of the polarized target were achieved with a pair of superconducting Helmholtz coils. This magnet geometry not only provided the necessary level of spatial field homogeneity at the midplane but also readily facilitated a transverse target polarization configuration by enabling the beam to pass through the space between the coils[†]. The superconducting core of the

[†]For a longitudinal target, the entire cryostat can be rotated such that the beam passes through the central axis shared by the two coils.

magnet coil windings were made of niobium-titanium alloy (NbTi) which has a typical critical temperature of $T_c \approx 10$ K. As depicted in Figure 3.10, the magnet coils and their support structures were immersed in liquid helium and thus maintained at a temperature around 4 K. The space between the coils (and coil support structures) spanned 8 cm–allowing ample space for the target. Each coil spanned the geometry of a open cone with inner diameter approximately 20 cm, and outer diameter roughly 50 cm. Along the bore of the magnet, this produced a scattered particle clearance of $\pm 50^\circ$ in both horizontal and vertical directions. For the transverse configuration, the scattered particle clearance was $\pm 17^\circ$ horizontally and $\pm 25^\circ$ vertically. The magnet was slowly energized to ~ 77.5 A by an Oxford 10 V/120 A power supply. Two trim coils were added to the magnet to enhance the homogeneity of its field to a level of 10^{-4} T in a small ~ 30 cm^3 volume centered at the target location, and for added stability, the magnet was operated in persistent mode.

Refrigerator

Maintaining the target at a temperature around 1 K was achieved by submerging the material in a LHe bath cooled by an evaporation refrigerator. The design of the refrigerator is illustrated in Figure 3.11. An evaporation refrigerator operates on the principle that lowering the vapor pressure of a liquid bath lowers the bath temperature. The target refrigerator supplied the bath by drawing LHe from the magnet reservoir and delivering it to a cavity surrounding the target cups (called the 'nose'). The vapor pressure of the bath was reduced by pumping out the evaporated helium that filled the inner space of the fridge. Moreover, as this helium was pumped-out, it cooled the fridge's inner components, which were in thermal contact with the LHe filling the nose, thus further reducing the liquid temperature.

The main fridge components are labeled in Figure 3.11. LHe drawn from the

magnet reservoir was passed through a phase separator to ensure that mostly liquid was delivered to the nose. The separator utilized a sintered bronze plate which had a high impedance to helium gas but readily allowed LHe to pass through it. The gas in the separator was pumped out by a small mechanical pump; this gas was used to cool a system of radiation baffles which shielded the inner fridge from thermal radiation emitted from the top plate. The delivery of liquid from the separator to the nose could occur by one of two pathways (or both) each with their own stepper-motor controlled needle valve. The run valve, which was the primary means of maintaining the nose

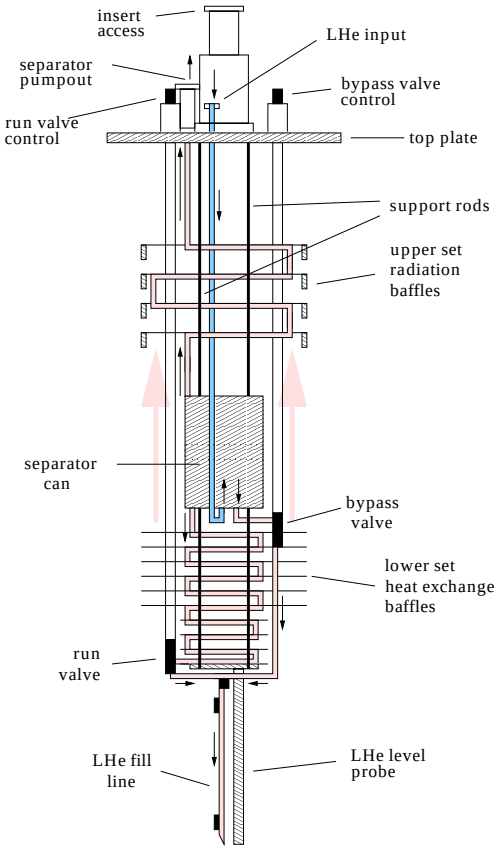

Figure 3.11: Target ^{4}He evaporation refrigerator (not to scale) [54]. The short, small black arrows denote the flow of LHe down through the system. Large shaded arrows show the direction of evaporated helium as it is pumped through and out of the fridge.

liquid level, regulated the flow of LHe spiraling through a system of heat-exchange plates cooled by the passage of pumped-out helium vapor through its perforations. The bypass valve circumvented the heat exchangers providing a quick way of filling the nose with (not as cold) LHe. The pumps used to lower the helium vapor pressure inside the fridge consisted of a system of three successively larger Roots blowers capable of maintaining the vapor pressure around 0.12 torr and thus the temperature of the target around 1.0 K.

3.2.3 Insert and Instrumentation

The target material, which consisted of 1 to 3 mm diameter granules or chips, was loaded into two cylindrical cups attached to the bottom of a long thin rod called the 'insert'. The insert was over a meter long and about four centimeters in diameter and was designed to position the material in the beamline by lowering it into the target cryostat through the bore of the refrigerator. The insert also contained all of the instrumentation needed to operate and monitor the polarized target. This included waveguides for delivering microwave radiation, NMR cables for the Q-meter circuit, temperature sensors and heater wires for target annealing–(discussed in Section 3.2.4), and a ^{3}He manometer for temperature measurements during thermal equilibrium calibrations–(presented in Section 3.2.7).

The insert consisted of a long stainless steel frame attached to an aluminum target ladder which held the target cups in place. The various hardware and electronic instrumentation entered through the top plate of the insert and traveled down its length to the target ladder. To reduce heat flow from the top plate to the target chamber, two copper radiation baffles and a heat-sink were mounted to the insert. The heat-sink was located roughly halfway down the insert such that it would be in

thermal contact with the refrigerator separator at 4 K. Figure 3.12 is a schematic of the insert. It details the configuration of the target cells at the bottom of the insert as well as the location of the various temperature sensors.

Polarized target material was contained in the two larger cells that are shown to be fitted with a microwave horn. These cells, referred to as 'Top' and 'Bottom', were 1 inch diameter by 3 inch long cylinders made of polymonochlorotrifluoroethylene (PCTFE) called Kel-F; this material contained no free protons and was moderately

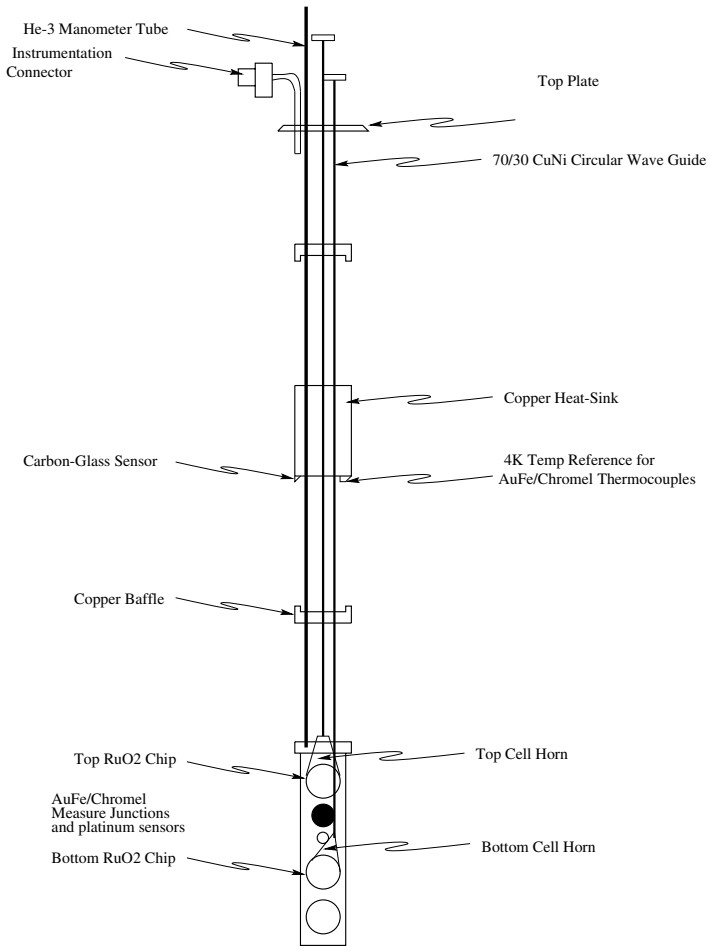

Figure 3.12: Target insert schematic [54]. Not shown are the NMR cables which couple to the NMR coils inside the polarized material cups as well as the heater coils used for annealing.

resistant to radiation damage. There were also three other possible target positions: A small unpolarized solid target located just under the top cell, a smaller 'no target' (or hole) position for straight through running with unrastered beam located just above the bottom cell, and a full-sized unpolarized solid 'dummy' target mounted inside a Kel-F cup at the very bottom. The two unpolarized solid targets consisted of either a carbon or beryllium disk of uniform density and known thickness. The primary function of these targets was to enable a determination of the polarized target thickness (via a comparison of spectrometer detection rates) used in the calculation of the dilution factor (presented in Section 4.4.3). Two different inserts were used during E155x. They were constructed identically except one had a solid carbon 'dummy' target, for $^{15}NH_3$ running, and the other had a solid beryllium 'dummy' target for ^{6}LiD running.

Each polarized target cell contained two NMR coils made of CuNi tubing. The deuteron coil used a four turn loop while the proton used a single loop coil. Each coil was connected to an RF transmission cable which ran up the length of the insert and out of the top plate. These cables consisted of a teflon insulated ($\beta = 0.695$), semi-rigid beryllium-copper coaxial-cable and provided a portion of the NMR $\lambda/2$-cable circuit which connected a Q-meter to the coil. A platinum resistor and AuFe/Chromel thermocouple mounted near each polarized material cell monitored the target temperature during anneals. Two small heater wires wrapped around the bottom of the up stream aluminum frame of the target ladder (and a few turns around each target cell) provided the anneal heating.

Microwaves, generated by an EIO tube mounted on a table above the target cryostat, were delivered to the target by a system of waveguides. Inside the insert, two 3/16 inch CuNi tubes guided the microwaves straight to each target cell. Outside the insert, an assembly of short waveguides and couplers linked the EIO tube to the

insert waveguides. The microwave assembly table and insert were attached to a motor driven actuating platform which moved the various targets (up and down) into the beamline; the platform motor used an optical encoder for positioning feedback.

3.2.4 Material

As mentioned at the beginning of Section 3.2.1, the crucial considerations when choosing a target material are its maximum polarization, concentration of polarizable nucleons, and resistance to radiation. Other deciding factors include rate of polarization buildup and percentage of free protons or deuterons compared to other polarizable nuclei. The latter is one of the important factors influencing the size of the dilution factor[‡] which affects the size of the raw asymmetry. Furthermore, the aforementioned 'other' polarizable nuclei create additional corrections that need to be applied to the raw asymmetry; these are known as nuclear corrections, C_1 and C_2 (briefly defined below), and are detailed in Section 4.4.4.

The C_1 factor corrects for the presence of polarizable nuclei, other than ^{1}H or ^{2}H, that are of the same spin species as the target nucleons, whereas C_2 corrects for the presence of polarizable spin species different from the target (e.g. protons in the deuteron target and vice versa). In general, fewer and/or smaller asymmetry corrections are more desirable as their uncertainty contributes to the error on the measurement. This is the reasoning behind the choice of ^{15}N ammonia ($^{15}NH_3$) as opposed to ^{14}N ammonia. Since ^{14}N is spin-1 and has a very large quadrupole moment [56] (broadening its NMR signal), its polarization is difficult to determine accurately and thus creates a significant source of error by way of a sizable C_2 correction. ^{15}N,

[‡]A material's concentration of the desired polarizable particles (^{1}H or ^{2}H) dictates the theoretical upper-limit on the size of its dilution factor. For protons in $^{15}NH_3$ this is 16.7 %, while for deuterons in ^{6}LiD, the upper-limit is 25.0 % assuming no ^{2}H content in ^{6}Li and 50.0 % assuming ^{6}Li can be viewed as ^{4}He + ^{2}H [55].

however, possesses only a single unpaired proton (spin-$\frac{1}{2}$) and hence no quadrupole broadening; this facilitates a more accurate determination of its polarization and thus contributes a much smaller error to the asymmetry by way of the C_1 correction[§].

The choice of an ammonia proton target was clear–extremely high polarizations (nearly 100%), fast buildup, good resistance to radiation damage, reasonable dilution factor and small nuclear corrections, and most importantly a well understood target material widely used for decades. The choice of ^{6}LiD as a deuteron target was not as clear-cut mainly because it was not widely used[¶] and understood, although it possessed many qualities superior to the 'mainstream' deuterated ammonia ($^{15}ND_3$) target. These qualities include extremely high resistance to radiation damage, a much improved dilution factor, a very narrow single-peak NMR signal (easier to measure), and maximum polarizations comparable to $^{15}ND_3$ ($\sim$ 30 - 40%). A detailed study of ^{6}LiD as a polarized target can found in reference [57]. The only major drawbacks of ^{6}LiD were its long thermalization time (see Section 3.2.7) and its extensive nuclear corrections (refer to Section 4.4.4) as compared to the ammonia targets.

Pre-irradiation

The pre-irradiation of the target material creates within the material the concentration of paramagnetic centers needed for DNP ($\sim 10^{19}$ centers/cm^3 [58]). Prior to the start of the experiment, two batches of $^{15}NH_3$ were irradiated with low energy electrons produced by the 30 MeV linac at the Stanford University Short Intense Electron Source (SUNSHINE) facility. These batches served as the primary target proton material used during E155x. The ^{6}LiD material used during E155x was irra-

[§]Note that ^{15}N was originally chosen because it eliminated the hard to measure background neutron polarization in deuterated ammonia targets.

[¶]SLAC experiment E155 was the first time ^{6}LiD was used in a high energy electron beam experiment.

diated at SUNSHINE prior to E155. During this irradiation, the ^{6}LiD was exposed to 1 to 5×10^{17} e$^-$/cm^2. Typically, $^{15}NH_3$ was exposed to $\sim 1 \times 10^{17}$ e$^-$/cm^2.

Radiation Damage and Annealing

When the target material is subjected to the intense high energy SLAC electron beam, its polarization decays as a result of radiation damage. This 'damage' is understood essentially as the creation of additional types and numbers of paramagnetic centers beyond the optimal density needed for DNP purposes. As these extra radicals accumulate, they eventually begin to counteract the DNP process by shortening the nucleon relaxation time and thus lowering its absolute polarization [58]. After the target material has experienced a certain amount of beam flux (referred to as 'dose'), causing its polarization to drop below the acceptable level deemed for the experiment, the material must be either annealed or replaced.

Annealing is the method used to recover the initial dilute concentrations of paramagnetic centers created during the warm irradiation doping. This process involves heating the target material up to the pre-irradiation temperature ($\sim$ 80 K for $^{15}NH_3$ and $\sim$ 120 K for ^{6}LiD) and keeping it there for a time sufficient enough to remove most of the unwanted radicals. The theory behind this is that the centers created by the beam while the target was cold (1 K) recombine at higher temperatures thus healing the beam induced damage. This is however not an exact science and other processes not mentioned here could also play an important role in recovering the target polarization performance. Moreover, after each successive anneal, the targets did not necessarily completely recover their initial performance. For the case of $^{15}NH_3$, this is evidenced by progressively faster rates of polarization decay after each anneal, leading to the eventual replacement of the material. For ^{6}LiD, the beam impact on its polarization was less dramatic, and the material's response to annealing has not

been fully tested.

Figure 3.13 displays the target polarization as a function of accumulated dose for a specific batch of $^{15}NH_3$. This plot tracks the behavior of the polarization through five anneals. Figure 3.14 displays the polarization as a function of dose for the ^{6}LiD targets. This plot displays the dose performance of all three batches of ^{6}LiD used in the top target cell during the entire experiment. Note the radiation resistance of ^{6}LiD is more than twice that of $^{15}NH_3$, moreover, it was run at twice the average beam current ($\sim$ 50 nA instead of $\sim$ 25 nA for $^{15}NH_3$) to maintain the same spectrometer event rates–because it is nearly half as dense as the $^{15}NH_3$ targets. The only ^{6}LiD target anneal occurred for batch 'Bottle 1020+1021' after it had received a dose of $\sim 45 \times 10^{15}$ electrons.

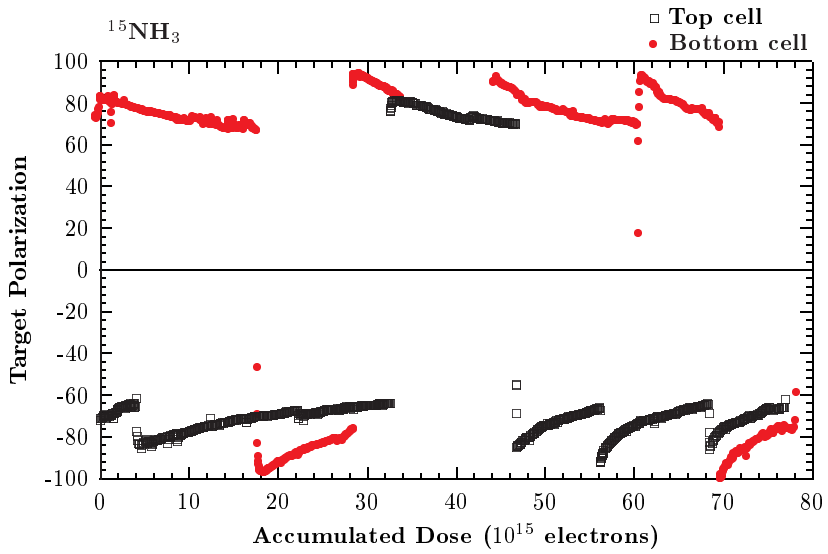

Figure 3.13: $^{15}NH_3$ polarization versus accumulated beam charge for top and bottom cell material batch G08 E155x #1 used between 03/17/1999 and 03/31/1999.

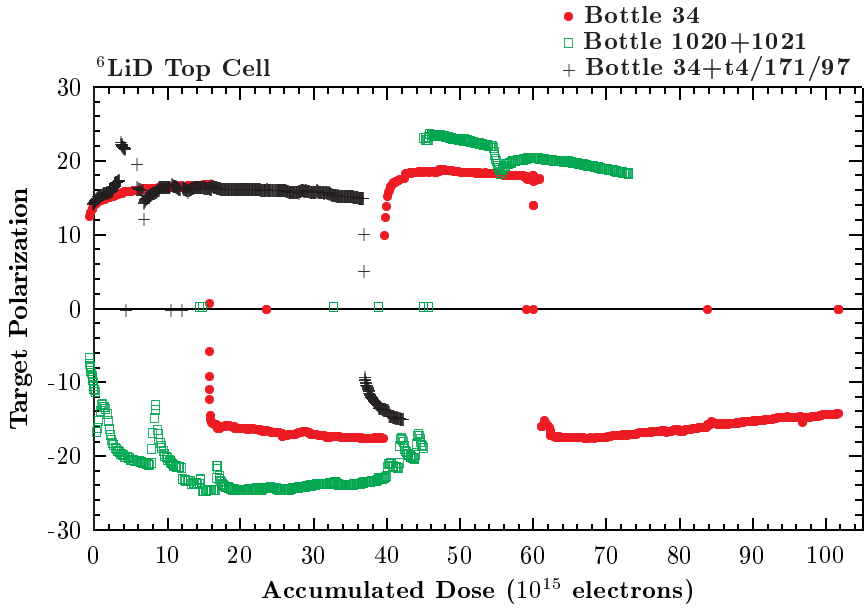

Figure 3.14: Polarization versus dose for all ^{6}LiD top cell material used during E155x.

3.2.5 Q-Meter NMR System

The circuit used to provide the target NMR measurement consisted of a Liverpool Q-meter module with a resonant transmission cable connected between the tuning capacitor and the target coil. This subsection will detail the operating principles of the Q-meter circuit, displayed in Figure 3.15, as well as the technique used to produce and acquire its signal.

The RF generator supplies the Q-meter input voltage (V_{RF}) which is a continuous wave RF signal swept through a small range of frequencies centered about the target Larmor frequency ($\frac{1}{2\pi}\omega_n$). After properly matching impedances at the input of the Q-meter, V_{RF} is directed along two parallel circuit paths: One through a phase-adjust cable to provide a reference signal for the phase-sensitive detector (PSD) (detailed below), and the other through R_{CC} and on to the RCL branch and output amplifier with input impedance R_A. The value of R_{CC} limits the nominal current in the amplifier

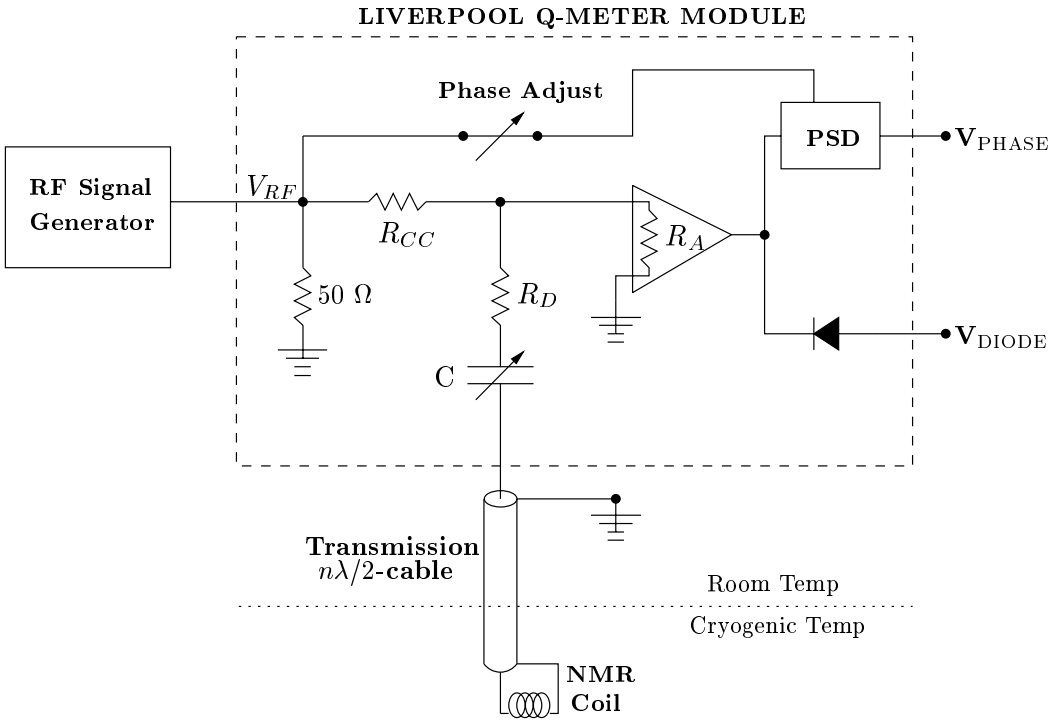

Figure 3.15: NMR circuit design for E155x using Liverpool series-tuned, constant current, RCL Q-meter.

and RCL branch to ~ 0.15 mA RMS, given $R_{CC} = 660\ \Omega$ and $V_{RF} = 100$ mV RMS. The approximation of constant current in the Q-meter circuit and more importantly the NMR coil is assumed in the analysis of the Q-meter signals. The actual current has a slight frequency dependence from the impedance of the RCL chain, $Z_{RCL}(\nu)$. To minimize the relative change in current, R_{CC} is chosen to be much greater than the parallel sum of $Z_{RCL}(\nu)$ and R_A. To further justify the assumption of constant current in the NMR coil, $Z_{RCL}(\nu) << R_A$. Table 3.1 gives the values of the resistors and capacitors used in the five Q-meters (one for each NMR coil plus an additional Q-meter for ^{15}N polarization measurements).

After sampling the impedance characteristics of the RCL branch, the voltage signal is amplified and then directed through two different outputs of the Q-meter. V_{DIODE}

			Q-meter Module Parameters				$\lambda/2$-cables	
Q-mtr	Target	ν_{res}	Resistances (Ω)			Capacitance (pf)		length
#	Species	(MHz)	R_{CC}	R_A	R_D	C	$\mathbf{n}\lambda/2$	(cm)
1	Proton	213.06	660	50	10	KAC + TC	7	365.13
2	Deuteron	32.71	660	50	5.6	KAC + 62	1	338.35
3	Proton	213.06	660	50	10	KAC + TC	7	365.13
4	^{15}N	21.60	660	50	5.6	KAC + TC + 200	1	521.98
5	Deuteron	32.71	660	50	5.6	KAC + 62	1	338.35

Table 3.1: Module parameters for the five Q-meters used during E155x. The various knob adjusted (KAC), trim (TC), and fixed capacitors were added in parallel. Also listed are the target resonant frequencies for a 5.004 T field and the $\lambda/2$-cable specifications–where the length is the total cable length from Q-meter to coil and the preceding column is the number of half wavelengths (n) contained in that total length.

yields the magnitude of the signal and is useful when tuning the circuit. V_{PHASE} is the output from the PSD which contains the NMR signal to be analyzed. The phase-sensitive detector consists of a balanced-ring modulator (BRM) which produces a signal proportional to the phase difference between its input and reference signal multiplied by the magnitude of the input signal. The length of the phase-adjust cable is chosen such that there is zero phase difference between the input and reference signal at resonance. The goal of the Q-meter design and setup is to establish, at resonance, a purely resistive input voltage to the BRM. This ensures that the NMR signal be as close as possible to a direct measurement of χ''.

To achieve this goal, the Q-meter employs a variable capacitance whose impedance can be tuned precisely to cancel the reactance of the coil at resonance. Also, the impedance of the transmission cable is made to be purely resistive at resonance by requiring that its length be an integer number of half wavelengths ($n\lambda/2$) of the resonant frequency inside the cable[‖]. Since V_{RF} is swept through a small range

[‖]Note that the transmission cable outside the cryostat is different than that inside; its dielectric is made of a micro-porous teflon ($\beta = 0.780$) whose characteristics do not exhibit a strong dependence

of frequencies, contributions from the reactive impedance of the $\lambda/2$-cable at non-resonant values give the Q-meter signal, plotted as a function of frequency and referred to as the Q-curve, its characteristic background shape which resembles a parabola. This background Q of the signal (known as the baseline) must be subtracted before integrating the NMR signal; this is done through computer software and will be discussed briefly in the next section.

The coil RF induces NMR transitions in the target sample. For a positively (negatively) polarized target, these transitions are mostly energy absorbing (emitting) (refer to Figure 3.9) and thus create an effective increase (decrease) in the coil resistance as the RF sweeps through resonance; this gives rise to the NMR signal. The value of the damping resistor, R_D, sets the voltage level of the baseline sufficiently high (up to 3 V DC) such that the tip of the maximally negative-enhanced signal peak never crosses zero.

After passing through the PSD, the Q-meter signal was sent through an 'offset card', for the purpose of subtracting the baseline voltage level created by R_D, in order to zero the background level of the signal before it was passed through two additional stages of amplification on its way to an ADC. The 'DC-subtract' level was specified by the size of V_{PHASE} during a computer-controlled trigger. The trigger was programed to occur at an off-resonance frequency where the background Q was near its average value. The purpose of the background subtraction was to prepare the signal for amplification–which increased its signal-to-noise ratio and allowed the full range of the ADC ($\pm$5 V) to be utilized. The V_{PHASE} signal was also directed through a buffer amplifier output where it was used for tuning and diagnostic purposes. This output, called the 'DC-monitor', was used to determine the baseline voltage (V_b) and

on temperature around 20 C as is the case for the solid teflon dielectric of the transmission cable inside the insert.

modulation strength (M) of the Q-meter signal. The modulation strength of the RF level in the Q-meter circuit is defined as

$$M = \frac{\Delta V_s}{V_b}, \tag{3.19}$$

where ΔV_s is the peak size of the enhanced NMR signal. The maximum modulation level is a critical parameter for materials with very large enhanced signals (e.g. protons in $^{15}NH_3$) because its size gives an indication of the reliability of the constant current assumption. For $M_{max} < 0.3$, the response of the Q-meter over the range of measured polarizations was expected to be linear.

The RF was swept back and forth through 400 equally spaced frequencies modulated by a 12.5 Hz digitized triangle wave. At each step of the triangle wave, the amplified Q-meter signal was acquired by a Stand-Alone CAMAC microprocessor system (STAC) [59] which consisted of an embedded Motorola 68000 series microprocessor and a 16bit ADC. The STAC generated the triangle wave and synchronized its signal acquisition to take place approximately 25 μs after each frequency step. This allowed settling time for the RF generator frequency changes which took place every 100 μs. The typical NMR measurement consisted of 200 back-and-forth frequency sweeps producing a total of 400 Q-meter signals for each frequency step. These signals accumulated in the STAC memory buffer until the set of sweeps was complete. The signals were then passed to the target data acquisition system for processing.

3.2.6 Target Data Acquisition System

The target data acquisition (DAQ) system was responsible for performing and monitoring most polarized target operations as well as logging to disk all information needed for the target data analysis. Approximately 1.2 gigabytes of target data were

logged to disk during the E155x run. A description of the DAQ software system components and their functionality will be given in this section.

The target DAQ was executed on two PCs located in CHA interfaced with rack-mounted hardware in ESA via General Purpose Interface Bus (GPIB). The control program (referred to as the target polarization system or TPS**) consisted of a collection of routines written in National Instruments LabView5.0 which ran on one of the PCs. The second PC acted simply as a display for additional target information. The TPS LabView routines were organized into 12 groups (called 'modules') each responsible for performing a specific set of duties. Table 3.2 gives a list of these modules along with their primary functions.

Module Name	Primary Task
PDP (Polarization Display Panel)	Main user interface, initiates all activities
TCL (Target Computer Logging)	Log event data to disk
NSE (NetServ Exchange)	Exchange information with ESA DAQ
STS (Slow-controls Tcp/ip Sender)	Send event data to SDP for display
TEB (Target Event Builder)	Compile data generated during an event
OLA (On-Line Analysis)	Process Q-curve to determine polarization
QCA (Q-curve Acquisition)	Initialize/perform NMR related tasks
SMC (Superconducting Magnet Control)	Operate/monitor magnet power-supply
TTM (Target Temperature Monitor)	Monitor ^{3}He & ^{4}He manometers
MWC (Microwave Control)	Monitor microwave frequency
SCM (Slow Controls Monitor)	Readout analog signals

Table 3.2: List of target DAQ LabView modules with a brief description of their functionality.

The target operator interacted with the TPS through the PDP module. There were two main operation modes: Take-data, and monitor. Take-data was the usual mode of operation in which NMR measurements were continuously performed. Each measurement lasted from $\sim$ 17 s for 200 sets of sweeps to $\sim$ 82 s for 1000 sets. During

**The original version of the TPS, executed on a single Macintosh computer, was written by P. McKee for E155.

each measurement (called an 'event'), all the so-called 'slow-control' target parameters were read out. These parameters included liquid levels, gas flows, valve settings, temperatures, RF power, microwave power and frequency, magnet power-supply status, and encoder position. These read-out values as well all other information relevant to each event, including the raw Q-curve returned from the STAC, were collected by the TEB module. Following the on-line processing of the Q-curve (described at the end of this section), TEB would package all the data and send it to TCL for disk storage; a portion of the event data was also sent to PDP for updating the user display, and to NSE for exchanging data[††] with the ESA DAQ–(which is briefly described in Section 3.4). In addition to being sent to TEB, the slow-control parameters were sent to STS as they became available. From here, the data was sent to the Slow-controls Display Panel (SDP) which was the only LabView process running on the second PC. This process simply displayed the information with no user interaction. The flow of commands and data through the TPS are illustrated in Figure 3.16. The other main operation mode of the TPS, monitor mode, was invoked when there was a need to monitor the slow-control parameters but no need for NMR measurements.

The processing of the raw Q-curve occurred in the OLA module. After averaging the Q-curve over the number of sweeps performed, three processing steps took place. First, the baseline was subtracted from the raw Q-curve. The baseline was acquired with the Q-meter in the same way as the NMR signals (same frequency range, sweep pattern, etc.), except that the static field was lowered about 2% causing the NMR signal to be absent from the measurement. Baselines formed in this way usually allowed for a very accurate subtraction of the background Q from the NMR signal. Baseline measurements took place prior to NMR measurements and were performed anytime

[††] Target data sent to the ESA DAQ included the event number, type of material, polarization, calibration constant, and magnet current. Data received by NSE included the run number, spill number, beam current, and the present total top and bottom target dose.

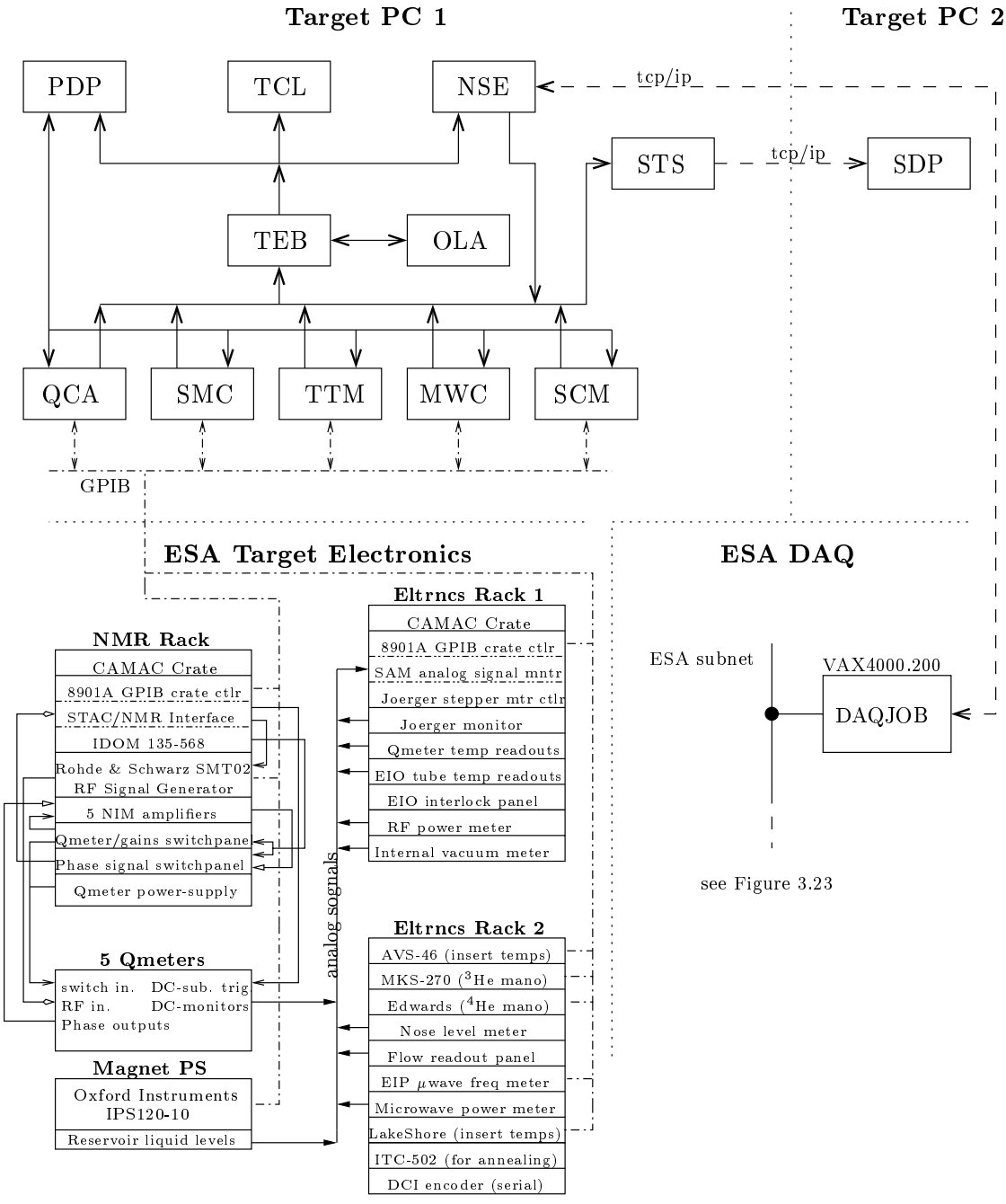

Figure 3.16: Flow of information between the components of the target DAQ.

the material or the Q-meter tune was changed. The second processing step was to fit the residual 'wings' of the baseline-subtracted signal with a 3rd order polynomial and then subtract it from the signal. This produced the final processed signal atop a flat background. The last step in the on-line analysis was to integrate this processed signal to yield its area. The area was then multiplied by a calibration constant to yield the polarization. The details of the NMR calibration are given in the next section.

3.2.7 Calibration and Performance

In order to determine the polarization of the target, the area under the NMR signal was calibrated to the natural polarization (P_{TE}) of the material at thermal equilibrium. Assuming the Q-meter circuit was properly tuned and operating within designed parameters (i.e. the modulation strength of the RF level remained sufficiently small), then the signal area increased linearly throughout the whole range of polarization enhancement. This resulted in a simple calibration constant (CC) relating the area of the signal to the absolute polarization, and it can be expressed as

$$CC = \frac{P_{TE}}{Area_{TE}}, \tag{3.20}$$

where $Area_{TE}$ is the integrated NMR signal at thermal equilibrium, and P_{TE} is calculated from Equations 3.13 or 3.15 depending on proton or deuteron target respectively.

New CCs were calculated each time the material was replaced and ideally after each anneal, although the later was not always possible given the time constraints of the experiment. If significant settling of the material occurred during an anneal, this could result in a change in the target coil filling factor (η) which affects the tune and the response of the Q-meter circuit and hence the NMR signal calibration; in these situations, a new CC was needed. Table 3.3 lists the CCs used during

the experiment. A detailed off-line analysis, performed by Stephen Büeltmann, was needed to determine these calibration constants after it was discovered during a target technical run (conducted immediately following the completion of E155x) that the ^{3}He manometer (used for the on-line determination of the CCs) was not functioning properly. The main results of that analysis will be given here; the details are located in reference [60].

The error associated with the target polarization measurement was dominated by the uncertainty of the TE calibration constants. For both targets, the main contri-

Date	**Mat.**	**Mat. Batch:** Top / Bottom	**Dose** 10^{15} e^-**:** Top / Bottom	CC**:** Top / Bottom	**Comments**
3/02/99 - 3/10/99	$^{15}NH_3$	E155(#8+15%#9)	47.0/47.0	0.9718	
		E155(#6+#8)	22.6/22.6	0.7932	1 anneal
3/10/99 - 3/17/99	$^{15}NH_3$	E155(#8+15%#9)	28.6/75.6	0.8704	2 anneals
		E155(#6+#8)	22.7/45.3	0.7932	Mat. change
3/17/99 - 3/22/99	$^{15}NH_3$	G08 E155x#1	28.6/28.6	0.8108	
		G08 E155x#1	18.2/18.2	0.7719	1 anneal
3/22/99 - 3/24/99	$^{15}NH_3$	G08 E155x#1	14.1/42.7	0.7744	
		G08 E155x#1	10.8/29.0	0.7926	1 anneal
3/24/99 - 3/31/99	$^{15}NH_3$	G08 E155x#1	34.7/77.4	0.7361	3 anneals
		G08 E155x#1	49.8/78.8	0.8398	Mat. change
3/31/99 - 4/09/99	^{6}LiD	Bottle 34	102.3/102.3	0.9484	
		Bottle 33	68.5/68.5	1.0314	Mat. change
4/09/99 - 4/17/99	^{6}LiD	Bottle 1020+1021	73.8/73.8	0.8983	1 anneal
		Bottle 58+1021	66.0/66.0	1.1570	Mat. change
4/17/99 - 4/22/99	^{6}LiD	Btl. 34+t4/171/97	42.4/42.4	1.4375	
		Bottle 33	17.1/17.1	1.4965	Mat. change
4/22/99 - 4/26/99	$^{15}NH_3$	G08 E155x#1	9.5/9.5	0.6717	
		G08 E155x#1	12.2/12.2	0.7529	Mat. change
4/26/99 - 5/05/99	$^{15}NH_3$	G09	34.9/34.9	0.7331	2 anneals
		G10	86.3/86.3	0.6402	E155x ends

Table 3.3: E155x target material history with cold dose and calibration constants. The first dose number shows the dose received during the given time interval, and the second number is the running count of the total dose for that batch.

butions to the CC error came from two sources: Temperature uncertainty from the ^{4}He manometer, and uncertainty in the $Area_{TE}$ measurement. The uncertainty in the ^{4}He temperature was primarily the result of a slight drift in the manometer's pressure zero point during the course of the experiment; this correction contributed less than $\pm 1\%$ uncertainty to the overall error. The uncertainty in the $Area_{TE}$ measurement was small for $^{15}NH_3$ (also less than $\pm 1\%$) but dominated the overall error for the ^{6}LiD polarization measurements. The reason for this was not a lack of precision in the actual area measurement, but rather the result of not waiting long enough for the material to thermalize. Since ^{6}LiD targets require several more hours to thermalize than $^{15}NH_3$ ($\sim$ 12 hours at 1.8 K and 5 hours at 3.3 K [57]), the decision was made by the collaboration to intentionally cut short its TE measurements and to instead extrapolate an asymptotic value for $Area_{TE}$ from the area data collected after only 6 to 8 hours. Thus the errors on the ^{6}LiD polarization were significantly increased by the uncertainties associated with the extrapolations. However this did not adversely affect the deuteron asymmetry measurement since its error was statistics dominated. The average value of the temperature and $Area_{TE}$ measurement errors are given in Table 3.4, where the last column gives the total combined averaged error on the enhanced polarizations for the entire experiment.

The bottom-line performance, or average polarization for all runs, was right on par with the value used in the experiment's proposal [61]: $\sim$ 70 % proton and $\sim$ 22 % deuteron average polarizations. A plot of the average polarization per run for the

	$\left(\frac{\Delta P}{P}\right)_{^4\text{He Temp}}$	$\left(\frac{\Delta P}{P}\right)_{Area_{TE}}$	$\left(\frac{\Delta P}{P}\right)_{pol}$
$^{15}NH_3$	$\pm 0.88\%$	$\pm 0.8\%$	$\pm 1.7\%$
^{6}LiD	$\pm 0.88\%$	$\pm 4.4\%$	$\pm 4.5\%$

Table 3.4: Errors associated with target polarization measurements.

entire experiment is shown in Section 4.4.2. A more concrete picture of the target polarization over time can found in Figure 3.17 which displays the same polarization data presented in Section 3.2.4 except as a function of time instead of dose.

The routine operations of the target went smoothly and efficiently; there was little loss of experimental run-time due to problems with the target. The NMR setup and operation occurred without any irregularities, and corrections to the polarization measurements due to non-linear signal distortions were small. Maximum signal modulations (M_{max}) near or greater than 0.3 occurred briefly for the last batch of $^{15}NH_3$ loaded in the bottom target cell. Subsequent comparisons of the event rates from this load with the rates from the dummy carbon target revealed that the target cell packing fraction (used in the calculation of the dilution factor) was ~ 15 % larger than its usual nominal value. This increased the coil filling factor (η) and as a result larger maximally enhanced signal sizes occurred–producing greater modulation strengths. However, this only resulted in a 2 to 3% non-linear correction for only the largest target enhancements of that load and did not pose any significant problem; overall, the non-linear corrections for $^{15}NH_3$ were $\pm 0.3\%$. With the exception of replacing a damaged microwave EIO tube power supply on two occasions, the biggest target mishap was the slight misalignment (2.4°) of the static $\vec{B}$ field from a purely transverse orientation. This was the result of not using the proper survey positions during the magnet's installation. The reason for this mishap along with its effect on the g_2 measurement are given in Section 4.6.

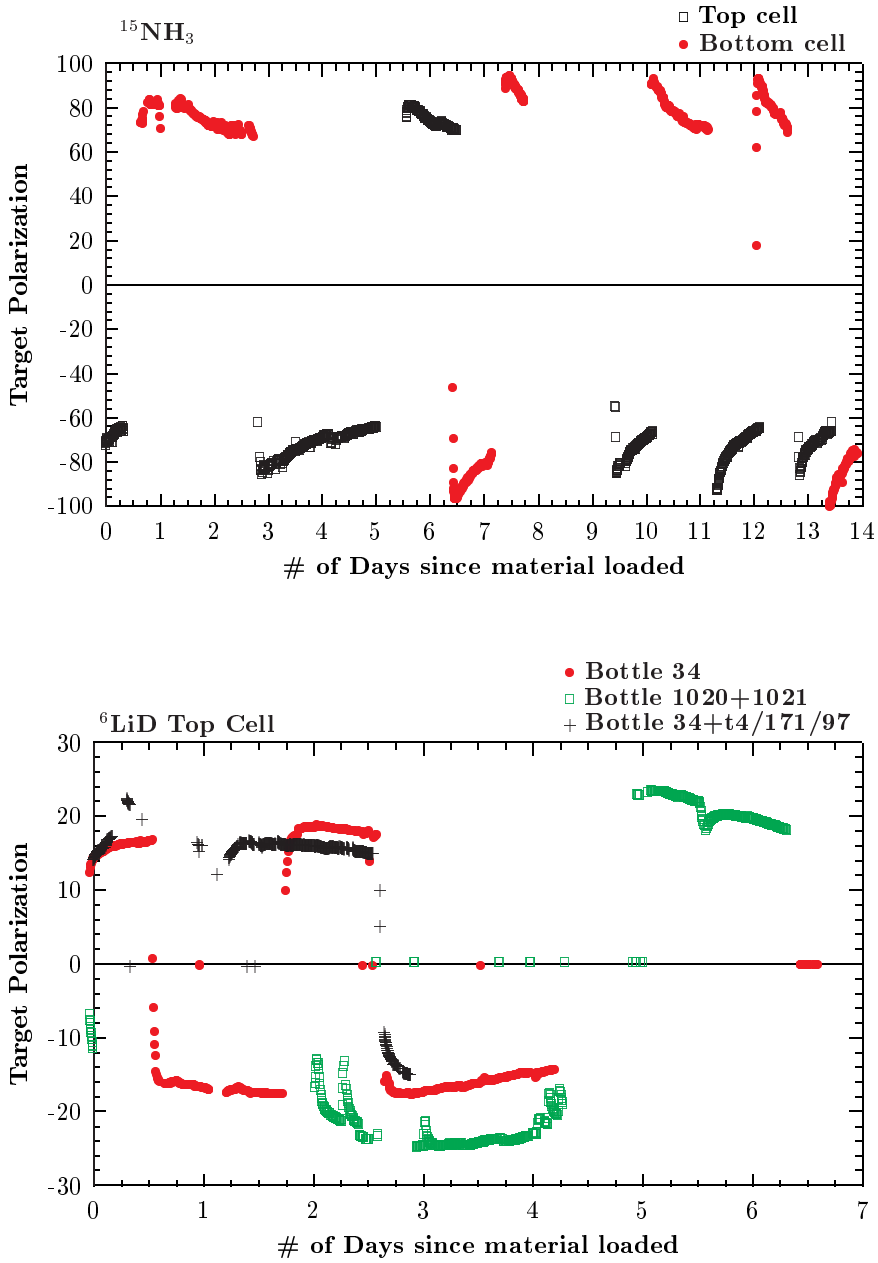

Figure 3.17: Upper plot: $^{15}NH_3$ polarization versus time for top and bottom cell material batch G08 E155x #1 used between 03/17/1999 and 03/31/1999. Lower plot: Polarization versus time for all ^{6}LiD top cell material used during E155x.

3.3 End Station A Spectrometers

The equipment used to quantify the characteristics of the scattered electron (i.e., its angle θ (and ϕ) and energy E, or equivalently x_{Bj} and Q^2) are collectively known as a spectrometer. E155x used three fixed-angle spectrometers positioned with average θ's of $2.75^\circ, 5.5^\circ$, and 10.5° (from the beamline) and with average ϕ's of $\sim 0^\circ$ (in the horizontal plane). With a beam energy around 30 GeV, this configuration leads to a spectrometer-combined kinematic range of $0.02 < x_{Bj} < 0.8$ and 0.7 (GeV/c)^2 $< Q^2 < 20$ (GeV/c)^2 as displayed in Figure 3.18.

A schematic of the spectrometer setup is given in Figure 3.19. Each spectrometer utilized its own magnetic transport system to deliver charged particles to its detector components. These components are grouped into three major detector subsystems:

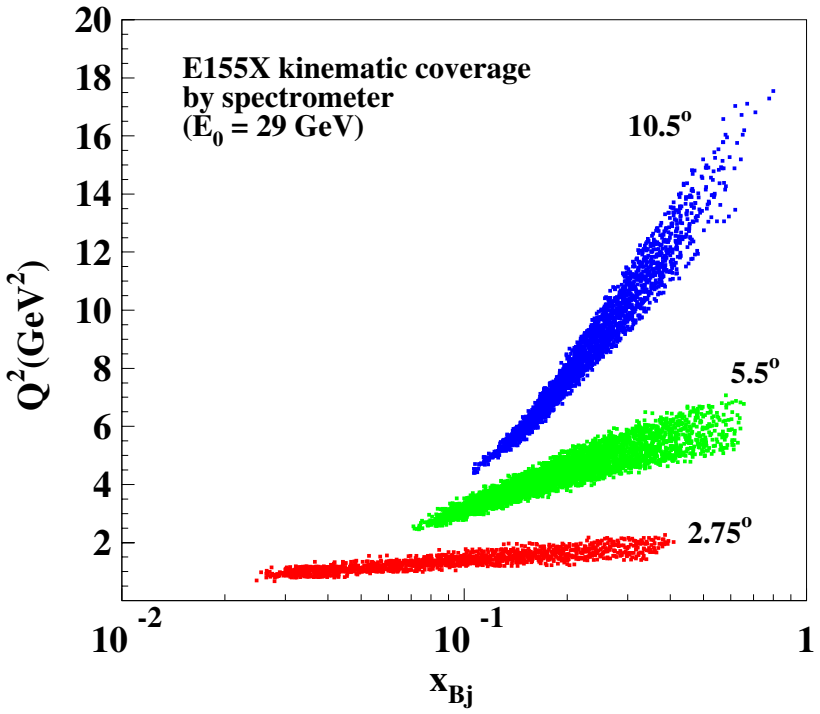

Figure 3.18: Kinematic coverage of E155x spectrometers.

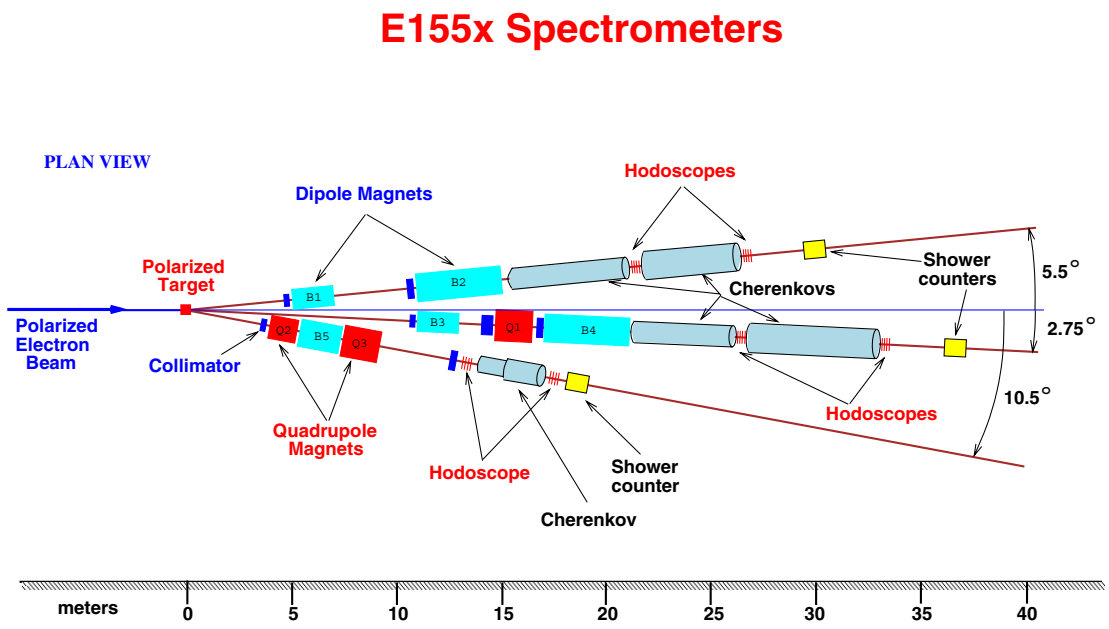

Figure 3.19: Schematic top view of the E155x spectrometers.

Hodoscopes to provide tracking information, Čerenkov tanks for particle identification, and an electromagnetic calorimeter for energy determination (as well as further particle identification). The functionality and application of each subsystem (as used during E155x) will be detailed in this section.

3.3.1 Transport Optics

The charged particles emanating from the DIS reaction with a certain trajectory and momentum are transported to the detector components via a series of magnets interleaved with collimators (as shown in Figure 3.19).

The collimators, which were placed in various locations throughout the magnets, provided a physical barrier that defined the extent of the θ and ϕ acceptance of each spectrometer. The typical collimator had two adjustable 'jaws' made of one inch of tungsten followed by four inches of lead; the settings of the 'jaws' were optimized (with

respect to particle detection rates) prior to the start of E155x production running and were adjusted only when the beam energy was changed. These settings were particularly important for the 2.75° spectrometer where both the scattered electron and background rates were highest.

The magnetic fields of the transport system bent electrons with different momentum by different amounts. Thus, determining the precise trajectory of an electron (traversing the detector components) gave a measure of its momentum. This is the underlying principle by which a momentum-analyzing spectrometer operates.

Both dipole and quadrupole type magnets were used to bend and focus/defocus, respectively, the scattered electrons into the detectors. The configuration of these magnets for each spectrometer are better illustrated in Figure 3.20. Here, it can seen that both the 2.75° and 5.5° employ two dipoles bending in opposite directions (first down and then up). Commonly referred to as a 'reverse bend', the advantages of this arrangement (in contrast to a same-bend setup) are two-fold: Larger momentum range of detectable particles, and increased shielding from neutral background particles (such as π^0's and photons). The 2.75° also used a quadrupole (Q1) between the two dipoles to defocus the electrons horizontally and refocus them vertically. This further reduced background rates and increased the uniformity of electron coverage across the face of the detector. This lowered instantaneous rates and increased its detection efficiency as well as enhanced its x_{bj} resolution.

The 10.5° used a different arrangement; a single dipole located between two quadrupoles. The upstream quadrupole (Q2) focused trajectories horizontally (providing greater θ acceptance) and defocused them vertically (for better momentum resolution), while the downstream magnet (Q3) performed the same way as Q1 (reducing background rates and enhancing x_{bj} resolution).

The optics (or trajectory-momentum correlation) of each transport system was

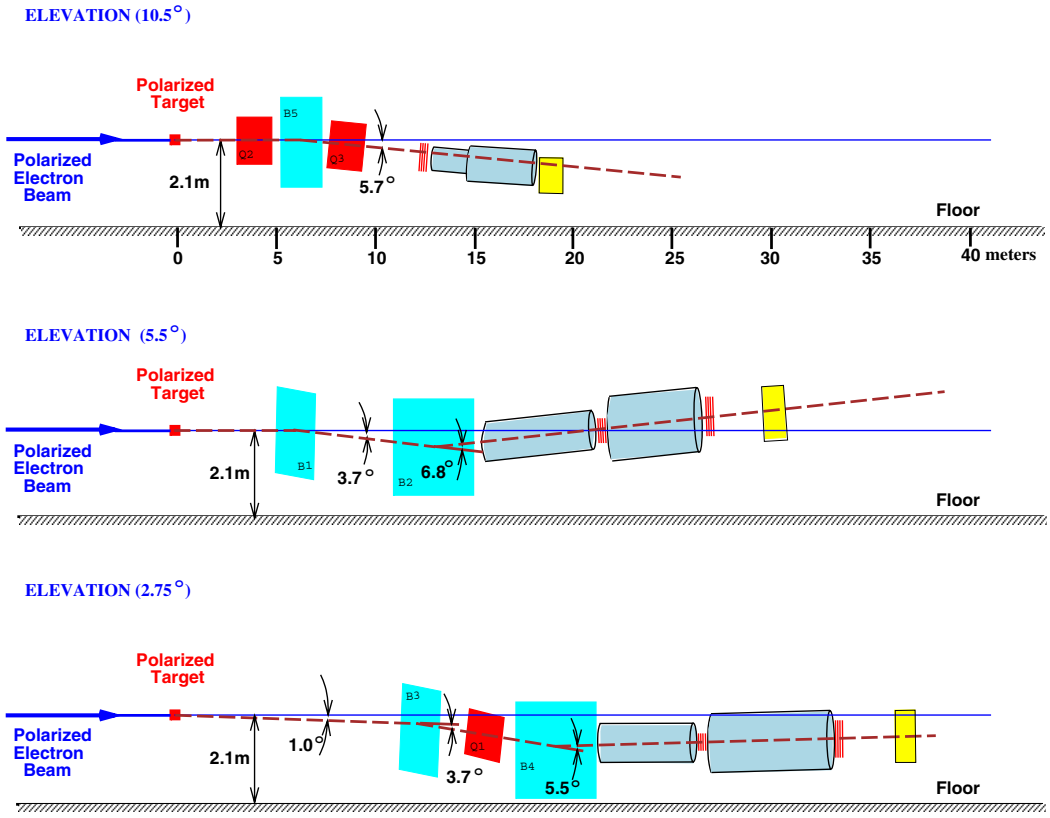

Figure 3.20: Schematic side-view of the E155x spectrometers with emphasis on the dipole bending angles.

defined and calibrated prior to E155x via computer Monte Carlo simulations in conjunction with detector subsystem response's to actual electrons with known kinematics. As a result, each spectrometer acquired its own coordinate system with a $\hat{z}$-axis along the central-momentum trajectory defined by its optics. To this end, a measurement of an electron's track (or trajectory) relative to this 'central-trajectory' could be transformed into a measurement of its momentum. The 2.75°, 5.5°, and 10.5° central momentum values were 20.0, 20.0, and 11.7 GeV/c respectively. The stability of the transport magnets were monitored throughout the experiment to ensure the reliability of the spectrometers' optics. Figure 3.21 is a plot of the dipole's (B1 through B5) field strength as measured, at sporadic intervals during E155x, by NMR coils

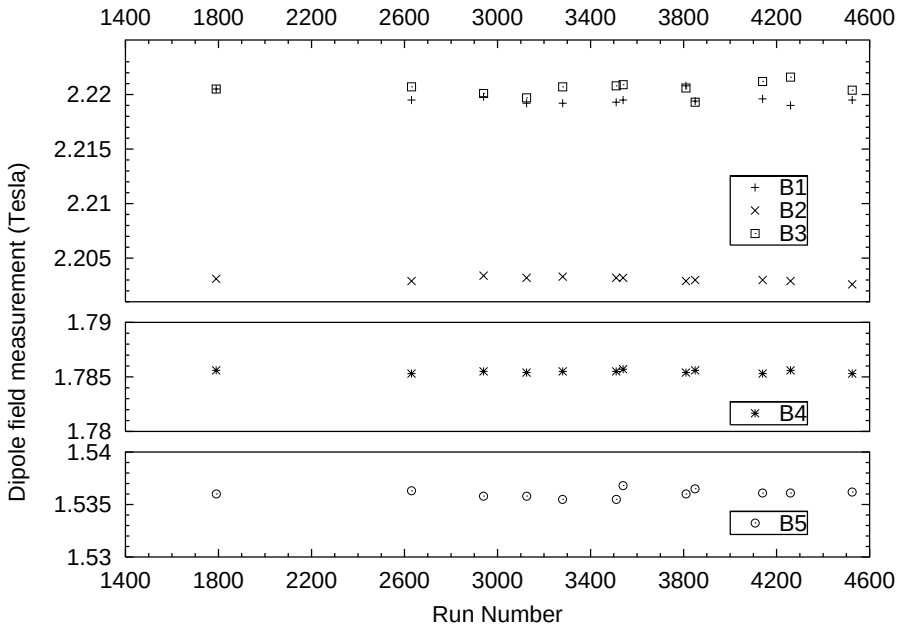

Figure 3.21: Spectrometer dipole NMR field measurements shown as a function of E155x run number.

embedded in the magnets. This plot indicates that the NMR readings were stable to better than 0.1% (for all dipoles) which was well within the experiment's acceptable limits [62]. Also, Hall probe measurements of the three spectrometer quadrupoles displayed comparable stability.

3.3.2 Hodoscopes

The primary instruments used to trace the paths of ionizing particles passing through the spectrometer are the hodoscopes. By design, the collective response of these devices yields at least two space-time coordinates (along the path of such a particle) separated by a large enough distance to provide the necessary trajectory reconstructing angular resolution.

To accomplish this task, the E155x spectrometers each employed two hodoscope

packages separated by a distance of approximately five to six meters; one placed immediately upstream and the other downstream of the 2.75° and 5.5° (10.5°) final (only) Čerenkov detector. The hodoscope packages consisted of several highly segmented planes of plastic scintillating strips, called 'fingers'. The fingers associated with each plane were grouped into two identical overlapping subplanes (front and back). Each subplane contained parallel, uniformly spaced fingers mounted side-by-side; the subplanes were attached to one another such that each front finger partially overlapped one of the back fingers. Table 3.5 gives some of the specifications of the hodoscope

Spectrometer (location)	Plane Name	# of Fingers	Finger orientation (°)	Finger width (mm)	Finger overlap (mm)
2.75° (upstream)	2H1U	44	+15 (diagonal)	15	5
	2H2V	44	−15 (diagonal)	15	5
	2H3X	64	90 (vertical)	13	1
	2H4Y	72	0 (horizontal)	13	1
	2H5Y	31	0 (horizontal)	30	10
	2H6X	34	90 (vertical)	20	7
2.75° (downstream)	2H7X	90	90 (vertical)	13	1
	2H8Y	90	0 (horizontal)	13	1
	2H9Y	55	0 (horizontal)	30	10
	2H10X	27	90 (vertical)	30	10
5.5° (upstream)	5H1U	25	−45 (diagonal)	45	15
	5H2X	23	90 (vertical)	30	10
	5H3Y	36	0 (horizontal)	30	10
	5H4V	25	+45 (diagonal)	45	15
5.5° (downstream)	5H5U	21	−45 (diagonal)	75	25
	5H6X	27	90 (vertical)	30	10
	5H7Y	55	0 (horizontal)	30	10
	5H8V	21	+45 (diagonal)	75	25
10.5° (upstream)	10H01Y	20	0 (horizontal)	25	–
	10H02Y	21	0 (horizontal)	25	–
	10H03Y	20	0 (horizontal)	25	–
10.5° (downstream)	10H04Y	24	0 (horizontal)	25	13
	10H05Y	25	0 (horizontal)	25	13

Table 3.5: Some details of the E155x hodoscope planes for the three spectrometers.

planes used for E155x. These planes were positioned in precise ($\hat{z}$) locations in the spectrometer (as shown in Figure 3.19) and with various finger orientations (vertical, horizontal, and diagonal). The plane's specific location fixed its subplane finger's z-coordinates (to the same value), while the planes orientation gave its fingers spatial variability in a direction perpendicular to $\hat{z}$. Thus, each plane provided a simultaneous determination of two space coordinates: z and x, y, or a combination of the two depending on vertical, horizontal, or diagonal orientations respectively.

A photomultiplier tube (PMT) mounted to one end of each finger quantified the light created in the scintillator when a charged particle passed through it. The PMT created a voltage pulse whose integrated charge was proportional to the number of photons absorbed by the PMT's photo-cathode. This pulse was passed through a threshold discriminator on its way to a time-to-digital converter (TDC) where a 'hit' was recorded at a specific time, for a specific finger, in a specific plane. This information was then used to reconstruct the particle's track. On average, the 2.75° generated $\sim$ 15 hodoscope finger hits per track, and the 5.5° and 10.5° produced $\sim$ 13 each.

3.3.3 Čerenkov Tanks

Due to the nature of DIS reactions combined with the high luminosity, low duty-rate SLAC beam characteristics, large numbers of background particles emerge from the scattering process along with the desired scattered electrons. The main purpose of the Čerenkov detectors was to distinguish these electrons from the various background particles (the vast majority of which were π^-'s in E155x). To do this, the detector exploits the fact that a high-enough energy electron travels faster than the speed that light travels through non-vacuum media; in doing this, the electron creates a coher-

ent electromagnetic disturbance, called Čerenkov radiation, that propagates outward from the particle in a conical 'shockwave' fashion. The detection of this radiation in real time indicates exactly when a high-momentum, low-mass particle (an electron) passes through the Čerenkov detector and thus provides a means of its identification.

To accomplish this task, each spectrometer employed a threshold gas Čerenkov counter (the 2.75° and 5.5° used two) that consisted of a large cylindrical aluminum tank several meters in length and over a meter in diameter. The tanks had 1.5 mm thick aluminum windows at either end and were filled with a gas mixture of 90% diatomic nitrogen (N_2) and 10% methane (CH_4) at sub-atmospheric pressures between $2-4$ psi. A heavily lead shielded PMT was mounted inside each tank (outside the spectrometer acceptance) to detect and quantify the Čerenkov radiation. Two screening baffles with rectangles cut out of the acceptance region were affixed inside each tank to minimize the ambient light reaching the PMT from N_2 gas scintillation caused by low energy secondary charged particles [63]. A set of large curved (concave) mirrors placed at the downstream end of each tank were used to focus the Čerenkov light onto the PMT. The PMT's anode signal was passed to a chain of four Flash ADCs which collectively digitized the signal every nanosecond–creating a waveform of the Čerenkov pulses occurring in the tank during a beam spill; this system served as the primary means of signal acquisition for the Čerenkov detectors. A secondary (backup) system, which utilized the PMT's dynode signal, processed the occurrence of a Čerenkov pulse via an array of four discriminating TDC's with progressively higher threshold levels. The Čerenkov detector pulses, correlated in time with the responses of the other subsystems, labeled a particular track and/or shower cluster (to be discussed in the next subsection) as resulting from an electron.

The density or pressure of the tank's gas mixture determined its index of refraction (n), which set the detector's minimum threshold velocity ($v_{th} = \frac{c}{n}$), below which a

charged particle will not emit Čerenkov radiation coherently. Translating this into a momentum threshold yields the following relation

$$p_{th} = \frac{mc}{\sqrt{n^2 - 1}}, \tag{3.21}$$

which indicates that particles of different mass have different thresholds. The pressure and temperature (and thus index of refraction) of each of the five tanks were adjusted to specific values which were monitored and maintained throughout the experiment. These values were tuned, per spectrometer, to accept electrons and reject pions and any other massive negatively charged hadrons. Table 3.6 displays the momentum thresholds of various particles for each tank at their operating pressures. The two sets of pressures and thresholds given in this table represent the fact that the 2.75° and 5.5° tank pressures where adjusted during the experiment to provide greater pion rejection (this occurred early in the experiment at run 2524).

	Čerenkov Tanks				
	2.75°		5.5°		10.5°
	2C1	**2C2**	**5C1**	**5C2**	**10C1**
Pressures (psi)	2.35/2.00	2.35/1.97	3.17/2.63	3.16/2.60	3.75/3.76
Particle:	Momentum Thresholds P_{th} (GeV/c)				
Electron	.052/.056	.052/.056	.045/.048	.045/.048	.041/.041
Pion	14.5/15.5	14.5/15.5	12.5/13.5	12.5/13.5	11.5/11.5
Kaon	51.3/54.9	51.3/54.9	44.2/47.8	44.2/47.8	40.7/40.7
Anti-proton	97.4/104	97.4/104	84.0/90.7	84.0/90.7	77.3/77.3

Table 3.6: Čerenkov tank particle momentum thresholds for the two given tank pressures. Values calculated using reference [64] at a temperature of 20° celsius.

3.3.4 Electromagnetic Shower Calorimeter

The final detector subsystem encountered by particles passing through the spectrometers was the electromagnetic shower calorimeter (or simply the shower counter). This detector's primary function was to measure the energy deposited by particles that traversed its components. By design, it is very efficient at extracting the energy of the scattered electron, and much less efficient at measuring the energy of hadrons[‡‡].

The shower counter determines the energy of a single high-energy scattered electron by converting it into an electromagnetic shower of many lower-energy charged particles; these lower-energy particles then deposit their energy within the calorimeter in some detectable form. The shower is a cascading succession of bremsstrahlung emissions and pair-production processes; it grows in size as it progresses through the calorimeter–peaking at about five radiation lengths in and then tapering away. For the E155x calorimeters, the energy of the incident particle was determined by measuring the number of Čerenkov photons emitted by the showering particles (e^-e^+ pairs) as they traversed the segmented, transparent lead-glass blocks that made-up the shower counter.

The two smaller angle spectrometers had identical shower counters, whereas the 10.5° used a different design. The 2.75° and 5.5° shower counters consisted of 200 lead-glass blocks stacked into a twenty row by ten column array as depicted in Figure 3.22. Each block was 6.2 cm × 6.2 cm × 75 cm and had an index of refraction of 1.58–which corresponded to a momentum threshold for electrons/positrons of approximately 0.7 MeV/c. The shower counter array was oriented such that the long sides of the blocks were roughly aligned with the spectrometer's central-trajectory. The lead-glass used was of Schott type F2 and was determined to have a 3.17 cm radiation

[‡‡] This feature, which is a consequence of how different particles interact differently with matter, greatly enhances the overall functionality of the calorimeter and is discussed later in this subsection.

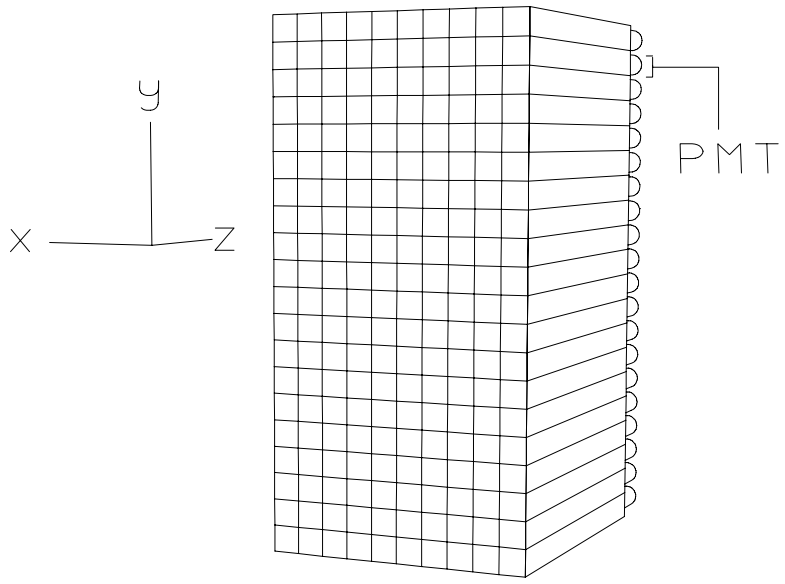

Figure 3.22: Schematic view of the 2.75° and 5.5° shower counters.

length [65] which induced and maintained a relatively quick, compact shower that could be contained within the 75 centimeters (23.7 radiation lengths) of the blocks, as well as the 450 ns beam spill. A PMT was mounted to the downstream end of each block to detect and quantify the Čerenkov radiation within that block. Each PMT signal was sent to both an ADC and a system of discriminators and TDCs. For the 5.5°, only one level of discriminators and TDCs were used because overlapping showers rarely occurred. For the 2.75°, where the event rates were much higher, two levels were used. Furthermore, 64 of the 2.75°'s PMT signals were passed through an additional level of discriminating TDCs (for a total of three); these 'hot' PMTs, located in the top-most seven rows, experienced the highest instantaneous rates.

The 10.5° shower calorimeter utilized the same concept as the 2.75° and 5.5° shower counters except it had a different design. It consisted of a two part system: An active pre-radiator (PR) with a lead passive pre-radiator (PbPPR) and a total-absorber (TA). The TA part of the shower counter had the same design as the 2.75°

and 5.5° counters, that is, it consisted of stacked lead-glass blocks designed to totally absorb the energy of the scattered electron with a PMT mounted to the downstream end of each block to detect Čerenkov light. However, there were only 30 stacked blocks in a five row by six column array, and the block's dimensions and properties were different. The majority of blocks were 14.6 cm × 14.6 cm × 40 cm and had radiation lengths of 2.47 cm [66]. This implied that the 40 cm length amounted to only ∼ 16 radiation lengths, which alone would not be enough to sufficiently contain a 12 GeV electromagnetic shower. Thus a PR system, to initiate and slightly develop the shower just upstream of the TA, was employed. In addition, for E155x, a 77 cm × 71 cm × 0.64 cm thick (1 radiation length) lead sheet, the PbPPR, was placed just upstream of the PR blocks to further aid in the TA's containment of the shower.

The active pre-radiator consisted of 10 bars, each identical to the 2.75° and 5.5° shower counter blocks, stacked vertically with their long axes perpendicular to the central-trajectory. To assist in tracking reconstruction as well as enhance the TA's ability to determine the shower position, a PMT was mounted to both ends of each PR bar. The vertical stack provided the $\hat{y}$ positioning ability, while the use of two PMTs provided an estimate of the horizontal ($\hat{x}$) hit location along the bar. The latter was accomplished by measuring the time difference between the two PMT signals; this time difference, converted to distance and calibrated with the TA's $\hat{x}$ shower position, proved to yield more consistent results than using a ratio of the PMT signal sizes (mainly due to significant light attenuation in the bar) [67]. The read-out electronics of the PR and TA blocks were similar to those of the 5.5° shower counter, that is, an ADC and one level of discriminating TDCs for each PMT.

In addition to providing a very accurate determination of an electron's energy, the shower counters provided supplemental particle identification as well as a reasonably

sensitive measurement of the shower's 'centroid', or central location of the shower maximum within the calorimeter. The ability for the 2.75° and 5.5° calorimeters to determine the shower centroid to better than ±0.5 cm was made possible by the segmentation of the lead-glass blocks combined with software analysis and aided significantly in tracking reconstruction. Particle ID was made possible by discerning the differences between hadronic showers, made by pions for example, and electromagnetic showers. These differences, which included size and shape of the shower, as well as the percentage of the particle's energy deposited in the shower, were revealed, in part, through an examination of the ratio of a particle's energy (as determined by the shower counter) to its momentum (as determined by the track trajectory). Commonly referred to as the E-over-P (E/P) ratio (discussed further in Section 4.2.3), it is unity for electrons/positrons and usually much less (< 0.5) for pions and other massive particles. The value of this ratio played a crucial role in characterizing an event (see Section 4.3.2), and careful analysis of the E/P spectra of specific data sets provided an assessment of the amount of background (pion and non-DIS electron) contamination in the data set used to calculate $A_\perp$ (see Section 4.5.1).

3.4 ESA Data Acquisition System

The computers, associated software, and electronic hardware used to control, collect, monitor, and archive the experimental data flowing from the various ESA beam and spectrometer subsystems is collectively referred to as the ESA data acquisition system (or ESA DAQ). The ESA DAQ was upgraded following experiment E143 to accommodate the higher event rates generated by the shorter beam pulses (450 ns as compared to 2.2 μs) which resulted from the SLAC energy doubling (SLED) [68] upgrade to the accelerator. The upgraded DAQ consists of a VME based system

capable of data transfer rates up to 1 MB/s using a reflective memory network [69]. A block diagram of the ESA DAQ is shown in Figure 3.23.

During the DAQ's open trigger (which lasted the duration of the beam-spill), data flowing from the spectrometers' various electronic components (TDCs, ADCs, discriminators, and FADCs) were read in by the 'Remote VME' Real-Time crate located in ESA. The 'Local VME' Real-Time crate, located in CHA, was interfaced to the beam data CAMAC branch and was responsible for acquiring the relevant

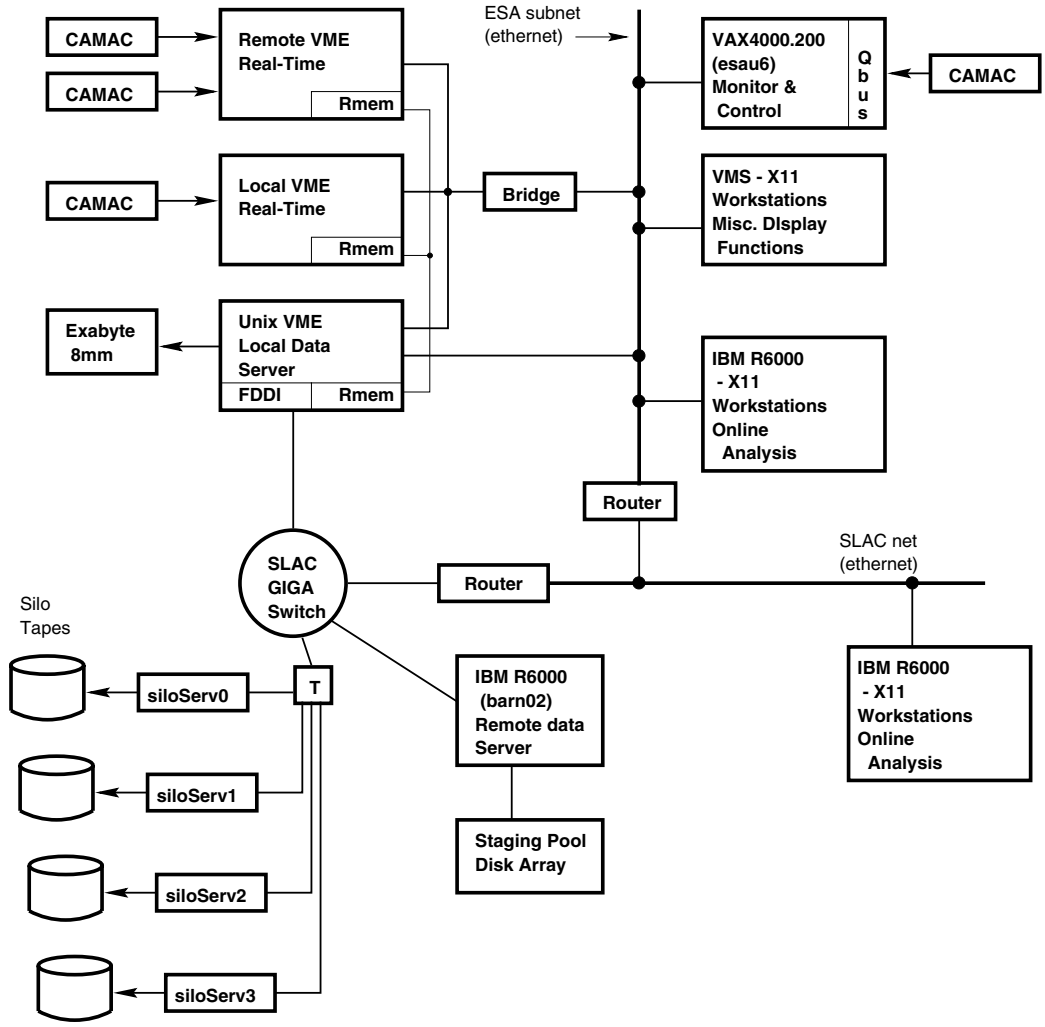

Figure 3.23: Block diagram of the ESA data acquisition system [69].

beam-related parameters like charge, helicity, spot-size, and position. The reflective memory network facilitated the combination of the spectrometer and beam data which was then available for logging in the 'Unix VME' crate (also housed in CHA).

The ESA DAQ employs several processes to control the state of the DAQ and monitor its performance. A process known as 'DAQCntrl' provides the DAQ's main user interface in which specific types of data runs can be started and stopped. DAQCntrl is essentially a stand-alone free running program used to control the flow of data through the DAQ; it polls VME crates and exchanges messages (via NetServ) with other free running processes used by the DAQ. One such process, known as 'DAQJob', monitors CAMAC branch data such as high voltage settings or scalar values, as well as information from the target DAQ via Ethernet connection using NetServ (see Figure 3.16). DAQJob makes the data it acquires available to DAQCntrl and other processes executing on the same processor [69]. Other processes include interactive and/or non-interactive control programs for altering or monitoring magnet current settings, low voltages, and scalar values.

Chapter 4

Analysis

4.1 Run Overview

Approximately 3,000 E155x runs were logged to tape between March and May 5^{th}, 1999. From an analysis standpoint, these runs can be sorted into two categories: Production and calibration. The production runs consisted of scattering events logged from polarized beam-polarized target interactions. The calibration runs consisted of spectrometer-component calibrations with and without beam, target dilution calibrations which used polarized beam scattering events from an unpolarized solid/dummy target (or no target), and dedicated Møller beam polarimetry runs.

4.1.1 Calibration Runs

There were many types of spectrometer-component calibrations logged to tape during the experiment, but the predominant ones were Toroid, Hodo-LED, and Pedestal. The Hodo-LED and Pedestal runs calibrated the hodoscope and shower counter PMTs respectively; these were performed without beam. The Toroid run was used to calibrate the beam-line toroids which were used to determine the beam current. This

calibration was performed both with and without beam to obtain a high and low coil current response from the toroids. Typically, these three calibration runs were performed at the beginning of each 3 hour run series. The target dilution calibrations were performed less often–at most once per day and at least once per target load. These calibrations were usually performed during the reversal of target enhancement to maximize use and efficiency of experimental resources; they involved scattering polarized electrons from unpolarized solid Carbon and Beryllium targets, for $^{15}NH_3$ and ^{6}LiD respectively, and lasted as long as a production run ($\approx$ 0.5 hour). This data was primarily used to determine the target packing fraction which was used to calculate the target dilution factor. Multiple Møller polarimetry runs (described in Section 3.1.3) were performed about a dozen times throughout the experiment. The results from the Møller measurements are given in Section 4.4.1.

4.1.2 Production Runs

The production data consisted primarily of the desired DIS electron events with a small contamination from other negatively charged particles (e.g. π^-'s and non-DIS electrons). A breakdown of the number of production runs used in the $A_\perp$ analysis for each spectrometer, target material, and energy is shown in Table 4.1. The production runs each contained (on average) the DIS events from roughly 200,000 beam pulses. Each pulse (or spill) contained 1 to 3×10^9 electrons (with 83% polarization) packed within a 450ns pulse and delivered at a rate of 120Hz. Only a minute fraction of the electrons per pulse both participated in the desired reaction and were analyzed by the spectrometers. On average, roughly 3 electron tracks per spill were collected by the 2.75°, 0.5 by the 5.5°, and 0.04 by the 10.5°. For all three spectrometers combined, roughly five kilobytes per spill of raw data were written to tape yielding a

$^{15}NH_3$	29 GeV		32 GeV	
	Runs	Events	Runs	Events
2.75°	428	188,986,346	687	219,298,061
5.5°	422	33,547,817	726	42,705,617
10.5°	327	3,137,902	711	5,273,707
^{6}LiD	29 GeV		32 GeV	
	Runs	Events	Runs	Events
2.75°	263	138,234,642	399	150,927,933
5.5°	282	25,659,598	404	34,059,045
10.5°	165	1,893,860	401	4,161,846

Table 4.1: Number of production runs and DIS electron events used in the $A_\perp$ analysis for each spectrometer, target, and beam energy.

total typical run size of just over a Gigabyte.

There was also another type of run performed with polarized beam on polarized target. This was called a positron run and was used to measure the non-DIS electron contamination in the production data. These runs had all the characteristics of a production run except that its events consisted of positrons from pair symmetric processes with a relatively large background of π^+'s. This mode of running was achieved by reversing the polarity of the spectrometer's transport magnets thereby allowing only positively charged particles to pass through the spectrometer. The ESA spectrometers could be individually set in positron mode, thus allowing each spectrometer to spend the minimum amount of time required to achieve the statistics necessary to perform the pion and non-DIS electron contamination correction on the $A_\perp$ data set (detailed in Section 4.5.1).

4.2 Raw Data Studies

Many data studies were performed on the raw data set for the purpose of verifying the integrity of the data, and improving the analysis code's ability to extract ac-

curately the relevant information. The latter was especially prevalent for the 10.5° analysis, where some spectrometer features were new for this experiment. There were several analyses performed on all aspects of the runs both during and after the experiment. These included beam quality, helicity, and raster studies, target studies (refer to Section 3.2.7), and spectrometer component calibration, efficiency, and resolution studies. Due to natural fluctuations in experimental conditions (e.g. temperature and high-voltage), the timing between detector component (Čerenkov, hodoscopes, and shower counter) responses needed to be corrected in the raw data set. Furthermore, new surveyed locations of certain hodoscope fingers required a correction of the momentum reconstruction from tracking information. And consequently, the shower counter's energy response calibration (determined from electron E/P distributions) needed to be corrected.

4.2.1 Timing

The TDCs read out by the DAQ provided the information needed to find out when an event occurred. But the TDCs relied on other electronics (PMTs, etc.) to send them the signal, and these devices' response times fluctuated due to changes in high voltage, temperature, etc. Thus there was a need to adjust the relative timing between the Čerenkov , Tracking, and Shower signals to compensate for these fluctuations. Timing run-blocks were determined based on high voltage changes and on changes in timing that occurred for unknown reasons [70]. The Čerenkov times were first adjusted to be consistent with the Shower Counter's time; the hodoscope fingers were then timed-in relative to the Čerenkov. Careful attention was given to this task as proper timing between the different detector components was a prerequisite to reconstructing an event track. The timing resolution of the different detector components was ~ 1 ns.

4.2.2 Tracking Momentum Reconstruction

The optics model, providing trajectory-momentum correlation for particles scattered from within the target cell and transported through the spectrometers, was generated by Monte Carlo simulation using measured transport magnet field maps and the precision alignment data for the magnets and detector components [71]. This provided a look-up table used to assign momentum and lab-frame scattering angles to tracks based on their hodoscope finger hits and associated shower cluster centroids (if any). Figure 4.1 gives a sample of the E155x electron tracking momentum distributions

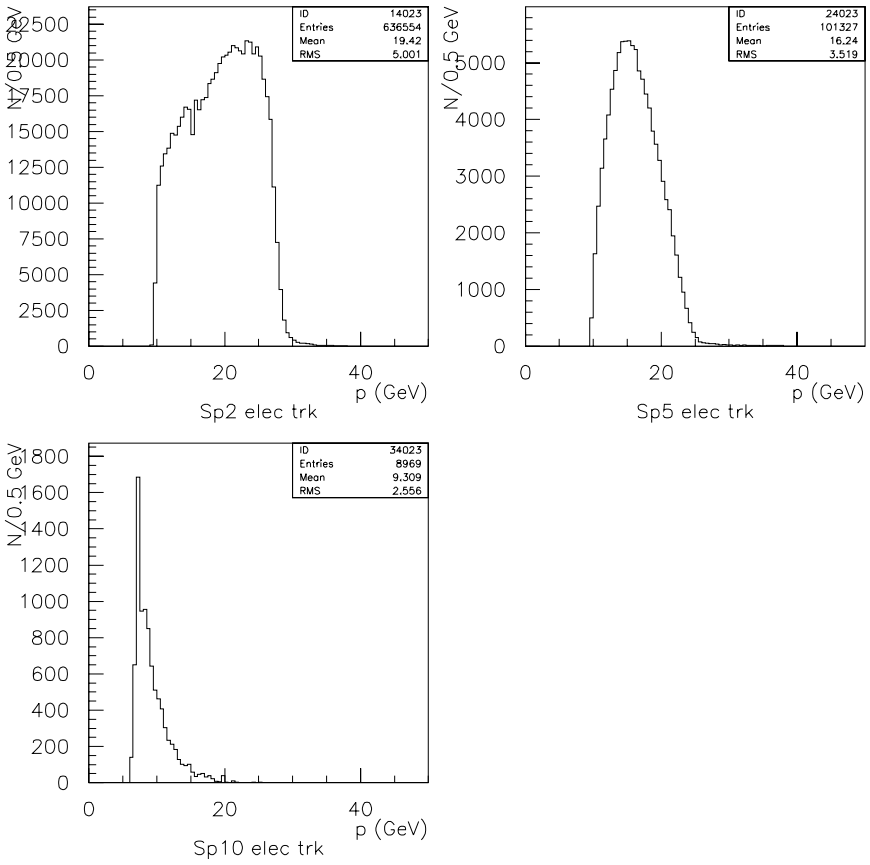

Figure 4.1: Electron tracking momentum distributions from run 4200 for the three spectrometers.

from the three spectrometers. The momentum resolution of the E155x detectors was ~ 3 % [72].

Prior to E155x, it was suspected that some of the 2.75° and 5.5° $\hat{y}$-measuring hodoscope fingers had inaccurate alignment data, however, a proper survey of the fingers was not performed until months after the experiment when the Čerenkov tanks could be lifted out of the way. The results of the survey indicated that nine 2.75° front hodoscope fingers were misaligned from 0.5 to 1.5 mm; two 5.5° front fingers were misaligned–one 3 mm lower and the other 1.5 mm higher than expected from the previous alignment data. The rear hodoscope planes had four 2.75° fingers averaging 5.5 mm higher than expected, and two 5.5° fingers $\sim$ 2 mm higher than expected. The details of the survey results can be found in references [73] and [74].

4.2.3 Shower Counter E/P

A detailed analysis of the 2.75° and 5.5° shower counter energy calibration was motivated following the changes in tracking momentum reconstruction. This analysis examined an electron shower cluster's central block E/P distribution to access the block's energy calibration. As described in Section 3.3.4, each calorimeter consisted of a 200 block array, the inner 144 block E/P responses were calibrated and studied for rate-dependent effects while the outer 56 edge-blocks required additional calibration studies due to the shower counter's partial coverage of clusters centered about their location. The specifics of this analysis can be found in reference [75], its main results are presented here.

The initial calibration, performed using three low current runs, led to much improvement in the mean E/P variations from block to block. This in turn lead to better overall E/P distributions with narrower peaks and Gaussian means closer to 1.

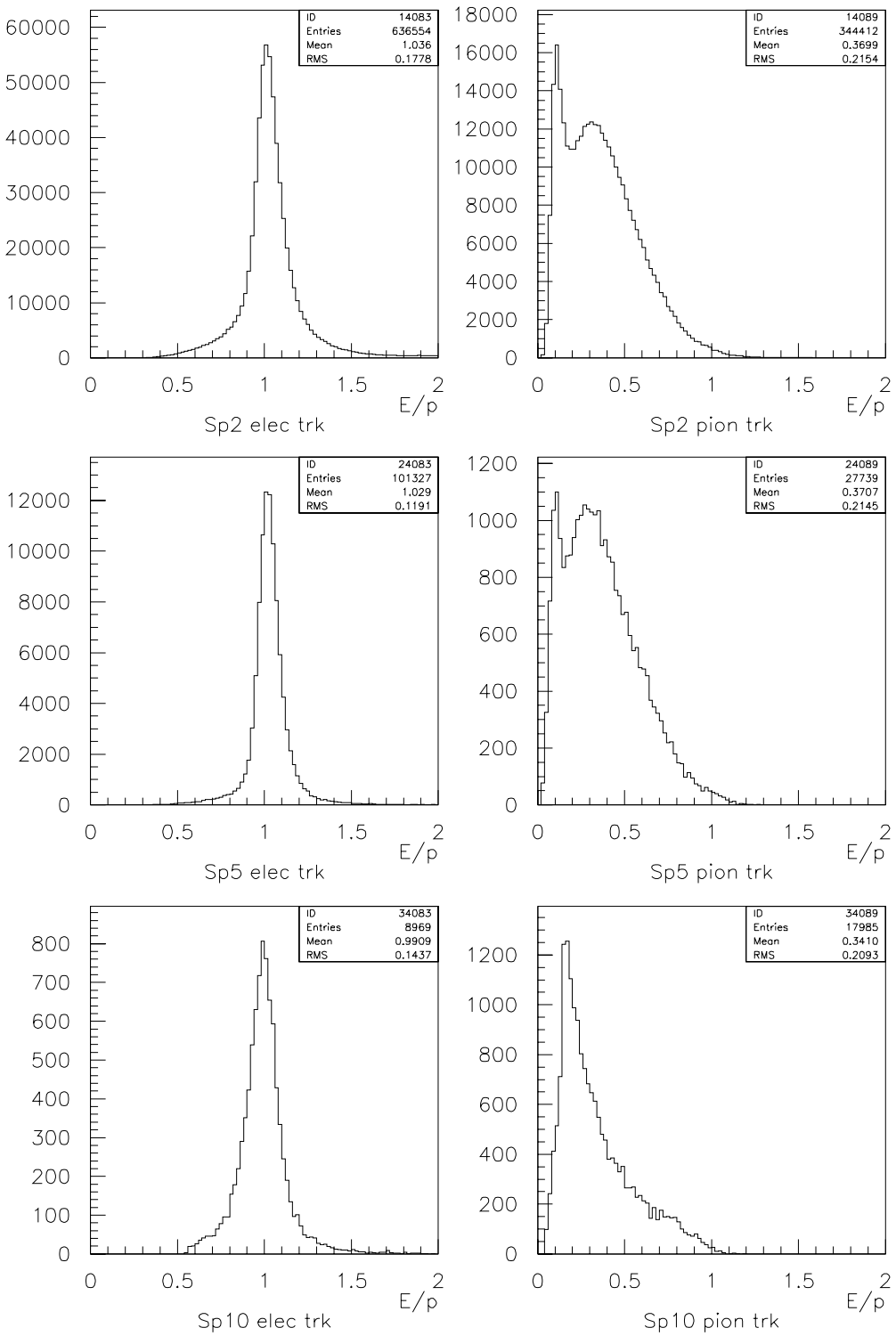

Figure 4.2: 2.75°, 5.5°, and 10.5° E/P histograms from run 4200. Histogram entries represent tracks identified as electrons (left plots) and pions (right plots).

As an example, Figure 4.2 displays the electron E/P distributions compared with the pion E/P distributions for the three spectrometers from one run. The partial shower containment in edge block clusters was studied by examining E/P distributions from tracks projected to 4 different regions inside the block from inner to outer edge. This revealed a gradual decrease in E/P from the inner to outer region with the outcome that half of the tracking events projected to the outermost region would not pass the 0.75 E/P-cut in the electron event definitions–(discussed in Section 4.3.2). This represented a very small percentage of events and thus was deemed an acceptable loss. Subsequent studies of the above calibrations for medium and high-current runs showed up to 6 % variation in E/P distributions as compared with low current runs. Since large blocks of runs were performed at similar currents, different shower counter block calibrations were used for run regions of different current. This provided the shower counters with more accurate energy determination and thus improved the overall E/P distributions from run to run. The energy resolution of the 2.75° and 5.5° shower counters ranged between ~ 3 and 5 % at the kinematics of E155x.

4.3 Data Reduction

Over 2 Terabytes of raw data were collected for the $\sim$ 2000 runs used in the $A_\perp$ analysis. The process of analyzing this data set occurred in two steps. First, following the bulk of the raw data studies, the raw data runs were processed, filtered and reduced into Data Summary Tapes (DSTs). This reduced the size of the data set by a factor of 10 and facilitated the next stage of analysis which was to produce 'count files' from the DSTs. The count files were then used to calculate the raw asymmetry–(detailed in the next section). This section briefly describes the DST and count file stages of the analysis.

4.3.1 DST Production

DSTs are simply a more compact form of the raw data tapes; by producing the DSTs, the vast amount of information, conveyed by each electronic component within each of the spectrometer subsystems, was reduced to the essential bits of information needed to characterize the individual events. This information included timing, particle ID, tracking momentum, and energy (to name a few) and was not limited to only the most pristine DIS events; it included pions, and any other particles that produced a reconstructable track and/or shower cluster within the DAQ's open trigger.

Run Selection

All production, target calibration, and positron runs were processed into DSTs. Before and during processing, bad runs were weeded-out by looking for obvious problems such as: The loss of a spectrometer magnet due to its power supply tripping off, unusually low event rates and/or small file size due to DAQ problems, low or no target polarization, and indeterminable beam helicity or large beam-charge asymmetry. During and after DST production, histograms created during the processing of individual runs were monitored by comparing them with the same histogram from a known good run. These histograms included spectrometer component hit-timing differences, Čerenkov tank signal peak voltages, electron and pion E/P spectra, electron tracking θ and ϕ hit distributions, and electron and pion tracking momentum distributions. Gross deviations from the expected behavior of the monitored histograms were investigated and repaired if possible by code modifications. Several passes of DST production were performed before all processed runs were considered satisfactory. In all, the runs used in the $A_\perp$ analysis consisted of 1777 production, 101 target calibration, and 32 positron runs (with an additional $\sim$ 250 positron runs for the

10.5° only).

4.3.2 Count Files

This was the stage of analysis where events that shared a common set of well-defined characteristics (called 'event definitions') were extracted from the DSTs and grouped together in a count file. These files (one for each run) contained the number of events per x-bin with left versus right beam helicity for each spectrometer and for each event definition; they also contained other necessary information such as the total charge for left versus right beam helicity and average Q^2, x, and E/P per x-bin. The 38 x-bin ranges used in the analysis are given in Table 4.2.

x-bin	Bjorken x range		x-bin	Bjorken x range
1	$0.0100 - 0.0112$		20	$0.0949 - 0.1067$
2	$0.0113 - 0.0126$		21	$0.1068 - 0.1202$
3	$0.0127 - 0.0142$		22	$0.1203 - 0.1353$
4	$0.0143 - 0.0160$		23	$0.1354 - 0.1523$
5	$0.0161 - 0.0180$		24	$0.1524 - 0.1714$
6	$0.0181 - 0.0203$		25	$0.1715 - 0.1930$
7	$0.0204 - 0.0229$		26	$0.1931 - 0.2173$
8	$0.0230 - 0.0257$		27	$0.2174 - 0.2446$
9	$0.0258 - 0.0290$		28	$0.2447 - 0.2757$
10	$0.0291 - 0.0326$		29	$0.2758 - 0.3100$
11	$0.0327 - 0.0367$		30	$0.3101 - 0.3489$
12	$0.0368 - 0.0414$		31	$0.3490 - 0.3928$
13	$0.0415 - 0.0466$		32	$0.3929 - 0.4422$
14	$0.0467 - 0.0524$		33	$0.4423 - 0.4978$
15	$0.0525 - 0.0590$		34	$0.4979 - 0.5604$
16	$0.0591 - 0.0665$		35	$0.5605 - 0.6308$
17	$0.0666 - 0.0748$		36	$0.6309 - 0.7102$
18	$0.0749 - 0.0842$		37	$0.7103 - 0.7994$
19	$0.0843 - 0.0948$		38	$0.7995 - 0.9000$

Table 4.2: Bjorken x ranges of 38 x-bins used for the analysis.

The students of E155x developed a set of analysis routines for producing count files independent of the collaboration analysis. This provided a way of comparing the two analyses which helped reduce analysis errors and improve the reliability of the result. A simplified representation of the student analysis routines is shown in Figure 4.3. This figure details the steps involved in filtering through event candidates from the DSTs and accumulating them based on specific criteria (defined below), for each spill and spectrometer.

Event Definitions

There were seven total event definitions used for the student analysis: Five electron and two pion. Tables 4.3 and 4.4 list the main electron and pion definitions for the three spectrometers. The 'standard' electron definition shown represents the cuts used for the final A_{raw} calculation. The standard pion definition represents the cuts used for the final pion asymmetry calculations used for $A_{\perp}$'s contamination correction. The cuts labeled 'F' in Table 4.3 were not used for these definitions, but were used in other definitions. The additional (non-standard) electron definitions consisted of two loosely-defined and one tightly-defined tracking-based definition, and a 'hybrid' (shower cluster and tracking-based) definition. Unlike the other 2.75° and 5.5° definitions, the hybrid definition did not require the event to have an associated track if it possessed a shower cluster. Note that all 10.5° definitions were hybrid in nature. The purpose of the various electron event definitions was to study the effect of different cuts and limits on the raw asymmetry. This produced a more thorough analysis in which the statistics of 'good' events could be optimized.

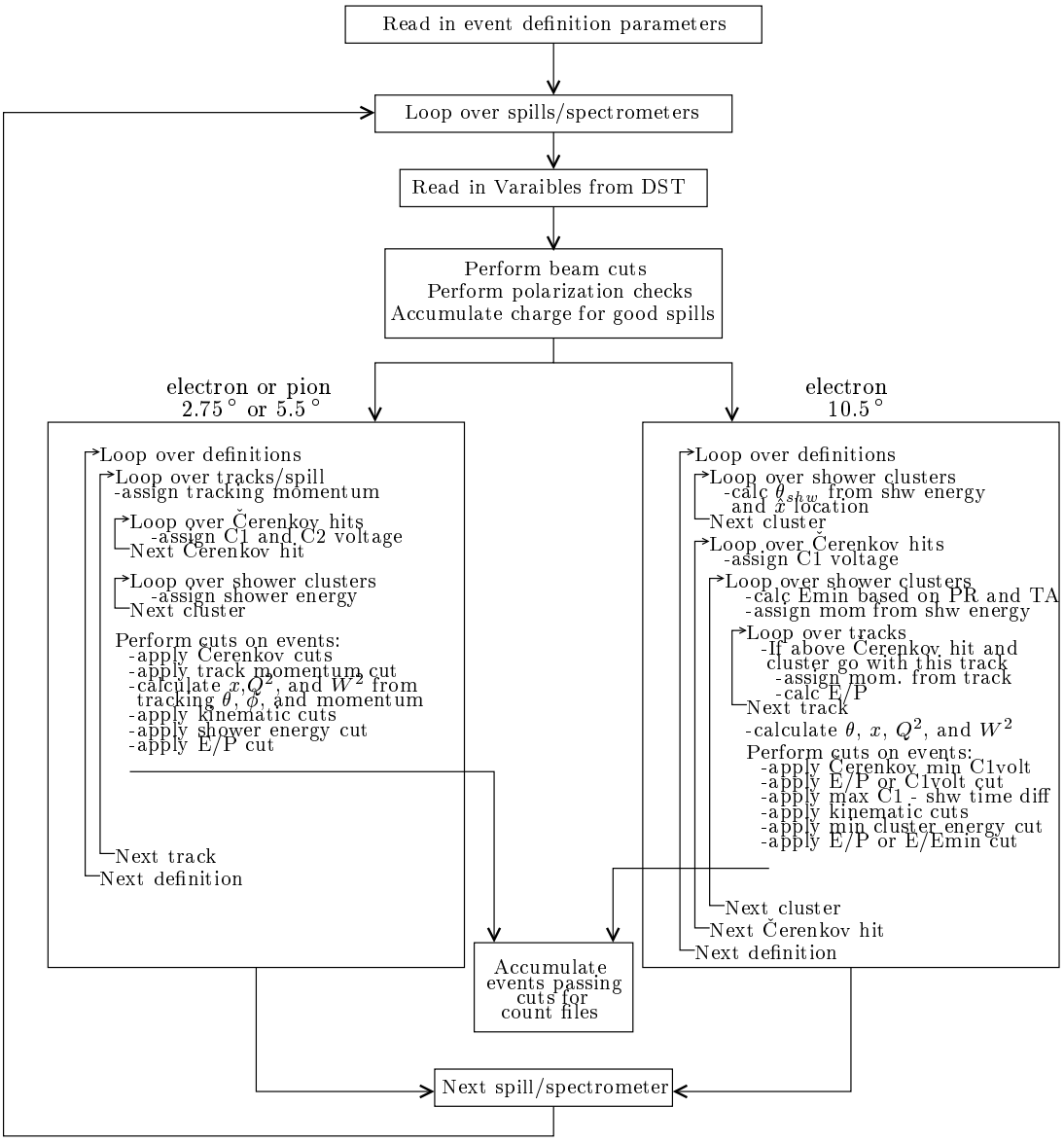

Figure 4.3: Schematic outline of the process used for generating the run-by-run count files. The process for extracting 10.5° pion events as well as 2.75° and 5.5° 'hybrid' electron events is not shown.

Parameter cut description	2.75°				5.5°			
	electron		pion		electron		pion	
	?	limits lwr upr	?	limits lwr/upr	?	limits lwr/upr	?	limits lwr/upr
Track momentum (GeV)	F	0.0/0.0	F	0.0/0.0	F	0.0/0.0	F	0.0/0.0
Shower energy (GeV)	T	8.0/100	F	0.0/8.0	T	8.0/100	F	0.0/8.0
Bjorken x	T	.01/0.9	T	.01/0.9	T	.01/0.9	T	.01/0.9
Q^2 transfer (GeV^2)	F	1.0/25	F	1.0/25	F	1.0/25	F	1.0/25
W^2 inv. mass (GeV^2)	F	4.0/ —	F	4.0/ —	F	4.0/ —	F	4.0/ —
E/P ratio	T	.75/2.5	T	0.0/0.6	T	.75/2.5	T	0.0/0.6
C1 peak voltage (mV)	T	30/500	F	20/500	T	30/500	F	20/500
C2 peak voltage (mV)	T	30/500	F	20/500	T	30/500	F	20/500
$\sqrt{\mathrm{C1} * \mathrm{C2}}$ (mV)	T	20/500	F	20/500	T	20/500	F	20/500

Table 4.3: Standard electron and pion definition for 2.75° and 5.5°. The True (T) or False (F) entries in the question mark column indicate whether the cut was applied.

Parameter cut description	value	
	electron	pion
Minimum cluster energy, Emin (GeV)	5.0	0.3
Minimum track momentum (GeV)	7.0	0.0
E/P minimum	0.75	0.0
E/Emin minimum	0.75	N/A
E/Emin maximum	N/A	0.8
C1 voltage 'low' minimum (mV)	20	0.0
C1 voltage 'high' minimum (mV)	30	0.0
Minimum C1 - shw time diff (ns)	3.7	3.7

Table 4.4: Standard electron and pion definition for 10.5°.

4.4 $A_\perp$ Extraction

The calculation of the experimental asymmetry begins with a run-by-run determination of the raw asymmetry, which is defined as*

$$A_{raw}^{\updownarrow,\Rightarrow}(x) = \left[\frac{\left(\frac{N(x)}{Q_b}\right)^{\downarrow,\Rightarrow} - \left(\frac{N(x)}{Q_b}\right)^{\uparrow,\Rightarrow}}{\left(\frac{N(x)}{Q_b}\right)^{\downarrow,\Rightarrow} + \left(\frac{N(x)}{Q_b}\right)^{\uparrow,\Rightarrow}} \right]. \tag{4.1}$$

The raw asymmetry per x-bin for each run was calculated for each spectrometer using the count files. From these files, the number of charge-weighted events ($\frac{N(x)}{Q_b}$), separated into left ($\downarrow$) and right ($\uparrow$) beam helicity, were used to calculate $A_{raw}(x)$ for both positive and negative target enhancements. The above asymmetry is referred to as the 'raw' asymmetry because, at this early stage in the calculation, it assumes idealized experimental conditions (i.e. 100% polarized beam and target and no dilution factor ($f = 1$)) as well as no contamination of the event data set from pions, non-DIS electrons, or electroweak scattering events. Moreover, radiative corrections must be applied to the final asymmetry to account for the scattering events' deviations from the single photon exchange ('Born') approximation assumed throughout this text. Finally, an additional modification to the asymmetry measurement must be made to account for the small mis-alignment ($\sim 2.4^\circ$) of the target field from a purely transverse orientation. The above inefficiency factors and corrections, and their application to the asymmetry are the subject of the remainder of this chapter.

The next step in extracting $A_\perp$ is to adjust the raw asymmetry for experimental inefficiencies P_b, P_t and f, and target nuclear corrections C_1 and C_2. The electroweak

*Note that this expression differs from Equation 2.19 in that the lepton flips helicity instead of the target nucleon. The two expressions are however equivalent, and this one is used because it is more representative of a run-by-run analysis. Furthermore, for opposite target polarizations, Equation 4.1 flips sign.

asymmetry (A_{EW}) correction is also applied here due to its application to the $A_\perp$ calculation being sensitive to the run-by-run target polarization direction. The adjusted asymmetry, labeled $A_\perp^{\text{uncorr}}$, is then defined as

$$A_\perp^{\text{uncorr}}(x) = \frac{1}{P_b P_t f(x) C_1(x)} \Big(A_{raw}(x) - P_b A_{EW}(x) \Big) + C_2(x) A_\perp^{\text{other}}(x), \qquad (4.2)$$

where $A_\perp^{\text{other}}$ is defined in Section 2.1.2 for Equation 2.18. The following subsections detail the analysis, results, and associated errors for each of these factors.

4.4.1 Beam Polarization

The average beam polarization for E155x, determined by Møller polarimetry, was $P_b = 0.832 \pm 0.002_{stat} \pm 0.031_{syst}$. Dedicated Møller runs were performed at various intervals throughout the experiment. The final results from these runs are shown in Figure 4.4, where the straight-line fit through the data points yielded the average P_b (quoted above) used for the entire asymmetry analysis. The details of the Møller runs as well as a description of the assigned systematic errors are discussed in reference [47].

4.4.2 Target Polarization

During the course of a production run, the polarization of the target was measured approximately every 30 seconds. Thus the target polarization (P_t) for each run was an average of roughly 60 measurements. P_t was calculated for all prospective 'good' runs. Runs with average polarizations below ± 10 % were omitted from the analysis. Figure 4.5 displays the average target polarization for each run used in the raw asymmetry calculation. A breakdown of the average $|P_t|$ for each of the experimental run regions is given in Table 4.5.

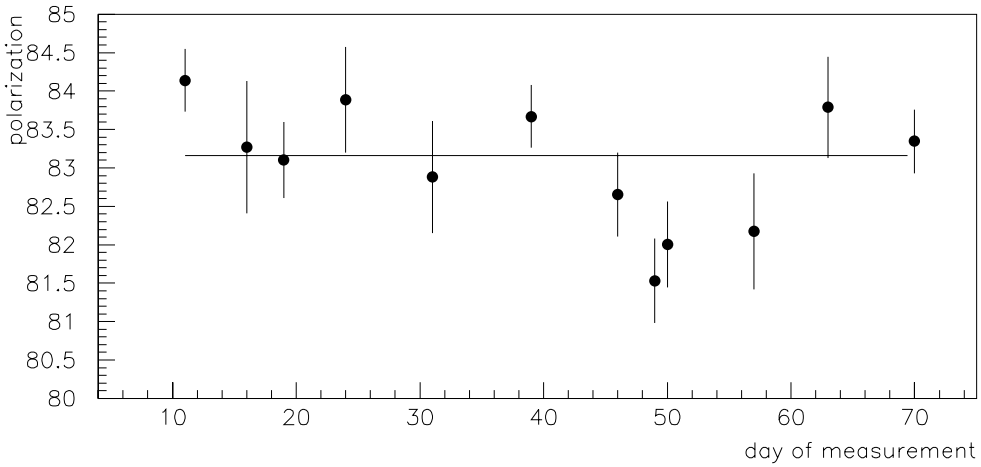

Figure 4.4: Møller beam polarization measurements during E155x. Each data point represents the average of the several measurements performed that day.

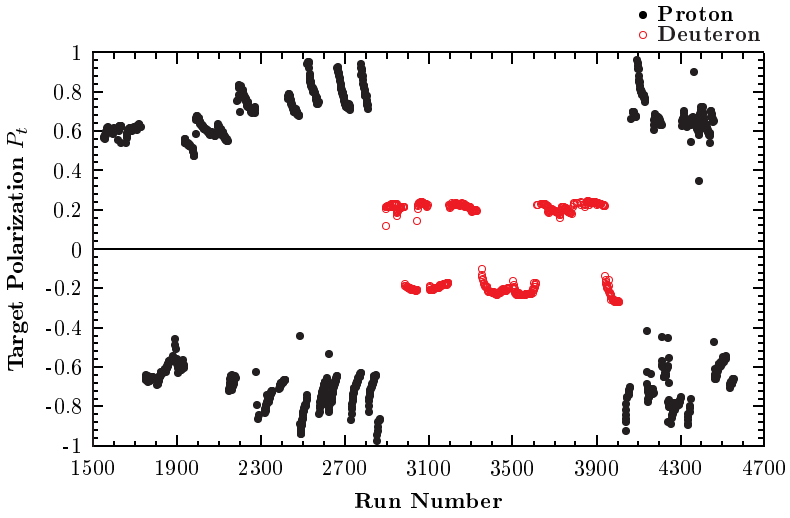

Figure 4.5: E155x average target polarization per run number. The proton polarizations are represented between runs $1558 - 2871$ and $4045 - 4559$ while the deuteron polarizations for runs $2917 - 4029$.

	$^{15}NH_3$ 29 GeV	$^{15}NH_3$ 32 GeV	^{6}LiD 29 GeV	^{6}LiD 32 GeV
2.75°	0.69554 ± 0.0118	0.72998 ± 0.0124	0.22531 ± 0.0101	0.21190 ± 0.0095
5.5°	0.69666 ± 0.0118	0.73122 ± 0.0124	0.22516 ± 0.0101	0.21173 ± 0.0095
10.5°	0.71175 ± 0.0121	0.73163 ± 0.0124	0.21538 ± 0.0097	0.21172 ± 0.0095

Table 4.5: Average $|P_t|$ for each spectrometer, target, and beam energy. The errors quoted represent the 1.7 % $^{15}NH_3$ and 4.5 % ^{6}LiD target polarization errors discussed in Section 3.2.7.

4.4.3 Dilution Factor

The dilution factor (f) is a quantity representing the fact that the targets were not purely protons or deuterons, but consisted of other scattering centers whose cross sections tended to dilute the desired measurement. Furthermore, any material other than target material within the acceptance of the spectrometers that the beam passed through (e.g. aluminum vacuum windows, NMR coil material, and liquid and gas helium) further diluted the asymmetry. Since the majority of collected events were from unpolarized scattering[†], for which the asymmetry is zero (by definition), the denominator of Equation 4.1 was inflated while the numerator was relatively unchanged. The dilution factor corrects for these extra unwanted events as well as the small percentage of unwanted polarized events (such as scattering off the unpaired proton in ^{15}N).

The dilution factor is defined as the fraction of the total scattering rate coming from the target nucleons (free protons or deuterons) and can be written as

$$f_{p;d} \equiv \left[\frac{R^{\downarrow,\Rightarrow}_{p;d} + R^{\uparrow,\Rightarrow}_{p;d}}{R^{\downarrow,\Rightarrow}_{total} + R^{\uparrow,\Rightarrow}_{total}} \right] = \frac{N_t \sigma_t}{N_t \sigma_t + \sum_{nt} N_{nt} \sigma_{nt}}, \tag{4.3}$$

[†]This is known because the theoretical upper limits on the size of the dilution factors for $^{15}NH_3$ and ^{6}LiD (mentioned in Section 3.2.4) are both well below 50 %. In addition, the target nucleons are not 100 % polarized.

where N_t and N_{nt} are the number of target and non-target nucleons, respectively, and σ_t and σ_{nt} are their corresponding cross sections. To determine N_t and N_{nt}, the composition of the target material as well as the target thickness must be known precisely. The composition of the $^{15}NH_3$ targets are known to be pure (3 protons for each nitrogen nucleus) except that 2% of the nitrogen is ^{14}N. The composition of the ^6LiD material was isotopically analyzed following E155; this revealed that 4.5% of the lithium nuclei were ^7Li and 2.4% of the deuterons were actually protons. A detailed write-up of the ^6LiD composition analysis can be found in appendix D of reference [54].

Since the target material consisted of irregular shaped granules of varying sizes contained in cylindrical cups with LHe and NMR coils, the target thickness was not directly calculable. Instead, the fraction of target material filling the cup, called the packing fraction (pf)–determined from spectrometer event-rate comparisons between the production and solid/dummy target calibration runs taken for a given load of target material–was used to calculate the target thickness. The packing fractions for the ammonia and lithium target are defined as

$$pf_{^{15}NH_3} = \frac{R_{^{15}NH_3}}{R_{^{12}C}}, \qquad pf_{^6LiD} = \frac{R_{^6LiD}}{R_{^9Be}}, \tag{4.4}$$

where the rates include the contributions from all scattering centers within the spectrometers acceptance. For $^{15}NH_3$, five different packing fractions were calculated for seven specific run regions for the two target cells. Only one packing fraction was needed for all the ^6LiD running. The packing fractions used in the dilution factor calculation are given in Table 4.6.

Material	Cell	Run Region	pf	pf error
$^{15}NH_3$	Top	$1558 - 1800$	0.550	0.013
		$1801 - 2871$	0.600	0.013
		$4045 - 4559$	0.600	0.013
	Bottom	$1558 - 1710$	0.550	0.013
		$1711 - 2871$	0.570	0.031
		$4045 - 4139$	0.480	0.019
		$4140 - 4559$	0.620	0.015
^{6}LiD	Top	$2917 - 4029$	0.550	0.017
	Bottom	$2917 - 4029$	0.550	0.017

Table 4.6: Target material packing fractions used in the dilution factor calculation.

Ammonia Target

Given the precise composition of the target materials, Equation 4.3 can be expressed explicitly for the two targets. For the ammonia target,

$$f_{^{15}NH_3} = \frac{N_p^{NH_3}\sigma_p}{N_p^{NH_3}\sigma_p + N_{^{15}N}\sigma_{^{15}N} + N_{^{14}N}\sigma_{^{14}N} + \sum_i N_i\sigma_i}, \tag{4.5}$$

where

$$N_{^{15}N} = (l_{tgt} \cdot pf)N_A \left[\frac{(1-\eta_{^{14}N}) \cdot \rho_{^{15}NH_3}}{A_{^{15}NH_3}}\right], \tag{4.6}$$

$$N_{^{14}N} = (l_{tgt} \cdot pf)N_A \left[\frac{\eta_{^{14}N} \cdot \rho_{^{14}NH_3}}{A_{^{14}NH_3}}\right], \tag{4.7}$$

and

$$N_p^{NH_3} = 3(N_{^{15}N} + N_{^{14}N}). \tag{4.8}$$

N_A is the Avogadro constant, l_{tgt} is the length of the cylindrical target cavity (3.0 cm), and the remaining quantities used in the above equations are listed and described in Table 4.7. The EMC factors [76] in this table correct for the fact that the individual

Variable	Value/Expression	Description
$\rho_{^{15}NH_3}$	0.917 g/cm^3	density of $^{15}NH_3$
$A_{^{15}NH_3}$	18.024 g/mol	atomic weight of $^{15}NH_3$
$\sigma_{^{15}N}$	$(7\sigma_p + 8\sigma_n)g_{^{15}N}^{EMC}$	cross section for ^{15}N
$g_{^{15}N}^{EMC}$	~ 1	EMC factor for ^{15}N
$\eta_{^{14}N}$	0.02	concentration of ^{14}N in nitrogen
$\rho_{^{14}NH_3}$	0.867 g/cm^3	density of $^{14}NH_3$
$A_{^{14}NH_3}$	17.027 g/mol	atomic weight of $^{14}NH_3$
$\sigma_{^{14}N}$	$(7\sigma_p + 7\sigma_n)g_{^{14}N}^{EMC}$	cross section for ^{14}N
$g_{^{14}N}^{EMC}$	~ 1	EMC factor for ^{14}N

Table 4.7: Description of the variables used in $^{15}NH_3$ dilution factor calculation.

scattering centers in nitrogen are bound inside a nucleus; σ_p and σ_n are the cross sections for scattering off free protons and neutrons respectively. The last term in the denominator of Equation 4.5 ($\sum_i N_i\sigma_i$) represents the contribution to the dilution from the unpolarized materials that were not part of the target material. As mentioned before, these consisted of several aluminum vacuum windows, CuNi NMR coils, and liquid and gas helium. Figure 4.6 displays the $^{15}NH_3$ dilution factor as a function of x for each spectrometer averaged over the two beam energies.

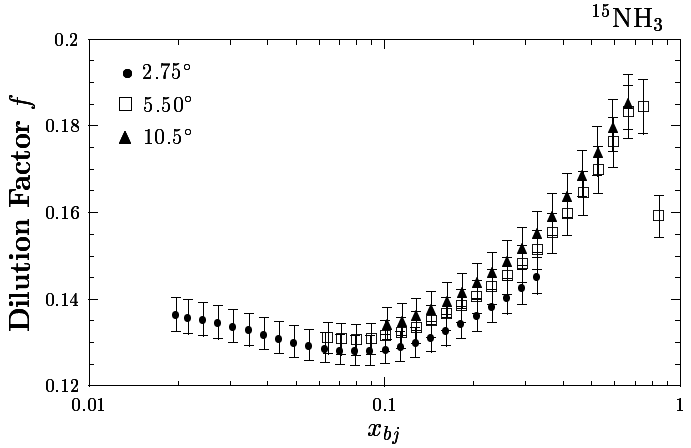

Figure 4.6: $^{15}NH_3$ dilution factor.

Lithium Target

For the lithium target, the numerator of the dilution factor is

$$f_{^6\mathrm{LiD}}^{numerator} = N_p^{\mathrm{LiD}}\sigma_p + N_n^{\mathrm{LiD}}\sigma_n, \tag{4.9}$$

and the denominator is

$$\begin{aligned} f_{^6\mathrm{LiD}}^{denominator} &= N_p^{\mathrm{LiD}}\sigma_p + N_n^{\mathrm{LiD}}\sigma_n + (N_{^6\mathrm{Li(D)}} + N_{^6\mathrm{Li(H)}})\sigma_{^6\mathrm{Li}} & (4.10)\\ &\quad + (N_{^7\mathrm{Li(D)}} + N_{^7\mathrm{Li(H)}})\sigma_{^7\mathrm{Li}} + \sum_i N_i\sigma_i, & (4.11) \end{aligned}$$

where

$$\begin{aligned} N_{^6\mathrm{Li(D)}} &= (l_{tgt}\cdot pf)N_A\left[\frac{(1-\eta_{^7\mathrm{Li}}-\eta_{^6\mathrm{LiH}}-\eta_{^7\mathrm{LiH}})\cdot\rho_{\mathrm{LiD}}}{A_{^6\mathrm{LiD}}}\right], & (4.12)\\ N_{^7\mathrm{Li(D)}} &= (l_{tgt}\cdot pf)N_A\left[\frac{\eta_{^7\mathrm{Li}}\cdot\rho_{\mathrm{LiD}}}{A_{^7\mathrm{LiD}}}\right], & (4.13)\\ N_{^6\mathrm{Li(H)}} &= (l_{tgt}\cdot pf)N_A\left[\frac{\eta_{^6\mathrm{LiH}}\cdot\rho_{\mathrm{LiD}}}{A_{^6\mathrm{LiH}}}\right], & (4.14)\\ N_{^7\mathrm{Li(H)}} &= (l_{tgt}\cdot pf)N_A\left[\frac{\eta_{^7\mathrm{LiH}}\cdot\rho_{\mathrm{LiD}}}{A_{^7\mathrm{LiH}}}\right], & (4.15) \end{aligned}$$

and

$$\begin{aligned} N_p^{\mathrm{LiD}} &= N_{^6\mathrm{Li(D)}} + N_{^7\mathrm{Li(D)}} + N_{^6\mathrm{Li(H)}} + N_{^7\mathrm{Li(H)}}, & (4.16)\\ N_n^{\mathrm{LiD}} &= N_{^6\mathrm{Li(D)}} + N_{^7\mathrm{Li(D)}}. & (4.17) \end{aligned}$$

The quantities used in the above equations are listed in Table 4.8. Figure 4.7 displays the ^{6}LiD dilution factor as a function of x for each spectrometer averaged over the two beam energies.

Variable	Value/Expression	Description
ρ_{LiD}	0.82 g/cm^3	density of lithium deuteride
$A_{^6\mathrm{LiD}}$	8.029 g/mol	atomic weight of ^{6}LiD
η^{7}_{Li}	0.045	concentration of ^{7}Li in lithium
$A_{^7\mathrm{LiD}}$	9.030 g/mol	atomic weight of ^{7}LiD
η^{6}_{LiH}	0.024	contamination of ^{1}H in D
$A_{^6\mathrm{LiH}}$	7.023 g/mol	atomic weight of ^{6}LiH
$\sigma_{^6\mathrm{Li}}$	$(3\sigma_p + 3\sigma_n)g^{EMC}_{^6\mathrm{Li}}$	cross section for ^{6}Li
$g^{EMC}_{^6\mathrm{Li}}$	≈ 1	EMC factor for ^{6}Li
η^{7}_{LiH}	0.001	concentration of ^{7}LiH
$A_{^7\mathrm{LiH}}$	8.024 g/mol	atomic weight of ^{7}LiH
$\sigma_{^7\mathrm{Li}}$	$(3\sigma_p + 4\sigma_n)g^{EMC}_{^7\mathrm{Li}}$	cross section for ^{7}Li
$g^{EMC}_{^7\mathrm{Li}}$	≈ 1	EMC factor for ^{7}Li

Table 4.8: Description of the variables used in ^{6}LiD dilution factor calculation.

4.4.4 Target Nuclear Corrections

The small percentage of unwanted polarized events, accounted for in the dilution factor calculation, require the use of additional corrections (C_1 and C_2) to the raw asymmetry known as the target nuclear corrections. As was stated in Section 3.2.4, C_1 corrects for the presence of polarizable material of the same spin-species as the

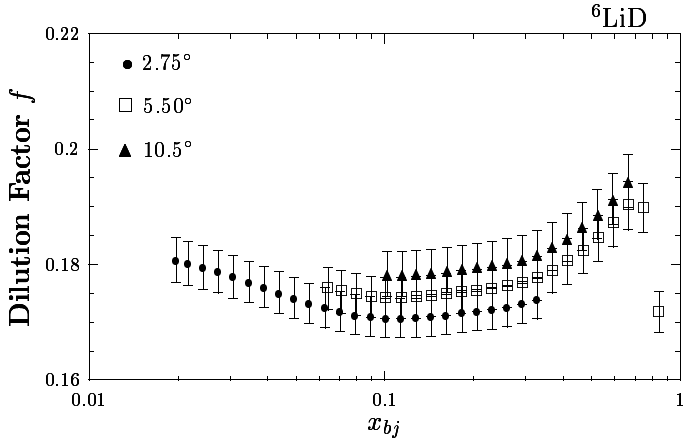

Figure 4.7: ^{6}LiD dilution factor.

target whereas C_2 corrects for the presence of polarization from spin-species different from the target. To calculate these factors, the polarization of the various non-target nuclei as well as their concentrations must be known.

For $^{15}NH_3$, C_1 corrects for the proton polarization in ^{15}N, and C_2 corrects for the 'non-proton' polarization in the ^{14}N contamination. Since the contamination is only 2 %, C_2 is considered negligible for the ammonia target and consequently set to zero. The asymmetry target nuclear corrections for $^{15}NH_3$ are

$$C_1^{^{15}NH_3} = 1 + (1 - \eta_{^{14}N}) \left(\frac{1}{3}\right) \left(\frac{P_{^{15}N}}{P_p}\right) \beta^p_{^{15}N} g^{EMC}_{^{15}N}, \tag{4.18}$$

$$C_2^{^{15}NH_3} = 0, \tag{4.19}$$

where P_p is the measured proton polarization for each run and $P_{^{15}N}$ is the polarization of ^{15}N calculated from P_p using the equation[‡]

$$P_{^{15}N} = -(0.13561 P_p - 0.18286 P_p^2 + 0.33482 P_p^3); \tag{4.20}$$

$\beta^p_{^{15}N}$ is the ratio of the unpaired proton to nitrogen polarization for ^{15}N (equal to $-1/3$), and $\eta_{^{14}N}$ and $g^{EMC}_{^{15}N}$ have been previously defined. Figure 4.8 displays C_1 for $^{15}NH_3$ as a function of x_{bj} for the three spectrometers averaged over the two beam energies.

For ^6LiD, C_1 corrects for the additional polarized deuteron in ^6Li, and C_2 corrects for the unpaired proton polarization in the ^7Li contamination as well as the free protons in the lithium hydride (LiH) contamination. The asymmetry target nuclear

[‡]The relationship between the target proton polarization and that of ^{15}N in ammonia was studied during target technical runs following E143 and E155. The result of these studies was the phenomenological fit of Equation 4.20.

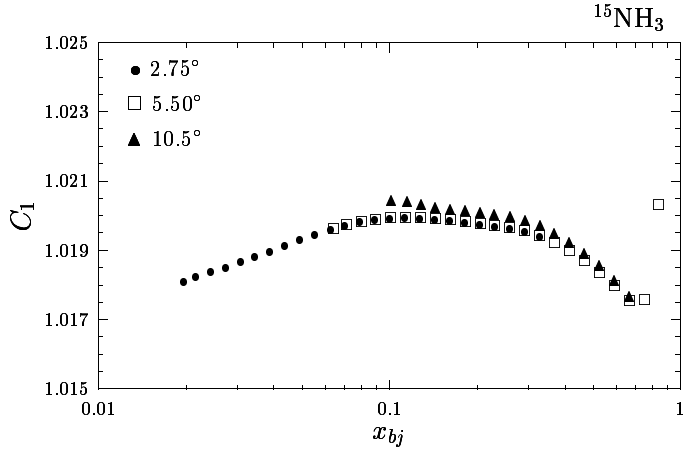

Figure 4.8: $^{15}NH_3$ C_1 correction factor.

corrections for ^{6}LiD are

$$C_1^{^6\mathrm{LiD}} = (1-\eta_{^6\mathrm{LiH}}) + (1-\eta_{^7\mathrm{Li}})\left(\frac{P_{^6\mathrm{Li}}}{P_d}\right)\left(\frac{1}{1-\frac{3}{2}\omega_D}\right)\beta^d_{^6\mathrm{Li}}g^{EMC}_{^6\mathrm{Li}}, \quad (4.21)$$

$$C_2^{^6\mathrm{LiD}} = -\frac{1}{C_1}\left[\eta_{^6\mathrm{LiH}}\left(\frac{P_p^{\mathrm{LiH}}}{P_d}\right) + \eta_{^7\mathrm{Li}}\left(\frac{P_{^7\mathrm{Li}}}{P_d}\right)\beta^p_{^7\mathrm{Li}}g^{EMC}_{^7\mathrm{Li}}\left(\frac{F_2^p}{2F_2^d}\right)\right], \quad (4.22)$$

where P_d is the measured deuteron polarization for each run, $P_{^6\mathrm{Li}}$ is the ^{6}Li polarization, P_p^{LiH} is the proton polarization in LiH (≈ 0.04), and $P_{^7\mathrm{Li}}$ is the ^{7}Li polarization. $\beta^d_{^6\mathrm{Li}}$ is the ratio of deuteron to lithium polarization for ^{6}Li (≈ 0.866) and $\beta^p_{^7\mathrm{Li}}$ is the ratio of the unpaired proton to lithium polarization for ^{7}Li ($\approx 2/3$); F_2^p and F_2^d are the unpolarized F_2 structure functions of the proton and deuteron respectively and ω_D is the D-state probability of the deuteron wavefunction (~ 0.05). The remaining variables are defined in Table 4.8 of the previous subsection.

The polarizations $P_{^6\mathrm{Li}}$ and $P_{^7\mathrm{Li}}$ are predicted to be $\sim P_d$ and $\sim 3P_d$, respectively, from equal spin temperature theory. The above factor $\beta^d_{^6\mathrm{Li}}$–indicating that the unpaired nucleons in ^{6}Li are aligned with the nuclear spin 86.6% of the time, and

$\beta^p_{^7\mathrm{Li}}$–indicating that the unpaired proton in ^{7}Li is aligned with the lithium polarization 66.7% of the time were determined from nuclear models of the different lithium isotopes [77] in which ^{6}Li was approximated as $^4\mathrm{He} + {}^2\mathrm{H}$ and ^{7}Li as $^4\mathrm{He} + {}^3\mathrm{H}$. Figure 4.9 displays C_1 and C_2 for ^{6}LiD as a function of x for the three spectrometers averaged over the two beam energies. The C_1 correction for ^{6}LiD is fairly extensive due to the large deuteron polarization in ^{6}Li. The plot of C_2 indicates that the contamination of $A_\perp^{\mathrm{proton}}$ (equal to $A_\perp^{\mathrm{other}}$ in Equation 4.2) in the measured deuteron asymmetry ranges between 2.5% at low x to 3.5% at high x.

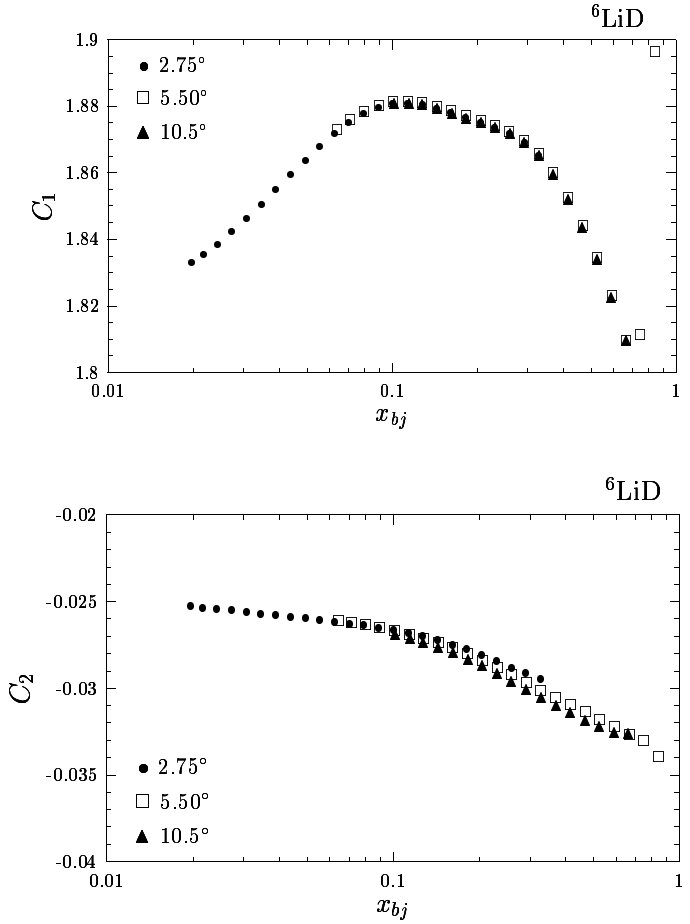

Figure 4.9: ^{6}LiD C_1 and C_2 correction factor.

4.4.5 Electroweak Asymmetry

The final asymmetry correction applied on a run-by-run basis was the electroweak asymmetry (A_{EW}) correction. This correction accounted for the small contamination in the A_{raw} data set from electroweak scattering events. These are parity violating interactions involving the interference between electromagnetic and weak scattering which tend to slightly skew the $A_\perp$ measurement. Since the weak interaction component of the interference amplitude has different couplings for left versus right handed states, the polarized SLAC electron beam produces an electroweak asymmetry even for unpolarized target scattering. For deep inelastic scattering with $Q^2 \ll M_{Z^0}$, this asymmetry is of the order $10^{-4} \times Q^2$ [78] (where Q^2 is in GeV^2). This is two orders of magnitude smaller than the measured $A_\perp$; thus this correction is not expected to impact the run-by-run results beyond the one percent level. Furthermore, since the target enhancement direction was periodically reversed–with roughly equal running time for each direction–the asymmetries arising from electroweak events theoretically average-out to zero for the entire experiment[§].

For E155x, the electroweak asymmetry for both targets was calculated using

$$A_{EW} = 5 \times 10^{-5} Q^2 \left[0.77(1 + 0.44R_s) + 0.11C_y\right], \tag{4.23}$$

where R_s is the ratio of light quark distributions and is defined as

$$R_s(x) \equiv \frac{2s(x)}{u(x) + d(x)} \approx \begin{cases} 0.5 & \text{if } x < 0.2, \\ 0 & \text{if } x \geq 0.2, \end{cases} \tag{4.24}$$

[§]This is because A_{EW} is independent of the target polarization orientation and thus does not change sign when the polarization direction is reversed (as A_{raw} does).

and

$$C_y = \frac{1-(1-y)^2}{1-(1-y)^2-\frac{y^2 R}{1+R}}, \tag{4.25}$$

where $y = \nu/E$ is the fraction of energy lost by the scattered lepton, and R is the ratio of total longitudinal to transverse photo-absorption cross sections (defined in Section 2.2) taken from the 1998 SLAC fit to $R(x, Q^2)$ [15]. The kinematic quantities, Q^2 and y, used in the above calculations represent their average value per x-bin for each run. Figure 4.10 displays the calculated electroweak asymmetry, averaged over the two beam energies, for each target and spectrometer as a function of x. The effect of this correction on the measured asymmetries is barely noticeable; the average percent difference between the measured asymmetry with and without the A_{EW} correction is 0.61% for $^{15}NH_3$ and 1.21% for ^{6}LiD.

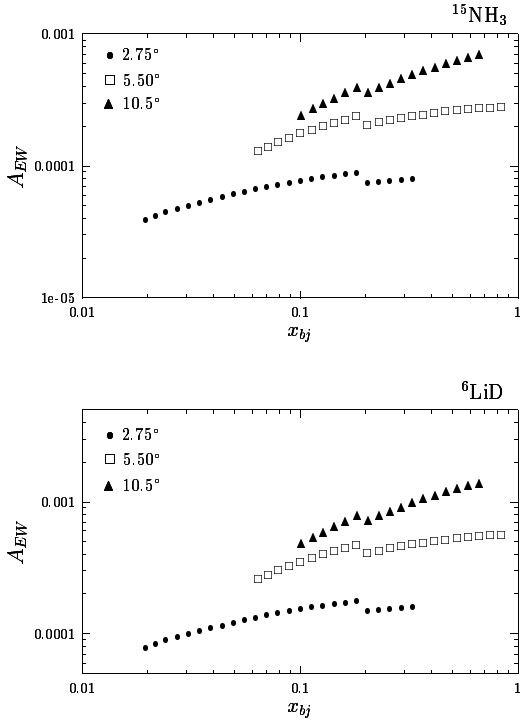

Figure 4.10: Electroweak asymmetry used in the $A_\perp$ analysis.

4.5 Corrections to $A_\perp$

Thus far, the run-by-run asymmetry extracted from the count files has been adjusted for experimental inefficiencies (P_b, P_t, f, and C_1) and contamination from electroweak scattering events as well as events produced by scattering off the 'other' spin species. In this section, the adjusted asymmetry accumulated for all runs is corrected for background contamination and radiative effects.

4.5.1 Background Contamination

The background contamination in the $A_\perp$ data set consisted primarily of pions (π^-'s) misidentified as electrons and non-DIS electrons (e^-_γ) from pair-symmetric processes (i.e. electron-positron pair production from photon or other particle decays). This implies that the measured asymmetry of Equation 4.2 can be written as

$$A_\perp^{uncorr}(x) = \alpha_{e^-}(x)A_\perp^{e^-}(x) + \alpha_{e^-_\gamma}(x)A_{e^-_\gamma}(x) + \alpha_{\pi^-}(x)A_{\pi^-}(x), \tag{4.26}$$

where $A_\perp^{e^-}$, $A_{e^-_\gamma}$, and A_{π^-} are the asymmetries for DIS electrons, non-DIS electrons, and pions respectively. The α coefficients are effective dilution factors which dictate the contribution of their respective asymmetry to the overall measured asymmetry ($A_\perp^{uncorr}$) and are defined as

$$\alpha_i(x) = \frac{N_i(x)}{N_{e^-} + N_{e^-_\gamma} + N_{\pi^-}}, \tag{4.27}$$

with

$$\sum_i \alpha_i(x) = 1, \tag{4.28}$$

where N is the number of events normalized to the incident beam charge.

From Equation 4.26, $A_{\perp}^{e^-}$ is the desired quantity, whereas $A_{e_{\gamma}^-}$ and A_{π^-} are contaminants that need to be removed. The π^- asymmetry was determined from the normal production runs using the count file events generated by the standard pion definition–detailed in Section 4.3.2. The non-DIS electron asymmetry was determined from the positron runs. For these runs, the measured asymmetry can be written as

$$A_{e^+}^{meas}(x) = \alpha_{e^+}(x)A_{e^+}(x) + \alpha_{\pi^+}(x)A_{\pi^+}(x), \tag{4.29}$$

where A_{e^+} and A_{π^+} are the asymmetries for positrons and π^+'s, respectively, and the α's are their corresponding dilution factors¶. The e^+ and π^+ asymmetries were extracted using the standard electron and pion definitions applied to the positron runs. The creation of positrons via pair-symmetric processes implies that the positron contamination is equal to the non-DIS electron contamination ($A_{e^+} = A_{e_{\gamma}^-}$). Using this fact together with Equation 4.29, Equation 4.26 can be rearranged to yield the form of the pion/positron background correction used to obtain the 'uncontaminated' perpendicular DIS electron asymmetry. That is

$$A_{\perp}^{e^-}(x) = \frac{1}{\alpha_{e^-}(x)}\left[A_{\perp}^{uncorr}(x) - \frac{\alpha_{e_{\gamma}^-}(x)}{\alpha_{e^+}(x)}\left(A_{e^+}^{meas} - \alpha_{\pi^+}(x)A_{\pi^+}\right) - \alpha_{\pi^-}(x)A_{\pi^-}\right].$$

The remainder of this subsection will detail the results for the contamination asymmetries, the calculation and results of the various α dilution coefficients, and a brief summary of the effect of this correction on $A_{\perp}^{uncorr}$.

The results of the pion asymmetries and the positron asymmetry were small and taken to be constant as a function of x. These values are given in Table 4.9. Unfortunately, there were insufficient statistics collected during the positron runs to

¶Note that these α coefficients are normalized to the measured positron run asymmetry ($\alpha_{e^+} + \alpha_{\pi^+} = 1$) in which the contribution of A_{π^+} is considered a contaminant.

		$^{15}NH_3$		^{6}LiD	
		29 GeV	32 GeV	29 GeV	32 GeV
A_{π^-}	2.75°	−0.011	−0.006	0.001	0.003
	5.5°	−0.008	−0.002	0.0035	−0.013
	10.5°	0	0	0	0
A_{π^+}	2.75°	0.005	0.001	0	−0.04
	5.5°	0.017	−0.006	0	0.219
	10.5°	0	0	0	0
$A_{e^+}^{meas}$	2.75°	0	0	0	0
	5.5°	0	0	0	0
	10.5°	0	0	0	0

Table 4.9: Constant values used for contamination asymmetries for both beam energies and targets for all three spectrometers.

distinguish $A_{e^+}^{meas}$ from zero; this was the consequence of a relatively large π^+ background amongst a small positron rate. Moreover, the lack of pion statistics in the 10.5° spectrometer resulted in all its contamination asymmetries being set to zero. The non-zero values in Table 4.9 were determined from straight-line fits to the measured x-dependent pion asymmetries. For the proton target, Figures 4.11 and 4.12 display the π^- and π^+ asymmetries, respectively, for the two beam energies.

The calculation of the various α dilution coefficients was accomplished by determining the average relative numbers of each type of particle present in the measured asymmetry data sets from the production and positron runs. Since the E/P distributions of pions and electrons/positrons are clearly distinct, they can be isolated, fit to a functional form, and then integrated over the same specific range[‖] to yield the number of particles they contain[**]. Ratios of these integrals can then be equated with the α factors. This procedure was complicated by low positron run statistics which

[‖]The integration was performed over the E/P range used to define electrons/positrons in the standard definition (from 0.75 to 2.5) since this would be where the 'contaminating' events occur.

[**]In order to properly count the number of π^- (π^+) contaminants, their E/P distributions–obtained using the pion definitions–were scaled to the pion rate observed in the electron (positron) E/P distributions before integration.

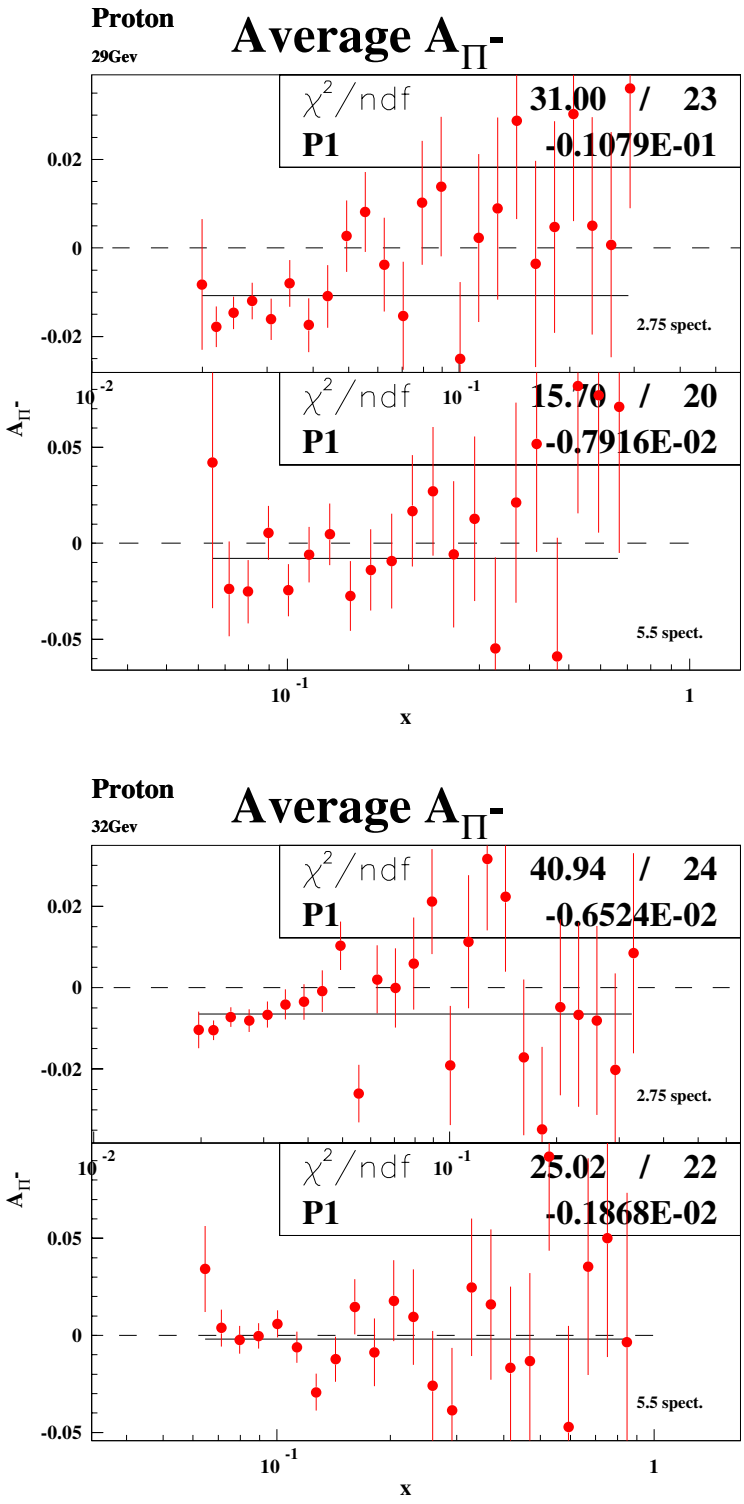

Figure 4.11: Extracted A_{π^-} from $^{15}NH_3$ production runs for both beam energies shown with straight-line fit [79]. The value and error of the fit are also shown.

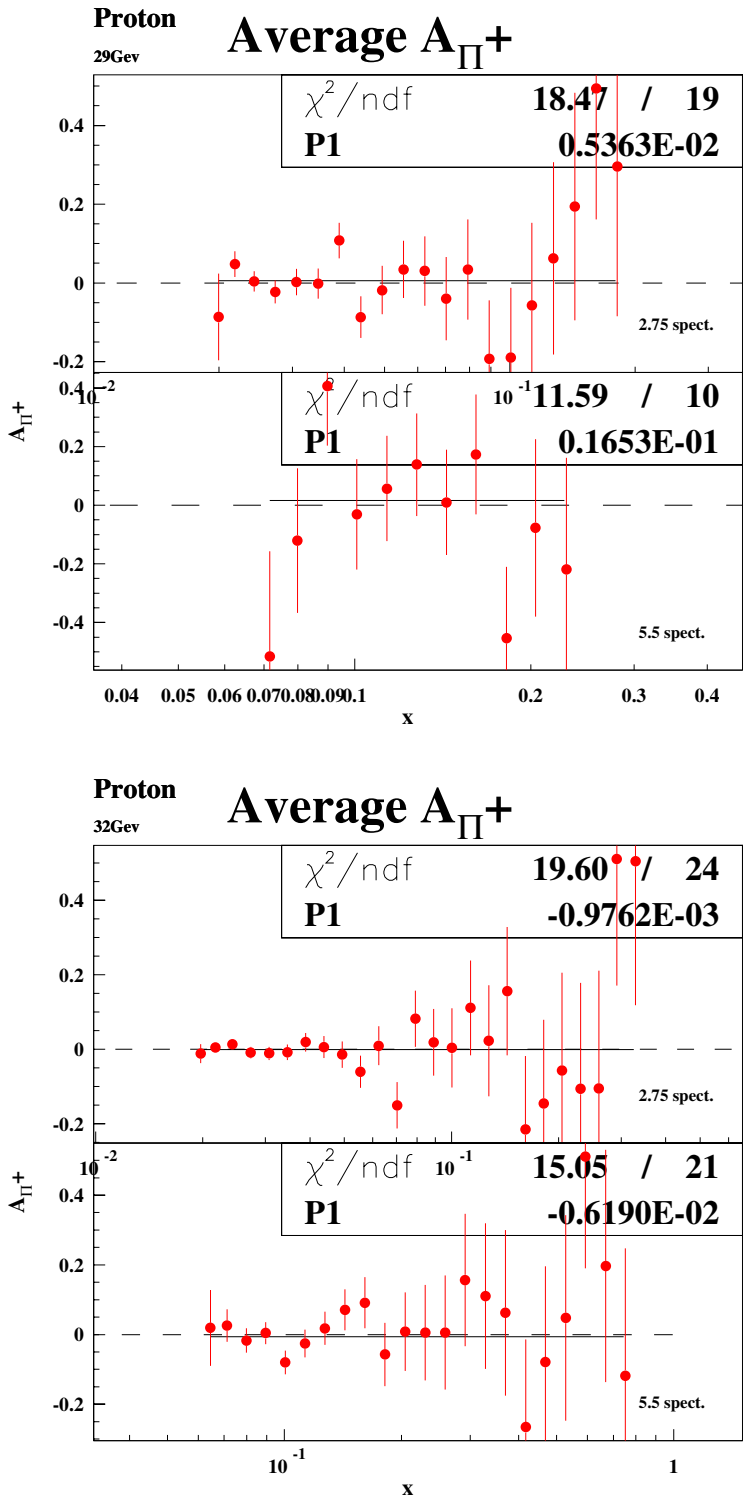

Figure 4.12: Extracted A_{π^+} from $^{15}NH_3$ positron runs for both beam energies shown with straight-line fit [79]. The value and error of the fit are also shown.

were further compounded by the individual x-bin analysis of the E/P distributions.

The results of the α factors for each spectrometer and target averaged over the two beam energies are shown in Figures 4.13 through 4.15. These plots show that the pion and non-DIS electron contamination in the production runs is at the few percent level for the lowest x-bins of each spectrometer with an overall decreasing trend toward higher values of x. The opposite trend in the $\pi+$ contamination of the positron runs is consistent with this result in that fewer positrons are produced at higher x values. All 10.5° pion dilution coefficients were zero due to insufficient statistics. The effect of the background contamination correction on the measured asymmetries for each target and spectrometer is shown in Figure 4.16. As expected, the correction has its greatest impact at the lowest x values of each spectrometer–where the effect was as high as $\sim 20\%$. On average, the percent difference per x-bin between the background subtracted and unsubtracted asymmetries is 5.2% for $^{15}NH_3$ and 5.6% for ^{6}LiD.

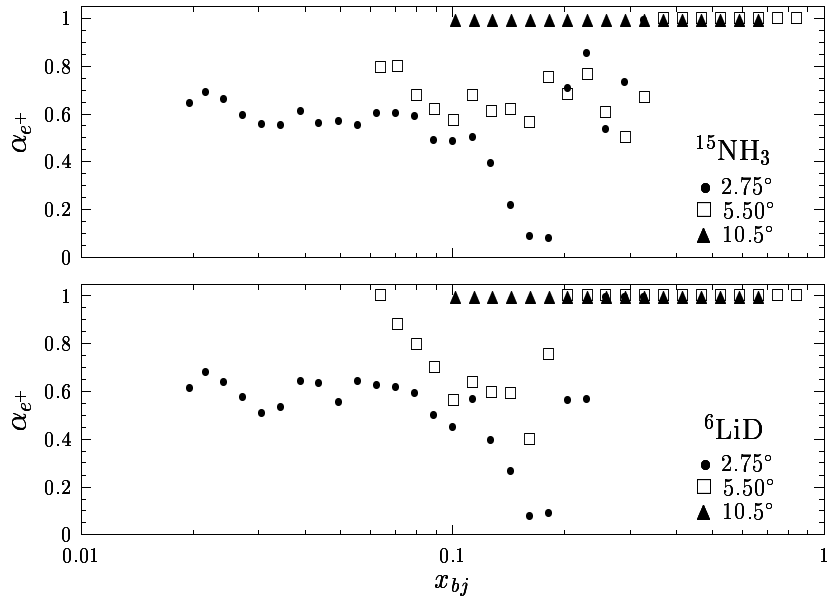

Figure 4.13: Fraction of positron events attributed to $A_{e^+}^{meas}$.

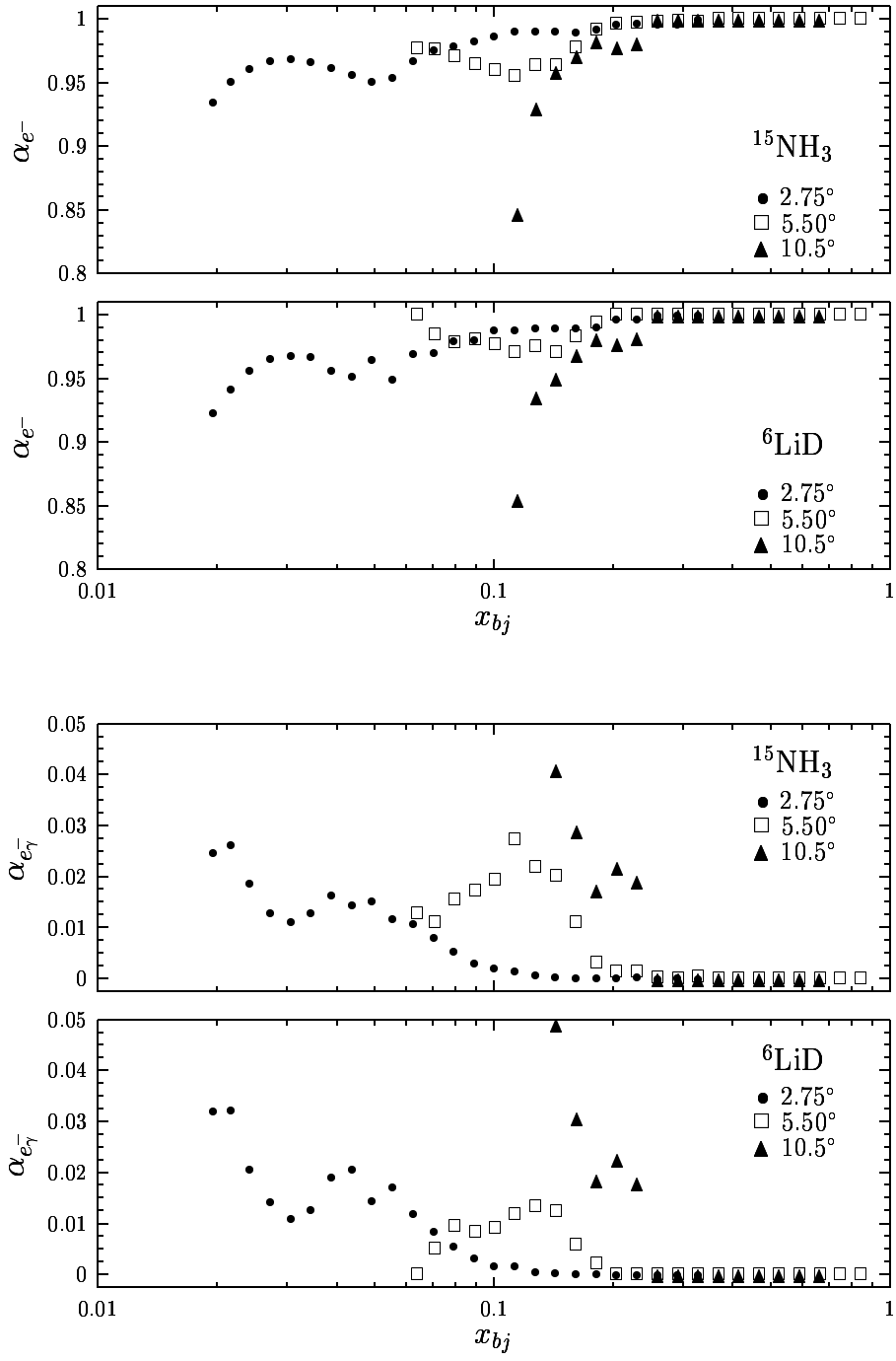

Figure 4.14: Fraction of production run events attributed to DIS electrons (top plot) and non-DIS electrons (bottom plot).

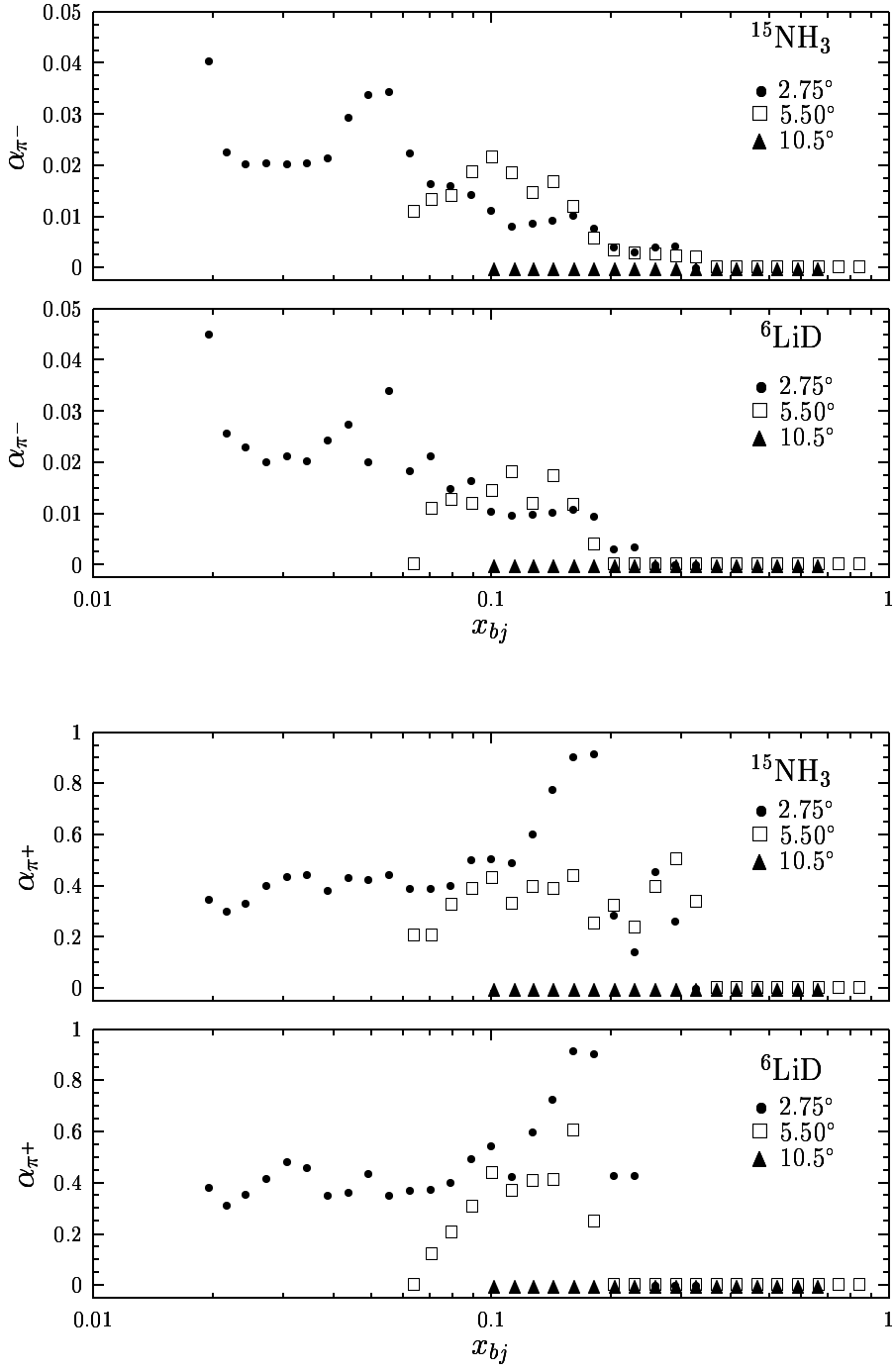

Figure 4.15: Hadron contamination in normal production runs (top plots) and positron runs (bottom plots).

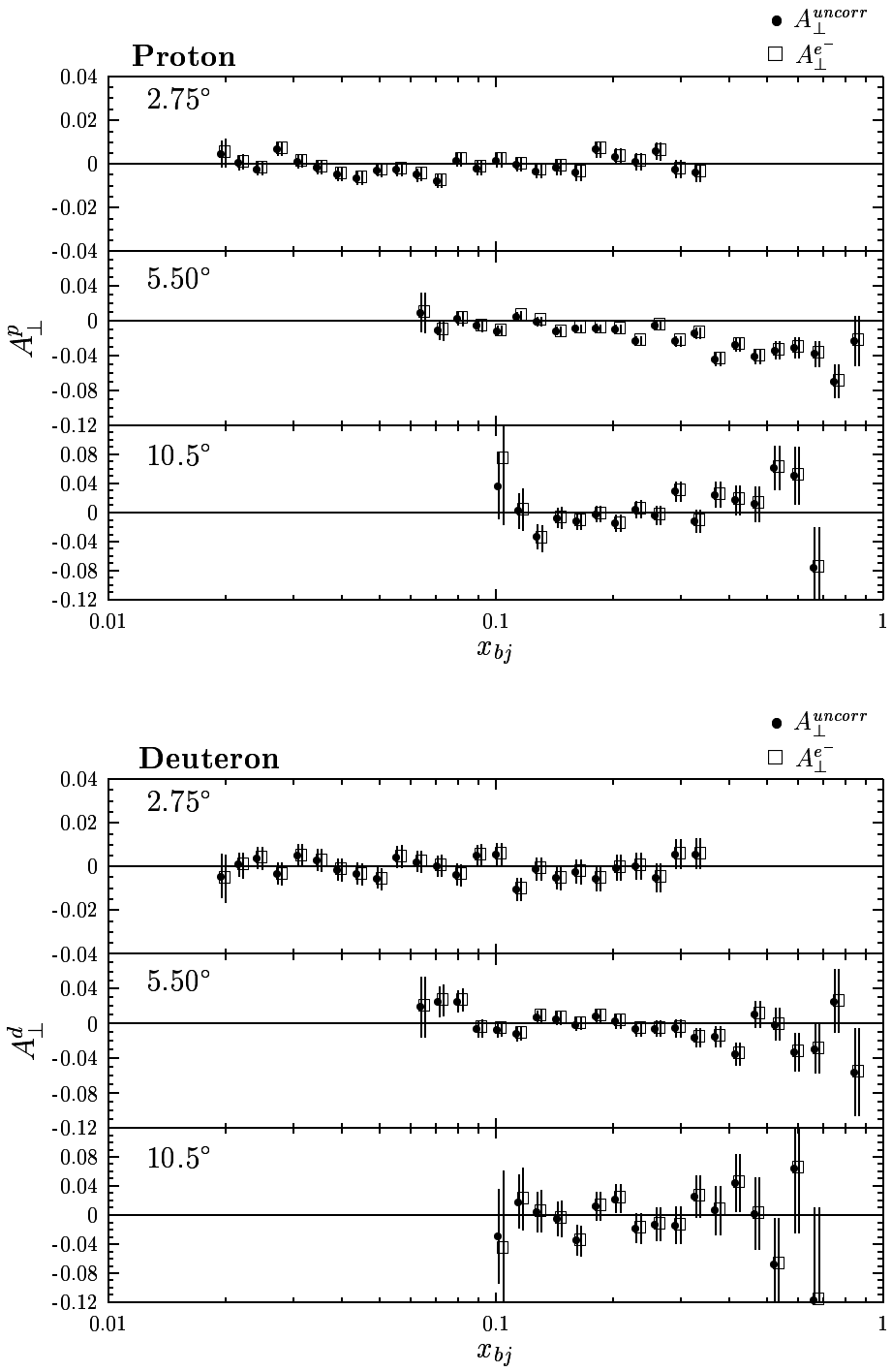

Figure 4.16: Effect of the background contamination correction on the measured asymmetry for the proton (top plot) and deuteron (bottom plot). Beam energies have been combined using a statistically weighted average. The x values for the background subtracted data points (squares) have been shifted by +2.5% for viewing clearity.

4.5.2 Radiative Corrections

The formalism developed in Chapter 2, used to relate the spin-dependent DIS structure functions to the perpendicular asymmetry, was based on the single photon exchange (Born level) process shown in Figure 2.1. This diagram together with knowledge of the incident beam energy and scattered electron energy and angle defines the kinematics at the vertex. However, modifications of these kinematics can occur as a result of radiative losses before or after the target scattering (known as 'external' radiative processes) and/or from higher-order, non-Born DIS interactions (known as 'internal' radiative processes). Thus, in order that the 'measured' perpendicular asymmetry be comparable with the first-order Born formalism, both internal and external radiative corrections must be applied to it.

The radiative losses incurred by the electron are primarily due to bremsstrahlung emissions as the electron traverses the extra target material located before and after the scattering event. The internal radiative effects, calculated to order α^3, include vertex corrections, vacuum polarization, and contributions from the tails of elastic and other inelastic peaks resulting from internal bremsstrahlung [80]. The Feynman diagrams representing these processes are shown in Figure 4.17.

The internally radiated asymmetry is expressed as

$$A_{int} \equiv \frac{(\sigma^{\downarrow,\Rightarrow} - \sigma^{\uparrow,\Rightarrow})_{int}}{(\sigma^{\downarrow,\Rightarrow} + \sigma^{\uparrow,\Rightarrow})_{int}} \equiv \frac{\sigma^p_{int}}{\sigma^u_{int}} = \frac{\sigma^p_{Born}(1+\delta_v) + \sigma^p_{el} + \sigma^p_{inel}}{\sigma^u_{Born}(1+\delta_v) + \sigma^u_{el} + \sigma^u_{inel}}, \tag{4.31}$$

where the p and u superscripts refer to polarized and unpolarized respectively, δ_v denotes the vertex and vacuum polarization corrections, and σ_{el} and σ_{inel} represent the corrections from internal bremsstrahlung. The fully radiated cross sections, σ^p_{rad} and σ^u_{rad}, (representing the quantities actually measured) were produced by applying the external corrections to σ^p_{int} and σ^u_{int} respectively. This was accomplished through

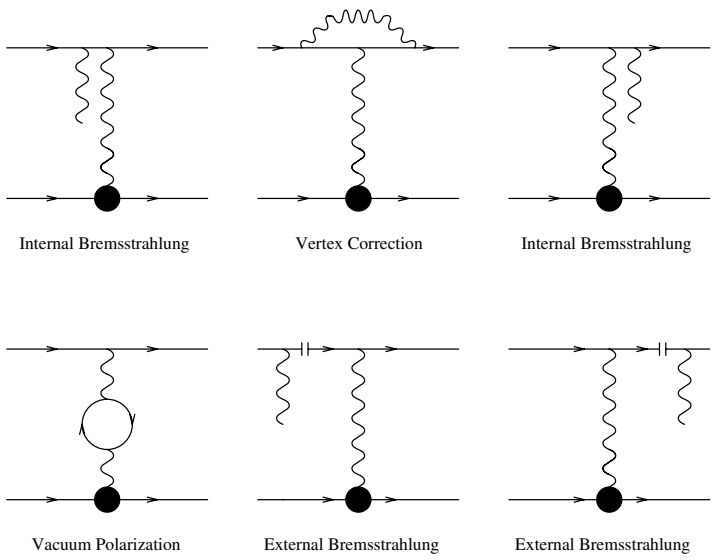

Figure 4.17: Feynman diagrams for internal and external processes considered in radiative corrections [81].

a convolution of the internally radiated cross section with the bremsstrahlung energy loss probabilities for traversing material before and after the primary scattering event[††] [82]. The fully radiated cross sections can then be used, together with the Born cross sections, to determine a single additive radiative correction:

$$\Delta A^{RC} \equiv A_{Born} - A_{rad} = \frac{\sigma^{p}_{Born}}{\sigma^{u}_{Born}} - \frac{\sigma^{p}_{rad}}{\sigma^{u}_{rad}}. \tag{4.32}$$

Since A_{Born} is the desired quantity and A_{rad} represents the experimentally measured asymmetry, Equation 4.32 can be re-written as

$$A_{Born} = A_{\perp}^{e^-} + \Delta A^{RC}. \tag{4.33}$$

Since the Born asymmetry was unknown, the code used to calculate the radiative

[††] Also considered in the calculation of σ^{p}_{rad} was the electron depolarization correction due to its emission of a photon before scattering.

corrections, known as RCSLACPOL (written by L. Stuart, modified by F. Wesselmann for E155, and then by K. Griffioen and S. Kuhn for E155x), required the use of an input model of A_{Born}. After calculating ΔA^{RC} (using the model of A_{Born}), the input model was compared with the radiatively corrected measured asymmetry; if they were not equal to each other, the input model was improved and the process was repeated. This procedure was iterated until the input model and the corrected asymmetry converged to better than 1%.

For the E155x radiative correction analysis, 26 different input models were evaluated and their results were compared with each other to provide an estimate of systematic uncertainties. The model that yielded the best estimate of the E155x radiative corrections was the one that used an E143 model for A_1, a rotated target model (which corrected for the target field misalignment–discussed in the next section) and g_2^{ww} with a 'realistic' twist-3 component obtained from fitting the E155x data.

Although the determination of ΔA^{RC} adequately corrects the measured asymmetry, it alone does not sufficiently account for the increased statistical uncertainty resulting from the correction. To properly propagate the statistical errors associated with this correction, ΔA^{RC} is split into two components: An additive term (A_{RC}–which does not impact the statistical error to first order) and a multiplicative factor (f_{RC}–which does impact the statistical error). The multiplicative correction is referred to as the radiative dilution factor because it corrects for the presence of additional unpolarized events beyond σ^u_{Born} which diluted the measurement. The two radiative correction terms are related to ΔA^{RC} through the expression

$$\Delta A^{RC} = \left(\frac{1}{f_{RC}} - 1\right) A_{rad} + A_{RC}, \tag{4.34}$$

and the final radiatively corrected measured asymmetry is written as

$$A_\perp(x) = \frac{1}{f_{RC}(x)} A_\perp^{e^-}(x) + A_{RC}(x). \tag{4.35}$$

The results for f_{RC} and A_{RC} averaged over the two beam energies for each spectrometer and target are shown in Figure 4.18. From the plots of f_{RC}, it can be seen that this correction effectively redistributes the number of events in a given bin resulting in an increase of the asymmetry at lower values of x. The effect of these correction factors on the measured asymmetry is shown in Figures 4.19 and 4.20. As expected from the plots of A_{RC}, the application of this correction shifts the 2.75° and 10.5° asymmetries to lower values while it shifts the 5.5° to higher values. The radiative dilution factor has the effect of increasing the statistical errors at low x. Of all the corrections applied to the measured asymmetry, the radiative corrections has the greatest impact; on average, the percent difference per x-bin between the asymmetry with and without radiative corrections is $\sim 40\%$ for $^{15}NH_3$ and $\sim 28\%$ for ^{6}LiD.

4.6 Target Field Misalignment and g_2 extraction

During the investigation of a strange Q^2 dependence of the E155x preliminary results for g_2, it was discovered that a slight misalignment of the target field from a purely transverse orientation could account for the irregularity. A subsequent evaluation of the precise target magnet orientation revealed that it was installed 2.4° off from perpendicular. The misalignment was the result of using the old (E143) survey locations of the four tooling balls located on top of the outer cryostat instead of the new ones that were determined at the Thomas Jefferson National Accelerator Facility

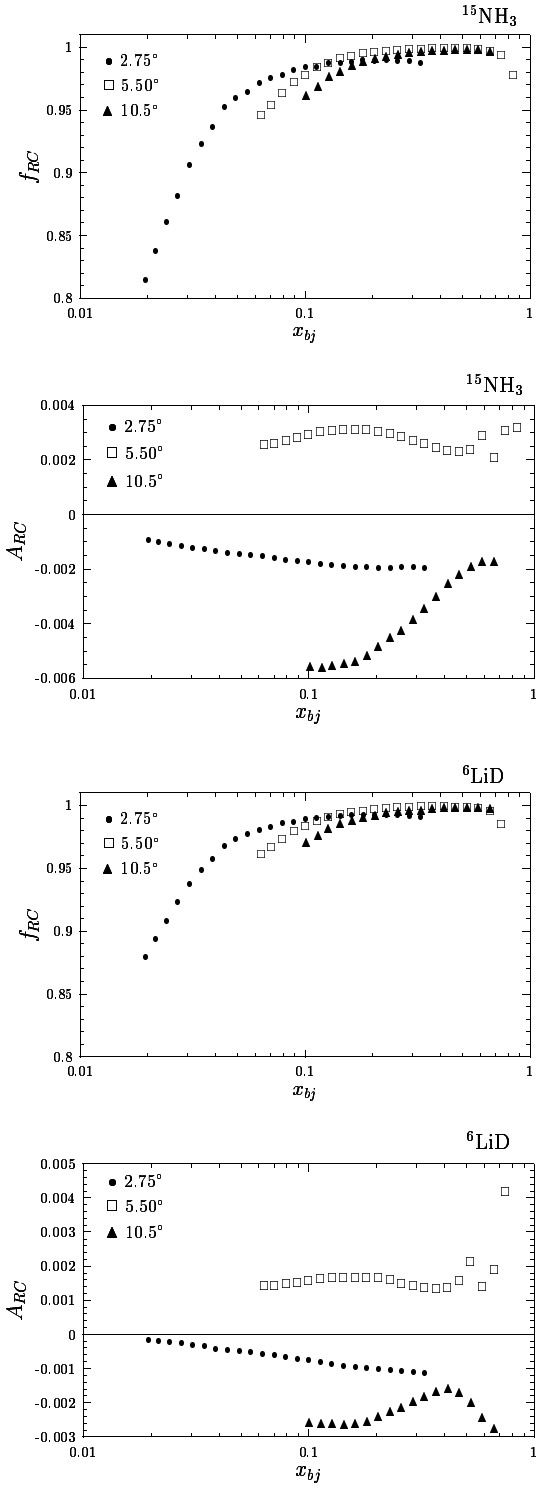

Figure 4.18: Radiative correction factors f_{RC} and A_{RC} for $^{15}NH_3$ (top plots) and ^{6}LiD (bottom plots).

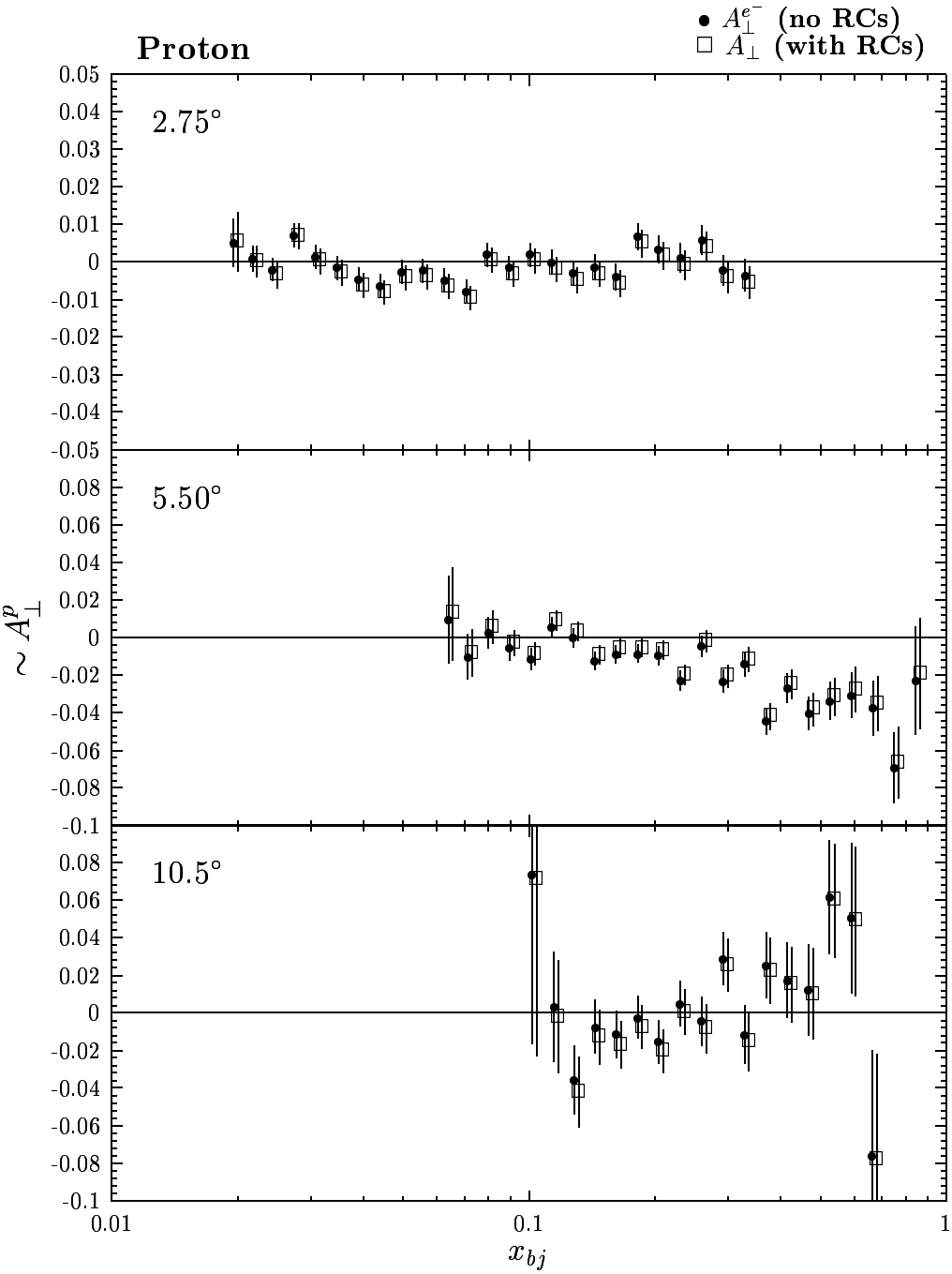

Figure 4.19: Effect of radiative corrections on the measured proton asymmetry. The x values for the radiatively corrected data points (squares) have been shifted by +2.5% for viewing clearity.

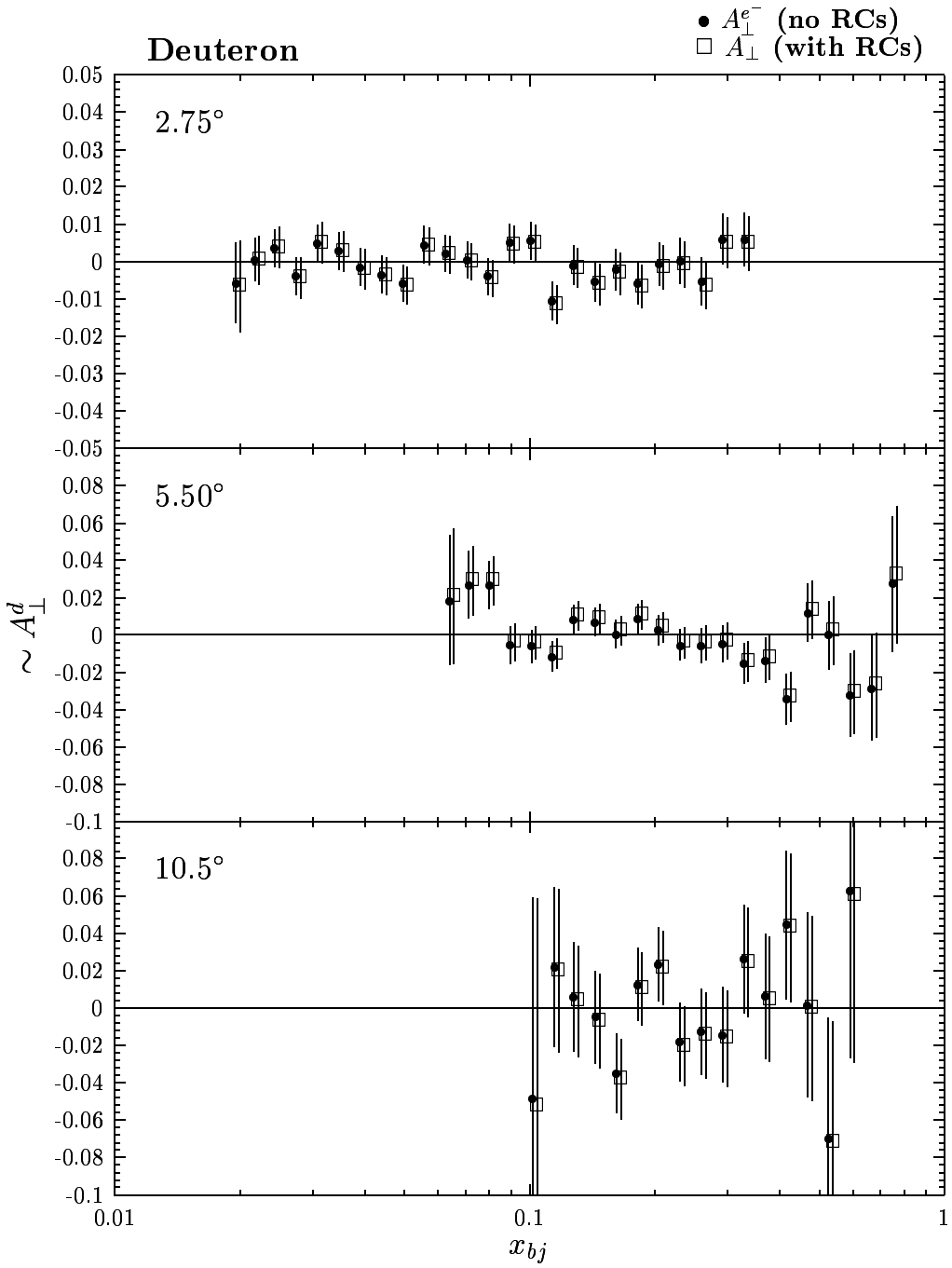

Figure 4.20: Effect of radiative corrections on the measured deuteron asymmetry.

(TJNAF) after the magnet was repaired due to an accident that occurred before it was shipped back to SLAC in late 1998.

As a result of the misalignment, there was a small contribution of the parallel asymmetry ($A_{\parallel}$) to the measured asymmetry. Figure 4.21 depicts the angular kinematics of this situation. Following the formalism laid out in Section 2.1.2, the angle between $\hat{S}$ and $\hat{k}$, denoted as α, is no longer $\frac{\pi}{2}$ or $\frac{3\pi}{2}$ but includes an additional $\pm\delta$. This means that Equation 2.14 no longer accurately describes the numerator of the measured asymmetry and that the full generalized expression of Equation 2.12 must be used. Using this equation, divided by twice the unpolarized cross section of Equation 2.9, the generalized expression for the measured asymmetry in the Born approximation is

$$A_{meas} = \frac{1-\epsilon}{\nu F_1(1+\epsilon R)}\left[(E'\cos\Theta + E\cos\alpha)g_1 + \frac{2EE'}{\nu}(\cos\Theta - \cos\alpha)g_2\right], \qquad (4.36)$$

where $\cos\Theta = \sin\theta\sin\alpha\cos\phi + \cos\theta\cos\alpha$ and use has been made of the expression for R (Equation 2.41) and the additional kinematic variables defined in Table 2.2.

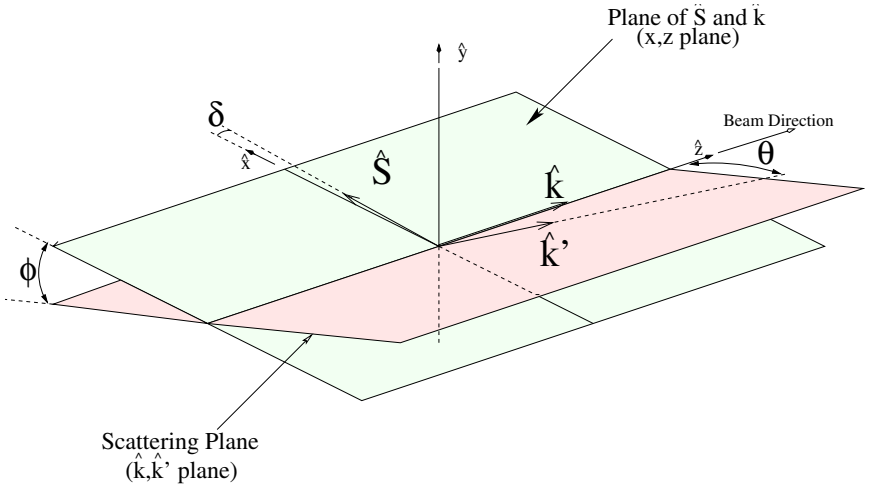

Figure 4.21: This figure displays the important kinematic angles for measuring g_2.

Re-arrangement of this equation to solve for g_2 yields the expression

$$g_2^{p,d} = \frac{\nu F_1^{p,d}}{2EE'(\cos\Theta - \cos\alpha)}\left[A_{meas}^{p,d}\frac{\nu(1+\epsilon R^{p,d})}{1-\epsilon} - \left(\frac{g_1}{F_1}\right)^{p,d}(E'\cos\Theta + E\cos\alpha)\right]. \tag{4.37}$$

This is the equation used to extract g_2 from the measured asymmetry ($A_\perp$ of Equation 4.35) using g_1/F_1 from the E155 phenomenological fits to world data [21, 22]

$$\left(\frac{g_1(x,Q^2)}{F_1(x,Q^2)}\right)^p = x^{0.70}(0.82 + 1.01x - 1.49x^2)\left(1 - \frac{0.037}{Q^2}\right), \tag{4.38}$$

$$\left(\frac{g_1(x,Q^2)}{F_1(x,Q^2)}\right)^d = x^{-0.34}(-0.013 - 0.33x + 0.76x^2)\left(1 - \frac{0.034}{Q^2}\right), \tag{4.39}$$

$F_1^{p,d}$ calculated from the 1995 NMC fits to $F_2(x,Q^2)^{p,d}$ [32], and $R^{p,d}$ from the 1998 SLAC fits [15].

To give a feel for these parameters, Figures 4.22 and 4.23 displays each of them for both the proton and deuteron at the average kinematics of all three spectrometers for both beam energies. A comparison of the results for g_2 with and without the slight target field rotation is given in Figures 4.24 and 4.25.

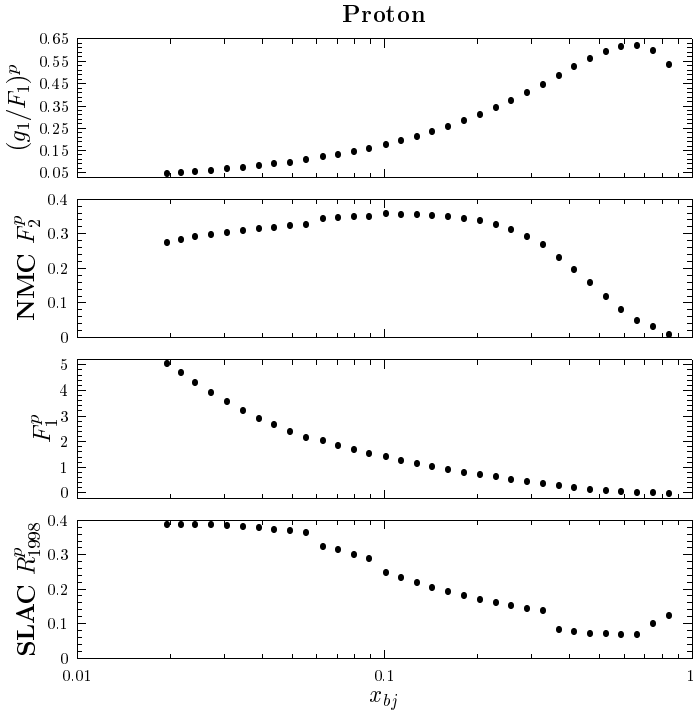

Figure 4.22: Parameters used in g_2^p extraction.

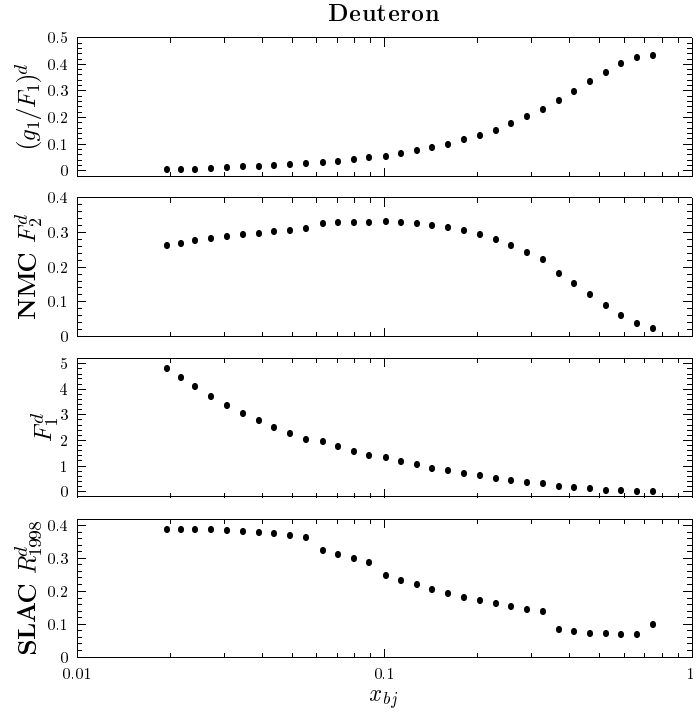

Figure 4.23: Parameters used in g_2^d extraction.

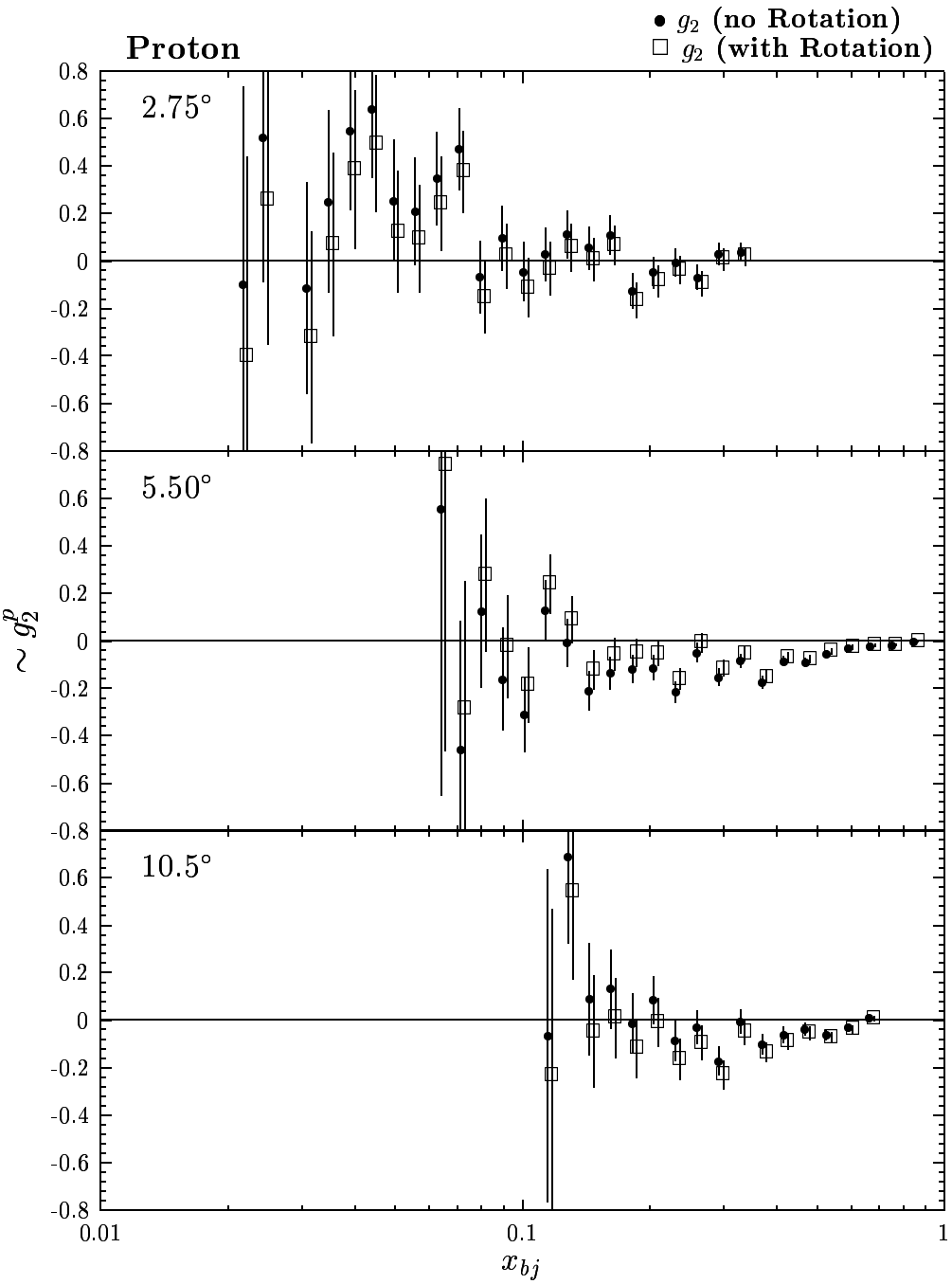

Figure 4.24: Effect of target field angle correction on g_2^p. The x values for g_2^p using the corrected target field orientation (squares) have been shifted by +2.5% for viewing clearity.

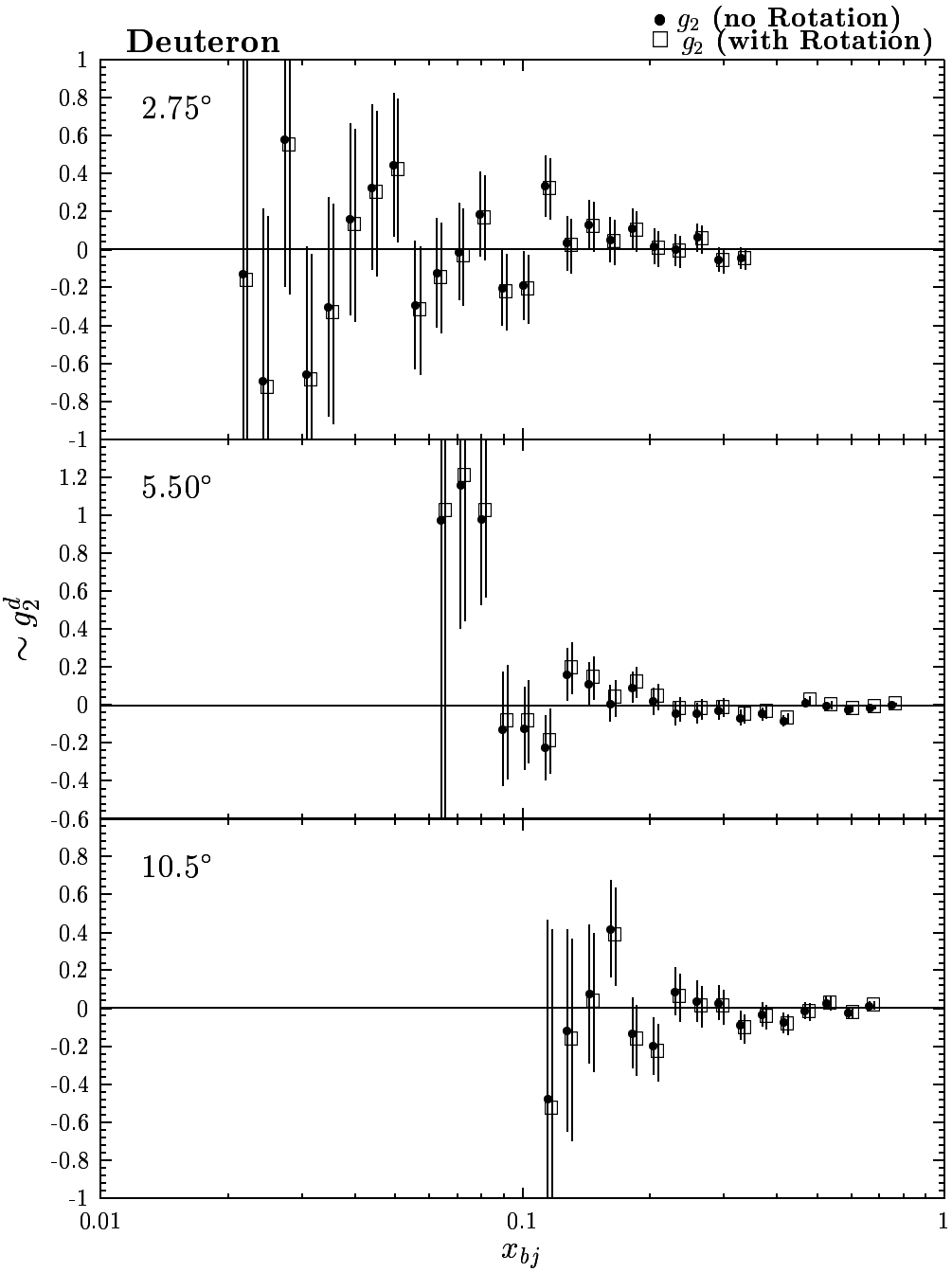

Figure 4.25: Effect of target field angle correction on g_2^d.

Chapter 5

Results

The final results from the E155x experiment for both the proton and deuteron are presented here. First, the final corrected measured asymmetries, produced by the analysis described in Chapter 4, are given both separately and combined for each beam energy. These results are then compared with the measured asymmetry produced by the collaboration's independent analysis. The fine-bin $g_2(x)$ and $xg_2(x)$ results are presented in various formats. These results are then re-binned into coarse ('world') x-bins using an evolution of the data to the common average Q^2 of each bin at each beam energy; the re-binned results are presented with E143 and E155 data and theoretical predictions. The Q^2 dependence of xg_2 is presented and compared with the Q^2 dependence of xg_2^{ww}. The results for $A_2(x)$ are given and compared with the positivity and Soffer limits as well as $A_2(x)$ calculated using g_2^{ww}. Finally, the results for the Burkhardt-Cottingham and Efremov-Leader-Terayev sum rules are given followed by the calculation of the twist-3 d_2 matrix element.

5.1 Measured Asymmetry

The final corrected results of the measured proton and deuteron asymmetry for each energy and spectrometer are shown in Figures 5.1 and 5.2. Note that the asymmetries are now labeled $\tilde{A}_\perp$ to reflect the fact that they contain a small contribution from their respective parallel asymmetries. It can be seen from these plots that the measured asymmetries at the two different energies are consistent with each other; the statistical errors for the 32 GeV values are smaller because more data was collected at this energy for each target. The asymmetries resulting from combining the data taken at the two beam energies, for the proton and the deuteron, are shown in Figures 5.3 and 5.4 respectively; the combined results were obtained using a statistical error weighted average. A comparison between these (student) measured asymmetries, and the asymmetries produced by the 'collaboration' analysis is shown in Figure 5.5. As can be seen, the results from the two independent analyses are in excellent agreement.

In these plots (as well as the measured asymmetry plots shown in the previous chapter), data is not displayed for all 38 x-bins of each spectrometer. Because of inadequate kinematic coverage at low values of x, significant numbers of events were not accumulated for bins $1-5$ in the 2.75°, $1-15$ in the 5.5°, and $1-19$ in the 10.5°. Furthermore, for this same reason, data in the last two bins in the 10.5° were omitted from the results as was the last data point for the 5.5° deuteron results. For the 2.75°, data collected at high x was omitted because of the spectrometer's poor momentum resolution for events accumulated beyond bin 30. Tables of the $\tilde{A}_\perp$ data for the proton and deuteron for each beam energy and spectrometer are given in Appendix A and B. The total multiplicative systematic error on $\tilde{A}_\perp$, calculated by adding the beam polarixation, target polarization, and dilution factor errors in quadrature, was ~ 5.2 % for the proton and ~ 6.7 % for the deuteron.

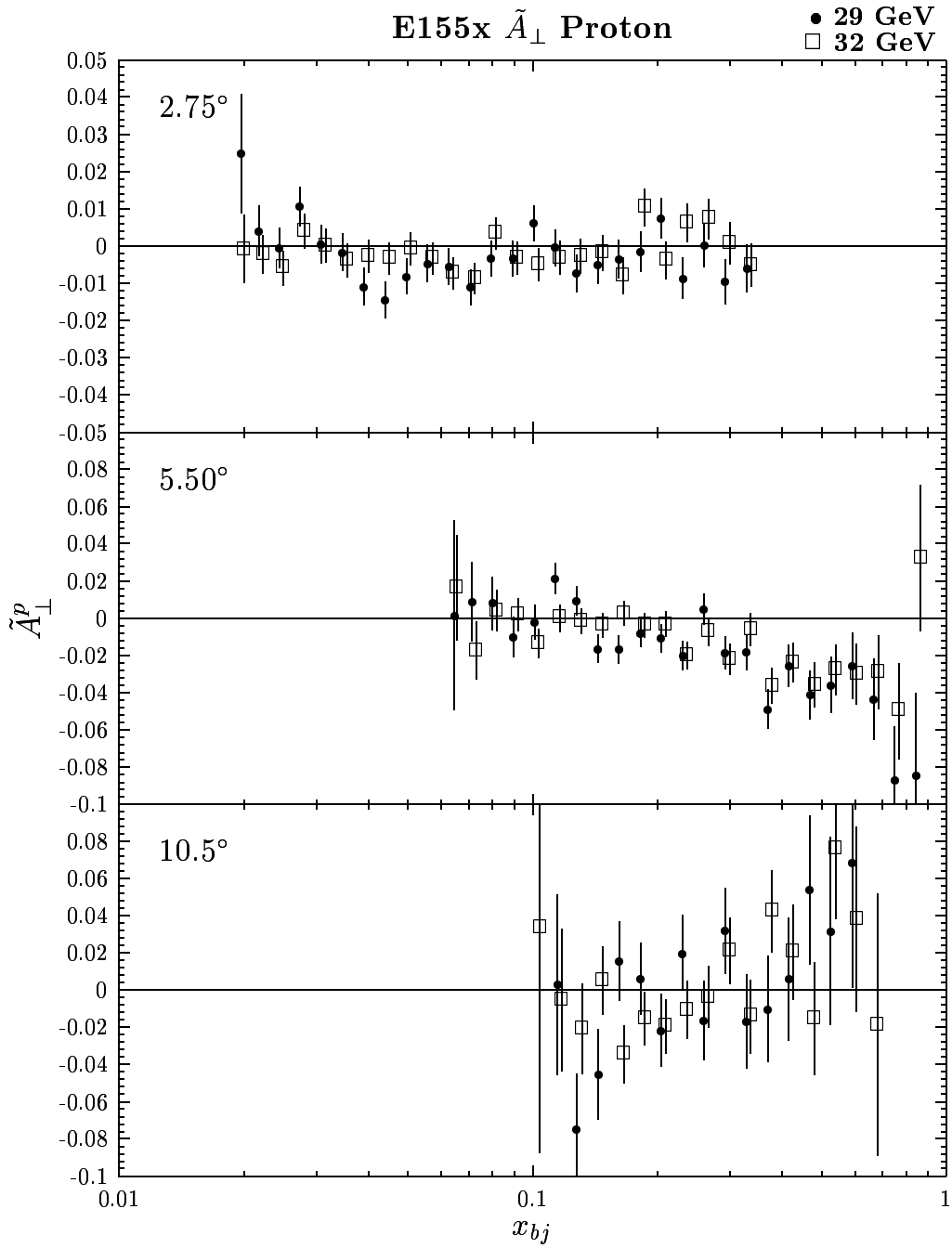

Figure 5.1: Comparison of E155x proton $\tilde{A}_\perp$ for the two beam energies. The x values for the 32 GeV data (squares) have been shifted by +2.5% for viewing clarity.

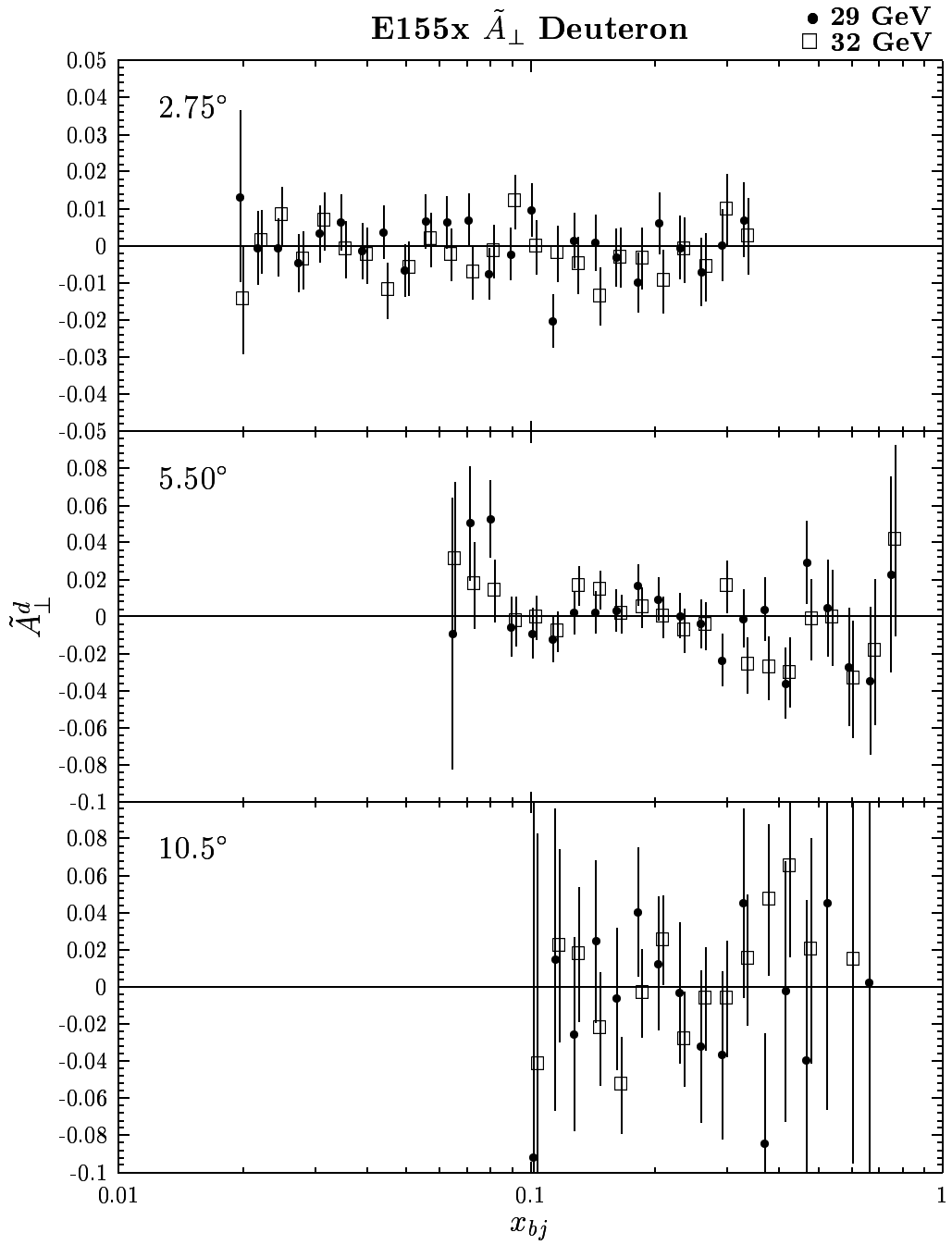

Figure 5.2: Comparison of E155x deuteron $\tilde{A}_\perp$ for the two beam energies.

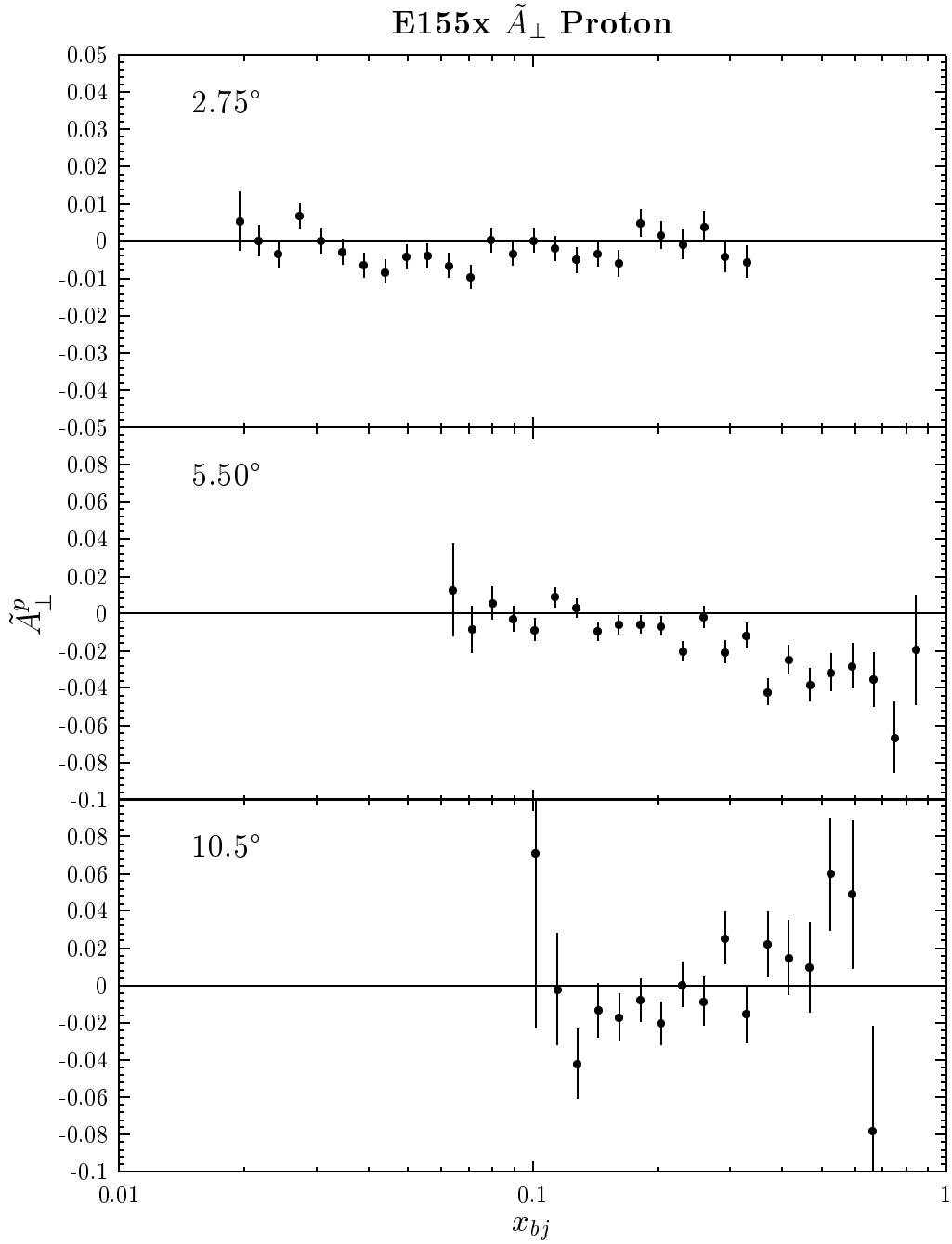

Figure 5.3: E155x proton $\tilde{A}_\perp$ combined for the two beam energies using a weighted average.

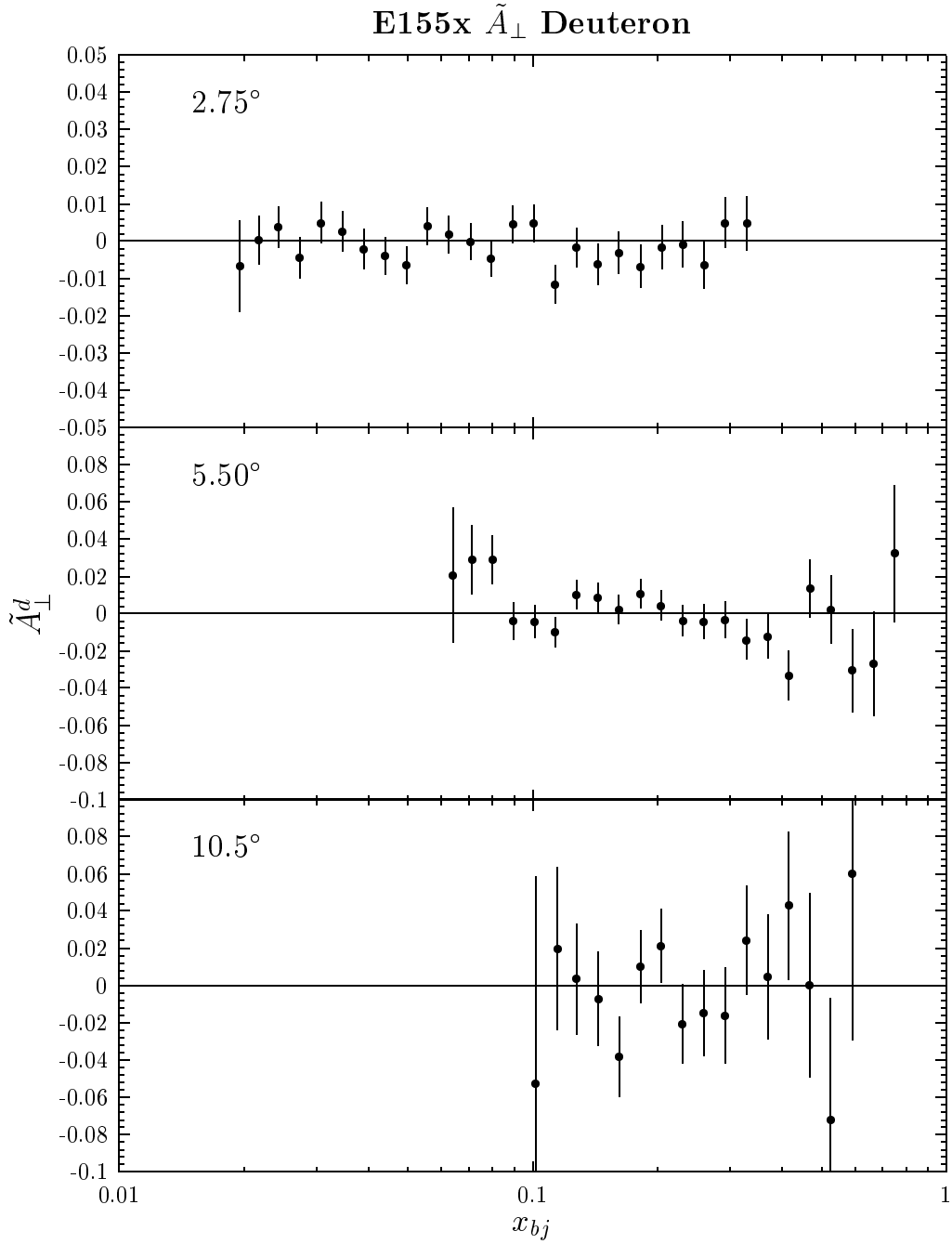

Figure 5.4: E155x deuteron $\tilde{A}_\perp$ combined for the two beam energies using a weighted average.

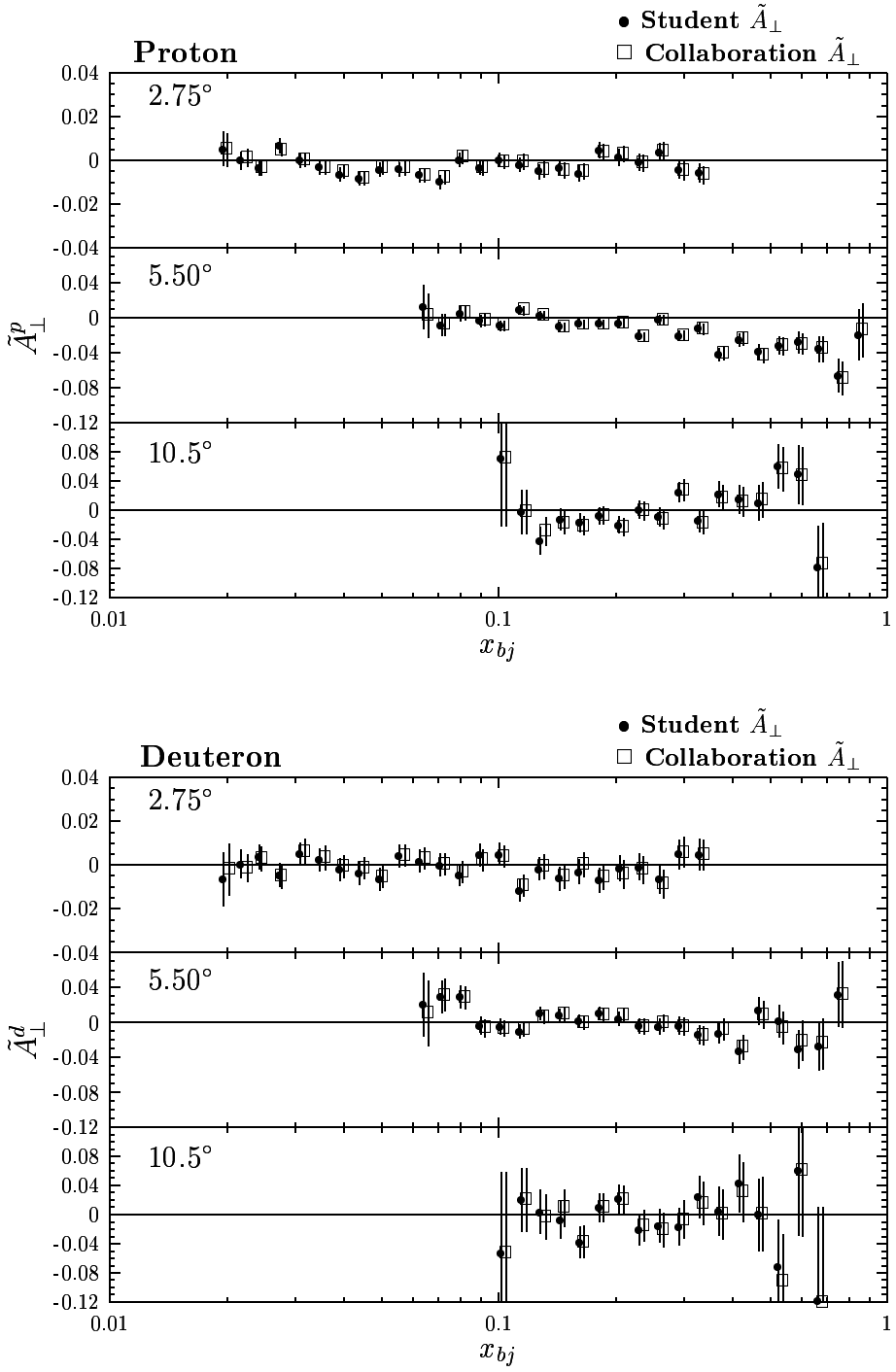

Figure 5.5: Comparison between the 'student' and 'collaboration' $\tilde{A}_\perp$ for the proton (top plot) and deuteron (bottom plot). The x values for the 'collaboration' data (squares) have been shifted by +2.5% for viewing clarity.

5.2 g_2 Structure Function

The results for $g_2(x)$ and $xg_2(x)$ of the proton for each spectrometer are shown in Figures 5.6 and 5.7. Figures 5.8 and 5.9 display the same plots for the deuteron. The calculation of the structure functions was performed using Equation 4.37 presented in Section 4.6. Again, the data in these plots have been combined for beam energies using just a weighted average. The spectrometer combined results for $g_2^{p,d}(x)$ are shown in Figure 5.10, and those of $xg_2^{p,d}(x)$ are shown in Figure 5.11. The data in these plots are simply the average of the data presented in the previous plots for all spectrometers (with no evolution of the data to a common Q^2 for each bin). Values of the xg_2 data for the proton and deuteron for each beam energy and spectrometer are given in the tables located in Appendix A and B.

The plots of $xg_2(x)$ are shown with a calculation of $xg_2^{ww}(x)$ at the same kinematics for comparison. The g_2^{ww} calculation was performed using Equation 2.75 with g_1 solved from the differential equation

$$g_1(x,Q^2)^{p,d} = \frac{A_1(x,Q^2)^{p,d}F_1(x,Q^2)^{p,d} + \gamma^2 \int_x^1 \frac{g_1(x',Q^2)^{p,d}}{x'}dx'}{1+\gamma^2}, \tag{5.1}$$

using the E155 phenomenological world data fit to A_1

$$A_1(x,Q^2)^p = 0.861x^{0.64}(1+0.487x-0.225x^2)\left(1-\frac{0.16}{Q^2}\right), \tag{5.2}$$

$$A_1(x,Q^2)^d = 2.579x^{1.48}(1-1.994x+1.424x^2)\left(1-\frac{0.20}{Q^2}\right), \tag{5.3}$$

and $F_1^{p,d}$ calculated from the NMC fit to $F_2^{p,d}$ [32]. As discussed in Section 2.5, g_2^{ww} is the twist-2 (only) approximation to g_2. As can been seen, the x-dependence of the data agree quite well with that of g_2^{ww}. However, there appear to be statistically signif-

icant differences in size, possibly indicating that higher twist (twist-3) contributions to g_2 are important. This subject will be further addressed in Section 5.5.

Figure 5.12 displays the final evolved, world-binned results for xg_2 of the proton and deuteron shown with E143 and E155 data, xg_2^{ww}, and theoretical predictions. The average x values for the 10 world bins are given in Table 5.1. The following procedure was used in the production of these plots. First, before combining the data for each spectrometer and beam energy, the structure function in each fine bin was evolved to a value corresponding to the average Q^2 of each fine bin. Then, the spectrometer and beam-energy combined fine-bin data was evolved to the average Q^2 of its corresponding world bin, and finally the result was rebinned. The evolution of the data was performed using the Q^2 dependence of g_2^{ww}. To obtain the value of g_2 at the average Q^2 of each bin (Q^2_{avg}), the following calculation was performed

$$g_2(Q^2_{avg}) = g_2(Q^2_{init}) - g_2^{ww}(Q^2_{init}) + g_2^{ww}(Q^2_{avg}), \tag{5.4}$$

where Q^2_{init} was the initial value of Q^2 before the evolution.

From the plot of xg_2^p in Figure 5.12, it can be seen that the E155x data clearly

x-bin	Bjorken x range
1	$0.018 - 0.023$
2	$0.023 - 0.029$
3	$0.029 - 0.047$
4	$0.047 - 0.075$
5	$0.075 - 0.120$
6	$0.120 - 0.193$
7	$0.193 - 0.310$
8	$0.310 - 0.498$
9	$0.498 - 0.700$
10	$0.700 - 0.900$

Table 5.1: Bjorken x ranges of 10 world x-bins.

distinguishes between xg_2^{ww} and zero. The bag model calculation of Stratmann is in good agreement with the data while that of Song is in clear disagreement. The chiral soliton calculations appear to be too negative around $x = 0.4$. For the plot of xg_2^d, the distinction between the E155x data, xg_2^{ww}, and zero is less obvious; in fact, the precision of this data only allows a distinction from zero around $x = 0.4$. Both the proton and deuteron systematic errors were calculating by adding in quadrature the radiative correction errors, the error on g_1, the error due to the target polarization direction, the error on F_2, and the error on R. The result followed approximately the linear form $a + bx$ where $a_p(a_d)$= 0.0016(0.0009) and $b_p(b_d)$= −0.0012(−0.0009).

A plot of the Q^2 dependence of $xg_2^{p,d}$ is given in Figure 5.13 along with that of E143 and E155 data. The Q^2 dependence of g_2^{ww} and the bag model calculation of Stratmann for the proton and deuteron are also shown for comparison. From this plot, the quantity and precision of the data are not yet at the level needed to make meaningful comparisons with theory. The data approximately follow the Q^2 dependence of g_2^{ww}, but are perhaps closer to the predictions of Stratmann.

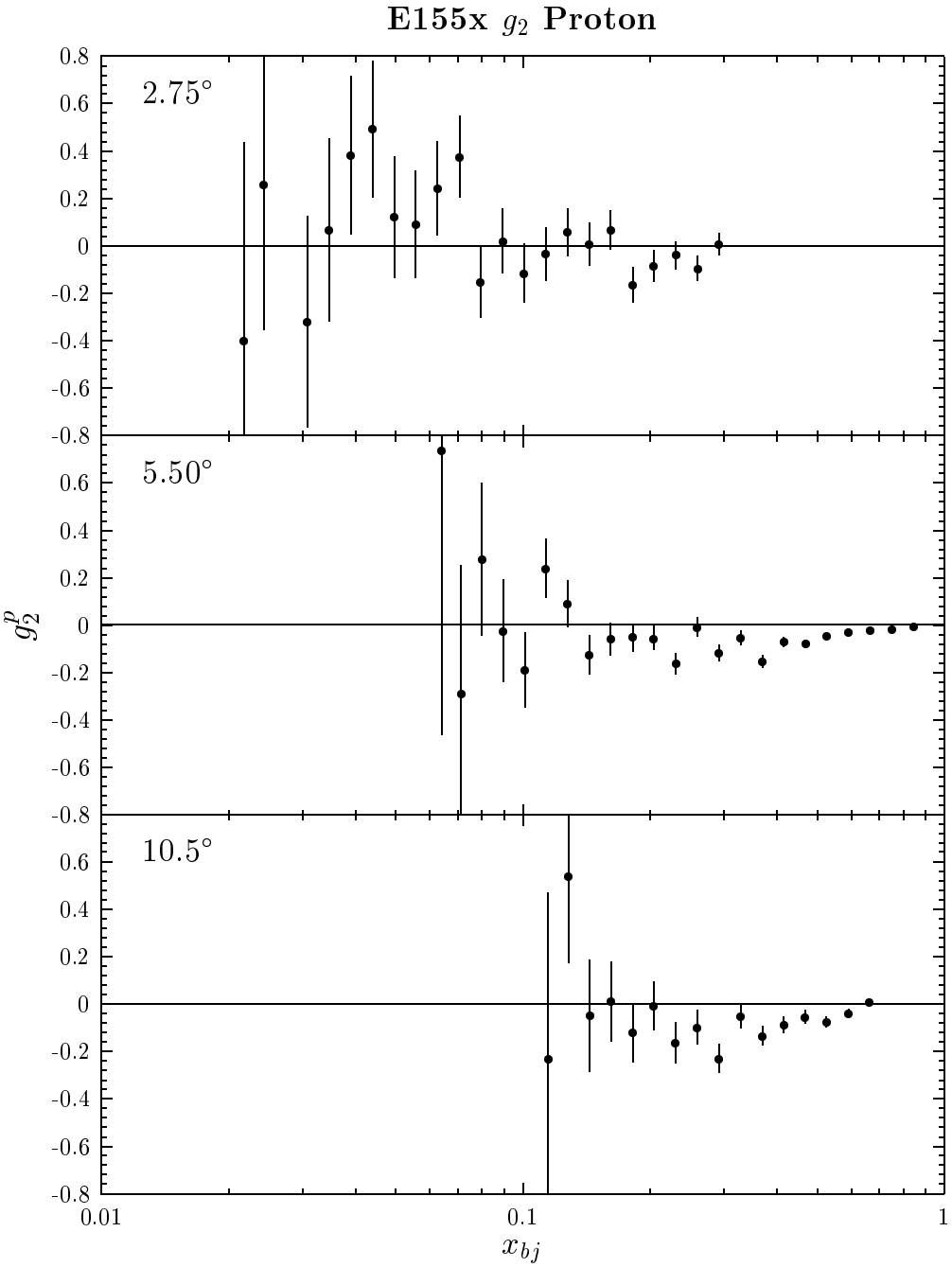

Figure 5.6: Beam energy combined E155x proton g_2 per spectrometer.

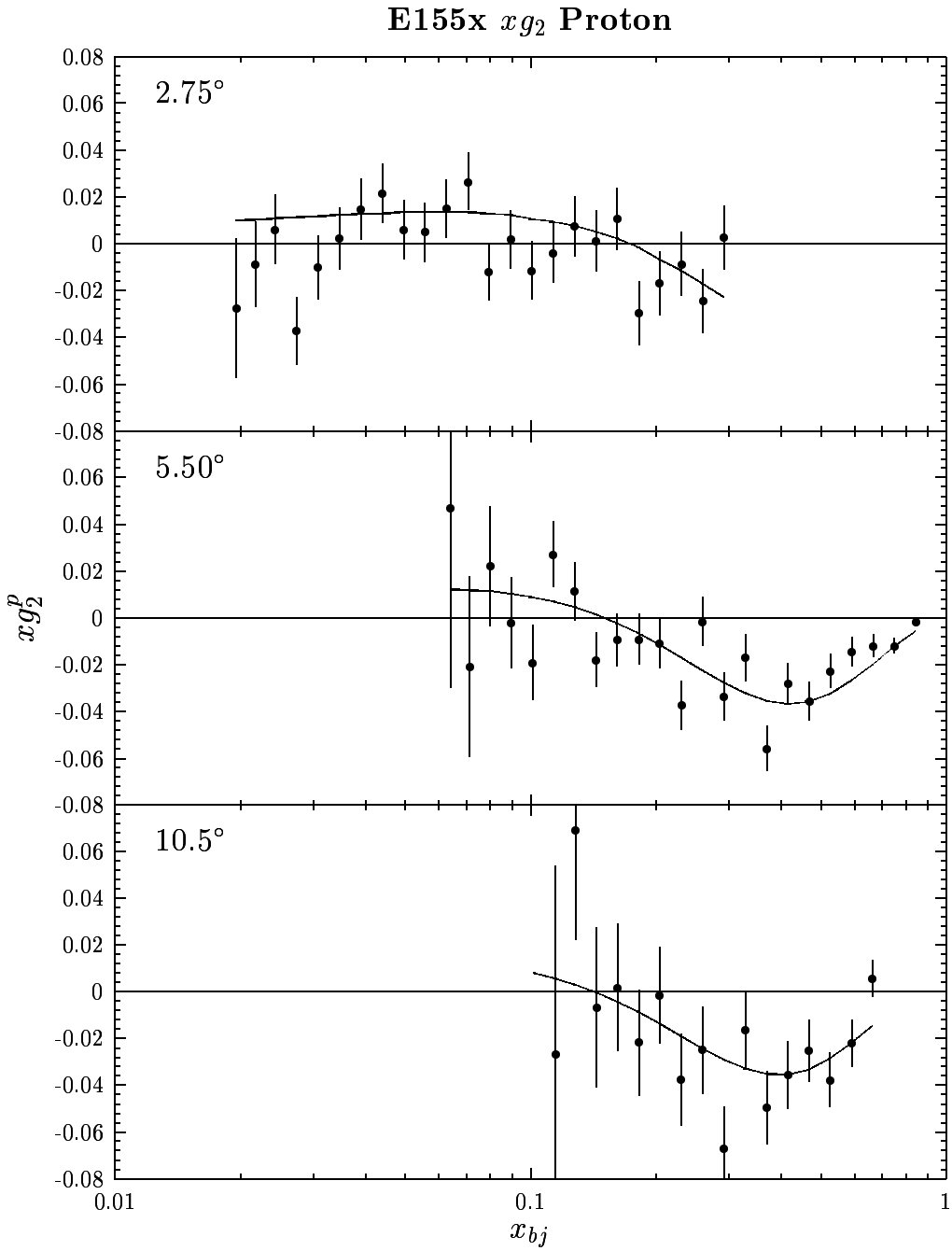

Figure 5.7: Beam energy combined E155x proton xg_2 per spectrometer. The solid line is xg_2^{ww} for the proton calculated at the average Q^2 of each bin.

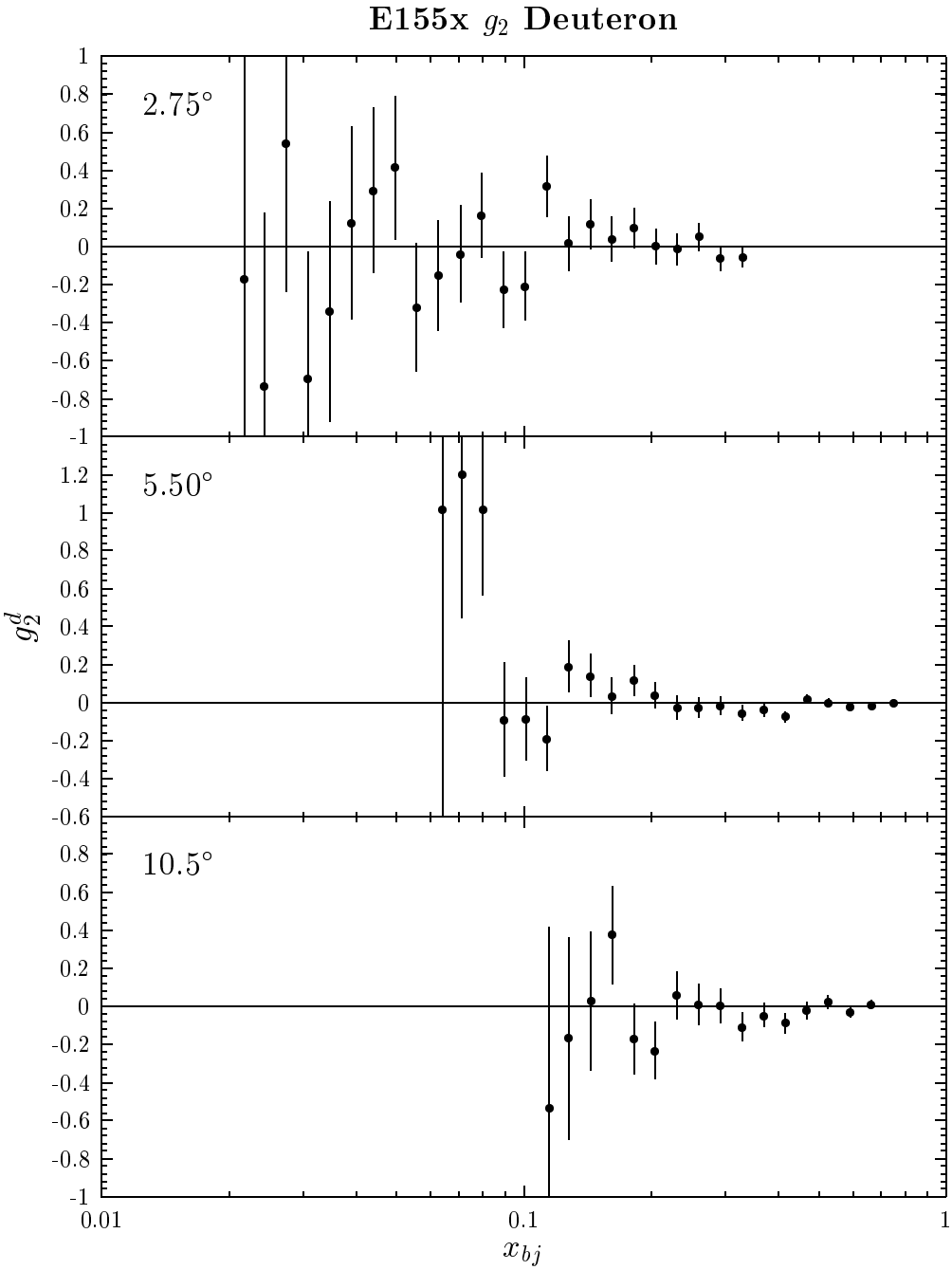

Figure 5.8: Beam energy combined E155x deuteron g_2 per spectrometer.

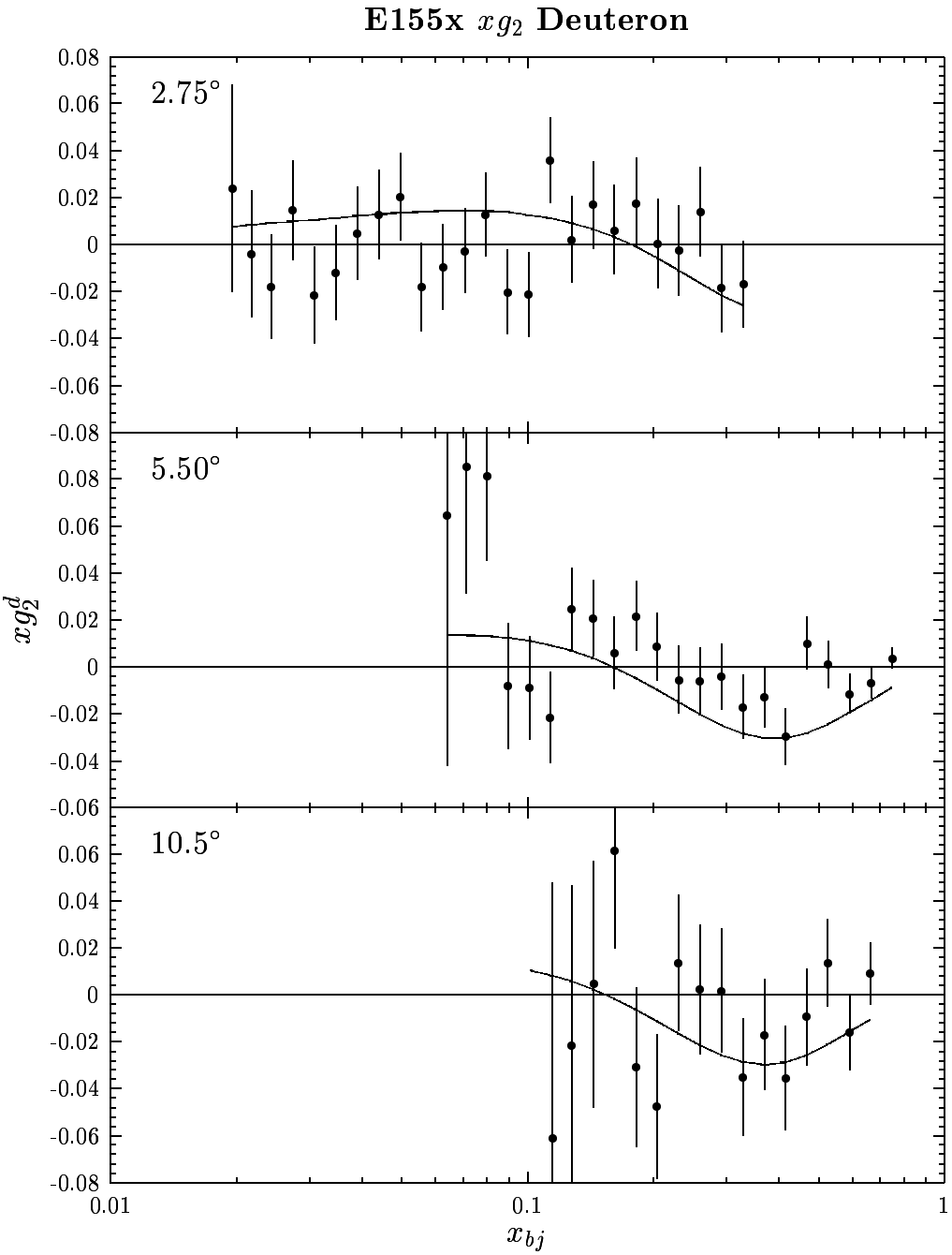

Figure 5.9: Beam energy combined E155x deuteron xg_2 per spectrometer. The solid line is xg_2^{ww} for the deuteron calculated at the average Q^2 of each bin.

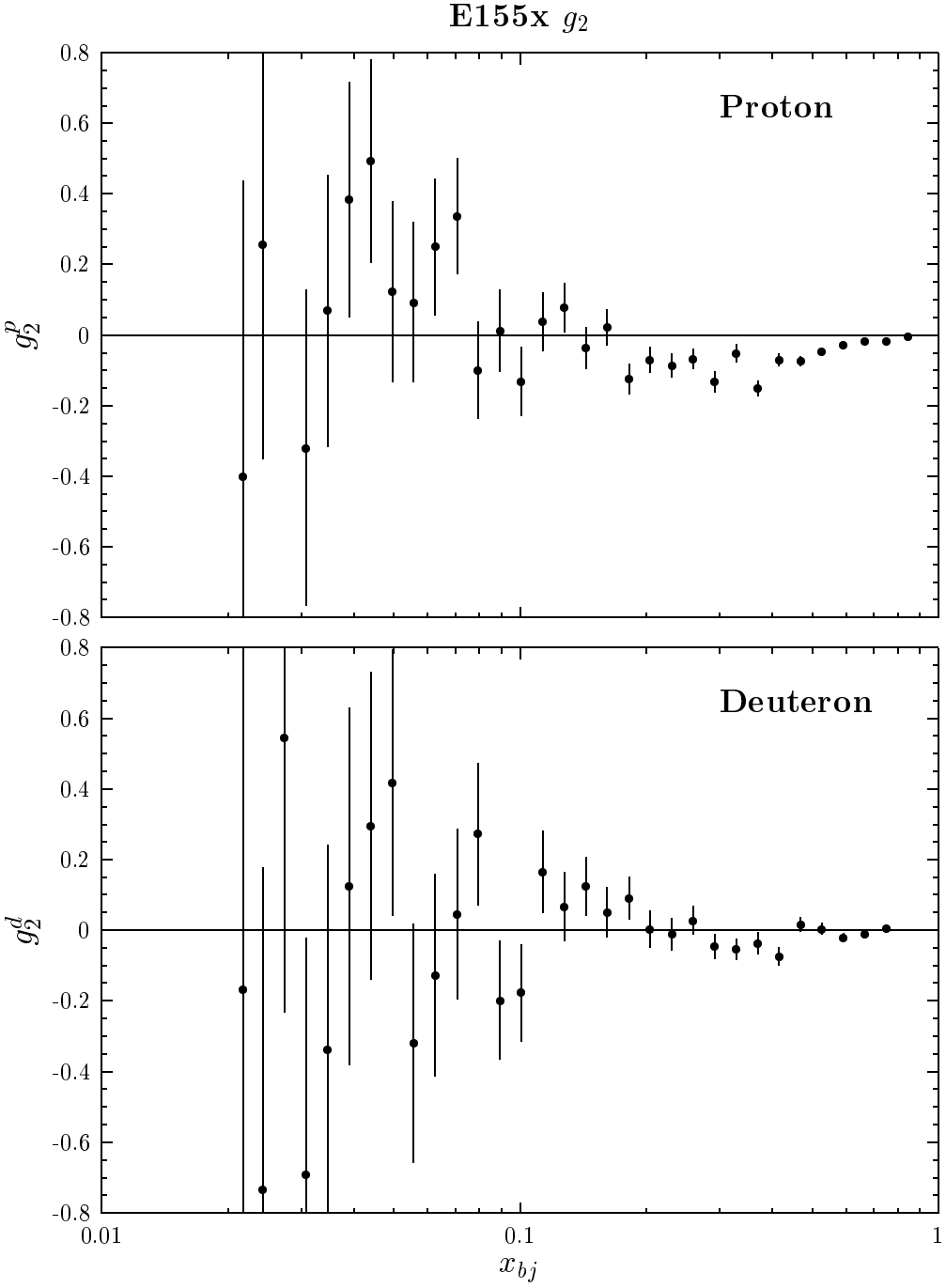

Figure 5.10: g_2^p and g_2^d combined for all spectrometers.

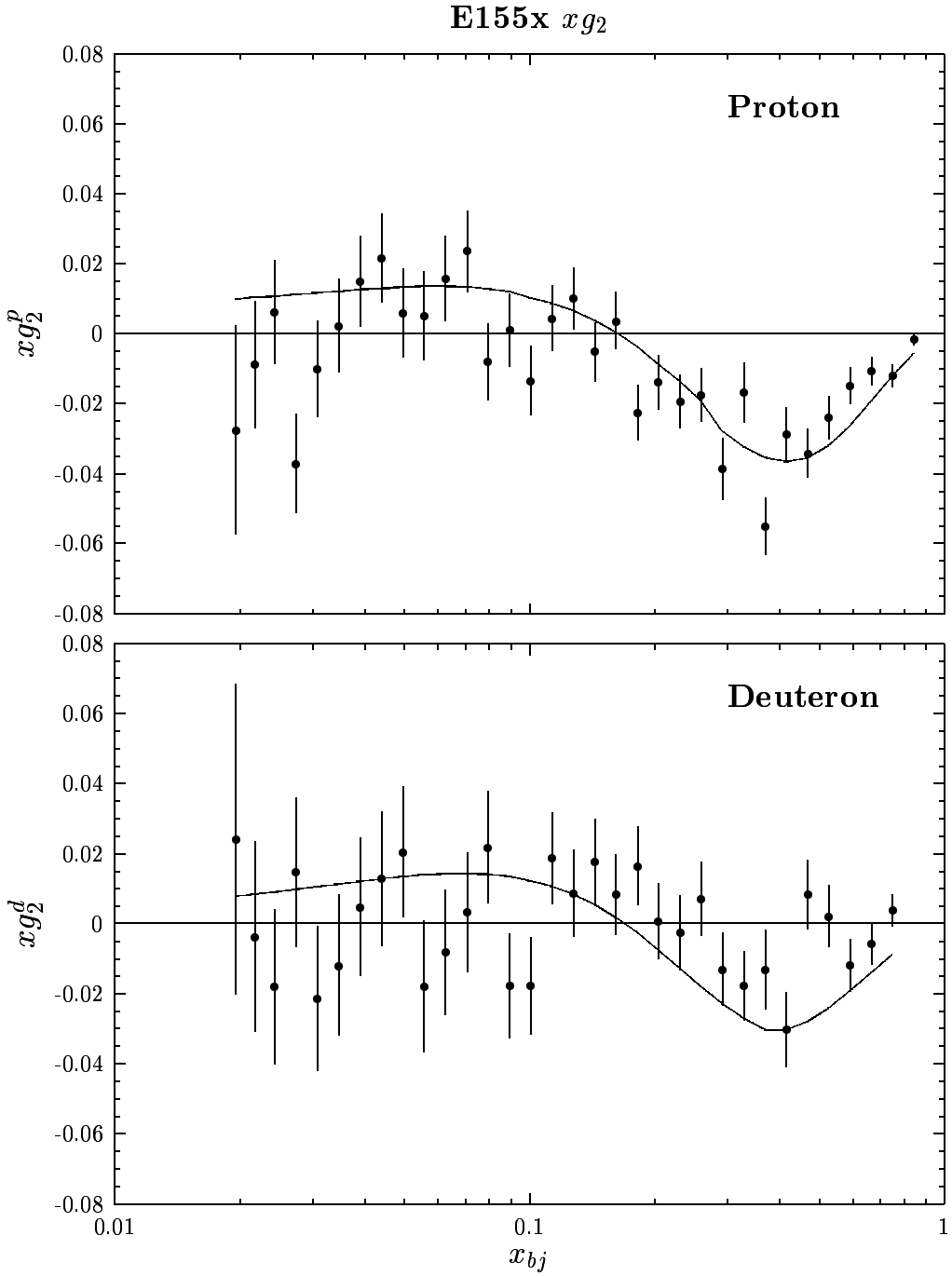

Figure 5.11: xg_2^p and xg_2^d combined for all spectrometers shown with respective xg_2^{ww} calculations.

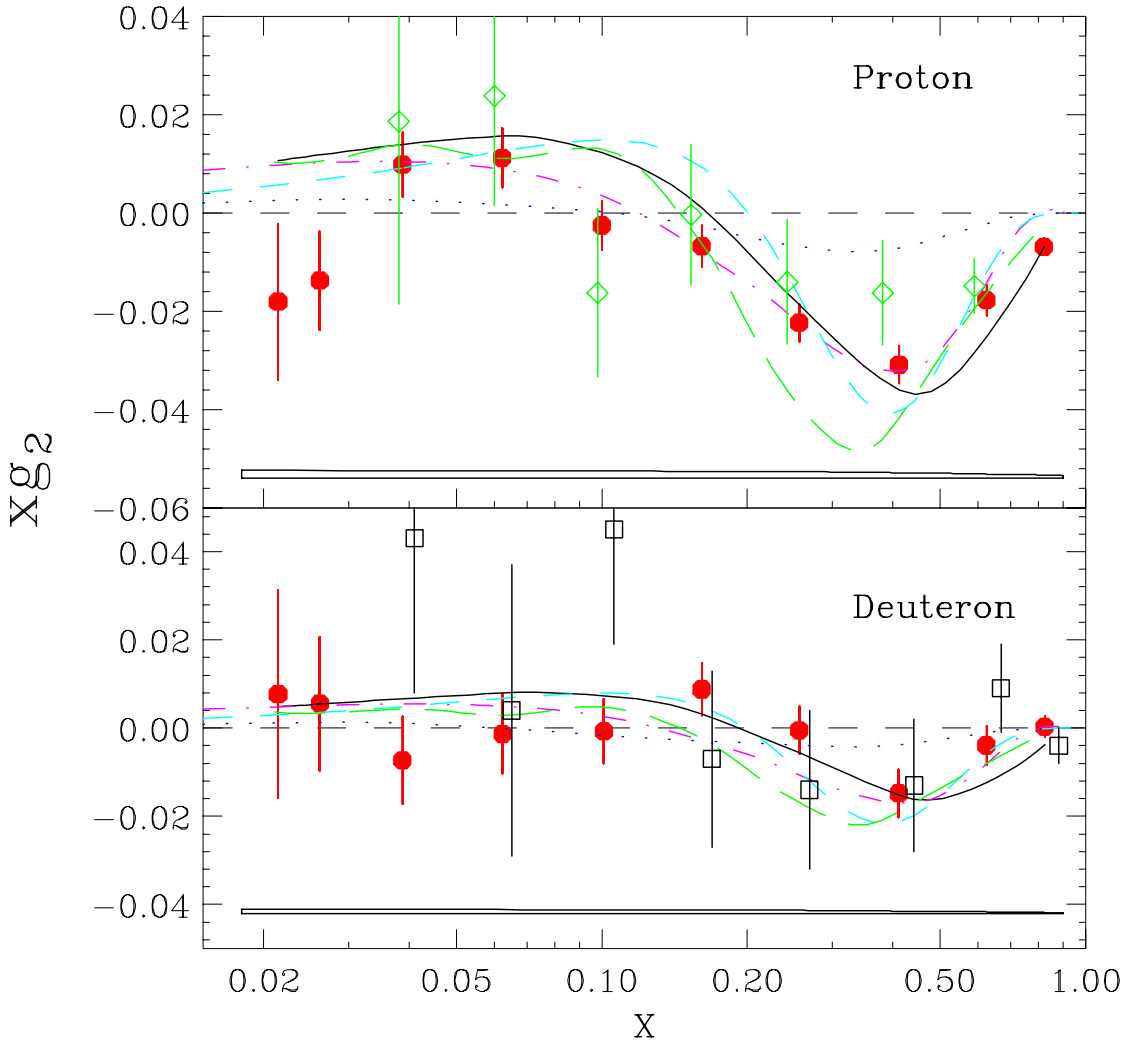

Figure 5.12: $xg_2^{p,d}$ structure function results, evolved to common Q^2 and rebinned to world bins for all spectrometers and both beam energies, shown with E143 [13] (open diamonds) and E155 [21, 22] (open squares) data. Also shown are the calculations of xg_2^{ww} at the common Q^2 of each x-bin (solid line), the chiral soliton models of Weigel and Gamberg [34] (short dash) and Wakamatsu [35] (long dash), and the bag model calculations of Stratmann [36] (dash-dot) and Song [37] (dot). The systematic errors are shown at the bottom of the plots.

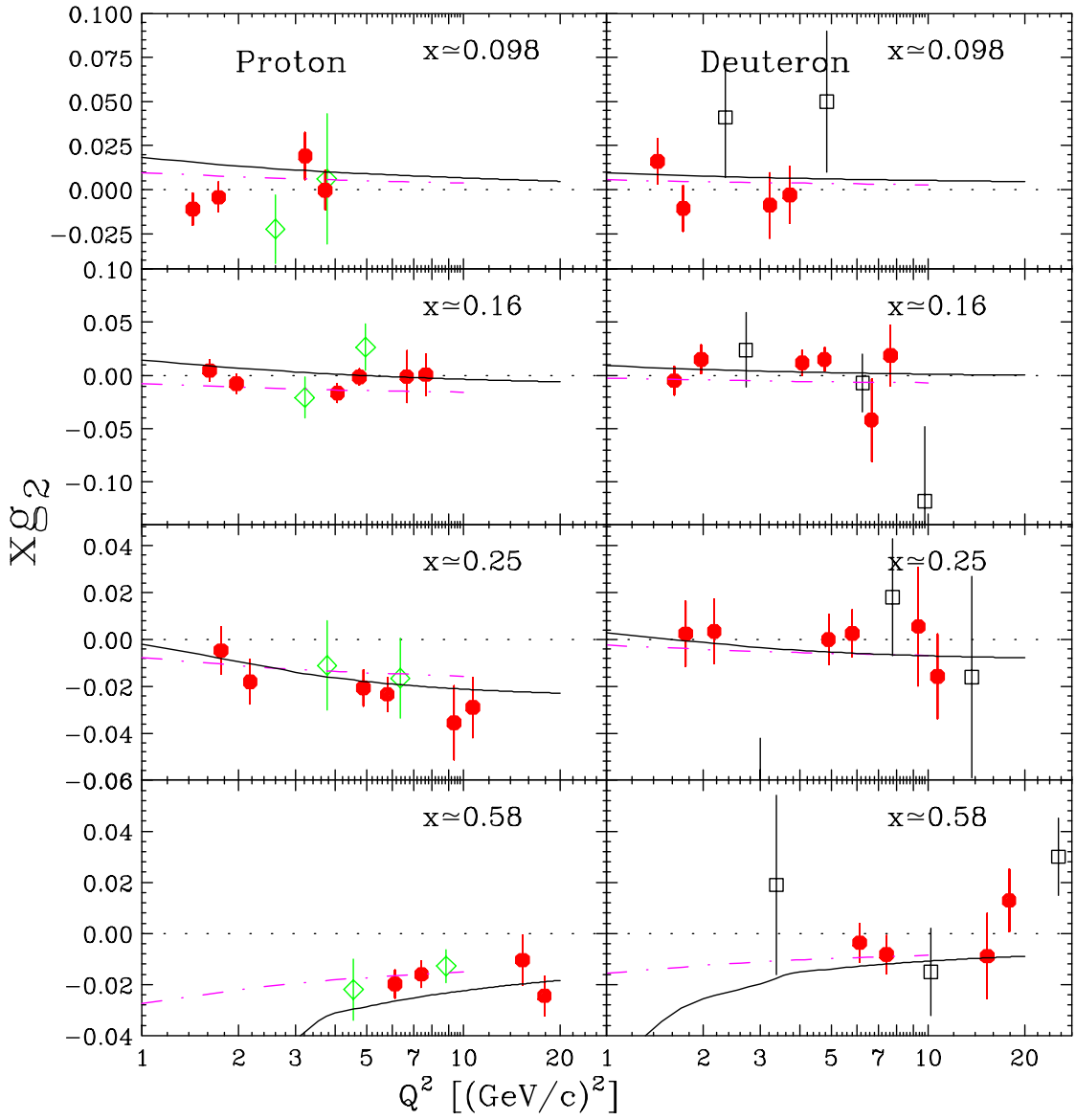

Figure 5.13: Q^2 dependence of xg_2^p and xg_2^d at selected values of x. Data points shown are from E155x (circles), E143 [14] (diamonds), and E155 [19] (squares). The solid and dashed curves show the Q^2 dependence of g_2^{ww} and the g_2 model of Stratmann [36] respectively.

5.3 Virtual Photon Asymmetry A_2

The results of $A_2^{p,d}$ for each spectrometer, combined for the two beam energies using a weighted average, are shown in Figures 5.14 and 5.15. $A_2^{p,d}$ is calculated using

$$A_2^{p,d} = \gamma \left(\frac{g_1}{F_1} \right)^{p,d} + \frac{g_2^{p,d}}{F_1^{p,d}}, \tag{5.5}$$

where g_1/F_1 is from the E155 phenomenological fit, g_2 is from the E155x calculation, and F_1 is calculated from the NMC fit to F_2. Figure 5.16 shows these same two graphs compared with the positivity and Soffer limits (for a discussion of these limits, refer to Section 2.2.1). As can be seen, most of the data is well below its theoretical upper-limit. Only one or two of the highest x-bin data points in the 5.5° and 10.5° are in violation of the limits; however, within statistical errors, all points satisfy the bounds. The spectrometer combined results of $A_2^{p,d}$, with no evolution of the data to a common Q^2, are given in Figure 5.17. Tables of the A_2 data for the proton and deuteron for each beam energy and spectrometer are given in the Appendices. The systematic errors on A_2 were small and determined from the same sources listed for xg_2.

The final evolved, rebinned results for $A_2^{p,d}$ are given in Figure 5.18. Also shown in this plot is the E143, E155, and SMC data as well as A_2 calculated using g_2^{ww}. Again, the E155x data was evolved using the Q^2 dependence of g_2^{ww}. From the plot of A_2^p, it can be seen that the value of the asymmetry is consistent with zero at low x and clearly positive at high x. It can also be seen to be significantly below the Soffer limit for all x. The plot of A_2^d is consistent with zero for all but the last few points at high x, however, it still generally follows the positive trend of the A_2 calculation (solid line in Figure 5.18).

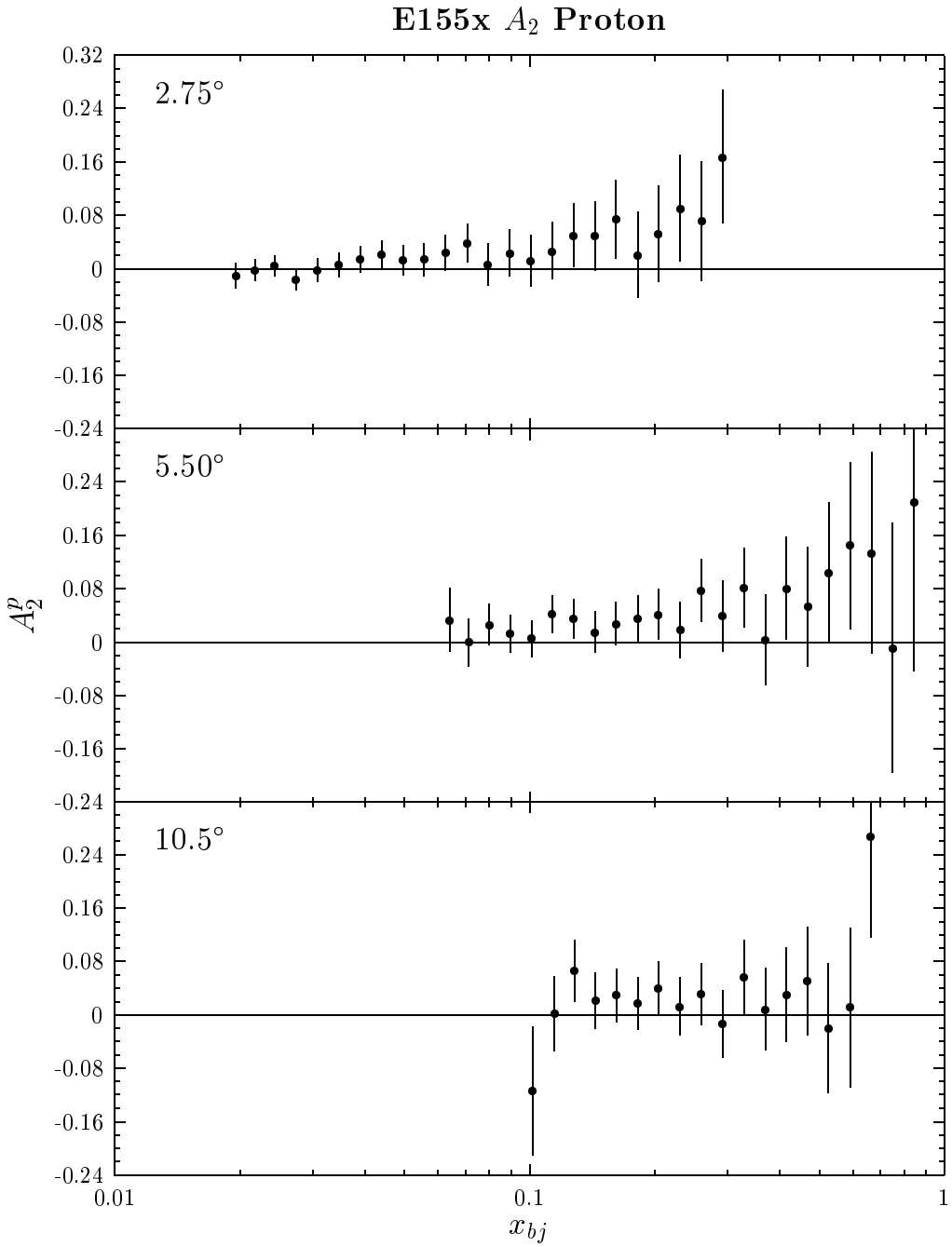

Figure 5.14: Beam energy combined E155x proton A_2 per spectrometer.

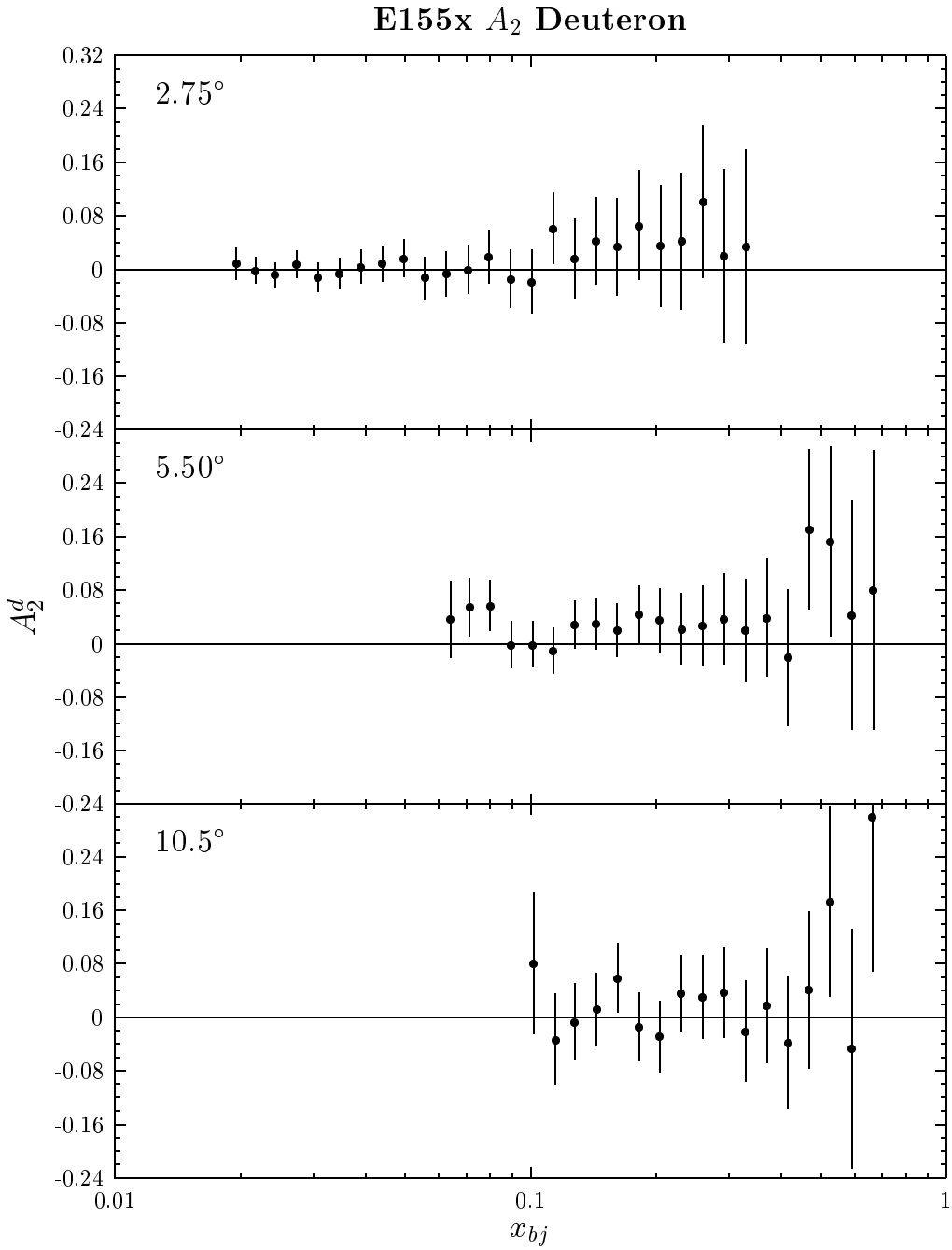

Figure 5.15: Beam energy combined E155x deuteron A_2 per spectrometer.

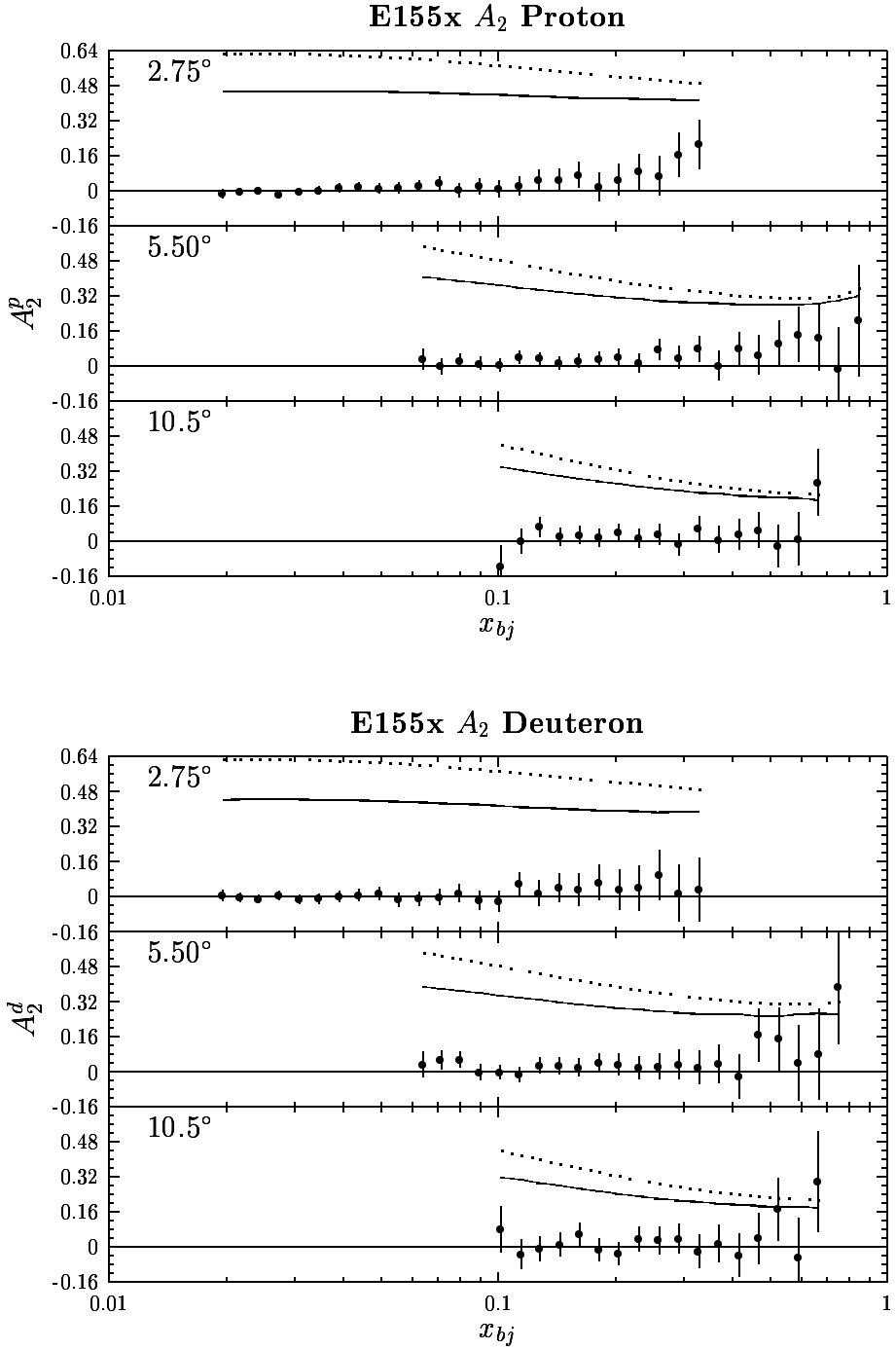

Figure 5.16: A_2 compared to positivity (dotted line) and Soffer (solid line) limits for the proton (top plots) and deuteron (bottom plots) for each spectrometer. Data for two beam energies has been combined using a weighted average.

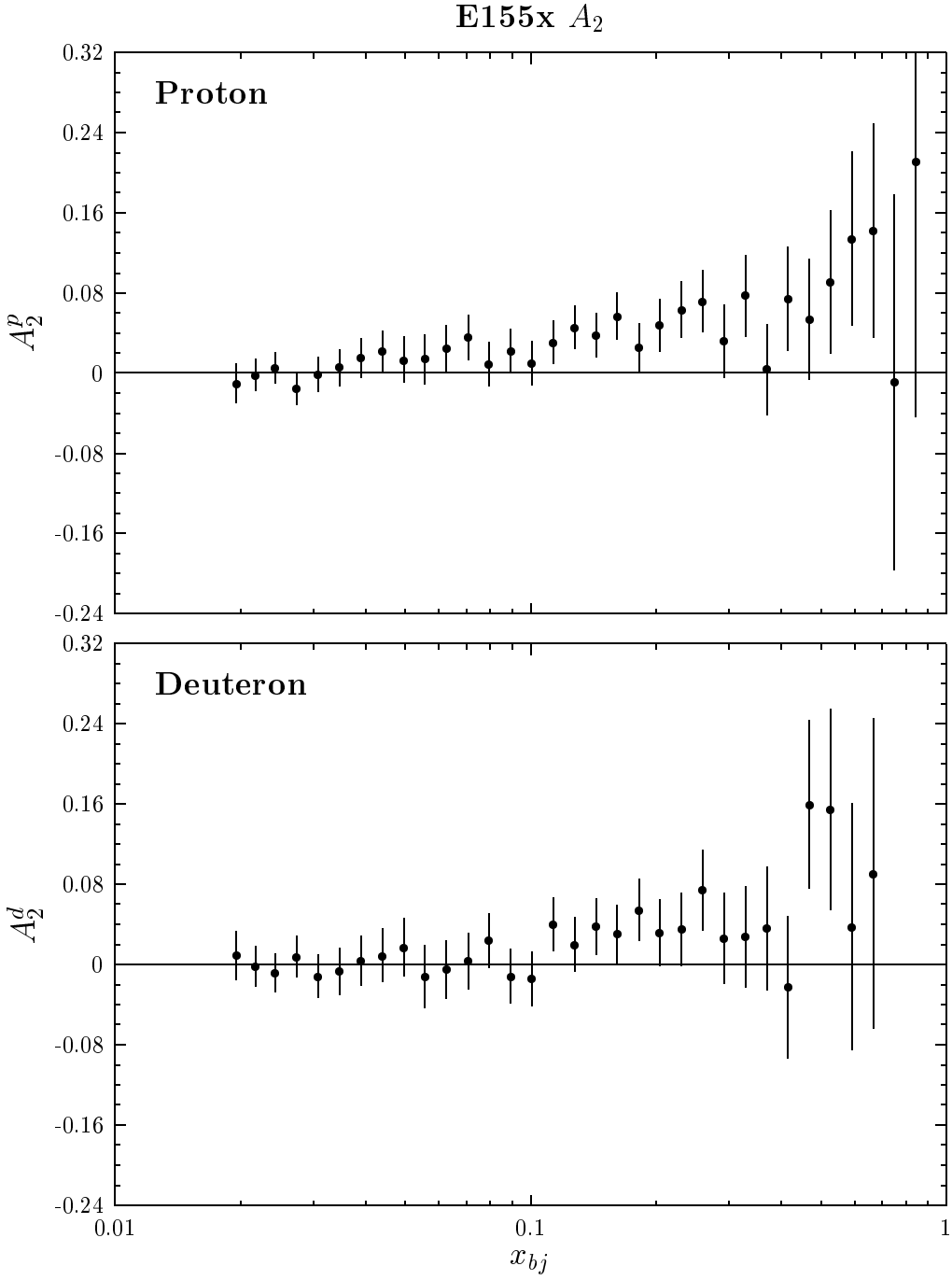

Figure 5.17: A_2^p and A_2^d combined for all spectrometers.

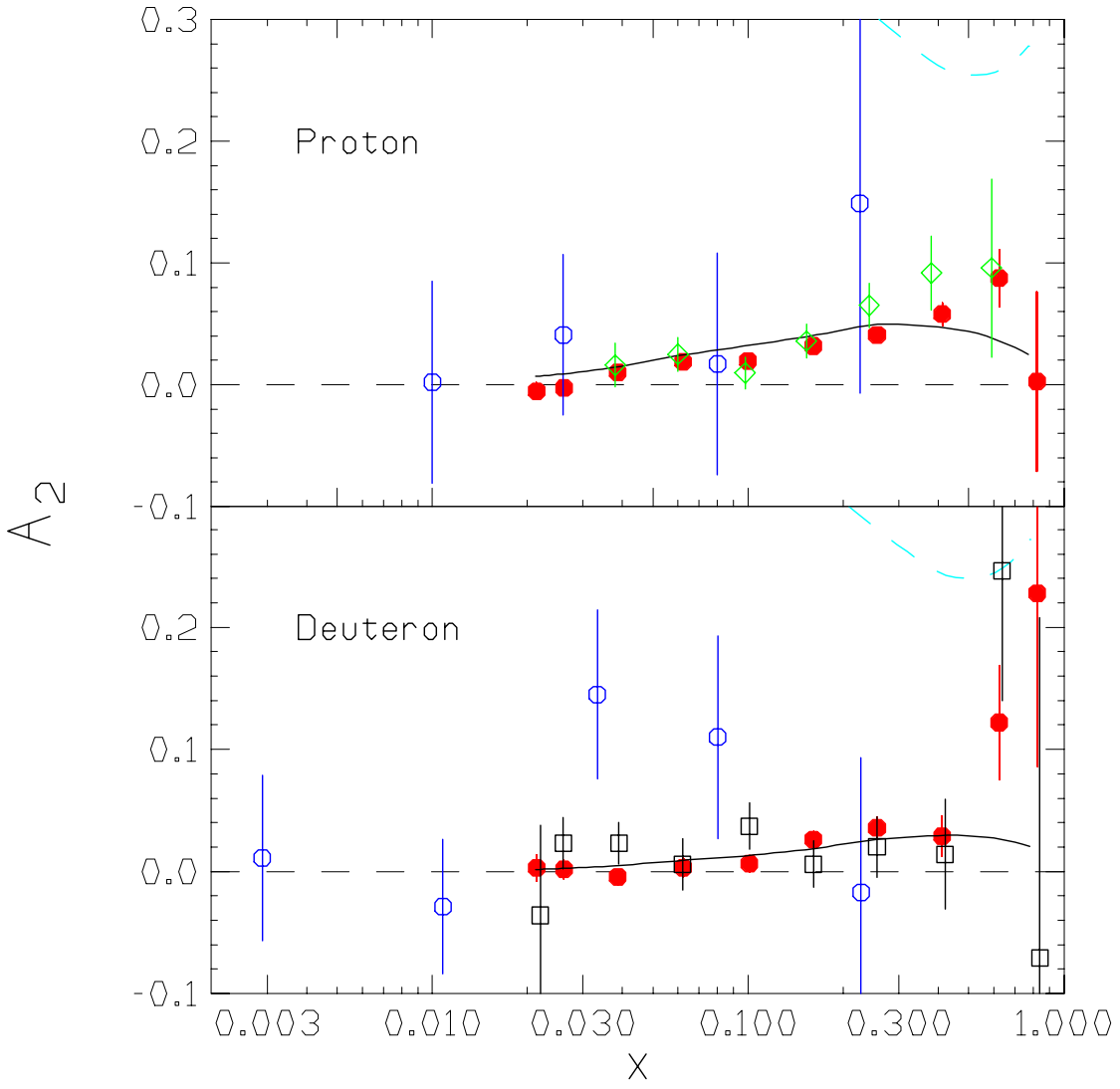

Figure 5.18: $A_2^{p,d}$ results, evolved to common Q^2 and rebinned to world bins for all spectrometers and both beam energies, shown with E143 [13] (open diamonds), E155 [20] (open squares), and SMC [7, 8] data. Also shown is the calculation of A_2 using g_2^{ww} at the common Q^2 of each x-bin (solid line). The Soffer limits are the dashed curves in the upper right part of the graphs.

5.4 Sum Rules

The sum rules discussed in Section 2.6 were evaluated in the measured region $0.02 \leq x \leq 0.8$ at an average evolved Q^2 of 5 $(\mathrm{GeV/c})^2$. The data was evolved in a manner similar to the procedure outlined in Section 5.2 using the Q^2 dependence of g_2^{ww}. That is,

$$g_2(x,5) = g_2(x,Q^2_{exp}) - g_2^{ww}(x,Q^2_{exp}) + g_2^{ww}(x,5), \tag{5.6}$$

where Q^2_{exp} was the original average Q^2 of each x-bin for the experiment. The results of the Burkhardt-Cottingham (BC) and Efremov-Leader-Terayev (ELT) sum rules are presented below.

The BC sum rule states that the first moment of the $g_2(x)$ structure function at large Q^2 is zero. The evaluation of this moment from the E155x data produced a value of $-0.044 \pm 0.008 \pm 0.003$ for the proton and $-0.008 \pm 0.012 \pm 0.002$ for the deuteron. The deuteron result is consistent with the BC sum rule within the precision of the data. From the proton result, the value of the first moment is over 5 standard deviations from zero indicating a violation of the BC sum rule. However, since the range of the data did not cover all x, this test of the sum rule is not complete. Since g_2 is expected to be zero at $x = 1$, the contribution to the sum rule for $x > 0.8$ is small and negative–causing further violation. The behavior of $g_2(x)$ as $x \longrightarrow 0$ is unknown; however, if the evaluation of the sum rule from $x = 0$ to 0.02 is performed using $g_2^{ww}(x)$, there is an additional contribution of 0.020. This means that the value of the BC sum rule for the proton is still ~ 3 standard deviations from zero. Thus, unless $g_2(x)$ deviates significantly from $g_2^{ww}(x)$ as $x \longrightarrow 0$, the sum rule appears violated.

The ELT sum rule states that the second moment of the valence quark contribution to $g_1(x)$ plus twice that of $g_2(x)$ is zero. Writing the sum rule in the form of Equation 2.82 enables a measure of the difference between sea quark contributions

to $g_1(x)$ and $g_2(x)$ for the proton versus the neutron. Evaluating this integral in the measured region using the E155x $g_2(x)$ data and the fit to $g_1(x)$ produces a value of $-0.013 \pm 0.008 \pm 0.002$–which is consistent with the expected value of zero. However, once again the behavior of the structure functions as $x \longrightarrow 0$ is unknown, but since the integral is suppressed by a factor of x, the contribution in this region can be expected to be reasonably small.

5.5 d_2 Twist-3 Matrix Element

The results for the d_2 matrix element at an average Q^2 of 5 $(\mathrm{GeV/c})^2$ for the proton, deuteron, and neutron are presented here. As was previously mentioned, the value of this matrix element gives a measure of the deviation of $g_2(x)$ from $g_2^{ww}(x)$ (denoted as $\overline{g_2}(x)$–see Section 2.5) and thus indicates the importance of higher twist (beyond twist-2) contributions to the structure function. The matrix element is evaluated using

$$d_2 = 3 \int_0^1 x^2 \overline{g_2}(x, Q^2) dx, \tag{5.7}$$

where $\overline{g_2}$ is assumed to be independent of Q^2 in the measured region which is not unreasonable since d_n depends only logarithmically on Q^2 [83]. The contribution to the above integral from $x = 0$ to 0.02 is assumed negligible because of the x^2 suppression. The contribution for $x > 0.8$ is calculated using $\overline{g_2}(x) \propto (1-x)^m$, where $m = 2$ or 3, normalized to the data for $x \geq 0.5$. The contribution from both functional forms at high x was found to be negligible. The result of the d_2 calculation from E155x data was $0.0025 \pm 0.0016 \pm 0.0010$ for the proton and $0.0054 \pm 0.0023 \pm 0.0005$ for the deuteron. Combining these results with those from other SLAC experiments on the proton and deuteron (E143 [14] and E155 [19]) and neutron (E142 [6] and E154

[16]) produces the values $d_2^p = 0.0032 \pm 0.0017$ and $d_2^n = 0.0079 \pm 0.0048$ which are both within 2 standard deviations from zero. These results are presented graphically in Figure 5.19 along with theoretical predictions.

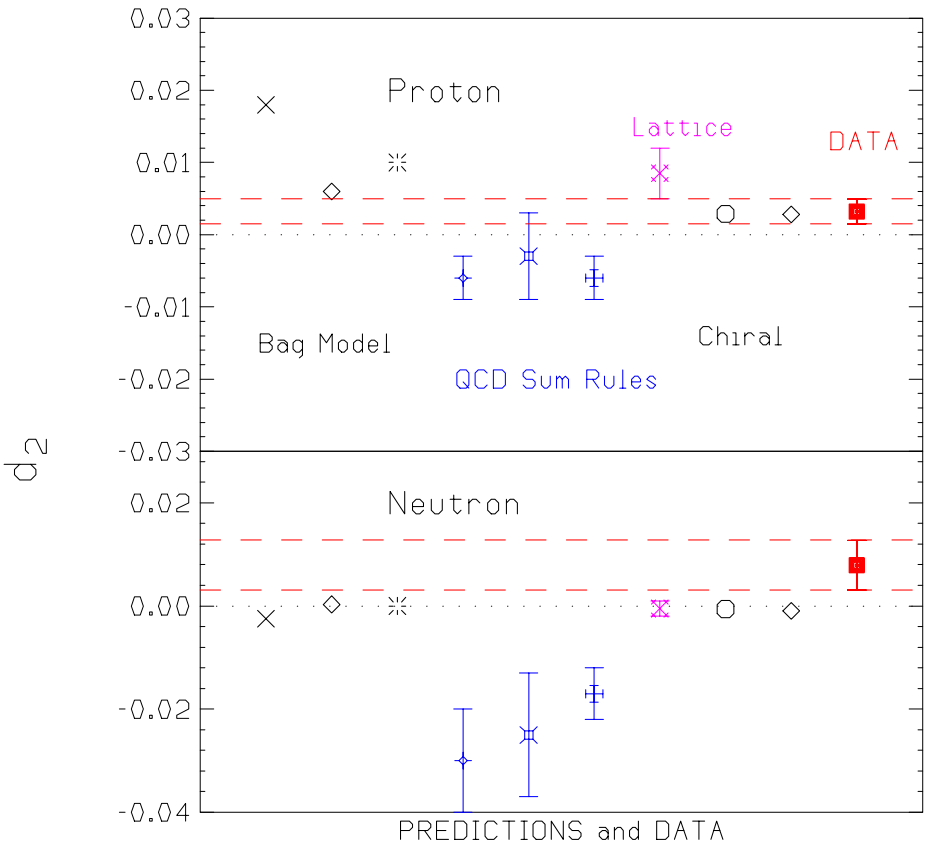

Figure 5.19: The d_2 twist-3 matrix element for the proton and neutron. The theoretical models, labeled in the proton plot, are from left to right: The bag model calculations of Song [37], Stratmann [36], and Ji and Unrau [84]; sum rules of Stein *et al.* [85], BBK [86], and Ehrnsperger and Schafer [87]; chiral soliton models of Weigel and Gamberg [34] and Wakamatsu [35]; and lattice QCD calculations of Göckeler *et al.* [88].

Chapter 6

Conclusions

New precision measurements of the deep inelastic g_2 spin structure function of the proton and deuteron and virtual photon asymmetries, $A_2^{p,d}$, have been presented. The statistical precision of these measurements allows for a meaningful comparison between the data and theory. The highest precision evaluation, to date, of the d_2 twist-3 matrix elements and the BC and ELT sum rules has been performed using the E155x data. The following paragraph will briefly summarize the experiment's results.

The measurement of $A_2^p(x)$ exhibits a clear positive trend toward high x consistent with the E143 data and the calculation of A_2 using the twist-2 g_2^{ww} model. The A_2^d data is mostly consistent with zero but also follows the trend of the calculation. Both A_2 measurements satisfy their Soffer limit. The E155x $g_2^p(x)$ data can make clear distinctions between its various models, while the statistical precision of the g_2^d data is unable to resolve them. The g_2^p bag model calculation of Stratmann is in especially good agreement with the data. Both g_2 data sets follow reasonably close to their g_2^{ww} model, although statistically significant deviations from this model have been used to calculate small but nonzero d_2 twist-3 matrix elements. The BC sum rule, for the

first moment of g_2^p, evaluated over the measured kinematic region has been found to be violated; the first moment of g_2^d was found to be consistent with the BC sum rule. The ELT sum rule result was found to be consistent with its theoretical prediction.

Although E155x was the last experiment in a long series of spin structure measurements at SLAC, the SLAC spin physics program has not ended. A new generation of high energy polarized photon-nucleon scattering experiments has been approved for running in end station A. These experiments propose to evaluate the g_1 structure function at $Q^2 = 0$, measure the deep inelastic contribution to the Gerasimov-Drell-Hearn (GDH) sum rule, and measure the polarized gluon distributions in the nucleon. Concerning the future prospects of spin physics elsewhere, the g_2 structure function measurements by the HERMES collaboration are expected soon. The first measurements of the proton quark transversity are being performed by HERMES, the PHENIX collaboration at the Relativistic Ion Collider (RHIC), and the COMPASS collaboration at CERN. PHENIX and COMPASS are also performing measurements of the polarized gluon distributions. The next decade is sure to produce significant advancements toward unraveling the puzzling nature of hadrons.

Appendix A

Proton Data Tables

x-bin	$< x >$	$< Q^2 >$	$\tilde{A}_{\perp}^{p}$	xg_2^p	A_2^p
6	0.0198	0.708	0.0251 ± 0.0160	-0.0962 ± 0.0568	-0.0410 ± 0.0336
7	0.0218	0.761	0.0041 ± 0.0067	-0.0250 ± 0.0283	-0.0090 ± 0.0248
8	0.0243	0.816	-0.0003 ± 0.0053	-0.0066 ± 0.0216	-0.0002 ± 0.0231
9	0.0274	0.863	0.0109 ± 0.0053	-0.0510 ± 0.0209	-0.0230 ± 0.0245
10	0.0308	0.912	0.0005 ± 0.0051	-0.0101 ± 0.0200	-0.0013 ± 0.0260
11	0.0347	0.965	-0.0016 ± 0.0051	-0.0021 ± 0.0196	0.0039 ± 0.0278
12	0.0390	1.018	-0.0108 ± 0.0050	0.0329 ± 0.0192	0.0273 ± 0.0299
13	0.0440	1.071	-0.0143 ± 0.0049	0.0459 ± 0.0187	0.0392 ± 0.0321
14	0.0495	1.126	-0.0081 ± 0.0048	0.0219 ± 0.0183	0.0253 ± 0.0345
15	0.0557	1.178	-0.0045 ± 0.0050	0.0085 ± 0.0189	0.0176 ± 0.0383
16	0.0627	1.233	-0.0054 ± 0.0049	0.0114 ± 0.0183	0.0229 ± 0.0411
17	0.0706	1.287	-0.0108 ± 0.0048	0.0315 ± 0.0181	0.0454 ± 0.0446
18	0.0795	1.342	-0.0033 ± 0.0048	0.0031 ± 0.0178	0.0221 ± 0.0484
19	0.0894	1.398	-0.0032 ± 0.0048	0.0027 ± 0.0180	0.0259 ± 0.0532
20	0.1007	1.450	0.0064 ± 0.0048	-0.0334 ± 0.0181	-0.0124 ± 0.0585
21	0.1133	1.500	-0.0003 ± 0.0049	-0.0085 ± 0.0184	0.0227 ± 0.0647
22	0.1276	1.544	-0.0072 ± 0.0050	0.0173 ± 0.0187	0.0659 ± 0.0717
23	0.1436	1.587	-0.0049 ± 0.0051	0.0084 ± 0.0190	0.0633 ± 0.0795
24	0.1616	1.630	-0.0034 ± 0.0052	0.0026 ± 0.0194	0.0656 ± 0.0886
25	0.1819	1.671	-0.0012 ± 0.0053	-0.0054 ± 0.0197	0.0647 ± 0.0984
26	0.2048	1.707	0.0077 ± 0.0054	-0.0380 ± 0.0197	0.0136 ± 0.1090
27	0.2305	1.741	-0.0085 ± 0.0056	0.0202 ± 0.0199	0.1578 ± 0.1217
28	0.2594	1.775	0.0003 ± 0.0058	-0.0108 ± 0.0200	0.1092 ± 0.1362
29	0.2920	1.801	-0.0095 ± 0.0061	0.0215 ± 0.0199	0.2287 ± 0.1527
30	0.3288	1.826	-0.0059 ± 0.0063	0.0090 ± 0.0194	0.2330 ± 0.1707

Table A.1: Final proton results for the 2.75° at 29 GeV.

x-bin	$< x >$	$< Q^2 >$	$\tilde{A}_\perp^p$	xg_2^p	A_2^p
16	0.0647	2.322	0.0020 ± 0.0508	0.0110 ± 0.1493	0.0165 ± 0.0828
17	0.0714	2.492	0.0090 ± 0.0213	0.0315 ± 0.0627	0.0307 ± 0.0567
18	0.0799	2.706	0.0085 ± 0.0142	0.0287 ± 0.0404	0.0319 ± 0.0484
19	0.0898	2.940	-0.0098 ± 0.0109	-0.0224 ± 0.0297	0.0010 ± 0.0444
20	0.1009	3.169	-0.0019 ± 0.0092	-0.0009 ± 0.0239	0.0185 ± 0.0428
21	0.1135	3.395	0.0215 ± 0.0084	0.0572 ± 0.0210	0.0670 ± 0.0433
22	0.1277	3.619	0.0098 ± 0.0078	0.0268 ± 0.0189	0.0496 ± 0.0445
23	0.1437	3.849	-0.0160 ± 0.0076	-0.0342 ± 0.0176	0.0018 ± 0.0468
24	0.1616	4.077	-0.0163 ± 0.0075	-0.0338 ± 0.0166	0.0060 ± 0.0496
25	0.1820	4.305	-0.0076 ± 0.0074	-0.0139 ± 0.0158	0.0322 ± 0.0529
26	0.2047	4.524	-0.0104 ± 0.0076	-0.0194 ± 0.0156	0.0338 ± 0.0580
27	0.2305	4.738	-0.0196 ± 0.0079	-0.0366 ± 0.0154	0.0199 ± 0.0639
28	0.2593	4.933	0.0053 ± 0.0084	0.0110 ± 0.0154	0.0996 ± 0.0714
29	0.2919	5.132	-0.0182 ± 0.0089	-0.0300 ± 0.0152	0.0478 ± 0.0800
30	0.3284	5.312	-0.0179 ± 0.0096	-0.0270 ± 0.0148	0.0651 ± 0.0903
31	0.3697	5.495	-0.0486 ± 0.0105	-0.0654 ± 0.0142	-0.0184 ± 0.1025
32	0.4159	5.660	-0.0252 ± 0.0115	-0.0289 ± 0.0133	0.0824 ± 0.1171
33	0.4680	5.811	-0.0406 ± 0.0131	-0.0383 ± 0.0123	0.0473 ± 0.1364
34	0.5266	5.959	-0.0356 ± 0.0150	-0.0259 ± 0.0110	0.0921 ± 0.1596
35	0.5923	6.081	-0.0253 ± 0.0178	-0.0133 ± 0.0094	0.1646 ± 0.1897
36	0.6665	6.196	-0.0430 ± 0.0217	-0.0148 ± 0.0075	0.1063 ± 0.2287
37	0.7500	6.303	-0.0864 ± 0.0281	-0.0161 ± 0.0052	-0.1036 ± 0.2834
38	0.8439	6.387	-0.0839 ± 0.0442	-0.0055 ± 0.0029	-0.1165 ± 0.3869
20	0.1018	4.397	0.1297 ± 0.1497	-0.3771 ± 0.4019	-0.2041 ± 0.1464
21	0.1149	4.886	0.0034 ± 0.0486	-0.0389 ± 0.1240	-0.0046 ± 0.0866
22	0.1280	5.344	-0.0744 ± 0.0300	0.1463 ± 0.0716	0.1185 ± 0.0698
23	0.1441	5.896	-0.0449 ± 0.0245	0.0670 ± 0.0543	0.0735 ± 0.0650
24	0.1620	6.507	0.0159 ± 0.0214	-0.0666 ± 0.0440	-0.0186 ± 0.0627
25	0.1821	7.173	0.0065 ± 0.0193	-0.0473 ± 0.0365	-0.0015 ± 0.0614
26	0.2047	7.847	-0.0214 ± 0.0195	0.0013 ± 0.0335	0.0445 ± 0.0638
27	0.2304	8.566	0.0201 ± 0.0202	-0.0667 ± 0.0314	-0.0141 ± 0.0674
28	0.2592	9.283	-0.0162 ± 0.0213	-0.0123 ± 0.0296	0.0470 ± 0.0723
29	0.2918	10.039	0.0323 ± 0.0229	-0.0729 ± 0.0280	-0.0211 ± 0.0785
30	0.3282	10.830	-0.0168 ± 0.0252	-0.0136 ± 0.0262	0.0642 ± 0.0860
31	0.3693	11.667	-0.0101 ± 0.0285	-0.0192 ± 0.0248	0.0643 ± 0.0963
32	0.4154	12.484	0.0063 ± 0.0331	-0.0284 ± 0.0232	0.0501 ± 0.1098
33	0.4672	13.296	0.0541 ± 0.0399	-0.0483 ± 0.0215	-0.0175 ± 0.1281
34	0.5255	14.101	0.0319 ± 0.0504	-0.0264 ± 0.0194	0.0349 ± 0.1536
35	0.5909	14.925	0.0687 ± 0.0671	-0.0265 ± 0.0168	-0.0186 ± 0.1892
36	0.6647	15.695	-0.1821 ± 0.0936	0.0209 ± 0.0133	0.4823 ± 0.2399

Table A.2: Final proton results for the 5.5° (top) and 10.5° (bottom) at 29 GeV.

x-bin	$< x >$	$< Q^2 >$	$\tilde{A}_{\perp}^{p}$	xg_2^p	A_2^p
6	0.0195	0.809	-0.0007 ± 0.0090	-0.0055 ± 0.0351	-0.0001 ± 0.0240
7	0.0217	0.875	-0.0022 ± 0.0052	0.0012 ± 0.0238	0.0029 ± 0.0208
8	0.0243	0.935	-0.0057 ± 0.0047	0.0163 ± 0.0205	0.0100 ± 0.0206
9	0.0274	0.993	0.0041 ± 0.0046	-0.0263 ± 0.0196	-0.0090 ± 0.0218
10	0.0308	1.055	0.0001 ± 0.0046	-0.0096 ± 0.0190	-0.0008 ± 0.0232
11	0.0347	1.121	-0.0037 ± 0.0045	0.0060 ± 0.0183	0.0080 ± 0.0245
12	0.0391	1.187	-0.0026 ± 0.0044	0.0014 ± 0.0178	0.0066 ± 0.0262
13	0.0440	1.257	-0.0032 ± 0.0043	0.0033 ± 0.0172	0.0090 ± 0.0280
14	0.0495	1.323	-0.0006 ± 0.0044	-0.0071 ± 0.0176	0.0035 ± 0.0308
15	0.0557	1.394	-0.0032 ± 0.0043	0.0028 ± 0.0169	0.0120 ± 0.0328
16	0.0627	1.464	-0.0072 ± 0.0043	0.0183 ± 0.0167	0.0261 ± 0.0354
17	0.0706	1.539	-0.0085 ± 0.0042	0.0230 ± 0.0164	0.0336 ± 0.0383
18	0.0794	1.611	0.0036 ± 0.0043	-0.0242 ± 0.0167	-0.0045 ± 0.0420
19	0.0894	1.680	-0.0031 ± 0.0044	0.0015 ± 0.0169	0.0224 ± 0.0464
20	0.1007	1.745	-0.0048 ± 0.0045	0.0078 ± 0.0172	0.0338 ± 0.0513
21	0.1133	1.809	-0.0030 ± 0.0046	0.0005 ± 0.0175	0.0315 ± 0.0566
22	0.1275	1.873	-0.0027 ± 0.0046	-0.0007 ± 0.0176	0.0367 ± 0.0625
23	0.1436	1.933	-0.0016 ± 0.0048	-0.0050 ± 0.0180	0.0387 ± 0.0694
24	0.1616	1.988	-0.0078 ± 0.0049	0.0180 ± 0.0184	0.0830 ± 0.0775
25	0.1819	2.037	0.0106 ± 0.0050	-0.0506 ± 0.0185	-0.0164 ± 0.0860
26	0.2048	2.087	-0.0037 ± 0.0051	0.0023 ± 0.0186	0.0873 ± 0.0955
27	0.2305	2.137	0.0063 ± 0.0052	-0.0334 ± 0.0186	0.0330 ± 0.1062
28	0.2595	2.178	0.0074 ± 0.0054	-0.0363 ± 0.0187	0.0405 ± 0.1189
29	0.2921	2.217	0.0008 ± 0.0056	-0.0131 ± 0.0183	0.1168 ± 0.1329
30	0.3286	2.260	-0.0051 ± 0.0059	0.0055 ± 0.0178	0.1999 ± 0.1482

Table A.3: Final proton results for the 2.75° at 32 GeV.

x-bin	$< x >$	$< Q^2 >$	$\tilde{A}_\perp^p$	xg_2^p	A_2^p
16	0.0638	2.645	0.0165 ± 0.0284	0.0586 ± 0.0900	0.0397 ± 0.0586
17	0.0712	2.873	-0.0171 ± 0.0155	-0.0480 ± 0.0488	-0.0153 ± 0.0458
18	0.0799	3.128	0.0043 ± 0.0110	0.0186 ± 0.0331	0.0234 ± 0.0402
19	0.0898	3.402	0.0022 ± 0.0088	0.0115 ± 0.0255	0.0221 ± 0.0377
20	0.1009	3.670	-0.0133 ± 0.0078	-0.0316 ± 0.0214	-0.0028 ± 0.0371
21	0.1135	3.943	0.0004 ± 0.0072	0.0054 ± 0.0188	0.0250 ± 0.0376
22	0.1277	4.220	-0.0014 ± 0.0068	0.0005 ± 0.0170	0.0257 ± 0.0387
23	0.1436	4.501	-0.0036 ± 0.0066	-0.0049 ± 0.0159	0.0262 ± 0.0407
24	0.1617	4.783	0.0029 ± 0.0065	0.0098 ± 0.0150	0.0450 ± 0.0431
25	0.1818	5.063	-0.0035 ± 0.0067	-0.0049 ± 0.0147	0.0388 ± 0.0467
26	0.2047	5.330	-0.0030 ± 0.0069	-0.0038 ± 0.0143	0.0484 ± 0.0509
27	0.2304	5.590	-0.0199 ± 0.0073	-0.0373 ± 0.0143	0.0177 ± 0.0566
28	0.2592	5.846	-0.0071 ± 0.0076	-0.0114 ± 0.0141	0.0604 ± 0.0628
29	0.2919	6.096	-0.0218 ± 0.0082	-0.0359 ± 0.0140	0.0343 ± 0.0706
30	0.3284	6.331	-0.0058 ± 0.0088	-0.0080 ± 0.0135	0.0954 ± 0.0794
31	0.3697	6.560	-0.0359 ± 0.0095	-0.0477 ± 0.0128	0.0219 ± 0.0899
32	0.4159	6.771	-0.0237 ± 0.0105	-0.0266 ± 0.0120	0.0801 ± 0.1029
33	0.4680	6.974	-0.0356 ± 0.0119	-0.0327 ± 0.0110	0.0599 ± 0.1198
34	0.5266	7.167	-0.0274 ± 0.0137	-0.0192 ± 0.0097	0.1140 ± 0.1402
35	0.5923	7.338	-0.0295 ± 0.0163	-0.0147 ± 0.0081	0.1304 ± 0.1669
36	0.6666	7.498	-0.0285 ± 0.0198	-0.0090 ± 0.0062	0.1570 ± 0.2012
37	0.7499	7.630	-0.0494 ± 0.0256	-0.0082 ± 0.0042	0.0704 ± 0.2496
38	0.8442	7.757	0.0327 ± 0.0394	0.0018 ± 0.0022	0.4731 ± 0.3378
20	0.1017	4.992	0.0335 ± 0.1206	-0.1296 ± 0.3525	-0.0543 ± 0.1273
21	0.1148	5.546	-0.0050 ± 0.0384	-0.0189 ± 0.1064	0.0075 ± 0.0746
22	0.1282	6.089	-0.0207 ± 0.0241	0.0194 ± 0.0623	0.0331 ± 0.0607
23	0.1441	6.715	0.0054 ± 0.0184	-0.0482 ± 0.0439	-0.0062 ± 0.0545
24	0.1621	7.417	-0.0341 ± 0.0157	0.0388 ± 0.0345	0.0564 ± 0.0518
25	0.1821	8.178	-0.0149 ± 0.0143	-0.0073 ± 0.0290	0.0290 ± 0.0511
26	0.2047	8.969	-0.0193 ± 0.0146	-0.0026 ± 0.0265	0.0384 ± 0.0530
27	0.2303	9.818	-0.0105 ± 0.0154	-0.0204 ± 0.0253	0.0291 ± 0.0565
28	0.2592	10.678	-0.0034 ± 0.0164	-0.0319 ± 0.0239	0.0236 ± 0.0607
29	0.2917	11.585	0.0216 ± 0.0178	-0.0629 ± 0.0226	-0.0082 ± 0.0659
30	0.3283	12.523	-0.0138 ± 0.0197	-0.0179 ± 0.0212	0.0535 ± 0.0723
31	0.3694	13.486	0.0424 ± 0.0221	-0.0674 ± 0.0198	-0.0242 ± 0.0806
32	0.4156	14.449	0.0205 ± 0.0255	-0.0397 ± 0.0183	0.0202 ± 0.0914
33	0.4674	15.406	-0.0149 ± 0.0303	-0.0117 ± 0.0165	0.0909 ± 0.1057
34	0.5257	16.382	0.0762 ± 0.0379	-0.0439 ± 0.0146	-0.0495 ± 0.1258
35	0.5911	17.346	0.0384 ± 0.0498	-0.0189 ± 0.0124	0.0286 ± 0.1540
36	0.6643	18.282	-0.0184 ± 0.0705	-0.0026 ± 0.0099	0.1477 ± 0.1963

Table A.4: Final proton results for the 5.5° (top) and 10.5° (bottom) at 32 GeV.

Appendix B

Deuteron Data Tables

x-bin	$< x >$	$< Q^2 >$	$\tilde{A}_\perp^d$	xg_2^d	A_2^d
6	0.0198	0.708	0.0135 ± 0.0231	-0.0465 ± 0.0777	-0.0216 ± 0.0403
7	0.0218	0.762	-0.0004 ± 0.0099	0.0004 ± 0.0394	0.0006 ± 0.0300
8	0.0243	0.816	-0.0004 ± 0.0079	0.0002 ± 0.0302	0.0006 ± 0.0280
9	0.0274	0.863	-0.0046 ± 0.0078	0.0158 ± 0.0292	0.0094 ± 0.0298
10	0.0308	0.912	0.0034 ± 0.0076	-0.0143 ± 0.0281	-0.0075 ± 0.0317
11	0.0347	0.965	0.0064 ± 0.0076	-0.0251 ± 0.0274	-0.0147 ± 0.0339
12	0.0391	1.018	-0.0012 ± 0.0075	0.0027 ± 0.0270	0.0032 ± 0.0364
13	0.0440	1.070	0.0038 ± 0.0072	-0.0158 ± 0.0260	-0.0097 ± 0.0389
14	0.0495	1.126	-0.0065 ± 0.0071	0.0212 ± 0.0254	0.0189 ± 0.0418
15	0.0557	1.178	0.0068 ± 0.0073	-0.0266 ± 0.0262	-0.0197 ± 0.0463
16	0.0627	1.234	0.0064 ± 0.0071	-0.0251 ± 0.0253	-0.0194 ± 0.0496
17	0.0706	1.287	0.0071 ± 0.0070	-0.0277 ± 0.0248	-0.0230 ± 0.0538
18	0.0795	1.343	-0.0074 ± 0.0069	0.0235 ± 0.0244	0.0313 ± 0.0583
19	0.0894	1.398	-0.0021 ± 0.0070	0.0046 ± 0.0247	0.0128 ± 0.0643
20	0.1007	1.450	0.0099 ± 0.0071	-0.0375 ± 0.0247	-0.0390 ± 0.0707
21	0.1133	1.500	-0.0200 ± 0.0072	0.0665 ± 0.0251	0.1055 ± 0.0783
22	0.1276	1.545	0.0016 ± 0.0074	-0.0088 ± 0.0255	0.0014 ± 0.0872
23	0.1436	1.587	0.0009 ± 0.0076	-0.0066 ± 0.0257	0.0078 ± 0.0968
24	0.1616	1.631	-0.0029 ± 0.0078	0.0061 ± 0.0263	0.0359 ± 0.1084
25	0.1819	1.672	-0.0097 ± 0.0081	0.0284 ± 0.0266	0.0900 ± 0.1210
26	0.2048	1.707	0.0062 ± 0.0083	-0.0239 ± 0.0266	-0.0158 ± 0.1348
27	0.2305	1.742	-0.0004 ± 0.0086	-0.0027 ± 0.0268	0.0435 ± 0.1512
28	0.2594	1.775	-0.0069 ± 0.0091	0.0166 ± 0.0269	0.1131 ± 0.1701
29	0.2920	1.802	0.0004 ± 0.0096	-0.0050 ± 0.0267	0.0649 ± 0.1918
30	0.3288	1.827	0.0072 ± 0.0101	-0.0222 ± 0.0259	0.0161 ± 0.2157

Table B.1: Final deuteron results for the 2.75° at 29 GeV.

x-bin	$< x >$	$< Q^2 >$	$\tilde{A}_\perp^d$	xg_2^d	A_2^d
16	0.0647	2.322	-0.0090 ± 0.0731	-0.0239 ± 0.2031	-0.0120 ± 0.0993
17	0.0714	2.492	0.0508 ± 0.0308	0.1427 ± 0.0857	0.0944 ± 0.0682
18	0.0799	2.706	0.0530 ± 0.0207	0.1426 ± 0.0553	0.1005 ± 0.0584
19	0.0898	2.940	-0.0052 ± 0.0159	-0.0121 ± 0.0406	-0.0039 ± 0.0537
20	0.1009	3.170	-0.0087 ± 0.0135	-0.0199 ± 0.0326	-0.0093 ± 0.0518
21	0.1136	3.396	-0.0116 ± 0.0124	-0.0257 ± 0.0285	-0.0139 ± 0.0525
22	0.1277	3.621	0.0025 ± 0.0116	0.0065 ± 0.0256	0.0155 ± 0.0541
23	0.1437	3.851	0.0027 ± 0.0113	0.0067 ± 0.0238	0.0188 ± 0.0571
24	0.1617	4.078	0.0036 ± 0.0112	0.0081 ± 0.0224	0.0242 ± 0.0608
25	0.1820	4.307	0.0172 ± 0.0112	0.0333 ± 0.0212	0.0599 ± 0.0652
26	0.2047	4.527	0.0097 ± 0.0117	0.0180 ± 0.0209	0.0490 ± 0.0718
27	0.2305	4.742	0.0007 ± 0.0123	0.0019 ± 0.0205	0.0339 ± 0.0796
28	0.2593	4.936	-0.0035 ± 0.0132	-0.0049 ± 0.0204	0.0306 ± 0.0894
29	0.2920	5.136	-0.0231 ± 0.0141	-0.0323 ± 0.0200	-0.0181 ± 0.1007
30	0.3284	5.317	-0.0008 ± 0.0155	-0.0006 ± 0.0195	0.0610 ± 0.1147
31	0.3697	5.500	0.0042 ± 0.0172	0.0048 ± 0.0187	0.0936 ± 0.1313
32	0.4160	5.663	-0.0356 ± 0.0192	-0.0323 ± 0.0175	-0.0307 ± 0.1514
33	0.4680	5.816	0.0294 ± 0.0222	0.0215 ± 0.0162	0.2371 ± 0.1778
34	0.5267	5.965	0.0050 ± 0.0261	0.0028 ± 0.0144	0.1706 ± 0.2103
35	0.5924	6.088	-0.0269 ± 0.0317	-0.0105 ± 0.0123	0.0603 ± 0.2530
36	0.6666	6.203	-0.0344 ± 0.0399	-0.0085 ± 0.0099	0.0498 ± 0.3096
37	0.7499	6.310	0.0232 ± 0.0528	0.0031 ± 0.0070	0.3610 ± 0.3879
20	0.1018	4.395	-0.0918 ± 0.2429	0.2199 ± 0.6041	0.1439 ± 0.1864
21	0.1149	4.881	0.0152 ± 0.0813	-0.0449 ± 0.1908	-0.0238 ± 0.1120
22	0.1280	5.340	-0.0250 ± 0.0521	0.0445 ± 0.1135	0.0399 ± 0.0920
23	0.1441	5.896	0.0250 ± 0.0439	-0.0609 ± 0.0880	-0.0374 ± 0.0872
24	0.1621	6.498	-0.0058 ± 0.0384	-0.0011 ± 0.0703	0.0113 ± 0.0840
25	0.1821	7.155	0.0407 ± 0.0347	-0.0804 ± 0.0578	-0.0590 ± 0.0825
26	0.2047	7.834	0.0130 ± 0.0359	-0.0325 ± 0.0534	-0.0145 ± 0.0865
27	0.2304	8.576	-0.0028 ± 0.0379	-0.0100 ± 0.0501	0.0117 ± 0.0923
28	0.2591	9.300	-0.0319 ± 0.0411	0.0232 ± 0.0477	0.0594 ± 0.1002
29	0.2917	10.050	-0.0364 ± 0.0452	0.0228 ± 0.0455	0.0711 ± 0.1102
30	0.3282	10.821	0.0456 ± 0.0512	-0.0516 ± 0.0431	-0.0517 ± 0.1227
31	0.3693	11.645	-0.0839 ± 0.0592	0.0459 ± 0.0410	0.1613 ± 0.1390
32	0.4154	12.455	-0.0021 ± 0.0701	-0.0096 ± 0.0384	0.0383 ± 0.1601
33	0.4673	13.249	-0.0393 ± 0.0863	0.0074 ± 0.0355	0.1126 ± 0.1888
34	0.5255	14.031	0.0457 ± 0.1115	-0.0198 ± 0.0322	-0.0239 ± 0.2291
35	0.5907	14.790	0.1516 ± 0.1544	-0.0326 ± 0.0287	-0.2118 ± 0.2888
36	0.6641	15.500	0.0027 ± 0.2237	-0.0028 ± 0.0235	0.0824 ± 0.3739

Table B.2: Final deuteron results for the 5.5° (top) and 10.5° (bottom) at 29 GeV.

x-bin	$< x >$	$< Q^2 >$	$\tilde{A}_\perp^d$	xg_2^d	A_2^d
6	0.0195	0.809	-0.0144 ± 0.0146	0.0524 ± 0.0539	0.0223 ± 0.0304
7	0.0217	0.875	0.0013 ± 0.0086	-0.0067 ± 0.0373	-0.0026 ± 0.0267
8	0.0243	0.935	0.0083 ± 0.0078	-0.0357 ± 0.0326	-0.0161 ± 0.0267
9	0.0274	0.992	-0.0038 ± 0.0077	0.0140 ± 0.0312	0.0075 ± 0.0282
10	0.0308	1.054	0.0068 ± 0.0077	-0.0285 ± 0.0305	-0.0144 ± 0.0301
11	0.0347	1.120	-0.0009 ± 0.0076	0.0019 ± 0.0295	0.0020 ± 0.0320
12	0.0391	1.185	-0.0024 ± 0.0076	0.0073 ± 0.0290	0.0057 ± 0.0344
13	0.0440	1.254	-0.0120 ± 0.0074	0.0435 ± 0.0282	0.0299 ± 0.0368
14	0.0495	1.321	-0.0059 ± 0.0073	0.0202 ± 0.0275	0.0162 ± 0.0394
15	0.0557	1.393	0.0018 ± 0.0072	-0.0091 ± 0.0271	-0.0043 ± 0.0426
16	0.0627	1.464	-0.0024 ± 0.0071	0.0063 ± 0.0262	0.0084 ± 0.0456
17	0.0706	1.538	-0.0071 ± 0.0071	0.0234 ± 0.0261	0.0248 ± 0.0497
18	0.0794	1.610	-0.0014 ± 0.0071	0.0022 ± 0.0259	0.0074 ± 0.0540
19	0.0894	1.677	0.0119 ± 0.0072	-0.0462 ± 0.0263	-0.0418 ± 0.0597
20	0.1007	1.742	-0.0001 ± 0.0073	-0.0029 ± 0.0263	0.0051 ± 0.0657
21	0.1133	1.806	-0.0020 ± 0.0075	0.0035 ± 0.0266	0.0150 ± 0.0726
22	0.1276	1.868	-0.0050 ± 0.0076	0.0140 ± 0.0266	0.0328 ± 0.0801
23	0.1436	1.927	-0.0135 ± 0.0078	0.0426 ± 0.0269	0.0819 ± 0.0891
24	0.1616	1.981	-0.0031 ± 0.0080	0.0067 ± 0.0274	0.0332 ± 0.0996
25	0.1820	2.031	-0.0034 ± 0.0083	0.0071 ± 0.0275	0.0413 ± 0.1110
26	0.2048	2.081	-0.0095 ± 0.0085	0.0263 ± 0.0273	0.0910 ± 0.1234
27	0.2305	2.128	-0.0008 ± 0.0088	-0.0017 ± 0.0273	0.0417 ± 0.1383
28	0.2595	2.169	-0.0055 ± 0.0092	0.0119 ± 0.0270	0.0903 ± 0.1549
29	0.2920	2.212	0.0099 ± 0.0096	-0.0315 ± 0.0266	-0.0233 ± 0.1740
30	0.3286	2.256	0.0027 ± 0.0103	-0.0109 ± 0.0260	0.0542 ± 0.1966

Table B.3: Final deuteron results for the 2.75 ° at 32 GeV.

x-bin	$< x >$	$< Q^2 >$	$\tilde{A}_\perp^d$	xg_2^d	A_2^d
16	0.0638	2.645	0.0309 ± 0.0418	0.0941 ± 0.1254	0.0539 ± 0.0711
17	0.0712	2.874	0.0173 ± 0.0234	0.0529 ± 0.0697	0.0334 ± 0.0563
18	0.0799	3.131	0.0141 ± 0.0167	0.0415 ± 0.0475	0.0290 ± 0.0496
19	0.0898	3.407	-0.0023 ± 0.0133	-0.0048 ± 0.0359	0.0013 ± 0.0462
20	0.1009	3.675	-0.0005 ± 0.0118	0.0002 ± 0.0299	0.0057 ± 0.0455
21	0.1135	3.946	-0.0080 ± 0.0109	-0.0179 ± 0.0263	-0.0065 ± 0.0463
22	0.1277	4.223	0.0168 ± 0.0105	0.0398 ± 0.0239	0.0417 ± 0.0480
23	0.1436	4.506	0.0144 ± 0.0104	0.0324 ± 0.0225	0.0405 ± 0.0508
24	0.1617	4.789	0.0016 ± 0.0103	0.0044 ± 0.0212	0.0185 ± 0.0542
25	0.1819	5.070	0.0053 ± 0.0107	0.0113 ± 0.0208	0.0304 ± 0.0591
26	0.2047	5.339	0.0001 ± 0.0111	0.0010 ± 0.0201	0.0239 ± 0.0646
27	0.2304	5.599	-0.0075 ± 0.0119	-0.0120 ± 0.0202	0.0116 ± 0.0724
28	0.2593	5.856	-0.0046 ± 0.0127	-0.0064 ± 0.0198	0.0256 ± 0.0809
29	0.2919	6.107	0.0164 ± 0.0139	0.0238 ± 0.0196	0.0918 ± 0.0918
30	0.3284	6.344	-0.0259 ± 0.0151	-0.0321 ± 0.0189	-0.0175 ± 0.1040
31	0.3697	6.574	-0.0274 ± 0.0168	-0.0291 ± 0.0180	-0.0124 ± 0.1191
32	0.4159	6.787	-0.0300 ± 0.0189	-0.0266 ± 0.0169	-0.0098 ± 0.1378
33	0.4680	6.991	-0.0013 ± 0.0219	-0.0008 ± 0.0156	0.1076 ± 0.1622
34	0.5265	7.185	-0.0001 ± 0.0258	-0.0000 ± 0.0137	0.1369 ± 0.1921
35	0.5923	7.359	-0.0334 ± 0.0315	-0.0122 ± 0.0116	0.0265 ± 0.2318
36	0.6666	7.524	-0.0185 ± 0.0395	-0.0042 ± 0.0090	0.1125 ± 0.2833
37	0.7498	7.653	0.0415 ± 0.0513	0.0049 ± 0.0061	0.4180 ± 0.3525
20	0.1017	4.985	-0.0417 ± 0.1246	0.1035 ± 0.3369	0.0651 ± 0.1294
21	0.1147	5.537	0.0225 ± 0.0520	-0.0673 ± 0.1325	-0.0358 ± 0.0868
22	0.1280	6.080	0.0179 ± 0.0363	-0.0529 ± 0.0854	-0.0278 ± 0.0744
23	0.1440	6.717	-0.0225 ± 0.0306	0.0367 ± 0.0658	0.0356 ± 0.0703
24	0.1621	7.424	-0.0526 ± 0.0261	0.0905 ± 0.0512	0.0823 ± 0.0669
25	0.1822	8.181	-0.0035 ± 0.0237	-0.0073 ± 0.0420	0.0079 ± 0.0657
26	0.2048	8.972	0.0253 ± 0.0240	-0.0539 ± 0.0377	-0.0339 ± 0.0680
27	0.2303	9.824	-0.0281 ± 0.0256	0.0245 ± 0.0357	0.0482 ± 0.0727
28	0.2591	10.671	-0.0064 ± 0.0279	-0.0069 ± 0.0340	0.0185 ± 0.0791
29	0.2916	11.574	-0.0064 ± 0.0311	-0.0079 ± 0.0325	0.0220 ± 0.0872
30	0.3282	12.520	0.0150 ± 0.0353	-0.0269 ± 0.0308	-0.0058 ± 0.0969
31	0.3693	13.493	0.0473 ± 0.0409	-0.0464 ± 0.0290	-0.0506 ± 0.1095
32	0.4154	14.472	0.0651 ± 0.0487	-0.0475 ± 0.0271	-0.0735 ± 0.1262
33	0.4672	15.458	0.0200 ± 0.0608	-0.0174 ± 0.0252	0.0067 ± 0.1494
34	0.5254	16.459	-0.1310 ± 0.0795	0.0309 ± 0.0229	0.2743 ± 0.1816
35	0.5908	17.466	0.0147 ± 0.1096	-0.0072 ± 0.0200	0.0372 ± 0.2274
36	0.6646	18.424	-0.1782 ± 0.1583	0.0154 ± 0.0159	0.4091 ± 0.2927

Table B.4: Final deuteron results for the 5.5° (top) and 10.5° (bottom) at 32 GeV.

References

[1] E80 Collaboration. *Phys. Rev. Lett.*, **37**, 1261 (1976).

[2] E80 Collaboration. *Phys. Rev. Lett.*, **41**, 70 (1978).

[3] E130 Collaboration. *Phys. Rev. Lett.*, **51**, 1135 (1983).

[4] EMC, J. Ashman et al. *Phys. Lett.*, **B206**, 364 (1988).

[5] E142 Collaboration. *Phys. Rev. Lett.*, **71**, 959 (1993).

[6] E142 Collaboration. *Phys. Rev.*, **D54**, 6620 (1996).

[7] SMC, D. Adams et al. *Phys. Lett.*, **B336**, 125 (1994).

[8] SMC, D. Adams et al. *Phys. Lett.*, **B396**, 338 (1997).

[9] SMC, B. Adeva et al . *Phys. Lett.*, **B412**, 414 (1997).

[10] E143 Collaboration. *Phys. Lett.*, **75**, 25 (1995).

[11] E143 Collaboration. *Phys. Lett.*, **74**, 346 (1995).

[12] E143 Collaboration. *Phys. Lett.*, **B364**, 61 (1995).

[13] E143 Collaboration. *Phys. Rev. Lett.*, **76**, 587 (1996).

[14] E143 Collaboration. *Phys. Rev.*, **D58**, 112003 (1998).

[15] E143 Collaboration. *Phys. Lett.*, **B452**, 194 (1999).

[16] E154 Collaboration. *Phys. Rev. Lett.*, **79**, 26 (1997).

[17] E154 Collaboration. *Phys. Lett.*, **B404**, 377 (1997).

[18] E154 Collaboration. *Phys. Lett.*, **B405**, 180 (1997).

[19] E155 Collaboration. *Phys. Lett.*, **B458**, 529 (1998).

[20] E155 Collaboration. *Phys. Lett.*, **B458**, 536 (1998).

[21] E155 Collaboration. *Phys. Lett.*, **B463**, 339 (1999).

[22] E155 Collaboration. *Phys. Lett.*, **B493**, 19 (2000).

[23] HERMES Collaboration. *Phys. Lett.*, **B404**, 383 (1997).

[24] HERMES Collaboration. *Phys. Lett.*, **B442**, 484 (1998).

[25] J. D. Bjorken and E. A. Paschos. *Phys. Rev.*, **185**, 1975 (1969).

[26] C. G. Callan and D. Gross. *Phys. Rev. Lett.*, **22**, 158 (1969).

[27] M. G. Doncel and E. De Rafael. *Nuovo Cimento*, **4A**, 363 (1971).

[28] J. Soffer and O. V. Teryaev. *Phys. Lett.*, **B490**, 106 (2000).

[29] R. P. Feynman. *Phys. Rev. Lett.*, **23** (1969).

[30] M. Gell-Mann. *Phys. Lett.*, **8**, 214 (1964).

[31] G. Zweig. *CERN-TH-412*, (1964).

[32] NMC, M. Arneodo et al . *Phys. Lett.*, **B364**, 107 (1995).

[33] M. Anselmino, A. Efremov, and E. Leader. *Phys. Rep.*, **261**, 1 (1995) [hep-ph/9501369].

[34] H. Weigel and L. Gamberg. *Nucl. Phys.*, **A680**, 48 (2000).

[35] M. Wakamatsu. *Phys. Lett.*, **B487**, 118 (2000).

[36] M. Stratmann. *Z. Phys.*, **C60**, 763 (1993).

[37] X. Song. *Phys. Rev.*, **D54**, 1955 (1996).

[38] B Lampe and E. Reya. *Phys. Rep.* **332** 1 (2000) [hep-ph/9810270].

[39] J. Kodaira et al. *Nucl. Phys.*, **B159**, 99 (1979).

[40] E. Leader and E. Predazzi. *An Introduction to Gauge Theories and Modern Particle Physics: Volume 2* (Cambridge, 1996).

[41] S. Wandzura and F. Wilczek. *Phys. Lett.*, **B72**, 195 (1977).

[42] H. Burkhardt and W. Cottingham. *Ann. Phys.*, **56**, 453 (1970).

[43] A. Efremov, O. Teryaev, and E. Leader. *Phys. Rev.*, **D55**, 4307 (1997).

[44] J. E. Clendenin et al. *SLAC-PUB-7619* (August 1997). Unpublished.

[45] R. Alley et al. *Nucl. Instr. and Meth.*, **A365**, 1 (1995).

[46] Charles Y. Prescott. *E155 Tech Note 24* (November 1996). Unpublished.

[47] T. R. Wright, H.R. Band. *E155 Tech Note 108* (February 2000). Unpublished.

[48] H. R. Band et al. *Nucl. Instr. and Meth.*, **A400**, 24 (1997).

[49] R. Dostert et al. In *Proceedings of the* 4^{th} *International Workshop on Polarized Target Materials and Techniques*, W. Meyer, editor, p. 33 (1984).

[50] C. D. Jeffries. *Phys. Rev.*, **117**, 1056 (1960).

[51] P. M. McKee *The Spin Structure Function of the Proton from SLAC Experiment E155.* Ph.D. thesis, University of Virginia (2000).

[52] A. Abragam. *Principles of Nuclear Magnetism* (Oxford University Press, 1961).

[53] M. Goldman. *J. Magn. Res.*, **17**, 393 (1975).

[54] W. Tobias. *Measurement of the Spin Structure Functions g_1 and g_2 of the Deuteron.* Ph.D. thesis, University of Virginia (2000).

[55] N. W. Schellingerhout et al. *Phys. Rev.*, **C48**, 2714 (1993).

[56] G. R. Court et al. In *Proceedings of the 4^{th} International Workshop on Polarized Target Materials and Techniques*, W. Meyer, editor, p. 122 (1984).

[57] Bültmann et al. *Nucl. Instr. and Meth.*, **A425**, 22 (1999).

[58] D. C. Crabb and W. Meyer. *Annu. Rev. Nucl. Part. Sci.*, **47**, 67 (1997)

[59] T. O. Ninikoski and A. Rijllart. *Nucl. Instr. and Meth.*, **199**, 485 (1982).

[60] S. Bültmann. *E155 Tech Note 84* (July 1999). Unpublished.

[61] E155 Collaboration. *E155 Tech Note 79* (August 1997). Unpublished.

[62] P. Bosted. *E155 Tech Note 34* (June 1997). Unpublished.

[63] M. Buénerd. *E155 Tech Note 15* (July 1996). Unpublished.

[64] Charles Y. Prescott. *E155 Tech Note 25* (December 1996). Unpublished.

[65] G. T. Bartha et al. *Nucl. Instr. and Meth.*, **A275**, 59-70 (1989).

[66] Paul King. *E155 Tech Note 74* (December 1998). Unpublished.

[67] Patrick D. Ryan. *E155 Tech Note 95* (August 1999). Unpublished.

[68] P. B. Wilson. *SLAC Tech Note 73-015* (December 1973). Unpublished.

[69] P. L. Anthony and Z. M. Szalata. *SLAC-PUB-7201* (June 1996). Unpublished.

[70] N. Benmouna. *E155 Tech Note 83* (June 1999). Unpublished.

[71] Y. Kolomensky. *Precision Measurement of the Neutron Spin Dependent Structure Functions*. Ph.D. thesis, University of Massachusetts, Amherst (1997).

[72] P. Bosted. *E155 Tech Note 52* (March 1998). Unpublished.

[73] N. Benmouna. *E155 Tech Note 106* (November 1999). Unpublished.

[74] N. Benmouna. *E155 Tech Note 107* (November 1999). Unpublished.

[75] L. Sorrell. *E155 Tech Note 113* (July 2000). Unpublished.

[76] EMC, J. Ashman et al. *Phys. Lett.*, **B202**, 603 (1988).

[77] O. A. Rondon. *Phys. Rev.*, **C60**, (1990) 035201.

[78] Peter Renton. *Electroweak Interactions: An Introduction to the Physics of Quarks & Leptons* (Cambridge, 1990).

[79] N. Benmouna. *A Precision Measurement of the Spin Structure Function* g_2^p. Ph.D. thesis, American University, Washington D.C. (2001).

[80] T. V. Kukhto and N. M. Shumeiko. *Nucl. Phys.*, **B219**, 412 (1983).

[81] G. Mitchell. *A Precision Measurement of the Spin Structure Function* $g_1(x, Q^2)$ *for the Proton and Deuteron.* Ph.D. thesis, University of Wisconsin, Madison WI. (1999).

[82] T. Tsai. *Rev. Mod.. Phys.*, **46**, 815 (1974).

[83] E. Shuryak and A. Vainshtein. *Nucl. Phys.*, **B201**, 141 (1982).

[84] X. Ji and P. Unrau. *Nucl. Phys.*, **B333**, 228 (1994).

[85] E. Stein et al. *Nucl. Phys.*, **B343**, 369 (1995).

[86] I. Balitsky, V. Braun, and A. Kolesnichenko. *Phys. Lett.*, **B242**, 245 (1990); **B318**, 648 (1993) (Erratum).

[87] B. Ehrnsperger and A. Schafer. *Phys. Rev.*, **D52**, 2709 (1995).

[88] M. Göckler et al. *Phys. Rev.*, **D63**, 074506 (2001).